UNIVERSITEIT ANTWERPEN

Faculteit Wetenschappen

Departement Natuurkunde

Vortex matter in mesoscopic superconductors

A theoretical study of the critical parameters and the vortex configuration in singly and multiply connected mesoscopic superconductors

---

Vortexmaterie in mesoscopische supergeleiders

Een theoretische studie van de kritische parameters en de vortexconfiguratie in enkelvoudig en meervoudig samenhangende mesoscopische supergeleiders

Proefschrift voorgelegd tot het behalen van de graad van
doctor in de wetenschappen
aan de Universitaire Instelling Antwerpen te verdedigen door

Ben Baelus

Promotor: Prof. dr. F. M. Peeters

Antwerpen, 2002

Contents

1

Introduction

The ongoing rapid miniaturization of electronic circuits requires access to increasingly smaller electrical components. Superconducting microelectronics is one of the favourites that are likely to emerge after the silicon area. In particular, if quantum computers ever come of age, a superconducting design is considered a strong candidate due to the robustness of the coherence in the system. To this end, one needs to learn in advance how individual elements of prospective circuits operate. Motivated by the recent experimental studies of single mesoscopic superconductors (see for example Refs. [1, 2]), we focus in this thesis on the theoretical study of mesoscopic superconductors.

Mesoscopic superconducting samples have sizes comparable to one of the two characteristic length scales: the coherence length ξ or the magnetic penetration length λ. While in bulk superconductors penetrating vortices form a triangular lattice due to the vortex-vortex repulsion and the critical parameters and the properties are determined by the material, in mesoscopic superconductors the situation is more complicated. In mesoscopic superconductors there is a competition between the triangular configuration of the vortex lattice and the boundary which tries to impose its geometry on the vortex lattice.

In this thesis we investigate theoretically how the critical parameters of mesoscopic superconductors can be improved (see Fig. 1.1) and how the superconducting state looks alike. On the one hand we will investigate the influence of the sample geometry on the critical parameters and on the vortex configuration. Changing the sample size and geometry will effect the critical field and the critical current, but not the critical temperature. On the other hand we investigate the influence of the sample surface on the critical

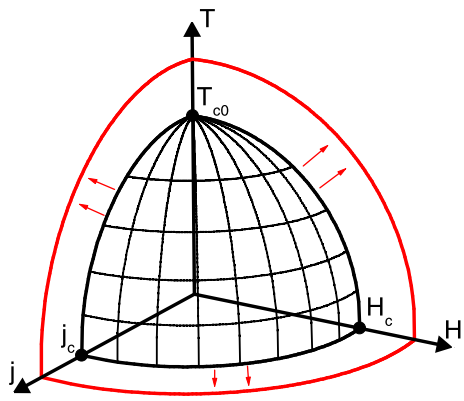

Fig. 1.1 Schematical representation of the expansion of the critical parameters.

parameters. Changing the properties of the surface does effect the critical temperature.

In the first part of this thesis, we will consider singly connected mesoscopic superconductors, which have only one closed superconductor/vacuum boundary in the plane of the superconductor. The initial step of this study was done earlier in our group by Schweigert, Deo and Peeters. They studied single mesoscopic superconducting disks and found that the vortex configuration and the critical parameters depend to a small extent on the material, but more importantly on the sample size. Their results and their theoretical formalisms are described in Chapter 2. We will adjust their formalism in order to investigate the effect of the geometry of the sample on the vortex structure of the superconductor. In Chapter 3 we compare the properties and the vortex configurations of superconducting disks, squares and triangles with the same sample surface. Will sharper sample corners influence the vortex configuration and the critical parameters? Is there any spontaneous nucleation of anti-vortices? Next, we studied the effect of the boundary condition of the superconductor surface on its properties. As an example, we consider infinitely long superconducting cylinders with enhanced superconductivity near the cylinder edge in Chapter 4. What will be the influence of the sample surface on the critical parameters and the vortex states?

In the second part of this thesis, we we study multiply connected superconducting systems. These are superconductors with more than one sample border. In Chapter 5 we study superconducting disks with a hole in the center. This hole can act as a pinning center for one or more vortices and will change the critical parameters and the vortex structure drastically. Furthermore, for mesoscopic rings it turns out that the flux is not quantized. In Chapter 6 we investigate what happens if a second superconductor is placed in the center of a superconducting ring. How does the magnetic coupling between

the two superconductors influence the vortex states and the superconducting properties?

Finally, in Chapter 7 we will study transitions between different superconducting states in disks and rings. How does flux enter and exit in a superconductor? These transitions are given by saddle point states in the energy landscape. The height of these energy points determine the energy barrier for flux entry and exit.

In this chapter we will give a general introduction to superconductivity. We will give a derivation of the Ginzburg-Landau equations which are the central equations in the theoretical framework of this thesis. Also the charateristic length scales and the difference between type-I and type-II superconductors are discussed. For mesoscopic superconductors we will define giant vortex and multivortex states, and the vorticity L which characterizes the different vortex configurations.

1.1 HISTORICAL SURVEY OF SUPERCONDUCTIVITY

The whole story of superconductivity started in 1911 at the Leiden laboratory. Three years after he first liquified helium (which resulted in the Nobel prize in 1913), H. Kamerlingh Onnes studied the variation of the electrical resistance of mercury with the temperature [3]. He observed that the resistance dropped sharply to zero at a critical temperature of 4.2K [see Fig. 1.2]. The same properties were observed in some other metals, such as lead and tin. This new phenomenon was called *superconductivity*. Until 1933, one believed that superconductivity and perfect conductivity were the same. That year, Meissner and Ochsenfeld found not only that a magnetic field is excluded from a superconductor, as might appear to be explained by perfect conductivity, but also that a field is expelled from an originally normal sample as it is cooled through the critical temperature [see Fig. 1.3] [4]. This behaviour is called perfect diamagnetism.

More than 20 years after the experimental discovery of superconductivity, the theoretical study got off the ground. In 1935, the first phenomenological theory describing the superconducting mechanism was developed by the brothers London (see paragraph 1.1.1.) [6]. Without giving a microscopical explanation of the superconducting mechanism, the London theory proved to be successful in describing the superconducting behavior and vortex states in extreme type-II superconductors. However, the London theory treats vortices as point-like objects and do not take into account the finite size and the inner structure of the vortex. A new phenomenological theory was developed by Ginzburg and Landau in 1950, the so-called Ginzburg-Landau theory (see paragraph 1.1.2.) [7]. They introduced quantum mechanics into the theory of superconductors and were able to describe the spatial distribution of superconducting electrons. In 1957, Abrikosov used the Ginzburg-Landau theory to describe the mixed state of type-II superconductors [8]. But what about

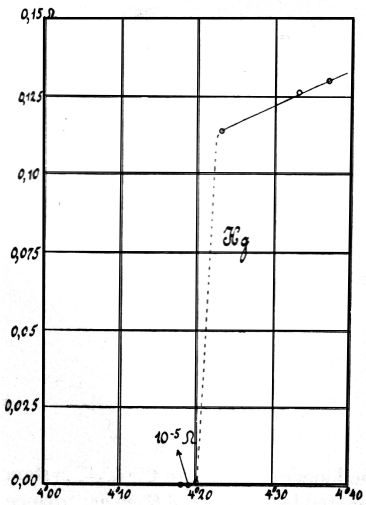

Fig. 1.2 Resistance in Ohm of a specimen of mercury versus absolute temperature. This plot of Kamerlingh Onnes marked the discovery of superconductivity. [From Ref. [5].]

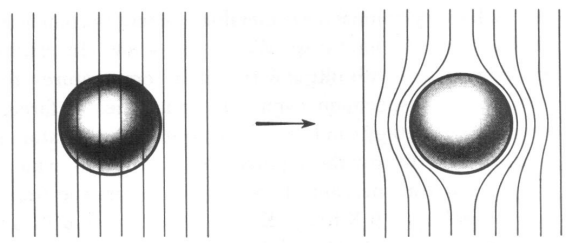

Fig. 1.3 Meissner effect in a superconducting sphere cooled in a constant applied magnetic field. On passing below the transition temperature, the lines of the induction are ejected from the sphere. [From Ref. [5].]

the microscopic level of superconductivity? Only in 1957, Bardeen, Cooper and Schrieffer succeeded in describing the microscopic mechanism of superconductivity in their BCS theory (see paragraph 1.1.3.) [9]. One year later, Gor'kov found microscopic interpretations for all phenomenological parameters of the Ginzburg-Landau theory [10]. For their work, Bardeen, Cooper and Schrieffer received the Nobel prize for physics in 1972.

Both theoretical and experimental studies seemed to be settled then until 1986. That year, Bednorz and Müller discovered the first high-T_c superconductor [11]. It was a layered copper oxide (cuprate) with T_c of 38K. Before this discovery the highest critical temperature was only 23K for Nb_3Ge. For

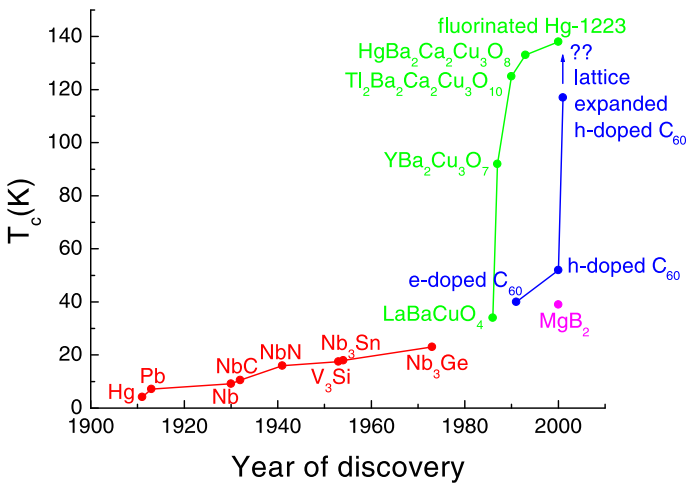

Fig. 1.4 The critical temperature T_c versus the year of discovery. Red represents the low T_c superconductors, green the cuprates, blue the fullerenes and magenta MgB_2.

this discovery, Bednorz and Müller received the Nobel prize in 1987. Subsequently different cuprates have been found with increasing critical temperature. By 1993, cuprates with a T_c of 133K at atmospheric pressure were found ($HgBa_2Ca_2Cu_3O_8$) [12]. After this discovery further efforts to find cuprates with higher T_c failed until 2000, when a slight increase in the transition temperature was detected for fluorinated Hg-1223 samples (T_c = 138K) [13].

The BCS theory was unable to describe many properties of the high-T_c materials. The electron-phonon mechanism became questionable. New mechanisms, such as the so-called d-wave pairing, has been proposed. But, at present, the question of why the high-T_c superconductors have such high-T_c values is still unanswered.

Cristalline C_{60} is normally an insulator, but in 1991 it was shown that electron-doped C_{60} fullerenes are superconducting with a critical temperature up to 40K [14]. Schön et al showed recently that the critical temperature can be raised to 52K by field-effect hole-doping [15] and later further to 117K by combining this technique with increasing the intermolecular distance [16, 17]. Simple extrapolations suggest that the T_c could be increased further, effectively ending the dominance of cuprates in the high-T_c arena [18]. Also smaller C_{36} fullerenes are expected to have higher critical temperatures [19].

Recently, magnetization and resistivity measurements established a transition temperature of 39K in MgB_2, which is the highest yet known for a non-copper-oxide and non-fullerene superconductor.[1]

[1]The description of the early history of superconductors is based on Ref. [20] and the one of the high-T_c superconductors on Ref. [18].

1.1.1 London theory

It took more than 20 years since the discovery of superconductivity before theoreticians developed a theory to describe superconductivity. The first phenomenological theory was developed by the brothers London in 1935 [6]. In addition to the Maxwell equations, they introduced two equations describing the two basic properties of superconductors. The first London equation describes perfect conductivity:

$$\vec{E} = \frac{\partial}{\partial t}\left(\Lambda \vec{j}_s\right) \ . \tag{1.1}$$

An electron is accelerated by an applied electric field. The second London equation is

$$\vec{H} = -c\vec{\nabla} \times \left(\Lambda \vec{j}_s\right) \ , \tag{1.2}$$

with

$$\Lambda = \frac{4\pi\lambda_L^2}{c^2} = \frac{m}{n_s e^2} \ . \tag{1.3}$$

λ_L is the London penetration depth and n_s is the density of superconducting electrons. According to the London theory, the total electron density $n = n_s + n_n$ in a superconductor is the sum of the density of the superconducting electrons n_s and the density of the normal electrons n_n. The number of the superconducting electrons decreases with increasing temperature and becomes zero at the critical field T_c.

The combination of the second equation (1.2) with the Maxwell equation $\vec{\nabla} \times \vec{H} = 4\pi \vec{j}_s/c$ leads to

$$\vec{\nabla}^2 \vec{H} = \frac{1}{\lambda_L^2}\vec{H} \ , \tag{1.4}$$

which expresses that a magnetic field is exponentially screened from the interior of the sample with penetration depth λ_L (Meissner effect).

Without giving a microscopic explanation of the superconducting mechanism, the London theory proved to be successful in describing the superconducting behavior and vortex states in extreme type-II superconductors, where vortices can be considered as point-like objects. However, for non-extreme type-II superconductors, the London theory does not give sufficiently accurate information about the vortex structure, and it is this information that is important for the purpose of this thesis.

1.1.2 Ginzburg-Landau theory

In 1950, Ginzburg and Landau developed a new phenomenological theory taking into account quantum effects [7]. They introduced the wavefunction

of superconducting electrons $\Psi(\vec{r})$ as a complex order parameter which is nonzero at $T < T_c$ and vanishes at $T \geq T_c$ (second order phase transition). This order parameter is related to the density of superconducting electrons n_s as $|\Psi(\vec{r})|^2 = n_s/2$.

The Ginzburg-Landau theory is based on Landau's theory of second-order phase transition [21] in which the free energy is expanded in powers of the order parameter. The derivation of the Ginzburg-Landau theory and its validity is described in full detail in section 1.3. Here, we just mention the two Ginzburg-Landau equations:

$$\alpha\Psi + \beta|\Psi|^2\Psi + \frac{1}{2m^*}\left(-i\hbar\vec{\nabla} - \frac{2e}{c}\vec{A}\right)^2\Psi = 0 \ , \tag{1.5}$$

$$\vec{j}_S = -\frac{i\hbar e}{m^*}\left(\Psi^*\vec{\nabla}\Psi - \Psi\vec{\nabla}\Psi^*\right) - \frac{4e^2}{m^*c}|\Psi|^2\vec{A} \ , \tag{1.6}$$

where the superconducting current density $\vec{j}_S$ is given by the Maxwell equation

$$\vec{j}_S = \frac{c}{4\pi} rot\, rot\, \vec{A} \ . \tag{1.7}$$

In 1957, Abrikosov calculated the properties of bulk type-II superconductors (see section 1.4) using the Ginzburg-Landau theory and he found the so-called mixed state where quantized units of magnetic flux penetrate in the superconductor in a regular array. This array of penetrating flux, which corresponds to the lowest energy configuration, is later called the Abrikosov vortex lattice.

With this theory it became possible to describe spatial distribution of superconducting electrons in type-I and type-II superconductors, taking into account the finite sizes of the vortices. This was impossible within the framework of the London theory.

1.1.3 BCS theory

Only 46 years after the discovery of superconductivity the microscopic mechanism of superconductivity was described by Bardeen, Cooper and Schrieffer in 1957 [9]. The formalism of this microscopic theory is much more complicated than the one of the Ginzburg-Landau theory which will be used in this thesis. The vortex structure and the critical parameters can be precisely calculated using the Ginzburg-Landau theory and the microscopic level is not necessary at all for the purpose of this thesis. Therefore, the discussion of the BCS theory will be limited to the basics.

One key to the understanding of the BCS theory is accepting the existence of a pair of electrons, the so-called Cooper-pair [22], which has a lower energy than two individual electrons. One electron slightly disturbs the lattice in its neighbourhood. The resulting phonon interacts quickly with another electron,

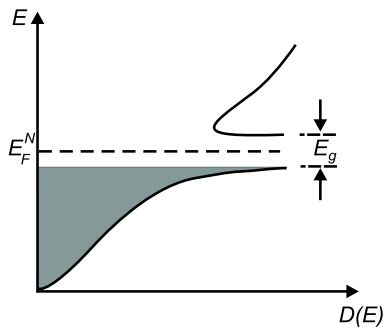

Fig. 1.5 Density of states $D(E)$ versus electron energy in the superconducting state. E_F^N is the Fermi energy of the normal state.

which takes advantage of the deformation and lowers its energy. The second electron emits a phonon by itself which interacts with the first electron and so on. It is that passing back and forth of phonons which couples the two electrons together and brings them into a lower energy state. Electrons in such a Cooper-pair are situated on the Fermi surface and have opposite momentum and opposite spin. These electrons form a cloud of Cooper-pairs which drift cooperatively through the crystal. In order to destroy one Cooper-pair, it is necessary to destroy all Cooper-pairs in a macroscopic region of a superconductor. It requires a lot of energy and, consequently, the probability of the process is very small. Thus, the superconducting state is an ordered state of conducting electrons.

Since the electrons of a Cooper-pair have a lower energy than two unpaired electrons, the Fermi energy of the superconducting state may be considered to be lower than that for the non-superconducting state. The lower state is separated from the normal state by an energy gap E_g (see Fig. 1.5). The energy gap stabilizes the Cooper-pairs and prevents them from breaking apart. The scattering of the lattice atoms is eliminated because of the presence of the superconducting gap, which causes zero resistance.

In 1959 Gor'kov showed that the Ginzburg-Landau theory was just a limiting form of the BCS theory, valid near T_c and suitable to deal with spatially varying situations [10]. He showed that the order parameter Ψ can be seen as the wavefunction of the center-of-mass motion of the Cooper-pairs.

1.2 MESOSCOPIC SUPERCONDUCTIVITY

In the field of superconductivity, samples are called mesoscopic when their sizes are smaller than or comparable to the coherence length ξ or the penetration length λ (see section 1.4). For example, mesoscopic aluminium samples have sizes of the order of 1μm. For such sizes the boundary of the sample

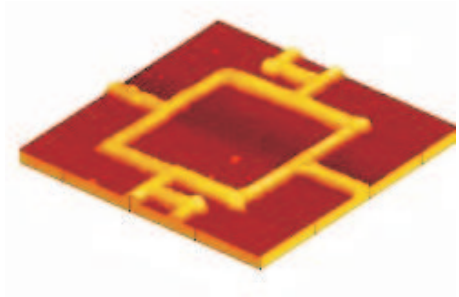

Fig. 1.6 AFM image of a square loop with leads attached. The sides of the loop equal $2\mu m$. [From Ref. [26].]

starts to compete with the triangular Abrikosov configuration of the vortex lattice and the boundary tries to impose its geometry on the vortex lattice. Therefore, the properties of mesoscopic superconductors are very different compared to those of bulk superconductors. In this thesis we will investigate the influence of the sample boundary on the vortex configurations and the critical parameters for mesoscopic samples with different geometries.

Let us now shortly describe two types of experiments on single mesoscopic superconductors. Later in this thesis some experimental results will be given and compared with our theoretical ones.

Resistance measurements were the first kind of experiments performed on superconductors by Kamerlingh Onnes [3]. The resistance of Pb dropped several orders of magnitude at the transition to the superconducting state. Also in the field of mesoscopic superconductivity, resistivity measurements are used to study the properties of single mesoscopic superconductors. In the past, these measurements were done, for example, in the group VSM at the KULeuven for single squares, triangles, square rings, wires, etc. [1, 23–25].

In order to measure the resistivity, leads are attached to the sample and a transport current is applied through the leads (see Fig. 1.6). By measuring the resistivity of the non-fully superconducting state one can obtain information about the superconducting/normal transition. This information is most of the time plotted in a $H - T$ phase diagram which shows transitions between vortex states with different vorticity L.

With this technique it is possible to investigate the dependence of the critical parameters on the sample geometry, but it does not provide any information about the real vortex structure. Another restriction is that the leads can influence the result.

Hall magnetometry is revealing itself as a powerful tool for obtaining information on a single mesoscopic superconductor away from the superconducting/normal phase boundary, i.e. deep inside the superconducting state. Thin superconducting samples are placed on top of a Hall probe created in a two-dimensional electron gas. In the ballistic regime the Hall resistance is

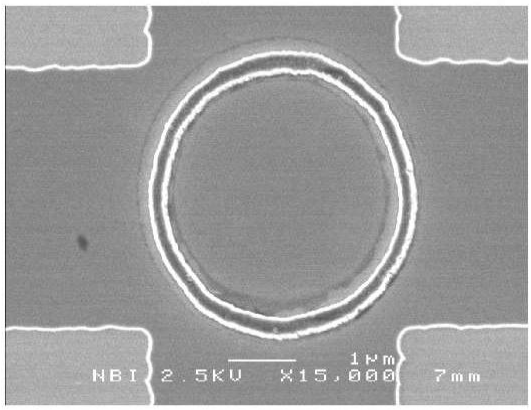

Fig. 1.7 Scanning electron microscopic image of a μ-Hall probe on which a superconducting aluminum loop is deposited. [From Ref. [32].]

directly proportional to the average value of the magnetic field through the junction [27]. The averaged value of the magnetic field $\langle \vec{H} \rangle$ in the junction area is determined by the expulsion of the field by the superconductor which is placed on top of the junction. Since the magnetization is given by the difference between the averaged field and the applied field, one can obtain the magnetization of single superconductors and compare them with the theoretical values (see for example Ref. [28]). Magnetization measurements on single superconducting disks are performed in the group of A. Geim [2, 29–31] and on single superconducting rings in the group of P. Lindelof [32] (see Fig. 1.7). By using this technique, it has been possible to show that a single mesoscopic superconductor in a magnetic field does not exhibit the standard magnetization dependences of bulk superconductors (see section 1.4).

1.3 DERIVATION OF THE GINZBURG-LANDAU THEORY

Ginzburg and Landau developed a phenomenological theory [7] based on the theory of second-order phase transitions developed by Landau. They assumed that the wavefunction of the superconducting electrons $\Psi(\vec{r})$ is the order parameter and they chose the normalization of this wavefunction such that $|\Psi(\vec{r})|^2$ gives the density of Cooper-pairs:

$$|\Psi(\vec{r})|^2 = n_s/2 \ , \tag{1.8}$$

where n_s is the density of the superconducting electrons.

The theory is based on an expansion of the free energy in powers of the order parameter, which is small close to the superconducting/normal transition at the critical temperature T_c. In this way, it is immediately clear that the GL theory is in principle valid only near T_c.

1.3.1 Convention of notation

Basically, we follow the notation of de Gennes [33] (and many others, like Tinkham [34] and Schmidt [20]), but instead of using $\vec{h}(\vec{r})$ as notation for the local value of the magnetic field we use $\vec{H}(\vec{r})$, which equals $rot\ \vec{A}(\vec{r})$. The magnetic induction $\vec{B}$ is the averaged value of $\vec{H}$ over microscopic lengths and will be written as $\langle\vec{H}\rangle$. The externally applied field will be denoted by $\vec{H}_0$. It is homogeneous and thus independent of $\vec{r}$.

1.3.2 Free energy

Near T_c the Gibbs free energy density can be expanded as [20]

$$G_{sH} = G_n + \alpha\,|\Psi|^2 + \frac{\beta}{2}\,|\Psi|^4 + \frac{1}{2m^*}\left|\left(-i\hbar\vec{\nabla} - \frac{2e}{c}\vec{A}\right)\Psi\right|^2 + \frac{H^2}{8\pi} - \frac{\vec{H}-\vec{H}_0}{4\pi}\cdot\vec{H}_0\ , \tag{1.9}$$

where H is the microscopic field at a given point of the superconductor and G_n is the free energy density of a superconductor in the normal state when no field is applied. When a field is applied, the free energy density of a superconductor in the normal state is given by $G_{nH} = G_n + H_0^2/8\pi$, where $H_0^2/8\pi$ is the magnetic energy density.

- The first part of Eq. (1.9) is the expansion of the free energy density for a homogeneous superconductor in the absence of an external magnetic field in powers of $|\Psi|^2$ near the zero-field critical temperature $T_{c0} \equiv T_c(H_0 = 0)$,

$$G_n + \alpha\,|\Psi|^2 + \frac{\beta}{2}\,|\Psi|^4\ , \tag{1.10}$$

  where α and β are some phenomenological expansion coefficients which are characteristics of the material. The coefficient α is negative and depends on the temperature as $\alpha \propto (T - T_{c0})$, while β is a positive constant. From Eq. (1.10) the Cooper-pair density corresponding to the free energy minimum at temperatures below T_{c0} can be calculated as

$$|\Psi_0|^2 = -\alpha/\beta\ . \tag{1.11}$$

- The next term is the kinetic energy of the Cooper-pairs:

$$\frac{1}{2m^*}\left|\left(-i\hbar\vec{\nabla}-\frac{2e}{c}\vec{A}\right)\Psi\right|^2 , \tag{1.12}$$

where the mass of a Cooper-pair m^* is two times the mass of an electron m, and the charge of the Cooper-pair is two times the charge of the electron e. In quantum mechanics, the kinetic energy density of a particle of mass m^* is

$$\frac{1}{2m^*}\left|-i\hbar\vec{\nabla}\Psi\right|^2 . \tag{1.13}$$

For a particle of charge $2e$ moving in the field with vector potential $\vec{A}$, the operator $-i\hbar\vec{\nabla}$ in the expression for the kinetic energy density has to be modified

$$-i\hbar\vec{\nabla} \rightarrow -i\hbar\vec{\nabla}-\frac{2e}{c}\vec{A} . \tag{1.14}$$

- The last but one term simply represents the magnetic energy density, i.e.

$$\frac{H^2}{8\pi} . \tag{1.15}$$

- The last term describes the reduction of the magnetic field due to the penetration of the field, i.e.

$$-\frac{\vec{H}-\vec{H}_0}{4\pi}\cdot\vec{H}_0 . \tag{1.16}$$

Without this term expression (1.8) would be the free energy F. For a superconductor in an external field, the energy that is a minimum at equilibrium is not the free energy F but the Gibbs free energy G which is defined as [35]:

$$G = F - \frac{\vec{H}-\vec{H}_0}{4\pi}\cdot\vec{H}_0 . \tag{1.17}$$

The overall Gibbs free energy of a superconductor is

$$\mathcal{G}_{sH} = \mathcal{G}_{nH} + \int\left\{\alpha\left|\Psi\right|^2 + \frac{1}{2}\beta\left|\Psi\right|^4 + \frac{1}{2m^*}\left|\left(-i\hbar\vec{\nabla}-\frac{2e}{c}\vec{A}\right)\Psi\right|^2 + \frac{H^2}{8\pi} + \frac{H_0^2}{8\pi} - \frac{\vec{H}\cdot\vec{H}_0}{4\pi}\right\}dV , \tag{1.18}$$

where the integration is carried out over the entire space V. Note that $\mathcal{G}_{sH}$ is a functional of $\Psi(\vec{r})$ and $\vec{A}(\vec{r})$. Minimizing $\mathcal{G}_{sH}$ with respect to these two functions leads to the Ginzburg-Landau equations which will be derived below.

Sometimes, one introduces extra terms in the expansion of the free energy (for example terms proportional to $|\Psi|^6$ and to $|\Psi|^2 \vec{\nabla} |\Psi|^2$ [36]), but the achieved corrections are very small.

1.3.3 First Ginzburg-Landau equation

In order to obtain the minimum of the total Gibbs free energy, we vary expression (1.18) with respect to Ψ^* [20]:

$$\int \left\{ \alpha \Psi \delta \Psi^* + \beta \Psi |\Psi|^2 \delta \Psi^* + \frac{1}{2m^*} \vec{\varphi} \cdot \left(i\hbar \vec{\nabla} - \frac{2e}{c} \vec{A} \right) \delta \Psi^* \right\} dV' = 0 \ , \tag{1.19}$$

where

$$\vec{\varphi} = \left(-i\hbar \vec{\nabla} - \frac{2e}{c} \vec{A} \right) \Psi \ , \tag{1.20}$$

and V' is the sample volume. The integration is restricted to the volume V' because outside this region Ψ is zero. The last term of Eq. (1.19) equals

$$\frac{i\hbar}{2m^*} \int \vec{\varphi} \cdot \vec{\nabla} \delta \Psi^* dV' - \frac{2e}{2m^* c} \int \vec{\varphi} \cdot \vec{A} \delta \Psi^* dV' \ , \tag{1.21}$$

and can be simplified to

$$\frac{i\hbar}{2m^*} \left[- \int \delta \Psi^* \vec{\nabla} \cdot \vec{\varphi} \, dV' + \int \vec{\nabla} \cdot (\delta \Psi^* \vec{\varphi}) \, dV' \right] - \frac{2e}{2m^* c} \int \vec{\varphi} \cdot \vec{A} \delta \Psi^* dV' \ , \tag{1.22}$$

by making use of $\vec{\nabla} \cdot (\delta \Psi^* \vec{\varphi}) = \vec{\varphi} \cdot \vec{\nabla} \delta \Psi^* + \delta \Psi^* \vec{\nabla} \cdot \vec{\varphi}$.

Substituting Eq. (1.22) in Eq. (1.19) results in

$$\int \left\{ \alpha \Psi \delta \Psi^* + \beta \Psi |\Psi|^2 \delta \Psi^* - \frac{i\hbar}{2m^*} \delta \Psi^* \vec{\nabla} \cdot \vec{\varphi} + \frac{i\hbar}{2m^*} \vec{\nabla} \cdot (\delta \Psi^* \vec{\varphi}) - \frac{2e}{2m^* c} \vec{\varphi} \cdot \vec{A} \delta \Psi^* \right\} dV' = 0 \ . \tag{1.23}$$

Using Gauss theorem $\int \vec{\nabla} \cdot \vec{A} dV' = \oint \vec{n} \cdot \vec{A} dS'$ this can be rewritten as

$$\int \left\{ \alpha \Psi \delta \Psi^* + \beta \Psi |\Psi|^2 \delta \Psi^* - \frac{i\hbar}{2m^*} \delta \Psi^* \vec{\nabla} \cdot \vec{\varphi} - \frac{2e}{2m^* c} \vec{\varphi} \cdot \vec{A} \delta \Psi^* \right\} dV' + \frac{i\hbar}{2m^*} \oint_{S'} \vec{n} \cdot \delta \Psi^* \vec{\varphi} dS' = 0 \ , \tag{1.24}$$

where S' is the sample surface, and thus

$$\int \left\{ \alpha\Psi\delta\Psi^* + \beta\Psi\left|\Psi\right|^2\delta\Psi^* - \frac{i\hbar}{2m^*}\delta\Psi^*\vec{\nabla}\cdot\vec{\varphi} - \frac{2e}{2m^*c}\vec{\varphi}\cdot\vec{A}\delta\Psi^* \right\} dV' = 0 \ , \tag{1.25}$$

and

$$\frac{i\hbar}{2m^*}\oint_{S'} \vec{n}\cdot\delta\Psi^*\vec{\varphi}dS' = 0 \ . \tag{1.26}$$

Substituting Eq. (1.20) into equations (1.24) and (1.25), and using $\vec{\nabla}\Psi\cdot\vec{A} = \vec{A}\cdot\vec{\nabla}\Psi + \left(\vec{\nabla}\cdot\vec{A}\right)\Psi = \vec{A}\cdot\vec{\nabla}\Psi$ since $\vec{\nabla}\cdot\vec{A} = 0$ we find

$$\int \left\{ \alpha\Psi\delta\Psi^* + \beta\Psi\left|\Psi\right|^2\delta\Psi^* - \frac{1}{2m^*}\left(-i\hbar\vec{\nabla} - \frac{2e}{c}\vec{A}\right)^2\Psi\delta\Psi^* \right\} dV' = 0 \ , \tag{1.27}$$

and

$$\frac{i\hbar}{2m^*}\oint_{S'} \vec{n}\cdot\delta\Psi^*(-i\hbar\vec{\nabla} - \frac{2e}{c}\vec{A})\Psi dS' = 0 \ . \tag{1.28}$$

As expressions (1.27) and (1.28) must be valid for an arbitrary function $\delta\Psi^*$, we obtain the first equation of the Ginzburg-Landau theory and its boundary condition:

$$\alpha\Psi + \beta\left|\Psi\right|^2\Psi + \frac{1}{2m^*}\left(-i\hbar\vec{\nabla} - \frac{2e}{c}\vec{A}\right)^2\Psi = 0 \ , \tag{1.29}$$

$$\vec{n}\cdot(-i\hbar\vec{\nabla} - \frac{2e}{c}\vec{A})\Psi\Big|_{boundary} = 0 \ , \tag{1.30}$$

where $\vec{n}$ is the unit vector normal to the surface of the superconductor.

1.3.4 Second Ginzburg-Landau equation

In order to obtain the minimum of the Gibbs free energy, we vary Eq. (1.18) with respect to $\vec{A}$ [20]:

$$\begin{aligned} &\frac{1}{2m^*}\int\left[\left(-\frac{2e}{c}\delta\vec{A}\Psi^*\right)\cdot\left(-i\hbar\vec{\nabla}\Psi - \frac{2e}{c}\vec{A}\Psi\right) + \right. \\ &\left.\left(i\hbar\vec{\nabla}\Psi^* - \frac{2e}{c}\vec{A}\Psi^*\right)\cdot\left(-\frac{2e}{c}\delta\vec{A}\Psi\right)\right]dV + \\ &\frac{1}{4\pi}\int\left(rot\,\vec{A} - \vec{H}_0\right)\cdot rot\,\delta\vec{A}dV = 0 \ , \end{aligned} \tag{1.31}$$

with $\vec{H} = rot\,\vec{A}$, and V the volume of the entire space. The variation $\delta\left(\vec{H}\right)^2 = \delta\left(rot\,\vec{A}\right)^2$ has been written as $2\,rot\,\vec{A}\cdot rot\,\delta\vec{A}$. Using the formula $div\left[\vec{a}\times\vec{b}\right] = \vec{b}\cdot rot\,\vec{a} - \vec{a}\cdot rot\,\vec{b}$ and taking $\vec{b} = rot\,\vec{A} - \vec{H}_0$ and $\vec{a} = \delta\vec{A}$ we find

$$\frac{1}{2m^*}\int\left[\left(-\frac{2e}{c}\delta\vec{A}\Psi^*\right)\cdot\left(-i\hbar\vec{\nabla}\Psi - \frac{2e}{c}\vec{A}\Psi\right) + \left(i\hbar\vec{\nabla}\Psi^* - \frac{2e}{c}\vec{A}\Psi^*\right)\cdot\left(-\frac{2e}{c}\delta\vec{A}\Psi\right)\right]dV + \frac{1}{4\pi}\int\left[\delta\vec{A}\cdot rot\,rot\,\vec{A} + div\left(\delta\vec{A}\times\left(rot\,\vec{A} - \vec{H}_0\right)\right)\right]dV = 0\ . \tag{1.32}$$

After making use of Gauss's theorem the last part of Eq. (1.32) can be written as

$$\int div\left(\delta\vec{A}\times\left(rot\,\vec{A} - \vec{H}_0\right)\right)dV = \oint_S d\vec{S}\cdot\left[\delta\vec{A}\times\left(rot\,\vec{A} - \vec{H}_0\right)\right]\ , \tag{1.33}$$

which is zero because S is the boundary of the entire space at infinity where $rot\,\vec{A} = \vec{H} = \vec{H}_0$. Combining the first terms Eq. (1.32) leads to

$$\int\left[\frac{i\hbar e}{m^*c}\left(\Psi^*\vec{\nabla}\Psi - \Psi\vec{\nabla}\Psi^*\right) + \frac{4e^2}{m^*c^2}\left|\Psi\right|^2\vec{A} + \frac{1}{4\pi}rot\,rot\,\vec{A}\right]\cdot\delta\vec{A}\,dV = 0\ . \tag{1.34}$$

For arbitrary $\delta\vec{A}$, this can be zero only if the expression in the square brackets is zero:

$$\frac{i\hbar e}{m^*c}\left(\Psi^*\vec{\nabla}\Psi - \Psi\vec{\nabla}\Psi^*\right) + \frac{4e^2}{m^*c^2}\left|\Psi\right|^2\vec{A} + \frac{1}{4\pi}rot\,rot\,\vec{A} = 0\ . \tag{1.35}$$

The current density $\vec{j}_S$ in the superconductor is given by the Maxwell equation

$$\vec{j}_S = \frac{c}{4\pi}rot\,rot\,\vec{A}\ , \tag{1.36}$$

and, consequently, we obtain the second Ginzburg-Landau equation:

$$\vec{j}_S = -\frac{i\hbar e}{m^*}\left(\Psi^*\vec{\nabla}\Psi - \Psi\vec{\nabla}\Psi^*\right) - \frac{4e^2}{m^*c}\left|\Psi\right|^2\vec{A}\ . \tag{1.37}$$

1.3.5 Characteristic length scales

The Ginzburg-Landau theory introduces two important characteristic length scales: the coherence length $\xi(T)$ and the penetration depth $\lambda(T)$.

Coherence length ξ. The coherence length $\xi(T)$ indicates the typical length scale over which the size of the order parameter can vary (Fig. 1.8). One can derive this length from the first Ginzburg-Landau equation (1.29) [33]. In this discussion we will limit ourselves to a semi-infinite superconductor with flat boundary at $x = 0$.

For a situation where no field is applied and for a gauge in which Ψ is real, Eq. (1.29) becomes in one dimension

$$\alpha\Psi + \beta\Psi^3 - \frac{\hbar^2}{2m^*}\frac{d^2}{dx^2}\Psi = 0 \ . \tag{1.38}$$

The nonzero solution describing the uniform superconducting state is given by

$$\Psi = \Psi_0 = \sqrt{-\frac{\alpha}{\beta}} \ . \tag{1.39}$$

Near the surface of the superconductor, for example, the value of $\Psi(x)$ is different from Ψ_0. To calculate the length scale over which the order parameter can vary, it is useful to write Ψ in dimensionless variables as

$$\Psi = f\Psi_0 \ . \tag{1.40}$$

Taking into account that $\alpha < 0$ Eq. (1.38) becomes

$$-\frac{\hbar^2}{2m^*\,|\alpha|}\frac{d^2 f}{dx^2} - f + f^3 = 0 \ , \tag{1.41}$$

which means that the charateristic length scale over which f (and thus Ψ) can change is given by

$$\xi(T) = \sqrt{\frac{\hbar^2}{2m^*\,|\alpha|}} \ . \tag{1.42}$$

Since α depends on the temperature as $\alpha \propto (T - T_{c0})$, the coherence length varies as a function of the temperature as

$$\xi(T) \propto (1 - T/T_{c0})^{-1/2} \ . \tag{1.43}$$

Notice that this is certainly not the same length as the BCS coherence length ξ_o [33, 34]. Near T_c the relation between $\xi(T)$ and ξ_o depends on the purity of the material, defined by the elastic mean free path l_{el}:

$$\xi(T) = 0.74\xi_o\,(1 - T/T_{c0})^{-1/2} \ \text{ when } l_{el} \gg \xi_o \text{ (pure)}, \tag{1.44}$$

$$\xi(T) = 0.855\sqrt{\xi_o l_{el}}\,(1 - T/T_{c0})^{-1/2} \ \text{ when } l_{el} \ll \xi_o \text{ (dirty)}. \tag{1.45}$$

Notice further that the coherence length $\xi(T)$ diverges at the critical temperature T_{c0}.

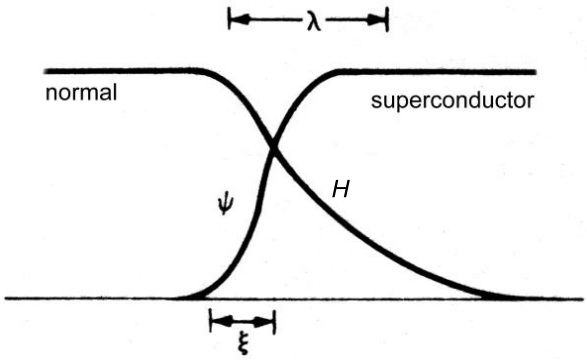

Fig. 1.8 The radial dependence of the order parameter Ψ and the magnetic field h at the superconducting/normal surface boundary. [from Ref. [34].]

Penetration depth λ. The typical length scale over which the magnetic field $\vec{H}$ can vary is the penetration depth $\lambda(T)$ (Fig. 1.8). This length scale can be derived in a similar way from the second Ginzburg-Landau equation (1.37) [33].

Let us consider the situation where $\Psi = \Psi_0$ and take the curl of both sides of Eq. (1.37):

$$rot\ \vec{j}_S = -\frac{4e^2}{m^*c}\left|\Psi\right|^2 rot\ \vec{A} \tag{1.46}$$

Using the Maxwell equation (1.36) we can rewrite this as

$$\vec{H} + \lambda^2 rot\, rot\, \vec{H} = 0\ , \tag{1.47}$$

and the charateristic length scale over which the magnetic field $\vec{H}$ can vary is given by

$$\lambda(T) = \sqrt{\frac{m^*c^2}{16\pi e^2\left|\Psi_0\right|^2}} = \sqrt{\frac{m^*c^2}{8\pi e^2 n_s}} = \sqrt{\frac{m^*c^2\beta}{16\pi\left|\alpha\right|e^2}}\ , \tag{1.48}$$

where the density of superconducting electrons $n_s = 2\left|\Psi_0\right|^2 = 2\left|\alpha\right|/\beta$ and the mass of a Cooper-pair is two times the electron mass m: $m^* = 2m$.

Also the penetration depth $\lambda(T)$ varies as a function of the temperature as

$$\lambda(T) \propto (1 - T/T_{c0})^{-1/2}\ , \tag{1.49}$$

since $\left|\Psi_0\right|^2 \propto \left|\alpha\right| \propto (T_{c0} - T)$. The relation between the temperature dependent penetration depth $\lambda(T)$ and the London penetration depth $\lambda_L(0)$ at

absolute zero temperature differs for pure and dirty materials [34]:

$$\lambda(T) = \frac{\lambda_L(0)}{\sqrt{2}}\,(1 - T/T_{c0})^{-1/2} \text{ when } l_{el} \gg \xi_o \text{ (pure)}, \tag{1.50}$$

$$\lambda(T) = \frac{\lambda_L(0)}{\sqrt{2}}\sqrt{\frac{\xi_o}{1.33 l_{el}}}\,(1 - T/T_{c0})^{-1/2} \text{ when } l_{el} \ll \xi_o \text{ (dirty)}. \tag{1.51}$$

Notice that the penetration depth $\lambda(T)$ diverges at the critical temperature T_{c0}.

1.3.6 Ginzburg-Landau equations

In summary, Eq. (1.29) and Eqs. (1.36) and (1.37) are the Ginzburg-Landau equations:

$$\alpha\Psi + \beta\,|\Psi|^2\,\Psi + \frac{1}{2m^*}\left(-i\hbar\vec{\nabla} - \frac{2e}{c}\vec{A}\right)^2 \Psi = 0\ , \tag{1.52}$$

$$\vec{j}_S = -\frac{i\hbar e}{m^*}\left(\Psi^*\vec{\nabla}\Psi - \Psi\vec{\nabla}\Psi^*\right) - \frac{4e^2}{m^* c}\,|\Psi|^2\,\vec{A}\ , \tag{1.53}$$

with

$$\vec{j}_S = \frac{c}{4\pi} rot\, rot\, \vec{A}\ . \tag{1.54}$$

The boundary condition for the order parameter is given by Eq. (1.30):

$$\vec{n}\cdot(-i\hbar\vec{\nabla} - \frac{2e}{c}\vec{A})\Psi\Big|_{boundary} = 0\ . \tag{1.55}$$

In this thesis, we will cast the Ginzburg-Landau equations into a dimensionless form. The distances will be measured in units of the coherence length $\xi = \hbar/\sqrt{-2m^*\alpha}$, the order parameter in $\Psi_0 = \sqrt{-\alpha/\beta}$ and the vector potential in $c\hbar/2e\xi$. $\kappa = \lambda/\xi$ is the Ginzburg-Landau parameter, and $\lambda = c\sqrt{m/\pi}/4e\Psi_0$ is the penetration length. The magnetic field is measured in the second critical magnetic field $H_{c2} = c\hbar/2e\xi^2 = \kappa\sqrt{2}H_c$, where $H_c = \sqrt{4\pi\alpha^2/\beta}$ is the critical field.

Using these dimensionless variables and the London gauge, $div\,\vec{A} = 0$, Eqs. (1.52)-(1.55) can be rewritten in the following form:

$$\left(-i\vec{\nabla} - \vec{A}\right)^2 \Psi = \Psi\left(1 - |\Psi|^2\right)\ , \tag{1.56}$$

$$-\kappa^2\Delta\vec{A} = \frac{1}{2i}\left(\Psi^*\vec{\nabla}\Psi - \Psi\vec{\nabla}\Psi^*\right) - |\Psi|^2\,\vec{A}\ , \tag{1.57}$$

with the boundary condition:

$$\vec{n} \cdot \left(-i\vec{\nabla} - \vec{A}\right) \Psi \Big|_{boundary} = 0 \ . \tag{1.58}$$

The temperature is included in ξ, λ, H_{c2}, through their temperature dependencies (see Eqs (1.43), (1.49) and $H_{c2} = c\hbar/2e\xi^2$)

$$\xi(T) = \frac{\xi(0)}{\sqrt{|1 - T/T_{c0}|}} \ , \tag{1.59}$$

$$\lambda(T) = \frac{\lambda(0)}{\sqrt{|1 - T/T_{c0}|}} \ , \tag{1.60}$$

$$H_{c2}(T) = H_{c2}(0) \left|1 - \frac{T}{T_{c0}}\right| \ , \tag{1.61}$$

where T_{c0} is the critical temperature at zero magnetic field.

1.3.7 Validity of the Ginzburg-Landau theory

A few points need to be discussed in relation to the validity of the Ginzburg-Landau equations [35]:

1. Landau assumes in his *theory of second order transitions* that the free energy can be expanded in powers of $|\Psi|^2$[21]. This is not generally valid, but Gor'kov showed theoretically that the Landau expansion is valid in the case of superconductors [10].

2. Ψ must be a *slowly varying function* over distances of the order of ξ_0. A necessary condition for the validity of the theory is, therefore, $\xi(T) \gg \xi_0$ or

$$\frac{T_{c0} - T}{T_{c0}} \ll 1, \tag{1.62}$$

   i.e. the temperature must be close to T_{c0}, the critical temperature in zero field.

3. The *local electrodynamic approximation* will be valid only if $\vec{H}$ and $\vec{A}$ are slowly varying functions over distances of the order of ξ_0. Therefore, it is necessary that $\lambda(T) \gg \xi_0$ or

$$\frac{T_{c0} - T}{T_{c0}} \ll \left[\frac{\lambda_L(0)}{\xi_0}\right]^2 \ , \tag{1.63}$$

   which expresses again that the temperature must be close to T_{c0}.

Although the Ginzburg-Landau theory has been derived only close to the superconducting/normal transition it turns out that its validity range is much larger. In particular, in mesoscopic superconductors the Ginzburg-Landau theory has been successfully used deep into the superconducting phase (see for example Ref. [28]).

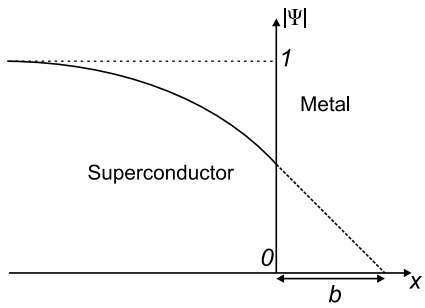

Fig. 1.9 Schematic presentation of the spatial dependence of the superconducting order parameter $|\Psi|$ at the interface between a superconducting and a normal metal. The extrapolation length b is indicated.

1.3.8 General boundary condition

The boundary condition for the order parameter in a superconductor in contact with an insulator or with vacuum is given by Eq. (1.55),

$$\vec{n} \cdot (-i\hbar\vec{\nabla} - \frac{2e}{c}\vec{A})\Psi\Big|_{boundary} = 0 \ , \tag{1.64}$$

where $\vec{n}$ is the unit vector normal to the surface of the superconductor. This condition expresses that no supercurrent can pass perpendicular to the sample boundary (Neumann boundary condition).

For a superconductor-normal metal interface the boundary condition must be modified. The more general expression, which assures that no supercurrent passes perpendicular to the sample boundary, can be written as [33]

$$\vec{n} \cdot (-i\hbar\vec{\nabla} - \frac{2e}{c}\vec{A})\Psi\Big|_{boundary} = \frac{i}{b}\Psi\Big|_{boundary} \ , \tag{1.65}$$

with b the extrapolation length over which the order parameter becomes zero in the normal metal by extrapolation (see Fig. 1.9). Notice that for a superconductor-normal metal interface b is positive.

The value of the extrapolation length is determined by the medium adjacent to the superconductor:

1. for vacuum or an insulator: $b \to \infty$,
2. for normal metals: $b > 0$, and for ferromagnets: $b \to 0$,
3. for a superconducting layer with a higher T_c: $b < 0$.

The latter case is of theoretical interest because then the order parameter near the surface will increase, which will lead to higher critical fields and critical temperatures. In Chapter 4 we will study a superconducting cylinder surrounded by a medium with enhanced superconductivity near the surface.

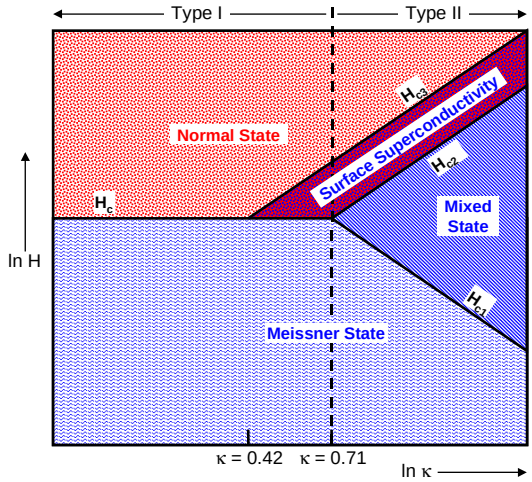

Fig. 1.10 The dependence of the characteristics of semi-infinite superconductors on the value of the Ginzburg-Landau parameter κ. H_{c3} is the surface superconducting field when the field is parallel to the surface. [after Ref. [37].]

1.4 TYPE-I AND TYPE-II SUPERCONDUCTORS

1.4.1 Bulk superconductors

Bulk superconductors can be separated into two types through their Ginzburg-Landau parameter $\kappa = \lambda(T)/\xi(T)$:

$$\kappa < 1/\sqrt{2} \rightarrow \text{ type-I superconductors,}$$
$$\kappa > 1/\sqrt{2} \rightarrow \text{ type-II superconductors.}$$

All superconducting elements except niobium are type-I superconductors. Niobium and all superconducting alloys and chemical compounds are type-II. Also the high-T_c superconductors belong to the second group. The dependence of the superconducting characteristics on the value of κ is shown in Fig. 1.10.

For $\kappa < 0.42$ the superconductor is a type-I superconductor. For fields below the thermodynamical critical field $\vec{H}_c$ the superconductor is in the Meissner state and all flux is expelled from the sample. At the critical field the magnetic field penetrates the sample, the superconductivity is destroyed and the sample becomes normal. For $0.42 < \kappa < 1/\sqrt{2} \simeq 0.71$ the superconductor is still a type-I superconductor, but now the Meissner state does not change immediately into the normal state with increasing field. At the field $\vec{H}_c$ flux can penetrate the inner part of the sample, while a layer remains

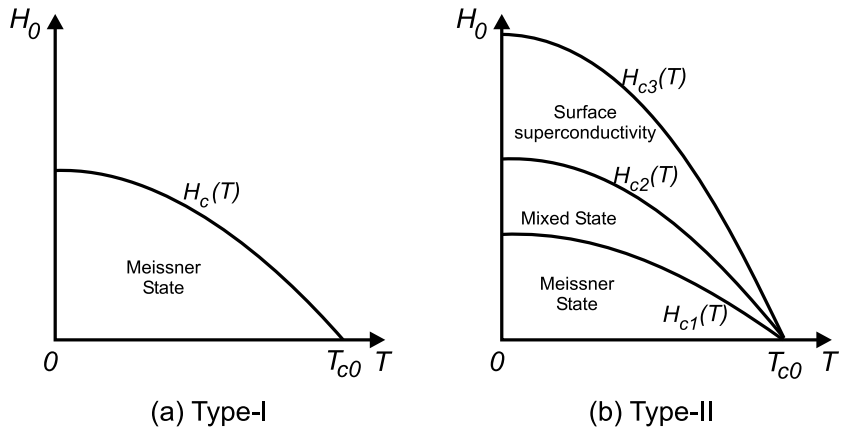

Fig. 1.11 $H-T$ phase diagram for a type-I (a) and a type-II (b) bulk superconductor.

superconducting near the surface of the sample. At the surface critical field $\vec{H}_{c3}$ the surface becomes normal too and the sample is in the normal state.

In type-II superconductors $\left(\kappa > 1/\sqrt{2}\right)$, on the other hand, a fourth possible state exists. In equilibrium, the Meissner state is only observed at applied fields $\vec{H}_0$ below the first critical field $\vec{H}_{c1}$. In the region between the first critical field $\vec{H}_{c1}$ and the second critical field $\vec{H}_{c2}$ the magnetic flux is able to penetrate the sample in quantized units of the flux quantum $\phi_0 = hc/2e$, called vortices. Abrikosov found that these vortices construct a triangular lattice inside the superconductor, the so-called Abrikosov vortex lattice. The state is called the Abrikosov vortex state or Mixed state. In the region $\vec{H}_{c2} < \vec{H}_0 < \vec{H}_{c3}$, superconductivity only exists at a thin layer near the sample edges, while the inner side of the sample is in the normal state. For bulk type-II superconductors the third critical field $\vec{H}_{c3}$ is approximately equal to $1.69\vec{H}_{c2}$. For larger fields superconductivity is destroyed and the entire sample is in the normal state.

The critical fields $\vec{H}_c$, $\vec{H}_{c1}$, $\vec{H}_{c2}$ and $\vec{H}_{c3}$ depend on the temperature. The $H-T$ phase diagram for type-I and type-II bulk superconductors are shown in Fig. 1.11.

Both types have also a different behavior of the magnetization as a function of the external magnetic field. This can be seen from Fig. 1.12. The magnetization of a superconductor is defined as

$$\vec{M} = \frac{1}{4\pi}(\vec{B} - \vec{H}_0) \ , \tag{1.66}$$

where the magnetic induction $\vec{B} = \langle \vec{H} \rangle$ and $\vec{H}_0$ is the applied magnetic field.

At $\vec{H}_0 < \vec{H}_c$ a type-I bulk superconductor is in the Meissner state and all flux is expelled from the sample: $\langle \vec{H} \rangle = 0$ and $-4\pi\vec{M} = \vec{H}_0$. At larger fields, the applied field penetrates into the superconductor which becomes normal:

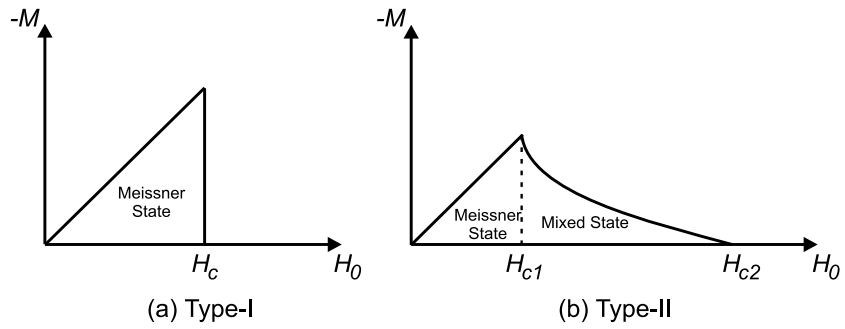

Fig. 1.12 The magnetization as a function of the applied magnetic field for type-I and type-II bulk superconductors.

$\langle \vec{H} \rangle = \vec{H}_0$ and $\vec{M} = 0$. Type-II superconductors are in the Meissner state at $\vec{H}_0 < \vec{H}_{c1}$ and $-4\pi\vec{M} = \vec{H}_0$. In the mixed state $\left(\vec{H}_{c1} < \vec{H}_0 < \vec{H}_{c2}\right)$ the absolute value of the magnetization $\left|\vec{M}\right|$ decreases with increasing field until it vanishes at the second critical field.

Also the surface energy is different for type-I and type-II superconductors (see for example Ref. [35]). The expulsion of the external field increases the energy of a superconductor by $H^2/8\pi$ per unit volume. It is then expected to be energetically favourable that the volume will be divided up into alternate normal and superconducting regions. The creation of such normal regions requires a negative interface surface energy σ_{ns} whose magnitude is such that its contribution exceeds the gain in magnetic energy. The two types of superconductors have a different behaviour with respect to the surface energy:

$$\begin{aligned} \text{Type-I}: &\ \sigma_{ns} > 0, \\ \text{Type-II}: &\ \sigma_{ns} < 0. \end{aligned}$$

As an illustration, we will give some values for the characteristic lengths λ_L and ξ_o and for the critical fields H_c, H_{c2} and critical temperature T_{c0} for a few type-I and type-II bulk superconductors [5, 38]:

Type-I	λ_L (Å)	ξ_o (Å)	H_c (T)	T_{c0} (K)
Al	340	16000	0.0105	1.1
Sn	160	2300	0.0305	3.7
Pb	370	830	0.0803	7.2
Cd	1100	7600	0.0028	0.52

Type-II	λ_L (Å)	ξ_o (Å)	H_{c2} (T)	T_{c0} (K)
Nb	390	380	0.1980	9.25
Nb_3Ge	900	300	38	23
YBCO(ab)	270	43	120-200	92
YBCO(c)	1800	7	120-200	92
MgB_2	1320	50	13-18	39

1.4.2 Mesoscopic superconductors

In thin superconducting films the distinction between type-I and type-II superconductivity does not depend only on the Ginzburg-Landau parameter κ, but also on the sample thickness. Since the effective London penetration depth $\Lambda = \lambda^2/d$ increases considerably in films with thickness $d \ll \lambda$, the vortex state can appear in thin films made from a material with $\kappa < 1/\sqrt{2}$. In this case one introduces the effective Ginzburg-Landau parameter $\kappa^* = \Lambda/\xi$ which defines the type of superconductivity: type-I when $\kappa^* < 1/\sqrt{2}$ and type-II when $\kappa^* > 1/\sqrt{2}$. In mesoscopic samples the distinction between type-I and type-II superconductors is determined not only by κ and the thickness d, but also by the lateral dimensions of the sample (see e.g. Refs. [39, 40]).

In confined mesoscopic samples there is a competition between the triangular Abrikosov distribution of vortices, as being the lowest energy configuration in bulk material and thin films, and the sample boundary which tries to impose its geometry on the vortex distribution. For example, a circular disk will favor vortices situated on a ring near the boundary and only far away from the boundary its influence diminishes and the triangular lattice may reappear.

Multivortex versus giant vortex state

Depending on the geometry, the size, the applied field and the temperature, different kinds of vortex states can nucleate in mesoscopic samples: giant vortex states and multivortex states, or a mixture of both of them, e.g. in triangular and square superconductors (see chapter 3).

The **multivortex** state in mesoscopic confined samples is the analogon of the Abrikosov vortex state in bulk superconductors. The flux penetrates the sample at several positions where vortices are created. These vortices can be very close to each other and overlap, but they are defined by their separate zeros of the Cooper-pair density. On the other hand, when the sample is sufficiently small, the vortices will overlap so strongly that it is more favorable to form one big **giant vortex**, corresponding with only one minimum in the Cooper-pair density. The shape of the giant vortex also depends on the sample geometry. Figs. 1.13(a,b) show the Cooper-pair density for a multivortex state and a giant vortex state in a superconducting disk with radius $R/\xi = 6.0$. High Cooper-pair density is given by red regions, low by blue regions. This means that in Fig. 1.13(a) the blue spots are the vortices.

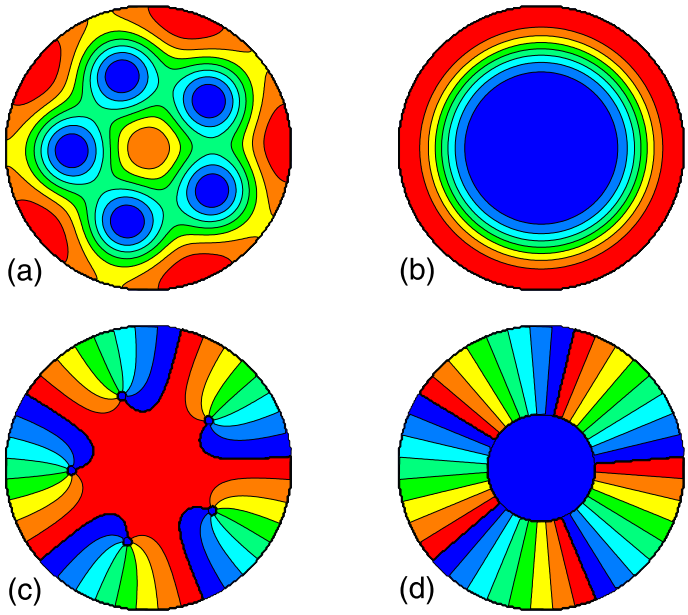

Fig. 1.13 The Cooper-pair density for the multivortex state (a) and the giant vortex state (b), and the phase of the order parameter for the multivortex state (c) and the giant vortex state (d) with vorticity $L = 5$ in a superconducting disk with radius $R/\xi = 6.0$. High (low) Cooper-pair density is given by red (blue) regions. Phases near 2π (0) are given by red (blue).

Vorticity

For a given mesoscopic sample, different superconducting states (giant vortex states and multivortex states) can nucleate for a particular magnetic field. These states have a different free energy and a different vortex configuration, and they can be characterized by their **vorticity** L. For multivortex states the vorticity is nothing else than the number of vortices. To determine the vorticity of the giant vortex state one has to look at the phase of the order parameter. Along a closed path around the vortex, the phase of the order parameter changes always with L times 2π. Fig. 1.13(c) shows the contour plot of the phase of the order parameter for the multivortex state of Fig. 1.13(a). Blue indicate phases near zero and red phases near 2π. By going around near the boundary of the disk, the phase changes 5 times with 2π. This means that the total vorticity of the disk is $L = 5$. By going around one single vortex the phase changes with 2π and $L = 1$. In Fig. 1.13(d) the phase of the order parameter is shown for the giant vortex configuration of Fig. 1.13(b). By going around the giant vortex, the phase of the order parameter changes 5 times with 2π, which means that the giant vortex state has vorticity $L = 5$.

2

Superconducting disks

2.1 INTRODUCTION

With the advent of nanofabrication technologies the study of mesoscopic superconductors revived. It became experimentally possible to study small and thin samples. Because of their simple geometry, mesoscopic disks have been the most popular study objects.

Buisson *et al.* [41] performed magnetization measurements on an ensemble of indium disks with large separation between them in order to make the dipolar interaction between the disks negligible. They found oscillatory behaviour in the magnetization near the superconducting transition temperature and showed that the linearized Ginzburg-Landau equations are able to explain qualitatively part of their experiments, but there were some major discrepancies in size and position of the jumps in the magnetization.

Geim *et al.* [2, 42, 43] used sub-micron Hall probes to detect the magnetization of single superconducting aluminium disks with sizes down to $0.1\mu m$ (see Fig. 2.1). At different applied fields the disks showed various kinds of phase transitions within the superconducting state and between the superconducting and normal state which can be first or second order depending on the sample dimensions and temperature. Later, Geim *et al.* studied also the paramagnetic Meissner effect in small superconductors [29] and the non-quantized penetration of magnetic field in the vortex state of superconductors [30, 44], which leads to fractional and negative vortices.

These experimental studies motivated theoreticians to study single mesoscopic superconductors of finite thickness during the last decade. Almost

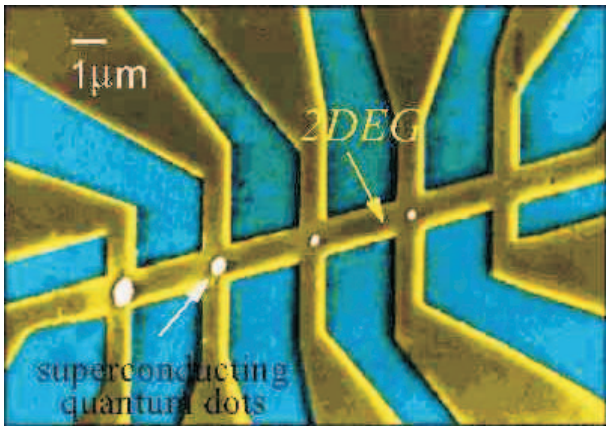

Fig. 2.1 SEM micrograph of the ballistic Hall micro-magnetometers with several mesoscopic samples in the sensitive area of the probes. [From Refs. [2, 42]]

all theoretical studies are based on the Ginzburg-Landau theory, but most of them make special assumptions to simplify the problem. The reason is that the solution of the coupled nonlinear Ginzburg-Landau equations is very complicated.

The main part of the theoretical studies covered disks of zero thickness [45–53]. In this case one can neglect the magnetic field induced by the supercurrents and one assumes that the total magnetic field equals the externally applied magnetic field, which is uniform. In other words, one only solves the first Ginzburg-Landau equation (1.52) and the second one (Eqs. (1.53), (1.54)) is neglected. A limited number of studies considered disks with finite thickness [28, 39, 54–57]. Then, the finite thickness of the disks influences the magnetic field profile and it is necessary to take into account the demagnetization effects. The magnetic field is expelled from the superconductor and, therefore, there will be a higher concentration of magnetic field near the sample edges. For this purpose both Ginzburg-Landau equations have to be solved, which is an order of magnitude more complicated.

Some studies were limited to the vicinity of the superconducting/normal transition, where the Ginzburg-Landau equations can be linearized, simplifying the problem considerably [45]. Other investigations included the nonlinear term and investigated the properties of the superconducting disks over a much broader range of magnetic field and temperature [28, 39, 46–50, 52, 54–57].

When the radius of the disk is sufficiently small one may assume that the vortex state is circular symmetric, the so-called giant vortex state [45, 55]. In this case the confinement effects dominate and the circular symmetric boundary imposes its symmetry on the vortex configuration. On the other hand, for sufficiently large disks the giant vortex states transforms into a

multivortex state. Then, an arbitrary superconducting state is generally a mixture of different angular harmonics [39, 46–50, 56].

The rest of this chapter will treat the results of Schweigert, Peeters and Deo [28, 39, 54–57], who considered thin mesoscopic superconducting disks of finite thickness within the nonlinear Ginzburg-Landau theory. For this purpose, they had to solve the coupled nonlinear Ginzburg-Landau equations in a selfconsistent way. Therefore, they produced two numerical programs. The first one, the so-called *2D program*, can only be used for small disks, because it assumes axial symmetry. The second one, the *3D program*, solves the general problem, including multivortices. Later in this thesis, we will adapt both programs to other geometries and therefore we start with a detailed description of the 2D and the 3D formalism.

2.2 THEORETICAL FORMALISMS

2.2.1 2D formalism

Let us consider a superconducting disk with radius R and thickness d. This disk is immersed in a insulating medium, for example vacuum, and is placed in a perpendicular applied magnetic field $\vec{H} = (0, 0, H_0)$. By solving the nonlinear Ginzburg-Landau equations in a selfconsistent way values for Ψ and $\vec{A}$ are found which can be used to calculate other quantities like the free energy, the magnetization and the current density.

Using dimensionless variables and the London gauge $div\,\vec{A} = 0$, the Ginzburg-Landau equations can be written as (see Eqs. (1.56), (1.57))

$$\left(-i\vec{\nabla} - \vec{A}\right)^2 \Psi = \Psi\left(1 - |\Psi|^2\right) , \tag{2.1}$$

$$-\kappa^2 \Delta \vec{A} = \frac{1}{2i}\left(\Psi^* \vec{\nabla}\Psi - \Psi\vec{\nabla}\Psi^*\right) - |\Psi|^2 \vec{A} . \tag{2.2}$$

The boundary condition for the order parameter (see Eq. (1.58)) is

$$\vec{n} \cdot \left(-i\vec{\nabla} - \vec{A}\right)\Psi\Big|_{boundary} = 0 , \tag{2.3}$$

which expresses that no supercurrent can pass perpendicular to the disk surface. The boundary condition for the vector potential is such that the total magnetic field far away from the superconductor equals the uniform applied magnetic field H_0, and thus

$$\vec{A}\Big|_{\vec{r}\to\infty} = \frac{1}{2}\vec{e}_\phi H_0 \rho . \tag{2.4}$$

Here $\vec{e}_\phi$ denotes the azimuthal direction and ρ is the radial distance from the disk center.

Free energy. The difference between the superconducting and the normal state Gibbs free energy, measured in $H_c^2 V/8\pi$, can be expressed through the integral

$$F = \frac{1}{V}\int \left[2\left(\vec{A} - \vec{A}_0\right)\cdot \vec{j} - |\Psi|^4\right] d\vec{r}\,, \tag{2.5}$$

over the disk volume $V = \pi R^2 d$. The external vector potential in the absence of a superconductor $\vec{A}_0 = \frac{1}{2}\vec{e}_\phi H_0 \rho$ and the dimensionless supercurrent is given by

$$\vec{j} = \frac{1}{2i}\left(\Psi^* \vec{\nabla}\Psi - \Psi\vec{\nabla}\Psi^*\right) - |\Psi|^2 \vec{A}\ . \tag{2.6}$$

Eq. (2.5) can be derived from Eq. (1.18), which can be rewritten in dimensionless variables as

$$\begin{aligned}\mathcal{G}_{sH} - \mathcal{G}_{nH} &= \frac{H_c^2}{4\pi}\int\left\{-|\Psi|^2 + \frac{1}{2}|\Psi|^4 + \frac{1}{2}\left|\left(-i\vec{\nabla} - \vec{A}\right)\Psi\right|^2\right\} dV \\ &+ \frac{H_c^2}{4\pi}\kappa^2\int H^2 dV + \frac{H_c^2}{4\pi}\kappa^2\int H_0^2 dV - 2\kappa^2 H_c^2\int \frac{\vec{H}\cdot\vec{H}_0}{4\pi} dV\ ,\end{aligned} \tag{2.7}$$

where $\mathcal{G}_{nH}$ is the free energy of the normal phase when an external field $\vec{H}_0$ is applied. Thus, the difference between the superconducting and normal state Gibbs free energy, measured in $H_c^2 V/8\pi$, can be expressed through the integral

$$\begin{aligned}F &= \frac{\mathcal{G}_{SH} - \mathcal{G}_{nH}}{H_c^2 V/8\pi}\ , \\ &= \int\left\{-2|\Psi|^2 + |\Psi|^4 + 2\left|\left(-i\vec{\nabla} - \vec{A}\right)\Psi\right|^2 + 2\kappa^2\left(\vec{H} - \vec{H}_0\right)^2\right\} dV\ .\end{aligned} \tag{2.8}$$

Using Gauss theorem $\int \vec{\nabla}\cdot\vec{A}\,dV = \oint \vec{n}\cdot\vec{A}\,dS$, the boundary condition (2.3), and the first Ginzburg-Landau equation (2.1) the first term on the right hand side of Eq. (2.8) can be written as

$$\int\left|\left(-i\vec{\nabla} - \vec{A}\right)\Psi\right|^2 dV = \int\left(|\Psi|^2 - |\Psi|^4\right) dV\ . \tag{2.9}$$

Therefore,

$$F = \int\left[\left(\vec{H} - \vec{H}_0\right)^2\kappa^2 - \frac{1}{2}|\Psi|^4\right] dV\ , \tag{2.10}$$

where $\vec{H} = rot\,\vec{A}$. Using the vector relations $\vec{\nabla}\cdot\left(\vec{a}\times\vec{b}\right) = \vec{b}\cdot\left(\vec{\nabla}\times\vec{a}\right) - \vec{a}\cdot\left(\vec{\nabla}\times\vec{b}\right)$ and $\vec{a}\times\left(\vec{\nabla}\times\vec{a}\right) = 0$, and the London gauge $\vec{\nabla}\cdot\vec{A} = 0$, the free energy becomes

$$F = \int\left\{\left(\vec{A} - \vec{A}_0\right)\cdot\left[\nabla^2\left(\vec{A} - \vec{A}_0\right)\right]\kappa^2 - \frac{1}{2}|\Psi|^4\right\} dV\ . \tag{2.11}$$

Finally, applying the relation $\vec{j} = -\kappa^2 \nabla^2 \vec{A}$, we arrive at Eq. (2.5).

Restriction to thin disks. The thickness of the disk is supposed to be smaller than the coherence length: $d < \xi$. For the rest there are no other limitations on the disk size. Since there are no restrictions on the penetration depth λ, the field can penetrate the disk over a distance λ and the variation of the vector potential in the z-direction can become rather strong. Nevertheless, this does not lead to important variations of the order parameter in the z-direction when the disk is thinner than the coherence length. Consequently, we can average the first Ginzburg-Landau equation over the disk thickness.

Since the order parameter does not vary in the z-direction, both the superconducting current and the vector potential have no z-component (at least over the thickness of the superconductor) and boundary condition (2.3) is fulfilled at the top and the bottom of the disk.

Fixed angular momentum. In the 2D formalism, axial symmetry is assumed and the Ginzburg-Landau equations (2.1) and (2.2) are solved for a fixed value of the angular momentum or vorticity L. Therefore, the order parameter has the following form:

$$\Psi(\rho, \phi) = f(\rho) e^{iL\phi} , \tag{2.12}$$

and, consequently, both the vector potential and the superconducting current are directed along $\vec{e}_\phi$. For a fixed angular momentum L, Eqs. (2.1), (2.2) can be reduced to

$$-\frac{1}{\rho}\frac{\partial}{\partial\rho}\rho\frac{\partial f}{\partial\rho} + \left\langle \left(\frac{L}{\rho} - A\right)^2 \right\rangle f = f(1 - f^2) , \tag{2.13}$$

and

$$-\kappa^2 \left(\frac{\partial}{\partial\rho}\frac{1}{\rho}\frac{\partial\rho A}{\partial\rho} + \frac{\partial^2 A}{\partial z^2}\right) = \left(\frac{L}{\rho} - A\right) f^2 \theta\left(\frac{\rho}{R}\right) \theta\left(\frac{2|z|}{d}\right) , \tag{2.14}$$

where $\theta(x) = 1$ for $x < 1$ and $\theta(x) = 0$ for $x > 1$, $\vec{A} = A\vec{e}_\phi$ and $\langle\rangle$ means averaging over the disk thickness $\langle g(r)\rangle = \frac{1}{d}\int_{-d/2}^{+d/2} g(z, r) dz$.

Limited simulation region. Since the magnetic field created by the supercurrents has a $H \propto 1/r^3$ dependence at large distance, the condition for the vector potential taken at infinity is transferred to the boundaries of the finite difference region

$$A(z, \rho = R_s) = \frac{1}{2} H_0 R_s , \tag{2.15}$$

$$A(|z| = d_s, \rho) = \frac{1}{2} H_0 \rho , \tag{2.16}$$

where $R_s, d_s \gg R, d$ are the radial and longitudinal sizes of the simulation region.

Boundary condition for the order parameter. In cylindrical coordinates, the boundary condition (2.3) for the order parameter becomes

$$\vec{n} \cdot \left[-i \left(\vec{e}_\rho \frac{\partial}{\partial \rho} + \frac{1}{\rho} \vec{e}_\phi \frac{\partial}{\partial \phi} + \vec{e}_z \frac{\partial}{\partial z} \right) - A \vec{e}_\phi \right] f(\rho) e^{iL\phi} \Big|_{boundary} = 0 \ . \tag{2.17}$$

This leads to following boundary conditions for the radial part F of the order parameter:

$$\left. \frac{\partial f}{\partial \rho} \right|_{\rho=R} = 0 \ , \qquad \rho \left. \frac{\partial f}{\partial \rho} \right|_{\rho=0} = 0 \ , \tag{2.18}$$

corresponding to a zero normal component of the current density at the disk surface and a possible finite value of the first derivative of f in the center of the disk.

Finite difference representation. To solve the system of equations (2.13) and (2.14) numerically, a finite difference representation is applied on the space grid ρ_i, z_i. Since the size of the simulation region exceeds by far the one of the disk, this space grid will be non-uniform outside the disk region to diminish computation time. Outside the disk region, the grid space increases exponentially with the distance. Doing this, it becomes possible to use the same number of grid points inside and outside the disk.

Integrating over the line $\rho_{i-1/2} < \rho < \rho_{i+1/2}$, where $\rho_{i+1/2} = (\rho_{i+1} + \rho_i)/2$ the first Ginzburg-Landau equation (2.13) becomes

$$\begin{aligned} -\frac{2}{\rho_{i+1/2}^2 - \rho_{i-1/2}^2} & \left(\rho_{i+1/2} \frac{f_{i+1} - f_i}{\rho_{i+1} - \rho_i} - \rho_{i-1/2} \frac{f_i - f_{i-1}}{\rho_i - \rho_{i-1}} \right) \\ & + \left\langle \left(\frac{L}{\rho} - A \right)^2 \right\rangle_i f_i = f_i - f_i^3 \ , \end{aligned} \tag{2.19}$$

where $f_i = f(\rho_i)$. The steady state solution of the Ginzburg-Landau equations will be obtained using an iteration procedure. Therefore, an upper index k is introduced to denote the iteration step. To speed up the convergency an iteration parameter η_f is added and the nonlinear term is expanded in $\left(f_i^k\right)^3 = \left(f_i^{k-1}\right)^3 + 3\left(f_i^{k-1}\right)^2 \left(f_i^k - f_i^{k-1}\right)$, which leads to the first equation to be solved numerically:

$$\begin{aligned} \eta_f f_i^k - \frac{2}{\rho_{i+1/2}^2 - \rho_{i-1/2}^2} & \left(\rho_{i+1/2} \frac{f_{i+1}^k - f_i^k}{\rho_{i+1} - \rho_i} - \rho_{i-1/2} \frac{f_i^k - f_{i-1}^k}{\rho_i - \rho_{i-1}} \right) \\ + \left\langle \left(\frac{L}{\rho} - A \right)^2 \right\rangle_i & f_i^k - f_i^k + 3\left(f_i^{k-1}\right)^2 f_i^k = \eta_f f_i^{k-1} + 2\left(f_i^{k-1}\right)^3 \ . \end{aligned} \tag{2.20}$$

To obtain the finite difference representation of the second Ginzburg-Landau equation (2.13), this equation has to be integrated over the square $z_{j-1/2} < z < z_{j+1/2}$, $\rho_{i-1/2} < \rho < \rho_{i+1/2}$. Introducing the upper index k denoting the iteration step and the iteration parameter η_a to speed up the convergence, the finite difference representation of the second Ginzburg-Landau equation becomes

$$\begin{aligned}\eta_a A^k_{j,i} - \frac{2\kappa^2}{\rho_{i+1/2}-\rho_{i-1/2}}\left(\frac{\rho_{i+1}A^k_{j,i+1}-\rho_i A^k_{j,i}}{\rho^2_{i+1}-\rho^2_i} - \frac{\rho_i A^k_{j,i}-\rho_{i-1}A^k_{j,i-1}}{\rho^2_i-\rho^2_{i-1}}\right)\\ -\frac{2\kappa^2}{z_{j+1/2}-z_{j-1/2}}\left(\frac{A^k_{j+1,i}-A^k_{j,i}}{z_{j+1}-z_j} - \frac{A^k_{j,i}-A^k_{j-1,i}}{z_j-z_{j-1}}\right)\\ -\left(\frac{L}{\rho_i}-A^k_{j,i}\right)\left(f^k_i\right)^2 = \eta_a A^{k-1}_{i,j}\ .\end{aligned} \tag{2.21}$$

The iteration parameters η_f and η_a correspond to an artificial time relaxation of the system to a steady-state with time steps $1/\eta_f$ and $1/\eta_a$.

Iteration process. In the 2D program two iteration loops are used. For every magnetic field, equations (2.20) and (2.21) must be solved selfconsistently, which means that a first iteration loop is needed to find the solutions f_i and A_i in all grid points. For the first applied field the calculation starts with the following initial conditions: the initial vector potential is the one corresponding with the external field. The initial order parameter is taken to be equal to the lowest eigenfunction of the operator

$$\widehat{L} = -\frac{1}{\rho}\frac{\partial}{\partial\rho}\rho\frac{\partial f}{\partial\rho} + \left(\frac{L}{\rho}-A_0\right)^2 - 1\ , \tag{2.22}$$

which means that it is the solution of the linearized first Ginzburg-Landau equation.

Since for a given set of $\{A_i\}$ Eq. (2.20) is nonlinear we need a second iteration loop to solve this equation. By filling in the previous values of $\{f_i\}$ in the nonlinear part, this equation becomes linear and one can calculate new values for $\{f_i\}$. After many iterations, convergency is reached and the value of the order parameter in grid point i is known. With these values of $\{f_i\}$ one calculates the vector potentials $\{A_i\}$ from Eq. (2.21). Then, the next iteration step begins by filling in these values of $\{A_i\}$ in the first Ginzburg-Landau equation (2.20). The iteration over the Eqs. (2.20) and (2.21) stops when convergency is reached and the selfconsistent values of $\{A_i\}$ and $\{f_i\}$ are found for given applied magnetic field and the vorticity L. For typical values of the iteration parameters $\eta_f = 2$, $\eta_a = 5$, convergency is reached after a few hundred iteration steps.

Then, we decrease or increase the magnetic field with a small step and the iteration over the two Ginzburg-Landau equations starts again. Now, the initial condition corresponds with the solutions $\{A_i\}$ and $\{f_i\}$ of the previous

magnetic field. The whole process must be done for every possible value of the vorticity L. It is possible to calculate the free energy, the magnetization, the Cooper-pair density, the current density and the local magnetic field for every value of the applied magnetic field and vorticity L.

2.2.2 3D formalism

In the 3D formalism we no longer assume axial symmetry and we are left with a three dimensional problem.

Restriction to thin disks. For disks with thickness $d < \lambda, \xi$ the order parameter can be assumed to be uniform in the z direction. Consequently, as far as the order parameter is concerned the disk is reduced to a 2D disk. But the 3D nature of the magnetic field distribution is completely retained. The Ginzburg-Landau equations (2.1) and (2.2) become

$$\left(-i\vec{\nabla} - \vec{A}\right)^2 \Psi = \Psi\left(1 - |\Psi|^2\right) , \tag{2.23}$$

and

$$-\Delta_{3D}\vec{A} = \frac{d}{\kappa^2}\delta(z)\vec{j}_{2D} , \tag{2.24}$$

with

$$-\vec{j}_{2D} = \frac{1}{2i}\left(\Psi^*\vec{\nabla}_{2D}\Psi - \Psi\vec{\nabla}_{2D}\Psi^*\right) - |\Psi|^2\,\vec{A} . \tag{2.25}$$

The boundary condition (2.3) becomes

$$\vec{n}\cdot\left(-i\vec{\nabla}_{2D} - \vec{A}\right)\Psi\Big|_{boundary} = 0 . \tag{2.26}$$

The indices 2D and 3D refer to two- and three-dimensional operators, and $\vec{j}_{2D}$ is the density of the superconducting current.

The boundary condition for the vector potential (2.4) becomes in cartesian coordinates:

$$\vec{A}\Big|_{|x|=R_s,|y|=R_s} = H_0(x,-y)/2 , \tag{2.27}$$

at the boundary R_s of a larger space grid.

Free energy. The difference between the superconducting and the normal state Gibbs free energy is still given by Eq. (2.5):

$$F = \frac{1}{V}\int\left[2\left(\vec{A} - \vec{A}_0\right)\cdot\vec{j} - |\Psi|^4\right]d\vec{r} . \tag{2.28}$$

Iteration process. Just like in the 2D formalism, two iteration loops are needed to solve the Ginzburg-Landau equations: One to solve the nonlinear part of Eq. (2.23) and one to find the self-consistent solution of the coupled Ginzburg-Landau equations at a fixed magnetic field. Once, a solution is obtained at a given magnetic field, the field is increased (or decreased) and this solution is used as the initial value in the iteration process. In doing so, the program stays within the same local minimum of the free energy and follows this minimum as a function of the magnetic field. At a certain field, the minimum cease to exist and the program runs towards a new minimum which is a different solution of the Ginzburg-Landau equations. Then, the magnetic field is changed further and one can investigate the magnetic field range over which the new minimum is stable by sweeping the field up and down.

Finite difference representation. To solve the system of equations (2.23)-(2.25) one applies a finite difference representation of the order parameter and the vector potential on a Cartesian space grid (x, y), which is uniform (contrary to the one of the 2D formalism). One uses the link variable approach [58] to calculate the values for the vector potential and the order parameters in the grid points. To find the steady-state solution of the Ginzburg-Landau equations, time derivatives of the order parameter and the vector potential are added to the left-hand side of equations (2.23) and (2.24), which are then iterated over time, similar to the method used to solve equation (2.20).

According to Kato *et al.* [58], the time dependent Ginzburg-Landau equation (2.23) can be written as

$$\frac{\partial \Psi}{\partial t} = -\frac{1}{12}\left[\left(\frac{\vec{\nabla}}{i} - \vec{A}\right)^2 \Psi + (1-T)\left(|\Psi|^2 - 1\right)\Psi\right] + \tilde{f}(\vec{r}, t) \ , \qquad (2.29)$$

where T is the temperature and $\tilde{f}(\vec{r}, t)$ is a dimensionless random force. The link variable between $\vec{r}_1$ and $\vec{r}_2$ is introduced as

$$U_\mu^{\vec{r}_1, \vec{r}_2} \equiv \exp\left[\int_{\vec{r}_1}^{\vec{r}_2} \vec{A}_\mu(\vec{r}) \cdot d\vec{\mu}\right], \qquad (2.30)$$

with $\mu = x, y$. For computer simulations, it is convenient to discretize the system. The discretized time dependent Ginzburg-Landau equation can be written as

$$\frac{\partial \Psi}{\partial t} = \frac{1}{12}\left[\frac{U^{kj}\Psi_k}{a_x^2} + \frac{U^{ij}\Psi_i}{a_x^2} + \frac{U^{mj}\Psi_m}{a_x^2} + \frac{U^{gj}\Psi_g}{a_x^2} - \frac{4\Psi_j}{a_x^2}\right. \qquad (2.31)$$

$$\left. + (1-T)\left(|\Psi_j|^2 - 1\right)\Psi_j\right] + \tilde{f}_j(t) \ , \qquad (2.32)$$

where the superscripts and subscripts $j, k, \ldots$ denote the lattice point as shown in Fig. 2.2, assuming $a_x = a_y$.

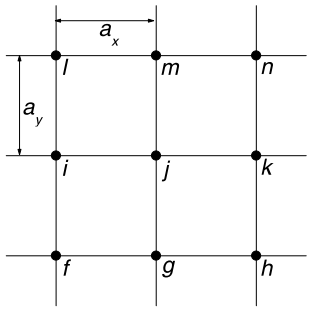

Fig. 2.2 The configuration of the lattice used in the simulations. [After Ref. [58].]

From the first equation we know the value of the order parameter Ψ in every grid point. From this value one can use equation (2.25) to calculate the current densities j_x and j_y in every grid point (where A is the vector potential found in the previous iteration step). In the finite difference representation equation (2.25) can be written as

$$j_{x,y} = \frac{1}{2}\left[\Psi^* \left(\frac{1}{i}\frac{\partial}{\partial x,y} - A_{x,y}\right)\Psi + \Psi\left(\frac{1}{i}\frac{\partial}{\partial x,y} - A_{x,y}\right)^* \Psi^*\right] , \qquad (2.33)$$

because, using the link variable method, it is known that

$$\left(\frac{1}{i}\frac{\partial}{\partial x} - A_x\right)\Psi \to -i\frac{U_x^{kj}\Psi_k - \Psi_j}{a_x} , \qquad (2.34)$$

and

$$\left(\frac{1}{i}\frac{\partial}{\partial y} - A_y\right)\Psi \to -i\frac{U_x^{mj}\Psi_m - \Psi_j}{a_x} . \qquad (2.35)$$

From the supercurrents one then calculates a new value for the vector potential using Eq. (2.24).

2.3 SMALL DISKS: GIANT VORTEX STATES

Using the 2D formalism Schweigert and Peeters investigated phase transitions between different giant vortex states in superconducting disks with sufficiently small radii. Figs. 2.3(a-d) show the free energy for superconducting disks with radii $R/\xi = 0.5$, 1.0, 1.5 and 2.0, respectively. The thickness of all disks is $d/\xi = 0.3$ and the Ginzburg-Landau parameter is $\kappa = 0.28$. For very small disks only the Meissner state can nucleate [see Figs. 2.3(a,b)], while for larger disks different giant vortex states can nucleate [see Figs. 2.3(c,d)], which leads to ground state transitions between states with different vorticity L. The

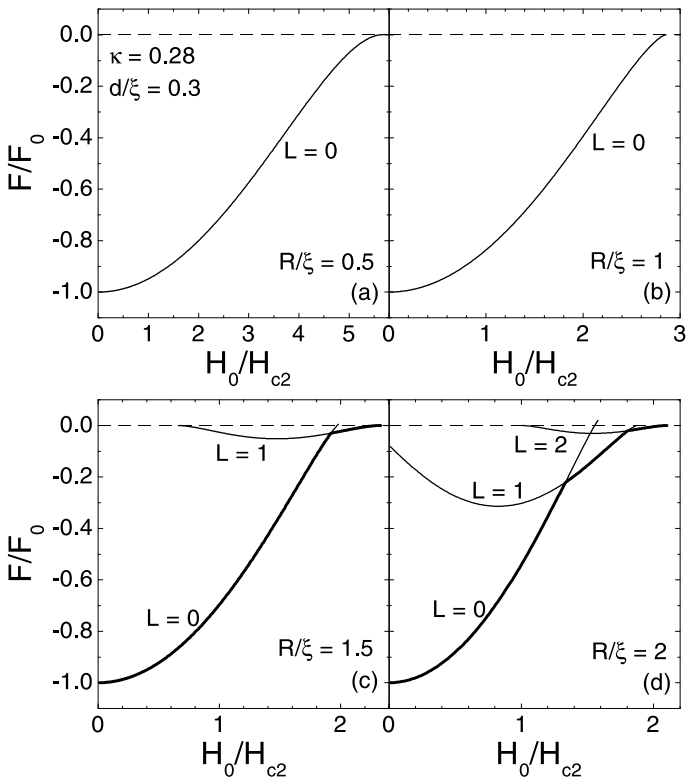

Fig. 2.3 The free energy as a function of the applied magnetic field for disks with thickness $d/\xi = 0.3$, $\kappa = 0.28$ and radius $R/\xi = 0.5$ (a), 1.0 (b), 1.5 (c), and 2.0 (d) for the different allowed vorticities L. The thick curves correspond to the ground state magnetization. [From Ref. [55].]

ground state, i.e. the state with the lowest free energy at the given magnetic field, is shown by the thick black curve. Notice that with increasing field, a particular L state is plotted until its free energy becomes zero or positive. This does not mean that these states are stable over the whole region. Within the 2D formalism it is impossible to check stability and, therefore, all curves are plotted completely. The free energy of some L states transits continuously to zero, corresponding to a second order phase transition, while the free energy of other L states increases until it is positive and then drops to zero, which result into a first order phase transition.

The radial distribution of the order parameter and the magnetic field for $d/\xi = 0.3$ and $\kappa = 0.28$ are depicted in Figs. 2.4(a-d) for two disk radii $R/\xi = 0.8$ and $R/\xi = 2.0$, respectively. For a small disk radius $R/\xi = 0.8$, the order parameter changes rather weakly with the distance from the disk center and exhibits an overall decrease with increasing field. The total magnetic flux

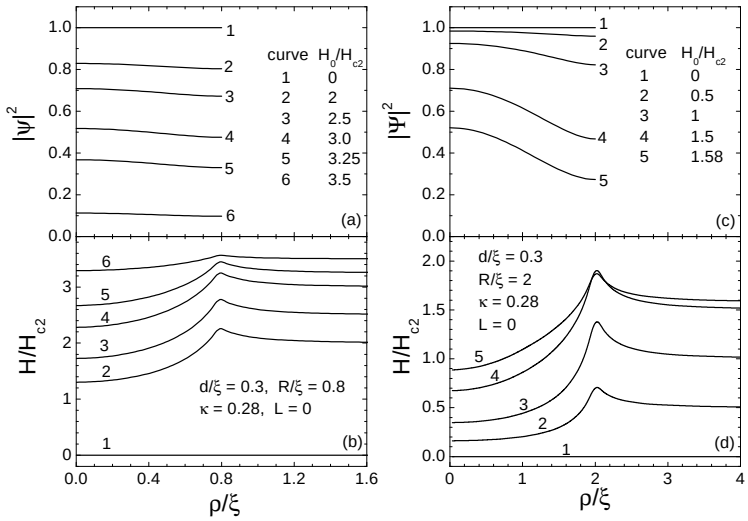

Fig. 2.4 The spatial distribution of the Cooper-pair density and the magnetic field for a disk with radius $R/\xi = 0.8$ (a,b) and $R/\xi = 2.0$ (c,d) for different applied fields. The thickness is $d = 0.3\xi$ and $\kappa = 0.28$. [From Ref. [55].]

through the disk and its surrounding region should be constant. Therefore, expulsion of the magnetic field from the disk leads to its enhancement at the disk boundary and the surrounding insulator media. For $R/\xi = 2.0$ the $L = 0$ state exhibits a first-order transition. In this case, the order parameter remains finite just before the transition to the normal state that occurs at $H/H_{c2} \approx 1.58$. Note also that the order parameter decreases much stronger near the disk boundary as compared to the smaller disk.

From the field distribution it is rather easy to calculate the magnetization, using formula (1.66), i.e.

$$M = \frac{\langle H \rangle - H_0}{4\pi} \ . \tag{2.36}$$

Figs. 2.5(a-d) show the magnetization curves corresponding to configurations of Figs. 2.3(a-d). The thick black curves correspond again to the ground state. For some curves, the transition from the superconducting to the normal state is accompanied by a jump in the magnetization. This behaviour is typical for first order phase transitions. For second order phase transitions the magnetization just decreases continuously to zero at the superconducting/normal transition.

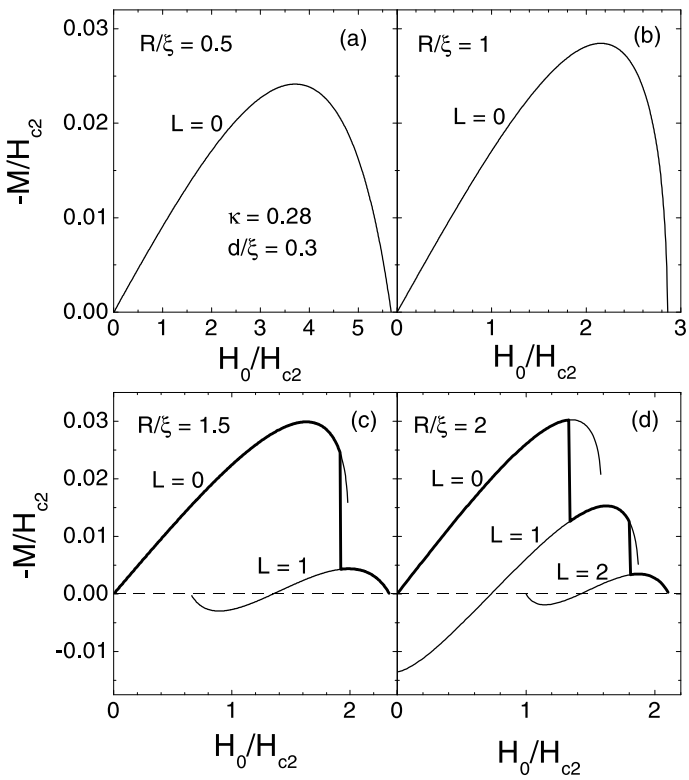

Fig. 2.5 The magnetic field dependence of the disk magnetization for disks with thickness $d/\xi = 0.3$, $\kappa = 0.28$ and radius $R/\xi = 0.5$ (a), 1.0 (b), 1.5 (c), and 2.0 (d) for the different allowed vorticities L. The thick curves correspond to the ground state magnetization. [From Ref. [55].]

2.4 LARGER DISKS: MULTIVORTEX STATES

Using the 3D formalism Schweigert, Deo and Peeters studied also larger disks where the multivortex state can nucleate [39, 49, 56]. The free energy of the different giant and multivortex configurations are shown in Fig. 2.6 by the blue and the green curves for zero disk thickness and for $R = 4.0\xi$. The vortex configuration can consist of up to six vortices which are arranged on the edge of an ideal polygon. The pentagon and hexagon clusters are always metastable states for $R = 4.0\xi$.

Contrary to the results within the 2D formalism, now the free energy of the different L states does not reach zero energy with increasing field. The reason is that, at a certain magnetic field, the state with vorticity L becomes a saddle point instead of a local minimum in the free energy landscape, and therefore it becomes unstable. The result is that one or more vortices enter or

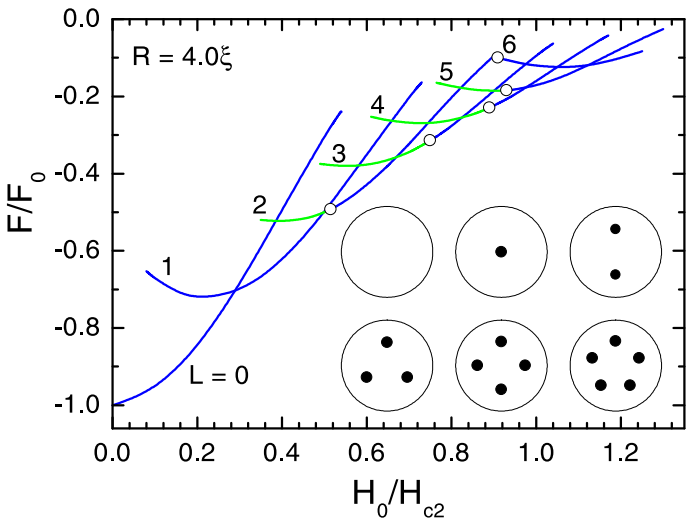

Fig. 2.6 The free energy of configurations with different number of vortices L for $R = 4.0\xi$, $d = 0.0\xi$ and $\kappa = 0.28$. The open circles indicate the transitions from a multivortex state (green curves) to a giant vortex state (blue curves). The insets show the possible multivortex configurations. [From Ref. [39].]

leave the superconductor and there is a transition to another L state. When using the 3D formalism, only the *stable states* are plotted. These states can be separated into two groups: the state which has the lowest energy at a certain magnetic field is called the *ground state*, while the other states are called *meta-stable states* (they are stable, in the sense that they correspond with a local minimum in the free energy landscape).

The gradual transition from the multivortex state to the giant vortex state with the same vorticity is illustrated in Fig. 2.7 which shows contour plots of the magnetic field distribution in the disk plane for the $L = 3$ state in a disk with radius $R = 4.0\xi$ and thickness $d = 0.5\xi\kappa^2$. Green regions correspond to the external field, while blue (red) regions indicate a field decrease (increase). Figs. 2.7(a-d) corresponds with different applied magnetic fields, i.e. $H_0/H_{c2} = 0.525$, 0.65, 0.75, and 0.8, respectively. For the lowest magnetic field the $L = 3$ multivortex state is meta-stable and a small decrease in the magnetic field will lead to a transition to the $L = 2$ state. With increasing magnetic field the vortices move to the center and, finally, they recombine in the center creating a giant vortex state. This is a second order transition, and, consequently, for fixed L, there is a unique solution with a reversible transition from the multivortex state to the giant vortex state. Therefore, there is no jump in the derivative of the free energy (nor in the magnetization) at the multivortex to giant vortex transition field.

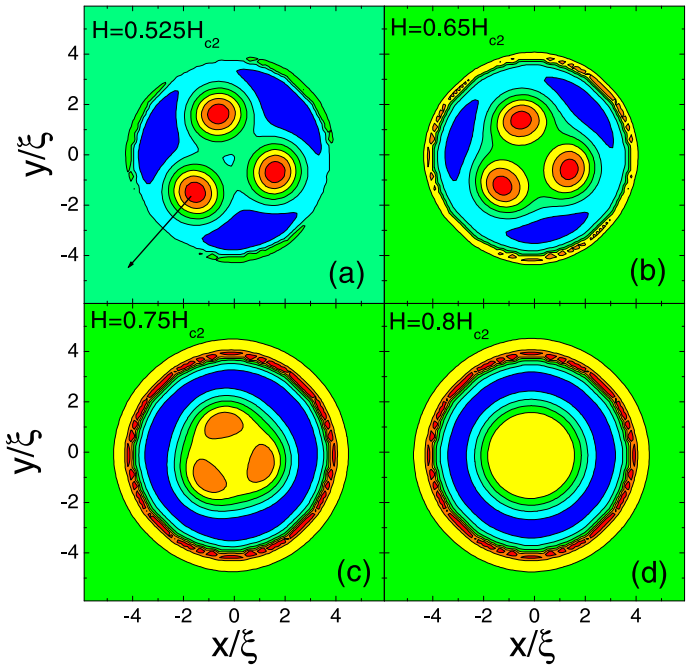

Fig. 2.7 Contour plot of the magnetic field distribution in the disk plane for the $L = 3$ state at applied magnetic fields $H_0/H_{c2} = 0.525$, 0.65, 0.75 and 0.8. Green indicate the externally applied field. Blue (red) corresponds with a decrease (increase) of the local field. [From Ref. [39].]

Having the free energies of different vortex configurations we construct an equilibrium vortex phase diagram which is shown in Figs. 2.8(a,b) for the two disk radii $R = 4.0\xi$ and $R = 4.8\xi$ respectively. The solid curves separate the regions with a different number of vortices and the dashed curves show the boundaries between the multivortex state and the giant vortex state. For $L = 1$ the single vortex state and the giant vortex state are identical. The shaded regions correspond to the multivortex state. The superconducting to normal transition occurs for $H_0/H_{c2} \approx 1.9$, which is outside the plotted region. Notice that the multivortex area in the phase diagram reduces in size with increasing disk thickness and it disappears in the limit of thick disks where only giant vortex states survive. With increasing radius the energy difference between the different L states decreases and consequently it becomes possible to build a lower energy multivortex state out of a linear combination of giant vortex states. For a decreasing radius this is more difficult to do and there exists a critical radius below which no multivortex states have the lowest energy.

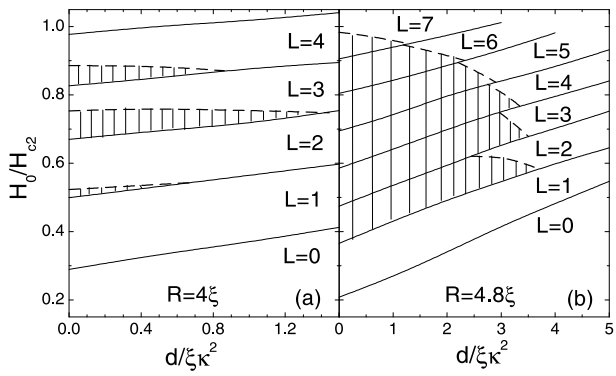

Fig. 2.8 The vortex phase diagram for two different disk radii $R = 4.0\xi$ (a) and $R = 4.8\xi$ (b). The shaded area corresponds to the multivortex states. [From Ref. [39].]

2.5 COMPARISON WITH EXPERIMENTS

Geim *et al.* [2, 59] investigated superconducting disks of different sizes. As an illustration, we show in Fig. 2.9 the experimental results (symbols) for an Al disk of radius $R \approx 0.5\mu m$ and thickness $d = 0.15\mu m$. The numerical results which includes a full self-consistent solution of the two nonlinear Ginzburg-Landau equations are given by the solid curve but which refers to the right axis ($\lambda(0) = 0.007\mu m$, $\xi(0) = 0.275\mu m$ and $\kappa = 0.28$). There is very good qualtitative agreement, but quantitatively the theoretical results differ by a factor of 50.5. The latter can be understood as due to a detector effect. Experimentally, the magnetization is measured using a Hall bar (see section

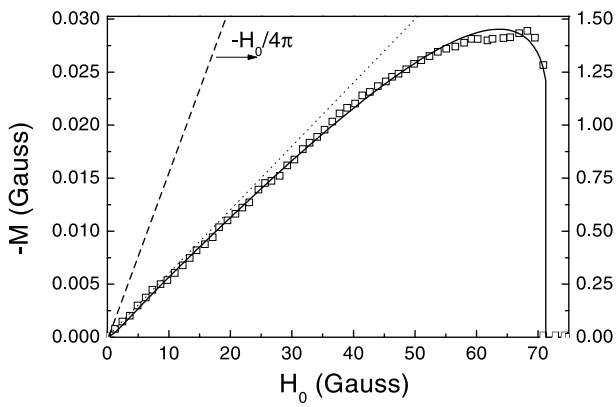

Fig. 2.9 Magnetization of an Al disk with radius $R = 0.44\mu m$ as a function of the applied magnetic field. The symbols are the experimental results and the curve is the theoretical one. [From Ref. [59].]

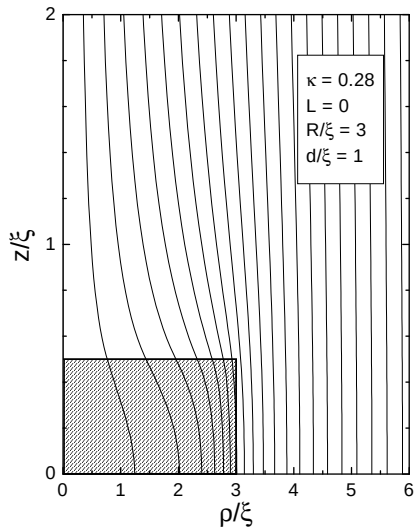

Fig. 2.10 The magnetic field distribution for the parameters given in the figure. [From Ref. [55].]

1.2). Consequently, the magnetic field is averaged over the Hall cross and it is the magnetization resulting from the field expelled from the Hall cross which is plotted, while theoretically the magnetization resulting from the field expelled from the disk is plotted. Using a Hall bar of width $W = 2.5\mu m$ separated from the superconducting disk results into a field which is a factor 50.44 smaller than the expelled field of the disk and brings the theoretical results in Fig. 2.9 in quantitative agreement with the experimental results. This averaging over the Hall cross scales the results but does not change the shape of the curve as long as the vorticity L is kept fixed. For different L this scale factor is slightly different because it leads to different magnetic field distributions.

Notice also that the magnetization as a function of the magnetic field is linear only over a small magnetic field range, i.e. $H < 20G$ and the slope [see the dotted curve in Fig. 2.9] is a factor 2.5 smaller than expected from an ideal diamagnet, where $M = -H_0/4\pi$ [see the dashed curve in Fig. 2.9] This clearly indicates that for such small thin disks there is a substantial penetration of the magnetic field into the disk. This is illustrated in Fig. 2.10 where, as an example, the magnetic field lines are shown for a superconducting disk of radius $R = 3.0\xi$ in the $L = 0$ state, i.e. the Meissner state. This strong penetration of the field inside the disk is also responsible for the highly nonlinear magnetization curve for $H \gg 20G$.

2.6 CONCLUSIONS

We will only mention the conclusions on the results of Schweigert, Peeters and Deo which are important for the purpose of this thesis.

Changing the size of the disk effects the superconducting/normal transtion field. With increasing disk radius, the transition field decreases. Changing the radius and the thickness of the disk also influences the number of possible L states. The vortex configuration depends on the sizes of the sample too. In small disks only giant vortex states are stable, while in larger disks multivortex states can nucleate in some magnetic field regions and the multivortices are situated on a ring.

By comparison with experiments, it is shown that the results from the nonlinear Ginzburg-Landau theory correspond with the experimental results using Hall magnetometry. This indicates that the Ginzburg-Landau theory is able to describe the properties of single mesoscopic superconductors, also deep inside the superconducting state, i.e. away from the superconducting/normal transition field.

3

Superconducting squares and triangles

3.1 INTRODUCTION

In mesoscopic samples there is a competition between a triangle configuration of the vortex lattice as being the lowest energy configuration in bulk material (and films) and the boundary which tries to impose its geometry on the vortex state. In previous chapter we considered circular symmetric superconductors which favoured vortices situated on a ring near the boundary and only far away from the boundary its influence diminishes and the triangular lattice may reappear. Therefore, it is expected that different geometries will favour different arrangements of vortices and will make certain vortex configurations more stable than others. In small systems vortices may overlap so strongly that it is more favourable to form one big giant vortex. As a consequence, it is expected that the giant to multivortex transition will be strongly influenced by the geometry of the boundary as will be also the stability of the giant vortex configuration.

These issues, the dependence of the stability of the giant vortex configuration and of the different multivortex configurations on the geometry of the sample will be investigated in the present chapter. As an example, we will compare the most important geometries: the circular disk, the square and the triangle. We will also investigate how the superconducting/normal transition fields are influenced by the sample geometry.

Mesoscopic superconductors with non-circular geometries have attracted less attention in the past than disks. Moshchalkov *et al.* [1] measured the superconducting/normal transition in superconducting lines, squares and square

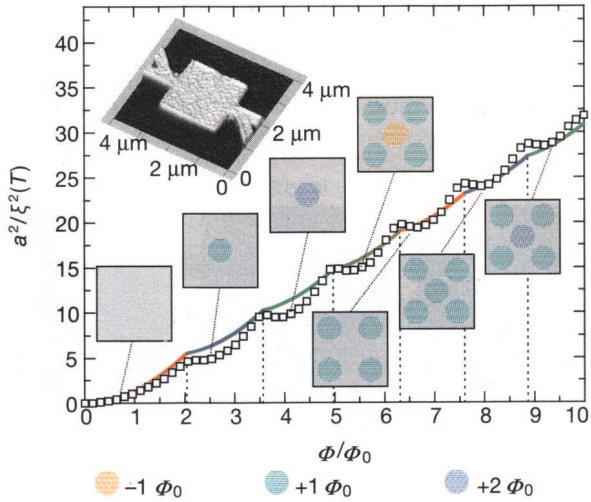

Fig. 3.1 Calculated (coloured lines) and measured (open squares) $T_c(\Phi)$ phase diagram. The top left inset shows the square sample with sides $a = 2\mu m$. In the seven insets the vortex structure in different regions of the phase diagram is shown schematically with coloured circles. [From Ref. [63].]

rings using resistance measurements. They showed the effect of the sample topology on the critical fields. Bruyndoncx *et al.* [24] calculated the $H - T$ phase diagram for a square with zero thickness in the framework of the linearized Ginzburg-Landau theory. The latter is only valid near the superconducting/normal boundary. They compared their results with the $H - T$ phase boundary obtained from resistance measurements and found good agreement. Fomin *et al.* [60, 61] studied square loops with leads attached to it and found inhomogeneous Cooper-pair distributions in the loop with enhancements near the corners of the square loop. Schweigert *et al.* [55, 57] calculated the nucleation field as a function of the sample area for disks, squares and triangles with zero thickness. Jadallah *et al.* [62] computed the superconducting/normal transition for mesoscopic disks and squares of zero thickness.

Chibotaru *et al.* obtained a "numerical" exact solution of the vortex entry and the nucleation of anti-vortices using the linearized Ginzburg-Landau theory for infinite thin superconducting squares [63] and triangles [64]. Within this linear theory they studied the superconducting/normal transition and they found near this transition the nucleation of multivortices and a combination of multivortices and anti-vortices instead of the expected surface superconductivity (see Fig. 3.1). They found that those anti-vortices appear such that the vortex state preserves the symmetry of the sample boundary. They also calculated the $H - T$ phase diagram for the square (see Fig. 3.1) and the triangle.

Bonča and Kabanov [65] studied the $\kappa \to \infty$ limit and extended the results of Chibotaru *et al.* for thin superconducting squares to include the nonlinear term in the Ginzburg-Landau theory. Within this nonlinear theory they showed that the vortex/anti-vortex configuration becomes rapidly unstable when moving away from the superconducting/normal transition.

In this chapter we consider superconductors of finite thickness and study the vortex configurations for arbitrary value of κ. The superconducting state will also be investigated far from the superconducting/normal boundary. Our main focus will be on the influence of the geometry of the superconductor on the vortex configuration, its stability, and the superconducting/normal transition fields. Our theoretical analysis is based on a full self-consistent numerical solution of the coupled nonlinear Ginzburg-Landau equations for arbitrary value of κ. No *a priori* shape or arrangement of the vortex configuration is assumed. The magnetic field profile near and in the superconductor is obtained self-consistently, and therefore the full demagnetization effect is included in our approach.

In section 3.2 we describe the theoretical formalism. We calculate and compare the free energy and the magnetization for disks, squares and triangles with the same surface area (section 3.3). Next, we make a distinction between multivortex states and giant vortex states and we investigate the influence of the sample geometry on the vortex lattice (section 3.4). The magnetic field distribution (section 3.5) and the current density (section 3.6) are studied. We also calculate the magnetic field range over which the vortex states with vorticity L are stable in disks, squares and triangles (section 3.7). The $H-T$ phase diagram is obtained (section 3.8). Finally, we summarize our results in section 3.9.

3.2 THEORETICAL FORMALISM

We consider thin superconducting samples having the same volume but with different geometry which are immersed in an insulating medium in the presence of a perpendicular uniform magnetic field H_0. To solve this problem we generalize the 3D approach for circular disks (see paragraph 2.2.2.) to superconductors with an arbitrary flat geometry. Therefore, we solve equations (2.23)-(2.25):

$$\left(-i\vec{\nabla}_{2D} - \vec{A}\right)^2 \Psi = \Psi\left(1 - |\Psi|^2\right), \tag{3.1}$$

$$-\Delta_{3D}\vec{A} = \frac{d}{\kappa^2}\delta(z)\,\vec{j}_{2D}, \tag{3.2}$$

where

$$\vec{j}_{2D} = \frac{1}{2i}\left(\Psi^*\vec{\nabla}_{2D}\Psi - \Psi\vec{\nabla}_{2D}\Psi^*\right) - |\Psi|^2\,\vec{A}, \tag{3.3}$$

is the density of superconducting current. The superconducting wavefunction satisfies the boundary conditions (2.26) and (2.27). The ground state and the meta-stable states can be found by comparing the dimensionless Gibbs free energy (2.5) of the different vortex configurations.

Opposite to the previous chapter, there exists no axially symmetric giant vortex states for non-axially symmetric systems and hence the superconducting state is always a mixture of different angular harmonics. The vorticity L of a particular superconducting sample can be calculated by considering the phase φ of the order parameter along a closed loop near the boundary of the sample, where the total phase difference is always $\Delta\varphi = L \times 2\pi$ (see paragraph 1.4.2). In this chapter we will show that in non-axially symmetric systems three possible vortex states exist:

1. a multivortex state which contains separate vortices,
2. a superconducting state which contains one giant vortex in the center, and
3. a state which is a mixture of both: a giant vortex in the center which is surrounded by single vortices.

The giant vortex is not necessary circular symmetric as in the case of a circular disk, but it may be deformed due to the specific shape of the sample boundary.

The temperature is indirectly included in ξ, λ, H_{c2} by Eqs. (1.59)-(1.61). We will only explicitly insert temperature if we consider the $H - T$ phase diagrams, while the other calculations are for fixed temperature.

As a typical example, we consider superconducting disks, squares and triangles with the same surface area $S = \pi 16\xi^2$, the same finite thickness $d = 0.1\xi$ and the same Ginzburg-Landau parameter $\kappa = 0.28$, which is typical for Al [2]. Thus the superconducting disk has a radius $R = 4.0\xi$, the square has a width $W = 7.090\xi$ and the triangle has a width $W = 10.774\xi$.

3.3 FREE ENERGY AND MAGNETIZATION

In the first step, we will compare the free energy and the magnetization for the three geometries. In Figs. 3.2(a,b) the free energy and the magnetization are shown for the disk as a function of the applied magnetic field, in Figs. 3.2(c,d) for the square and in Figs. 3.2(e,f) for the triangle. The results for the different giant vortex states are given by blue curves, those for the multivortex states by red curves and the open circles indicate the transition from the multivortex state to the giant vortex state at the transition fields H_{MG}. This transition is of second order (see section 2.4). In Figs. 3.2(b,d,f) the vertical black lines indicate the ground state transitions. There exists vortex states with vorticity up to $L = 11$ for the disk and the square and up to 13 for the triangle. The superconducting state is destroyed at $H_{c3}/H_{c2} \approx 1.95$ for the disk, at $H_{c3}/H_{c2} \approx 2.0$ for the square and $H_{c3}/H_{c2} \approx 2.5$ for the triangle. *Thus for samples with scharp corners the superconducting/normal transition moves to higher field (for fixed surface area)* [57]. Multivortex states can

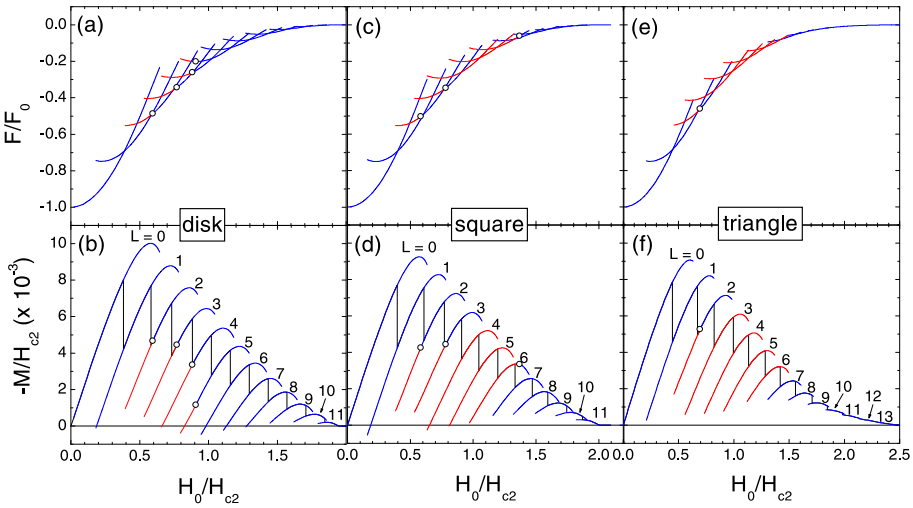

Fig. 3.2 The free energy and the magnetization as a function of the applied magnetic field for the disk, the square, and the triangle with the same surface area $S = \pi 16\xi^2$ and thickness $d = 0.1\xi$ for $\kappa = 0.28$. (a,c,e) The free energy and (b,d,f) the magnetization of the giant vortex state (blue curves) and the multivortex states (red curves) and the multivortex to giant vortex transition fields (open circles). The vertical lines in (b,d,f) give the ground state transitions.

nucleate in the disk for vorticity $L = 2, 3, 4$ and 5 and in the square and the triangle for $L = 2, 3, 4, 5$ and 6. Moreover, for the disk, with increasing field, the multivortex state always transits to a giant vortex state for fixed L, while for the square and the triangle some L states are multivortex states over the whole magnetic field range. For the triangle this is the case for the states with vorticity $L = 3, 4, 5, 6$ and for the square for the states with $L = 4$ and 5. This indicates that breaking the axial symmetry favors the multivortex state over the giant vortex state. In some magnetic field regions, the vortex state exhibits a paramagnetic response, i.e. $-M < 0$. This occurs in the disk for metastable states with $L = 1$, $4 - 8$ and in the square for metastable states with $L = 1$, 4, 5. For the triangle $-M$ is always positive, i.e. only diamagnetic behaviour is observed.

3.4 MULTIVORTEX STATES

3.4.1 Square

To distinguish whether the superconducting state is a multivortex state or a giant vortex state and to determine the multivortex to giant vortex state transition field, we considered the Cooper-pair density $|\Psi|^2_{center}$ in the center

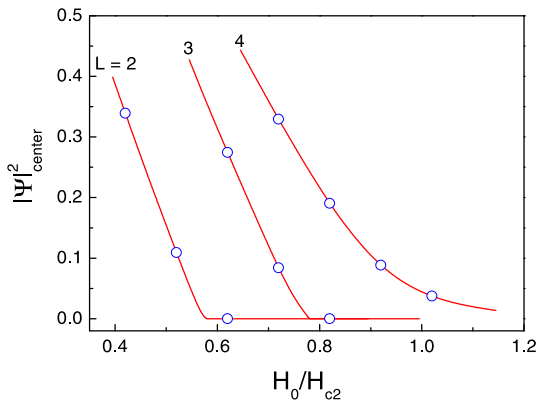

Fig. 3.3 The Cooper-pair density in the center of the square as a function of the applied magnetic field for the states with vorticity $L = 2, 3$ and 4.

of the superconductor [39]. We can be sure that the superconducting state is a multivortex state if $|\Psi|^2_{center} \neq 0$ for $L > 1$. The reason is that giant vortices are always in the center of the superconductor, and hence $|\Psi|^2_{center} = 0$. Fig. 3.3 shows the Cooper-pair density in the center of the square as a function of the applied magnetic field. The Cooper-pair density $|\Psi|^2_{center}$ is finite for $H_0/H_{c2} < H_{GM}/H_{c2} \approx 0.5825$ and 0.7825 for $L = 2$ and 3, respectively, and $|\Psi|^2_{center} = 0$ for $H_0/H_{c2} > H_{GM}/H_{c2}$. For $L = 4$ the Cooper-pair density in the center differs from zero over the whole magnetic field region where the $L = 4$ state is stable. On the other hand $|\Psi|^2_{center} = 0$ does not guarantee that the superconducting state is a giant vortex state. For example, the multivortex state in a square for $L = 5$ shows 4 vortices away from the center situated on the diagonals and one vortex in the center, and hence $|\Psi|^2_{center} = 0$. Therefore, we studied the Cooper-pair density distribution in detail. If two vortices are very close to each other, then the Cooper-pair density on the axis between these two vortices will become very low too, which means that the separation between two vortices becomes invisible in the contour plots. Therefore we have to define another criterion to determine the multivortex to giant vortex transition. If the maximum between two minima in the Cooper-pair density (i.e. the vortices) is lower than 0.5% of the maximum Cooper-pair density $|\Psi|^2_{max}$ in the sample, then we will say that the vortices form a giant vortex state instead of a multivortex state. With this criterion we find that for the square geometry the $L = 5$ state is always a multivortex state and the $L = 6$ state is a multivortex state for $H_0/H_{c2} < 1.37$ and a giant vortex state for $H_0/H_{c2} > 1.37$.

How do the multivortex states look like? Figs. 3.4(a-c) show the Cooper-pair density for a multivortex state with $L = 2$, 3, and 4 at $H_0/H_{c2} = 0.42$, 0.67, and 0.745, respectively. High Cooper-pair density is given by red regions, low Cooper-pair density by blue regions. For $L = 2$ the vortices are along the

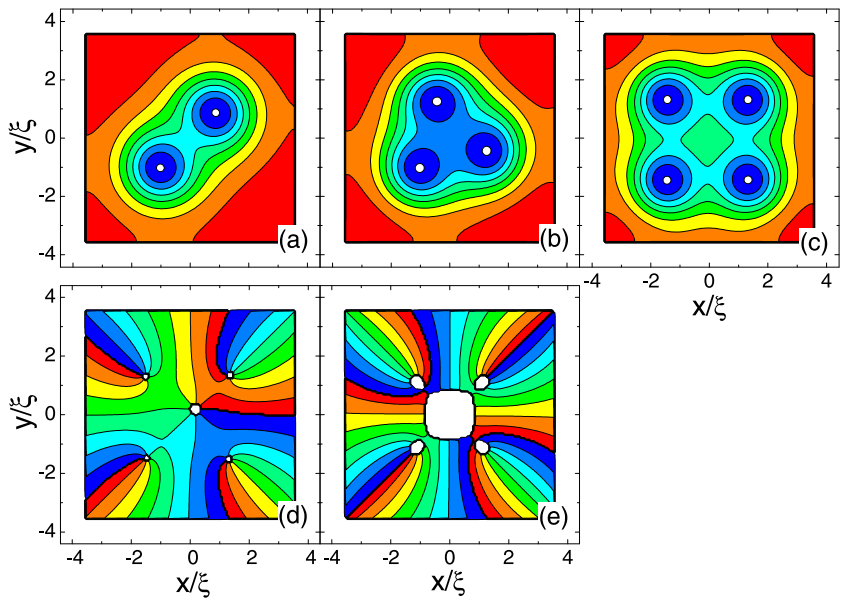

Fig. 3.4 (a-c) The Cooper-pair density for a multivortex state in a square with $L = 2$, 3, and 4 at $H_0/H_{c2} = 0.42$, 0.67, and 0.745, respectively. High Cooper-pair density is given by red regions, low Cooper-pair density by blue regions. (d,e) The phase of the order parameter for the multivortex states with $L = 5$ at $H_0/H_{c2} = 0.82$ and with $L = 6$ at $H_0/H_{c2} = 1.32$. Phases near zero are given by blue regions, phases near 2π by red regions.

diagonal, for $L = 3$ the vortices are on a triangle, and for $L = 4$ they are on a square. For $L = 4$ only the multivortex state is found which is favoured over the giant vortex state. The reason is that the square vortex lattice easily fits in the sample. Figs. 3.4(d,e) show the phase of the order parameter for the multivortex states with $L = 5$ at $H_0/H_{c2} = 0.82$ and with $L = 6$ at $H_0/H_{c2} = 1.32$. Phases near zero are given by blue regions and phases near 2π by red regions. By going around the superconductor, the phase changes 5 times 2π in Fig. 3.4(d) and 6 times 2π in Fig. 3.4(e). For $L = 5$ there are 4 vortices on a square and the fifth vortex is in the center. The latter has clearly vorticity one. For $L = 6$ there are also 4 vortices on a square and the other vortices are in the center forming one giant vortex with vorticity 2. Thus in this case we have the remarkable coexistence of a giant vortex in the center with vorticity 2 and 4 clearly separated vortices around it. For this case the multivortex to giant vortex transition field is defined as the field where separate vortices appear with decreasing field. This means that in Fig. 3.2 some states are indicated as multivortex, even though there exist a (giant) vortex in the center with vorticity $L > 1$. Thus we consider a state no longer as a giant vortex state when not all flux of the vortex is confined

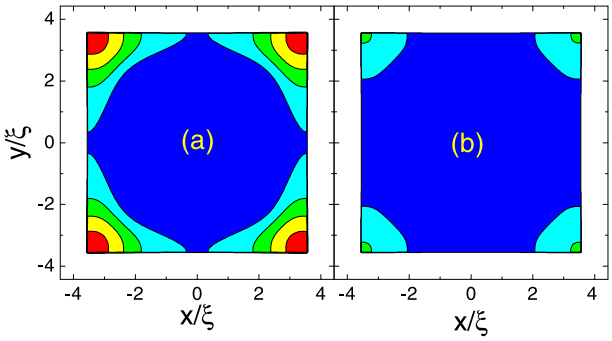

Fig. 3.5 The Cooper-pair density for the $L = 11$ state in a square at $H_0/H_{c2} \approx 1.9$ (a) and 1.95 (b).

in a single connected region. Notice also that not only the configuration of the multivortices tries to have the same geometry as the sample, but also the giant vortex geometry depends on the sample geometry.

We found that for this size of the square sample, the states with $L > 6$ are always in the giant vortex state. With increasing L this giant vortex grows and superconductivity only occurs in the corners of the square. This is illustrated in Figs. 3.5(a,b) which shows the Cooper-pair density for the $L = 11$ state at $H_0/H_{c2} \approx 1.9$ and 1.95. It is obvious that further increasing the field pushes the superconducting condensate more to the corners. At the superconducting/normal transition field $H_0/H_{c2} \approx 2.0$ the corners become normal too. Only extremely close to the superconductor/normal transition the order parameter exhibits additional separate zero's in the central part of the sample which correspond to the predicted vortex/anti-vortex configurations. We refer to Refs. [63, 64] for a detailed study of these states. But note that our calculation also provides the amplitude of the order parameter which turns out to be very small $\left(|\Psi| < 10^{-3}\right)$ in the central area of the sample. As a consequence, additional zero's of the order parameter in this central region will lead to an extremely small variation of the Cooper-pair density ($|\Psi|^2 < 10^{-6}$). The corresponding variations in the magnetic field will also be extremely small $\left(\Delta H/H_0 < 10^{-5}\right)$ and probably impossible to detect experimentally.

Fig. 3.6 shows the positions of the vortices for the $L = 3$ state in a square at applied magnetic fields $H_0/H_{c2} = 0.545$, 0.62, 0.695, and 0.77. The latter one is just below the multivortex to giant vortex state transition field $H_{GM}/H_{c2} \approx 0.7825$. The solid lines indicate the square boundaries. With increasing field the vortices move towards the center of the square and at $H_{GM}/H_{c2} \approx 0.7825$ they combine in the center and form one giant vortex with vorticity $L = 3$. In the multivortex state, one vortex is always situated on the diagonal of the square, regardless of the magnetic field. The other two vortices are located such that the three vortices form a equilateral triangle which is centered in the center of the square. Since the vortices move to the center with increasing

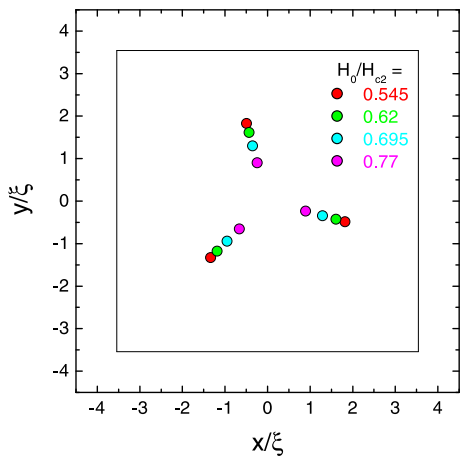

Fig. 3.6 The position of the vortices for the $L = 3$ state in a square for different applied magnetic fields $H_0/H_{c2} = 0.545$, 0.62, 0.695, and 0.77.

field, the width W of the triangular vortex lattice decreases, i.e. $W = 3.27$, 2.89, 2.32, 1.61 at $H_0/H_{c2} = 0.545$, 0.62, 0.695, 0.77, respectively.

3.4.2 Triangle

For the triangle geometry multivortex states nucleate with vorticity $L = 2, 3, 4, 5$ and 6 [see Figs. 3.2(e,f)]. Figs. 3.7(a-c) show the Cooper-pair density for a multivortex state with $L = 2$, 3, and 4 at $H_0/H_{c2} = 0.495$, 0.82, and 0.745, respectively. High Cooper-pair density is given by red regions and low Cooper-pair density by blue regions. In the multivortex state with vorticity $L = 2$ the vortices are situated along one of the perpendicular bisectors of the triangle. In the $L = 3$ state the vortices are on a triangle which easily fits in the sample, while the $L = 4$ state consists of 3 vortices on a triangle and the fourth vortex is situated in the center. Instead of the square configuration as in the case of the square geometry, the vortex lattice tries to copy the geometry of the sample, i.e. the triangular geometry. For the multivortex states with $L = 5$ and $L = 6$, the separation of vortices becomes invisible in the contourplots of the Cooper-pair density, which show one big vortex in the center. The reason is that the maximum Cooper-pair density on the axis between two vortices is very low. Therefore, we show the phase of the order parameter in Figs. 3.7(d,e) for the multivortex states with $L = 5$ at $H_0/H_{c2} = 1.27$ and with $L = 6$ at $H_0/H_{c2} = 1.345$. Phases near zero are given by blue regions and phases near 2π by red regions. In both cases there is a coexistence of a giant vortex in the center and 3 separated vortices around it placed in the direction of the corners. Taking a loop around the giant vortex, the phase changes respectively by 2 and 3 times 2π, which means that the vorticity of

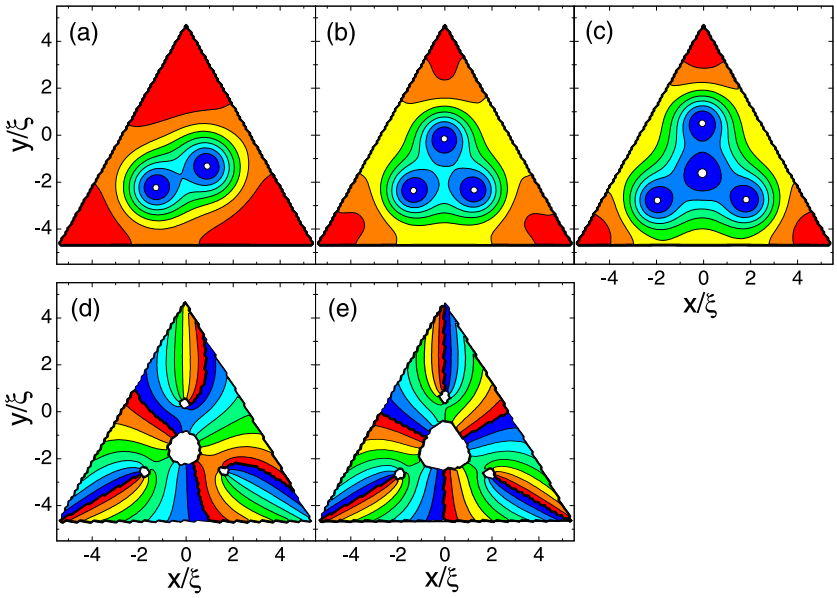

Fig. 3.7 (a-c) The Cooper-pair density for the multivortex states in a triangle with $L = 2$, 3, and 4 at $H_0/H_{c2} = 0.495$, 0.82, and 0.745, respectively. High Cooper-pair density is given by red regions and low Cooper-pair density by blue regions. (d,e) The phase of the order parameter for the multivortex states with $L = 5$ at $H_0/H_{c2} = 1.27$ and with $L = 6$ at $H_0/H_{c2} = 1.345$. Phases near zero are given by blue regions, phase near 2π by red regions.

the giant vortex is 2 in the case of the $L = 5$ multivortex state and 3 in the case of the $L = 6$ multivortex state. Notice also that for $L = 6$ the geometry of the giant vortex is not axial symmetrical, but triangular. States with $L > 6$ are always giant vortex states as we also found for the square. With increasing L this giant vortex grows and for large vorticities superconductivity only occurs in the corners of the triangle. Further increasing the field pushes the superconductivity more to the corner until these corners become normal too at the superconducting/normal transition field.

3.4.3 Disk

For the circular disk we find multivortex states with vorticity $L = 2, 3, 4$ and 5 [see Figs. 3.2(a,b)]. Figs. 3.8(a-d) show the Cooper-pair density for the multivortex states with vorticity $L = 2, 3, 4, 5$ at $H_0/H_{c2} = 0.495$, 0.62, 0.965 and 0.82, respectively. High Cooper-pair density is given by red regions, low by blue regions. Multivortex states for disks were already studied in chapter 2. Therefore, in this chapter we only stress that in a disk the multivortices are

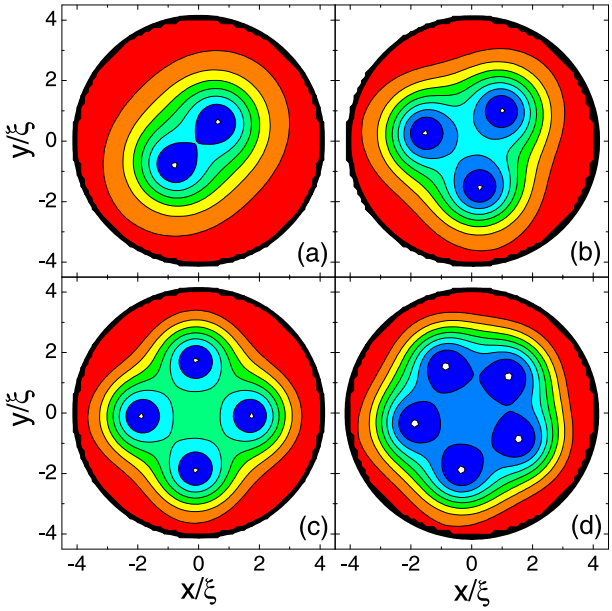

Fig. 3.8 (a-d) The Cooper-pair density for the multivortex states in a disk with vorticity $L = 2, 3, 4, 5$ at $H_0/H_{c2} = 0.495$, 0.62, 0.965 and 0.82, respectively. High (low) Cooper-pair density is given by red (blue) regions.

positioned on a ring, which means that also in this case the sample imposes its symmetry on the vortex lattice.

From the study of the Cooper-pair density and the phase of the order parameter we learned that: (i) multivortex states nucleate in disks as well as in squares and triangles for several values of the vorticity L, and (ii) the vortex lattices trie to have the same geometry as the sample.

3.5 MAGNETIC FIELD DISTRIBUTION - DEMAGNETIZATION EFFECTS

Since we studied samples with finite thicknesses, demagnetization effects are important and therefore we had to solve for the magnetic field distribution around the sample. In this section we will describe the magnetic field distribution for the square. The results for the disk and the triangle are analogous.

In Figs. 3.9(a-f) the magnetic field distribution is shown for the square geometry for the state with vorticity $L = 2$ at $H_0/H_{c2} = 0.42$, 0.52 and 0.62 [see open circles in Fig. 3.3], and with vorticity $L = 3$ at $H_0/H_{c2} = 0.62$, 0.72 and 0.82, respectively. Green regions correspond with the external magnetic field. Higher magnetic field is given by red regions and lower by blue regions.

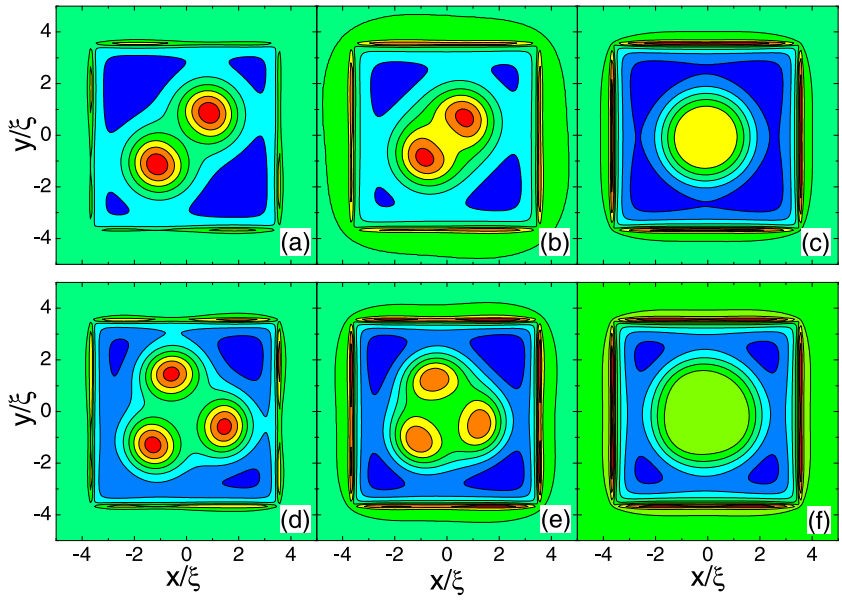

Fig. 3.9 The magnetic field distribution for the square for the state with vorticity $L = 2$ at $H_0/H_{c2} = 0.42$ (a), 0.52 (b) and 0.62 (c), and with vorticity $L = 3$ at $H_0/H_{c2} = 0.62$ (d), 0.72 (e) and 0.82 (f), respectively. Green indicates the external magnetic field. Higher magnetic field is given by red regions and lower by blue regions.

The magnetic field is clearly non-uniform in and around the sample. The red/yellow spots in the square are the vortices and the red/yellow regions near the sample surface are due to the compression of the magnetic lines when they are forced to go around the sample. These regions are responsible for the demagnetization effects. It is clear that with increasing external field and fixed number of vortices, the demagnetization effects are more pronounced, because the superconductor has to expel more magnetic field. In Figs. 3.9(a,b,d,e) the superconducting state is a multivortex state and the separated vortices are clearly visible, while in Figs. 3.9(c,f) where $H_0/H_{c2} > H_{MG}/H_{c2} \approx 0.5825$ and 0.7825 for $L = 2$ and 3, respectively, there is one giant vortex in the center. With increasing field the vortices move towards the center and at $H_0 = H_{MG}$ they combine to one giant vortex state. Notice that the giant vortex state is not necessarily axial symmetric as was in the case of the disk.

In Figs. 3.10(a-d) the magnetic field distribution is shown for the square geometry for the state with vorticity $L = 4$ at the magnetic fields indicated by the open circles in Fig. 3.3, i.e. $H_0/H_{c2} = 0.72$, 0.82, 0.92 and 1.02, respectively. Now, there is no transition from multivortex to giant vortex state and the four vortices are cleary visible as red/yellow spots. Notice that from the magnetic field distribution one clearly observes that the vortex

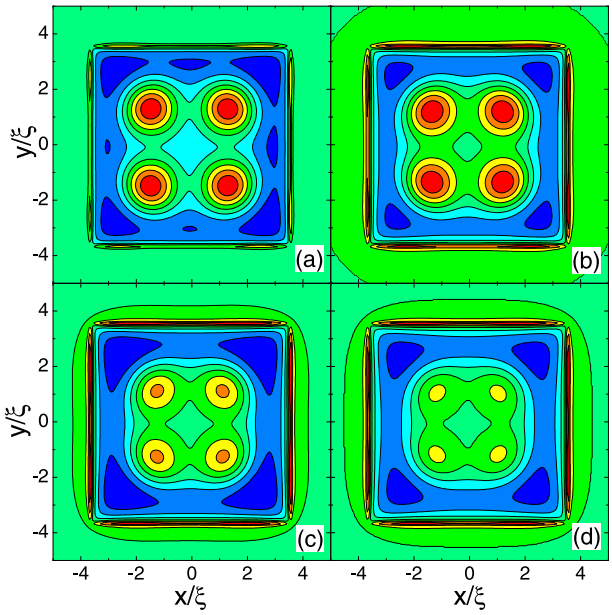

Fig. 3.10 The magnetic field distribution for the square for the state with vorticity $L = 4$ at $H_0/H_{c2} = 0.72$ (a), 0.82 (b), 0.92 (c) and 1.02 (d). Green corresponds to the external field. Higher (lower) magnetic fields are given by red (blue) regions.

lattice is a square lattice, i.e. the lattice geometry is the same as the sample geometry, and that the vortices move towards the center with increasing field.

For the multivortex states with higher vorticity, the separated multivortices are not visible anymore in the contour plots of the magnetic field distribution. The problem is the same as for the contour plots of the Cooper-pair density, i.e. the vortices are too close to each other and the spots corresponding to high magnetic fields are overlapping in the picture. For high vorticity and high external fields, the total magnetic field appreciably differs from the externally applied field only in the corners of the square. Figs. 3.11(a,b) shows the magnetic field distribution for the same configuration as in Figs. 3.5(a,b), i.e. the $L = 11$ state at $H_0/H_{c2} \approx 1.9$ and 1.95, respectively. A local decrease in magnetic field is given by the blue regions, an increase by the red regions. In both pictures the magnetic field is only substantially expelled in the corners and consequently only near the corners there is a higher density of magnetic field lines at the outside of the square. Further increasing the field destroys the superconductivity and, thus, the total field becomes equal to the external one over the whole sample.

Next, we investigate the dependence of the magnetic field on z (Remember that the superconductor is situated in the x, y plane). Figs. 3.12(a-f) show the magnetic field distribution for the $L = 4$ state in a square for different values

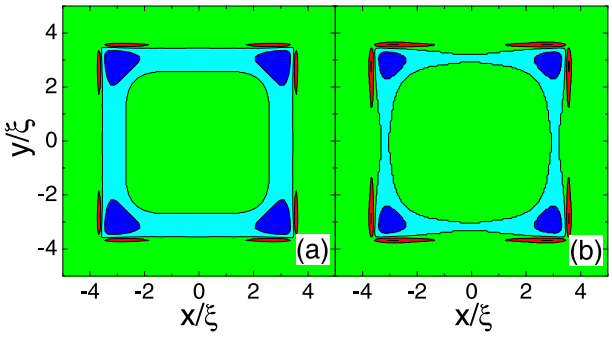

Fig. 3.11 The magnetic field distribution for the $L = 11$ state in a square at $H_0/H_{c2} \approx 1.9$ (a) and 1.95 (b). Green regions correspond with the external field. Higher (lower) magnetic fields are given by red (blue) regions.

of z, $z/\xi = 0.0$, 0.1, 0.3, 0.6, 1.0 and 10.0, respectively. The applied magnetic field is $H_0/H_{c2} = 0.77$. High magnetic field is given by red regions, low magnetic field by blue regions. In the plane of the superconductor, i.e. $z = 0$, the magnetic field which penetrates the superconductor is either compressed into multivortices or expelled to the outside of the sample. Therefore, the four yellow spots in Fig. 3.12(a) indicate the vortices and the blue regions towards the sample boundary are due to the expulsion of the magnetic field towards the outside of the superconductor. As a consequence, the magnetic field increases in a small strip near the sample boundary. With increasing z and $|z| > d/2$, the magnetic field will still be influenced by the superconductor. The demagnetization effects decrease with increasing z and the compression of the magnetic field lines into vortices becomes smaller. Therefore, the vortices and the expulsion of the field will become less pronounced with increasing z. At $z = 0.1\xi$, the vortices and the results of the magnetic field expulsion are still visible by the yellow and blue regions [see Fig. 3.12(b)]. In Fig. 3.12(c) and (d), at $z = 0.3\xi$ and 0.6ξ, respectively, the contrast in the picture decreases which means that the influence of the superconductor, i.e. the compression and expulsion of the magnetic field lines, decreases. At $z = 1.0\xi$ the magnetic field just slightly decreases right above the superconductor compared to the external field [see Fig. 3.12(e)]. At $z = 10.0\xi$ the total magnetic field is homogeneous. Far away from the superconductor, the magnetic field is not influenced by the superconductor and equals the external field. This is clearly shown in Fig. 3.12(f).

3.6 SUPERCONDUCTING CURRENT DENSITY

When a superconducting sample is placed in an external magnetic field, the magnetic field is expelled from the superconductor due to screening currents

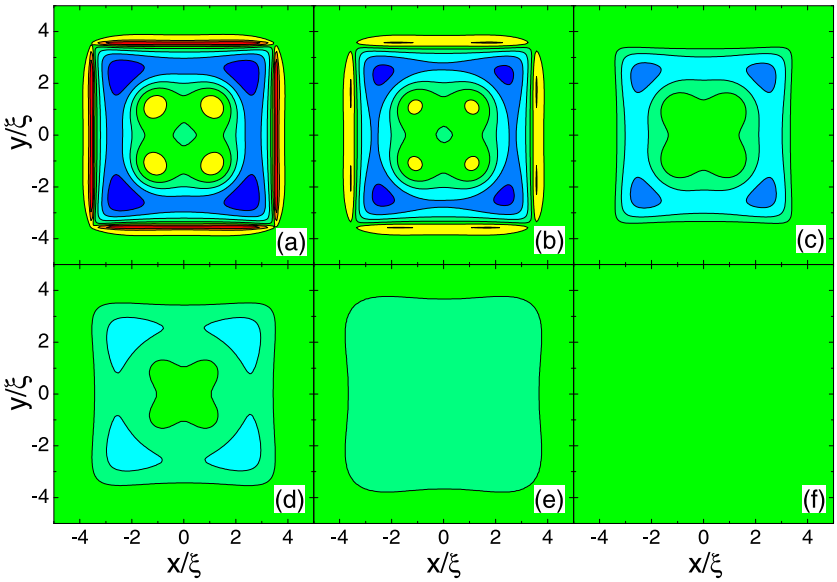

Fig. 3.12 The magnetic field distribution for the $L = 4$ state around a square at different heights from the plane of the square: $z/\xi = 0.0$ (a), 0.1 (b), 0.3 (c), 0.6 (d), 1.0 (e) and 10.0 (f), respectively. The applied magnetic field is $H_0/H_{c2} = 0.77$. Green regions correspond to the external field. Higher (lower) magnetic fields are given by red (blue) regions.

near the sample boundary. The direction of the screening currents is such that the corresponding magnetic field is opposite to the external one, which leads to a lower total field in the superconductor. Magnetic field penetrating the superconductor creates currents flowing in the opposite direction to the screening currents. The competition between these currents and the screening currents results in the existence of vortices.

Figs. 3.13(a-d) show vector plots (yellow arrows) of the supercurrent in the superconducting square for the $L = 1$ state at $H_0/H_{c2} = 0.27$, the $L = 2$ state at $H_0/H_{c2} = 0.42$, the $L = 3$ state at $H_0/H_{c2} = 0.67$ and the $L = 4$ state at $H_0/H_{c2} = 0.745$, respectively. The coloured background of Figs. 3.13(a-d) shows the corresponding contour plots of the phase of the order parameter. Phases near 2π are given by red regions, phases near zero by blue regions. From the phase of the order parameter one can easily determine the number and the positions of the vortices. In Fig. 3.13(a) it is clear that the screening currents near the sample boundary flow clockwise and the currents around the vortex in the center counterclockwise. In Figs. 3.13(b,c,d) there are currents flowing counterclockwise around 2, 3 and 4 vortices, respectively. Around one vortex, the size of the current, indicated by the length of the arrows in Figs. 3.13(a-d), is not the same for every angle. In Fig. 3.13(b) it is clear that

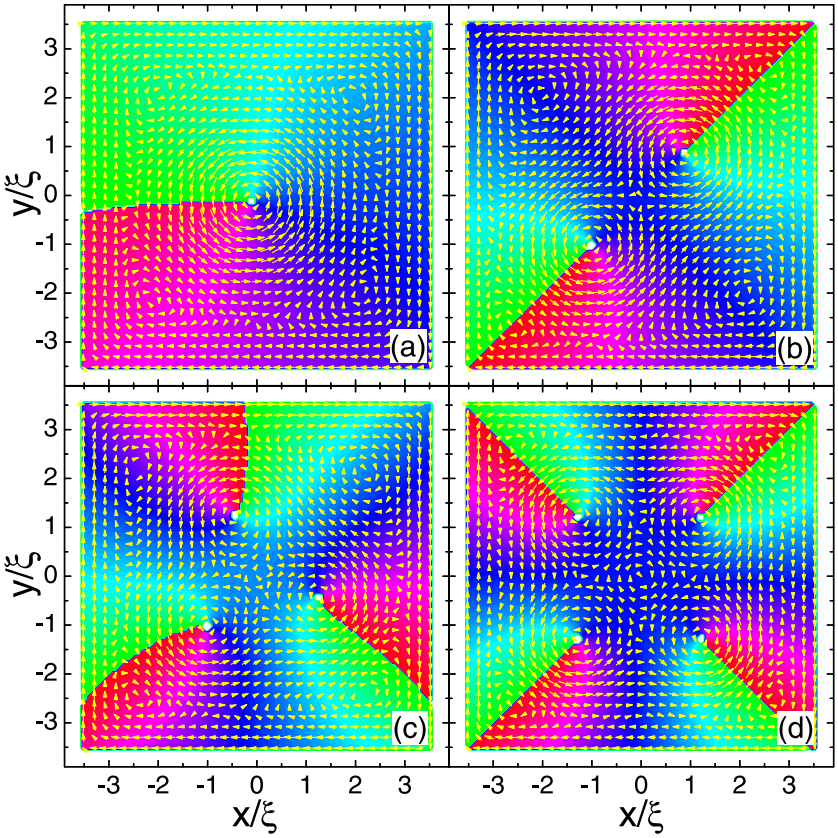

Fig. 3.13 (a-d) Vector plots of the supercurrent in the superconducting square (yellow arrows) and contour plots of the phase of the order parameter for the $L = 1$ state at $H_0/H_{c2} = 0.27$ (a), the $L = 2$ state at $H_0/H_{c2} = 0.42$ (b), the $L = 3$ state at $H_0/H_{c2} = 0.67$ (c) and the $L = 4$ state at $H_0/H_{c2} = 0.745$ (d). Phases near 2π (0) are given by red (blue) regions.

in the region between the two vortices the currents around these two vortices cancel each other out. Also, in the case of $L = 3$ and $L = 4$ the currents around the different vortices cancel out each other in the center of the sample [see Fig. 3.13(c,d)].

From the vector plot of the current density one expects anti-vortices towards the corners, because there are some spots where the currents flow in clockwise direction. That these are not really anti-vortices can be seen from the phase of the order parameter. By going around an anti-vortex, the phase changes with -2π and this is clearly not the case here. Moreover, the Cooper-pair density, shown in Figs. 3.4(a-c), is not zero at these positions. Such back

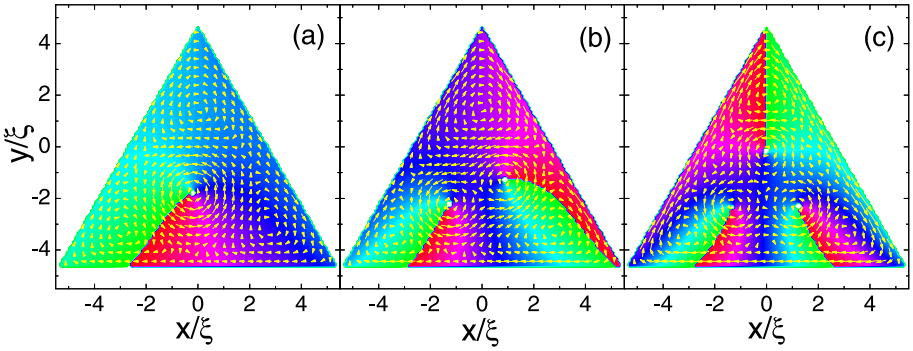

Fig. 3.14 (a-c) Vector plots of the supercurrent in the superconducting triangle (yellow arrows) and contour plots of the phase of the order parameter for the $L = 1$ state at $H_0/H_{c2} = 0.27$ (a), the $L = 2$ state at $H_0/H_{c2} = 0.495$ (b), and the $L = 3$ state at $H_0/H_{c2} = 0.82$ (c). Phases near 2π (0) are given by red (blue) regions.

flow currents were also found in square superconductor cylinders by Aftalion *et al.* [66].

Next, we investigate the superconducting current density in the triangular sample. Figs. 3.14(a-c) show vector plots of the supercurrent (yellow arrows) in the superconducting triangle for the $L = 1$ state at $H_0/H_{c2} = 0.27$, the $L = 2$ state at $H_0/H_{c2} = 0.495$, and the $L = 3$ state at $H_0/H_{c2} = 0.82$, respectively. The corresponding phase of the order parameter is given by the contour plots in the background of Figs. 3.14(a-c). Phases near 2π are given by red regions, phases near zero by blue regions. The behavior of the supercurrent in triangular samples is similar to the one in square samples. The screening currents flow clockwise and the current around the vortices in the opposite direction. The currents around different vortices cancel each other in the region between them. Towards the corners, there are some spots where the current flows in a clockwise direction, but these spots are not anti-vortices. This can be seen from the phase of the order parameter [see Figs. 3.14(d-f)] and from the Cooper-pair density [see Figs. 3.7(a-b)]. Notice further that these results are very similar to the currents in the tip of a wedge [67, 68].

3.7 STABILITY OF THE VORTEX STATES

Not only the stability region of the multivortex states with respect to the giant vortex states depends on the sample geometry, but also the stability of each individual superconducting state is sensitive to the geometry. In Fig. 3.15 we show the magnetic field range ΔH over which the vortex state with vorticity L is stable, i.e. $\Delta H = H_{expulsion} - H_{penetration}$, as a function of the vorticity L, for $L \leq 6$ and in the inset for $L \geq 6$. For the disk the result is shown by

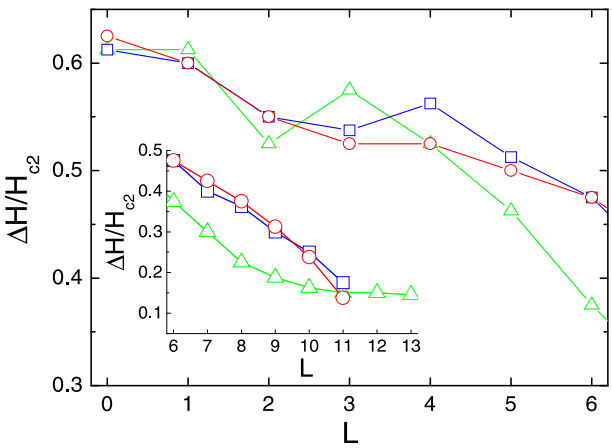

Fig. 3.15 The magnetic field range over which the vortex states with vorticity L are stable as a function of the vorticity L for the disk (red circles), the square (blue squares) and the triangle (green triangles).

the red circles, for the square by the blue squares and for the triangle by the green triangles while the curves are guides to the eye. For the circular disk the stability region $\Delta H/H_{c2}$ uniformly decreases with increasing L with a slight dip at $L = 2, 3$. The square and the triangle exhibit a peak structure in the region $L < 5$. For the square we find that the state with $L = 4$ is stable over a larger magnetic field region than the state with vorticity $L = 3$, which is a consequence of the fact that the vortex lattice tries to keep the same geometry as the sample. For the triangle we find a peak at $L = 3$ and a dip at $L = 2$ for the same reason. Notice that: i) the peak structure is more pronounced for structures which fit more closely the triangular Abrikosov lattice; ii) for $L > 4$ no clear peaks are found; iii) the vortex states in the square and circle geometry have almost the same stability range for $L \leq 2$ and $L \geq 6$; iv) for $L \geq 4$ the stability range for the vortex state in the triangular geometry becomes substantially smaller than for the other two geometries which have less sharp corners. Thus, sharp corners decrease the stability range of the vortex states.

3.8 H-T PHASE DIAGRAM

Until now, all our calculations were done for fixed temperature T. Now we will include temperature and our lateral dimensions and fields will be expressed in the zero temperature results $\xi(0)$ and $H_{c2}(0)$, respectively. Temperature will be expressed in units of the criticial temperature T_{c0} at zero magnetic

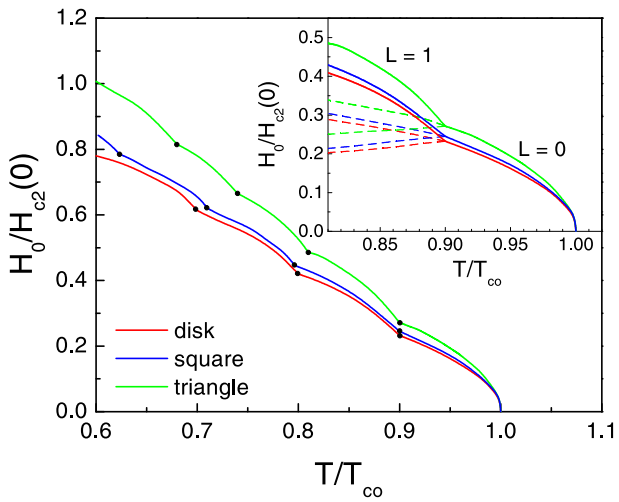

Fig. 3.16 The $H-T$ phase diagram for the disk (red curve), the square (blue curve) and the triangle (green curve). Only the superconducting normal transition H_{c3} is shown as a function of the temperature. The inset shows the $H-T$ phase diagram for the states with vorticity $L=0$ and $L=1$. The solid curves are the superconducting/normal transitions and the dashed curves indicate the penetration and the expulsion.

field. We take the surface area of our samples $S = 16\pi\xi^2(0)$ and the thickness $d = 0.1\xi(0)$.

The $H-T$ phase diagram is shown in the inset of Fig. 3.16 for the disk (blue curves), the square (red curves) and the triangle (green curves) for the states with vorticity $L=0$ and $L=1$, thus for low fields and temperatures close to T_{c0}. The solid curves are the superconducting/normal transitions and the dashed curves indicate the expulsion and the penetration fields, i.e. the boundaries of the stabilitiy region of the state with vorticity L. The lower dashed curves show the transition from the state with vorticity $L=1$ to $L=0$ with decreasing field (expulsion) and the upper dashed curves show the transition from $L=0$ to $L=1$ with increasing field (penetration). Fig. 3.16 shows the $H-T$ phase diagram for higher fields. For the sake of clarity only the superconducting/normal transition H_{c3} is shown as a function of temperature. The black dots indicate the transition fields between the different L states. For every (fixed) temperature the superconducting/normal transition field is highest for the triangle and lowest for the disk. For every (fixed) magnetic field, the critical temperature is highest for the triangle and lowest for the disk. This means that for sharper corners, the critical temperature and critical field are enhanced due to an enhanced surface superconductivity. These results are in good agreement with the phase diagrams found in Refs. [24, 63, 64].

3.9 CONCLUSIONS

We investigated theoretically the influences of the geometry of thin superconducting samples on the vortex configuration. Therefore, we considered superconducting disks, squares and triangles with the same surface area $S = \pi 16\xi^2$ and the same thickness $d = 0.1\xi$ for $\kappa = 0.28$. For these three geometries we calculated the free energy and the magnetization of the different giant and multivortex states as a function of the applied magnetic field and we indicated the multivortex to giant vortex transitions for fixed vorticity L.

Multivortex states were found for disks as well as for squares and triangles for several values of the vorticity. For given L, the vortex lattice was different in the three geometries due to the fact that it tries to adapt to the geometry of the sample. This influences considerably the stability range of the different vortex states. For squares and triangles we found magnetic field regions where there is a coexistence between a giant vortex state in the center and several separated vortices in the direction of the sample corners. Near the superconducting/normal transition we do not find multivortices, anti-vortices or a combination of them, but we find surface superconductivity. Only extremely close to the superconducting/normal transition vortex configurations containing anti-vortices are possible, as was shown by Chiboraru *et al.* and Bonča *et al.*

We studied the magnetic field distribution across the superconductor and around the superconductor which clearly shows the demagnetization effects, which are very important for samples of finite thickness. The vector plots of the superconducting current showed spots where the current flows in clockwise direction. From the phase of the order parameter and the Cooper-pair density we conclude that these spots are not anti-vortices, but correspond to back flow currents which are typically present near sharp obstacles, i.e. corners in our case.

We also investigated the stability of the vortex states with vorticity L by calculating the magnetic field range over which the vortex states with vorticity L are stable. We found that this stability range sensitively depends on the sample geometry. As a function of L we found enhanced stability for the triangle for $L = 3$ and for the square for $L = 4$.

In the last section, we also included temperature by calculating a $H - T$ phase diagram for the disk, the square and the triangle. With sharper sample corners, we found that for fixed temperature, the superconducting/normal transition field H_{c3} moves to higher fields, and for fixed field, the critical temperature increases. The theoretical phase boundaries were in good agreement with the experimentally measured results of Refs. [24, 63, 64].

Publications. The results presented in this chapter were published as:

- B. J. Baelus and F. M. Peeters, *Dependence of the vortex configuration on the geometry of mesoscopic flat samples*, Phys. Rev. B **65,** 104515 (2002).
- F. M. Peeters and B. J. Baelus: *Vortex structure in mesoscopic superconductors*, will be published in the proceedings of the NATO Advanced Research Workshop on: "New trends in superconductivity" (Yalta (Ukraine), September 16-20, 2001).

4

Effect of the boundary condition

4.1 INTRODUCTION

In the previous chapters we described how the critical parameters and the vortex configuration are influenced by the sample size and geometry for thin mesoscopic superconductors. Varying the sample size, the geometry and the Ginzburg-Landau parameter, one can decrease or increase the critical field, and thus the critical current, but it does not influence the critical temperature. In this chapter, we describe how one can increase the critical temperature.

Fink and Joiner [69] considered a semi-infinite superconducting half-space where the surface was treated by cold working in such a way that the superconductivity near the surface was enhanced, i.e. the slope of the superconducting order parameter increased near the sample surface. They found that such a surface treatment leads to higher critical temperatures [see Fig. 4.1], larger critical fields, and larger critical currents. Another way to enhance superconductivity near the surface is by bringing the superconductor in contact with a well chosen superconducting layer [70]. The added superconducting layer must have a higher transition temperature than the superconducting sample and in this case the surface enhancement of superconductivity is caused by the proximity effect.

Montevecchi and Indekeu [71, 72] performed a theoretical study of the effect of confinement on the superconducting/normal transition for systems with surface enhancement. Using the linear Ginzburg-Landau theory they studied the critical temperature at zero field for a thin film, an infinite cylinder and a sphere [see Fig. 4.2]. For all geometries they found that at $H = 0$ the critical

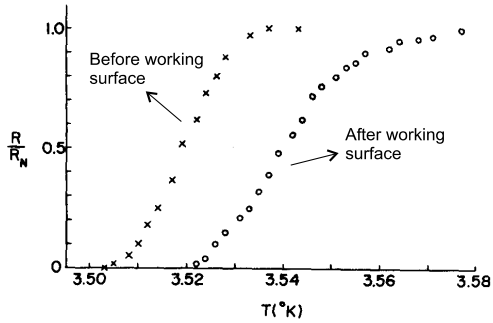

Fig. 4.1 The normalized resistance R/R_N versus temperature for an $In_{0.993}Bi_{0.007}$ foil with unworked and worked surfaces. [From Ref. [69].]

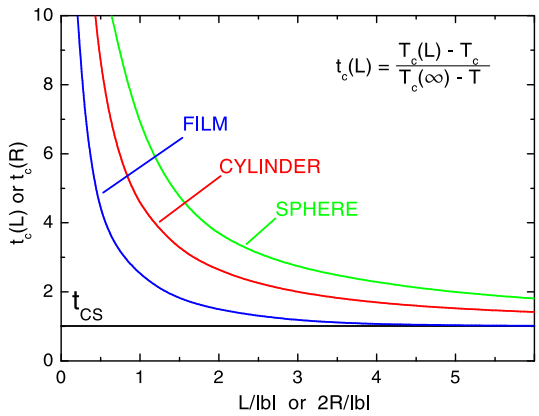

Fig. 4.2 The increase of the critical temperature as a function of the thickness L or diameter $2R$ of mesoscopic superconductors with surface enhancement. $T_c(\infty)$ equals the surface critical temperature T_{cs}. [From Ref. [71].]

temperature increases with the enhancement of surface superconductivity. For thin films in a parallel field, they also calculated a $H-T$ phase diagram. They found that surface enhancement leads to an increase of the critical field H_{c3} and of the critical temperature.

Yampolskii and Peeters [50] investigated theoretically the vortex structure of thin mesoscopic disks in a perpendicular magnetic field surrounded by a medium which enhances surface superconductivity. If the size of these thin disks is sufficiently large, they found giant vortex states as well as multivortex states appearing as meta-stable states and as ground states. The enhancement of the superconductivity near the surface leads to a stabilization of the multivortex states as ground states. They also calculated a $H-T$ phase di-

agram which showed that the critical temperature and the critical field were significantly increased by enhancing the surface superconductivity.

In the present chapter we consider superconducting cylinders with radii equal to a few coherence lengths ξ. We will investigate the effect of the enhancement of surface superconductivity on the critical field, the critical temperature and the vortex configuration. We also study the influence of the Ginzburg-Landau parameter κ. Our theoretical analysis is based on a full self-consistent numerical solution of the coupled nonlinear Ginzburg-Landau equations. No a priori arrangement of the vortex configuration or of the type of vortex configuration is assumed.

In section 4.2 we present our theoretical model. We explain how the enhancement of superconductivity near the surface is taken into account. In section 4.3 we consider *small cylinders*, i.e. infinitely long superconducting cylinders with small radius. In such small cylinders only axially symmetric states or giant vortex states nucleate. We discuss how the critical field and the critical temperature are influenced by the surface enhancement of superconductivity. In section 4.4 *larger cylinders* are studied where multivortices appear. We investigate the dependence of the nucleation of these states on the surface enhancement. Our results are summarized in section 4.5.

4.2 THEORETICAL FORMALISM

We consider infinite superconducting cylinders with radius R surrounded by a medium which enhances superconductivity at the edge of the cylinder. Along the axis of the cylinder a uniform magnetic field $\vec{H}_0$ is applied. To deal with this problem we use the Ginzburg-Landau theory and we solve numerically and self-consistently the system of two coupled Ginzburg-Landau equations (1.56)-(1.57), just like we did for thin superconductors. The general boundary condition (1.65) for the order parameter becomes in dimensionless variables:

$$\vec{n} \cdot \left(-i\vec{\nabla} - \vec{A}\right) \Psi \Big|_{r=R} = \frac{i}{b} \Psi \Big|_{r=R} , \tag{4.1}$$

where $\vec{n}$ is the unit vector normal to the cylinder and b is the surface extrapolation length. We are interested in the case $b < 0$, which means that the order parameter increases near the boundary (see paragraph 1.3.8.).

In order to determine which vortex state corresponds to the ground state we calculated the difference in free energy density between the superconducting state and the normal state

$$\begin{aligned} \frac{F}{F_0} = \frac{2}{V} \int_V dV \Big[- |\Psi|^2 + \frac{1}{2} |\Psi|^4 + \left| \left(-i\vec{\nabla} - \vec{A}\right) \Psi \right|^2 \\ + \kappa^2 (\vec{H} - \vec{H}_0)^2 \Big] + \frac{2}{bV} \oint_S dS \, |\Psi|^2 , \end{aligned} \tag{4.2}$$

where $\vec{H} = rot\ \vec{A}$, V is the volume of a cylinder with unit height, S the surface of the infinite cylinder and $F_0 = H_c^2 V/8\pi$. The contribution of the surface is taken into account by the last term of Eq. (4.2). By comparing the dimensionless free energy of the different giant and multivortex configurations, we obtain the ground states and the meta-stable states.

The temperature is indirectly included in ξ, λ, H_{c2} through their temperature dependencies (see Eqs. (1.59) - (1.61))

$$\xi(T) = \frac{\xi(0)}{\sqrt{|1 - T/T_{c0}|}}\ , \tag{4.3}$$

$$\lambda(T) = \frac{\lambda(0)}{\sqrt{|1 - T/T_{c0}|}}\ , \tag{4.4}$$

$$H_{c2}(T) = H_{c2}(0)\left|1 - \frac{T}{T_{c0}}\right|\ , \tag{4.5}$$

where T_{c0} is the critical temperature at zero magnetic field for the normal boundary condition, i.e. $-\xi(0)/b = 0$. We will only insert the temperature explicitly if we consider the $H-T$ phase diagrams, while the other calculations are for (arbitrary) fixed temperature.

4.3 SMALL CYLINDERS: GIANT VORTEX STATES

First we discuss infinitely long cylinders with a small radius, where we may limit ourselves to the giant vortex states. The reason is the same as for small disks: the confinement effects are dominant and they impose the cylindrical symmetry of the boundary of the cylinder on the vortex state. Consequently, the dimensions of the Ginzburg-Landau equations are reduced, which improves the accuracy and the computation time.

4.3.1 Type-I cylinders

We consider infinitely long cylinders with radius $R = 2.0\xi$ for a Ginzburg-Landau parameter $\kappa = 0.28$.

Figs. 4.3 (a,b) show the *ground state* free energy and the magnetization as a function of the applied magnetic field for such a superconducting cylinder for the usual boundary condition, i.e. $-\xi/b = 0.0$ (red curves), and for $-\xi/b = 0.2$ (green curves) and 0.4 (blue curves), which correspond to surface enhancement. With increasing $-\xi/b$ the free energy at zero magnetic field becomes more negative, which means an enhancement of superconductivity. Also the ground state superconducting/normal transition moves to higher fields. Notice that the magnetization [see Fig. 4.3(b)] is enhanced with increasing $-\xi/b$.

Figs. 4.4(a-c) show the radial dependence of the Cooper-pair density, the magnetic field and the current density, respectively, for the previously consid-

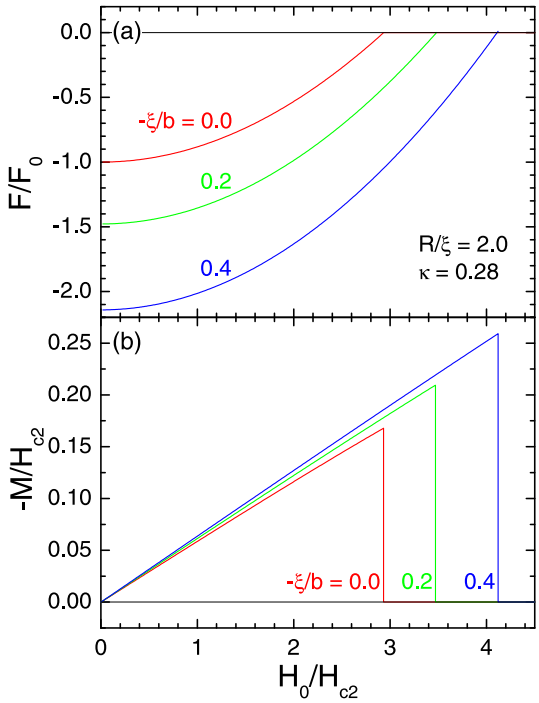

Fig. 4.3 (a) The ground state free energy and (b) the magnetization as a function of the applied magnetic field for a superconducting cylinder with radius $R = 2.0\xi$ for $\kappa = 0.28$ and $-\xi/b = 0$ (red curves), 0.2 (green curves) and 0.4 (blue curves).

ered cylinder at the applied magnetic field $H_0/H_{c2} = 2.02$ and for vorticity $L = 0$. The red curves give the result for $-\xi/b = 0$, the green curves for $-\xi/b = 0.2$ and the blue curves for $-\xi/b = 0.4$. From Fig. 4.4(a) it is very clear that the Cooper-pair density near the surface, and hence the surface superconductivity, increases with increasing $-\xi/b$. For a small cylinder radius, also the Cooper-pair density in the center of the cylinder is influenced by the boundary condition. From Fig. 4.4(b) one can see that enhancing the surface superconductivity results in a more pronounced Meissner effect, i.e. the magnetic field expulsion becomes more complete with increasing $-\xi/b$. Notice that the magnetic field for this situation is always zero in the center of the cylinder. To expel the magnetic field more, the superconductor has to induce more superconducting current near the surface. Fig. 4.4(c) shows that the current density is zero in the center of the superconductor and becomes more negative near the surface. The superconducting Meissner currents are also more concentrated near the surface with increasing $-\xi/b$. For the Meissner state the current has the same sign in the whole sample and is thus flowing in the whole sample in the same direction.

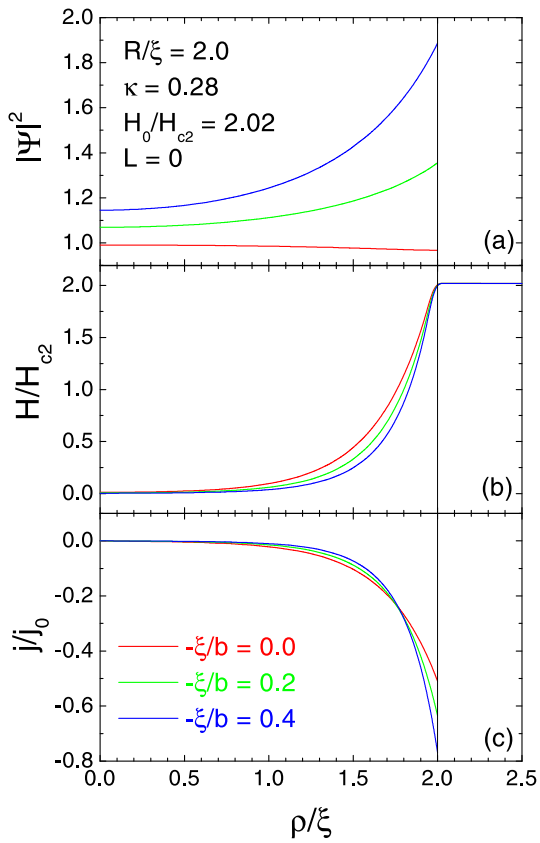

Fig. 4.4 (a) The Cooper-pair density, (b) the magnetic field, and (c) the current density as a function of the radial position for a cylinder with radius $R = 2.0\xi$ and for $\kappa = 0.28$. The external field is $H_0/H_{c2} = 2.02$ and the vorticity is $L = 0$.

In Fig. 4.5 the dependence of the transition fields for the different giant vortex states on the surface enhancement b is given for a superconducting cylinder with radius $R = 2.0\xi$ and $\kappa = 0.28$. The blue curves give the ground state transitions between the different L states and the red curve indicates the superconducting/normal transition. For the normal boundary condition, $-\xi/b = 0$, it is evident that the ground state consists of the Meissner state, i.e. $L = 0$, since κ is sufficiently small. The superconducting/normal transition occurs at $H_0/H_{c2} \approx 2.9$. What happens with increasing $-\xi/b$? (i) For $-\xi/b < 0.65$ the ground state is still given by the Meissner state, and with increasing $-\xi/b$ the superconducting/normal transition moves to higher fields. (ii) For $-\xi/b > 0.65$ different L states become the ground state. This is in agreement with the results of Montevecchi [73] who also found transitions between different L states for $b < 0$ for a fixed cylinder radius $R/|b| = 1.2$

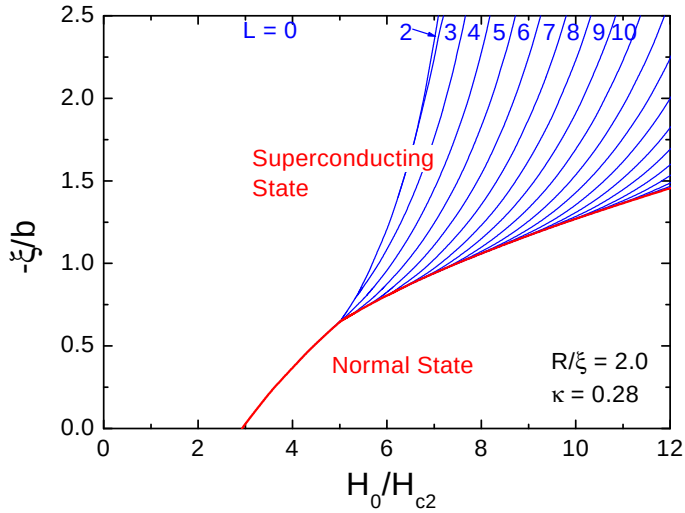

Fig. 4.5 The $(-\xi/b) - H$ phase diagram for a superconducting cylinder with radius $R = 2.0\xi$ and $\kappa = 0.28$. The blue curves indicate the transitions between the different L states and the thick red curve gives the superconducting/normal transition.

and $\kappa = 0.3$ (see Fig. 1.14 of Ref. [73]). Remarkably we find that the ground state does not evolve from the Meissner state to a state with vorticity $L = 1$. Rather it evolves to a state with larger vorticity. For $0.65 \lesssim -\xi/b \lesssim 0.8$ the ground state changes from the Meissner state to a state with $L = 4$, for $0.8 \lesssim -\xi/b \lesssim 1.8$ to a state with $L = 3$, and for $-\xi/b \gtrsim 1.8$ to a state with $L = 2$. (iii) Further increasing $-\xi/b$ the ground state will change first from $L = 0$ to $L = 1$. The latter transition corresponds to type-II behavior which only occurs in the absence of surface enhancement for κ larger than some critical Ginzburg-Landau parameter κ_2.

The three different regimes which we found for the case of increasing $-\xi/b$ for fixed small κ are very similar to the three regimes for the case of increasing κ for the normal boundary condition, i.e. $-\xi/b = 0$: (i) For the normal boundary condition it is known [see also Fig. 1.10] that only the Meissner state is the ground state for κ smaller than a critical parameter κ_1. (ii) For $\kappa_1 \lesssim \kappa \leq \kappa_2$ surface superconductivity can occur and states with vorticity larger than one exist. For example, Fink and Presson [74, 75] found ground state transitions from the Meissner state with $L = 0$ into surface superconducting states with $L = 4$ for a superconducting cylinder with radius $R = 3.0\xi$ and $\kappa = 0.5$. (iii) For $\kappa > \kappa_2$ (type II superconductivity) the ground state transits from the Meissner state to states with $L = 1, 2, ..., n$, successively, where the value of n depends on the radius and the Ginzburg-Landau parameter (see

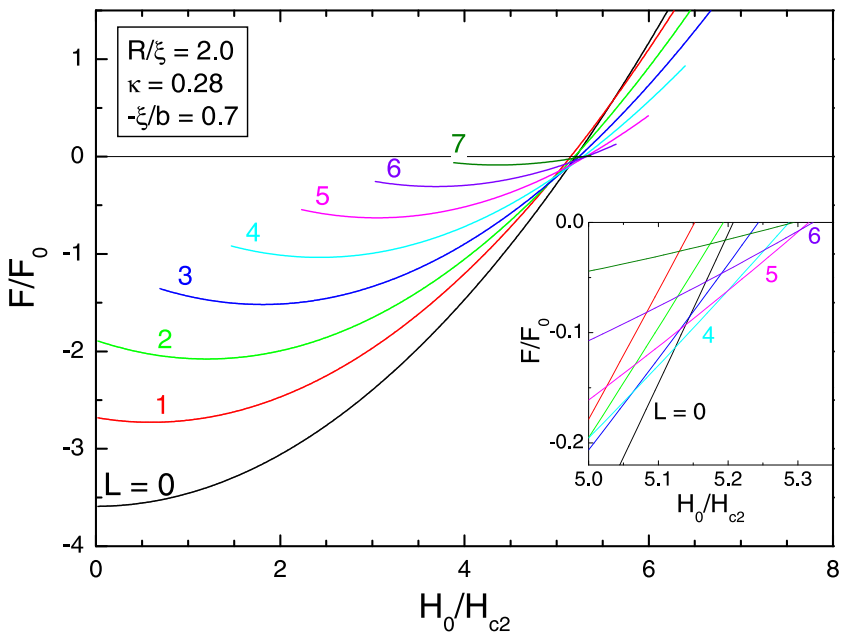

Fig. 4.6 The free energy for a superconducting cylinder with radius $R/\xi = 2.0$ and $\kappa = 0.28$ for $-\xi/b = 0.7$ as a function of the external magnetic field.

for example Ref. [74]). In bulk superconductors $\kappa_1 \approx 0.42$ and $\kappa_2 = 1/\sqrt{2}$, but for cylinders these parameters are radius dependent [40, 76].

What is the reason for this remarkable behaviour of the ground state for increasing $-\xi/b$? (i) For $-\xi/b < 0.65$ the order parameter, and thus the Cooper-pair density, near the cylinder boundary increases with increasing $-\xi/b$ which also leads to an enhancement of the order parameter in the center, albeit less pronounced [see also Fig. 4.4(a)]. Consequently, the free energy at zero magnetic field becomes more negative and the superconducting/normal transition moves to higher fields [see also Fig. 4.3 (a)]. (ii) With increasing $-\xi/b$ the Cooper-pair density in the center for the $L = 0$ state is not increasing as strongly as the Cooper-pair density near the boundary and the cylinder remains superconducting at higher fields. For $-\xi/b \gtrsim 0.65$ it becomes energetically less favourable to expell rather high fluxes from the sample. The effect of the increase of vorticity on the free energy is shown in Fig. 4.6 for $-\xi/b = 0.7$. From the inset it is clear that the free energy of the $L = 4$ state becomes lower than the one of the Meissner state at $H_0/H_{c2} \approx 5.12$. This means that for this field the penetration of 4 fluxes becomes more favourable than the expulsion of the field. At $H_0/H_{c2} \approx 5.20$, 5.30 and 5.32 the ground state changes respectively into the $L = 5$ state, the $L = 6$ state and the normal state. Further increasing $-\xi/b$ leads to higher Cooper-pair density near the boundary and, consequently, to higher induced supercurrents. As a result,

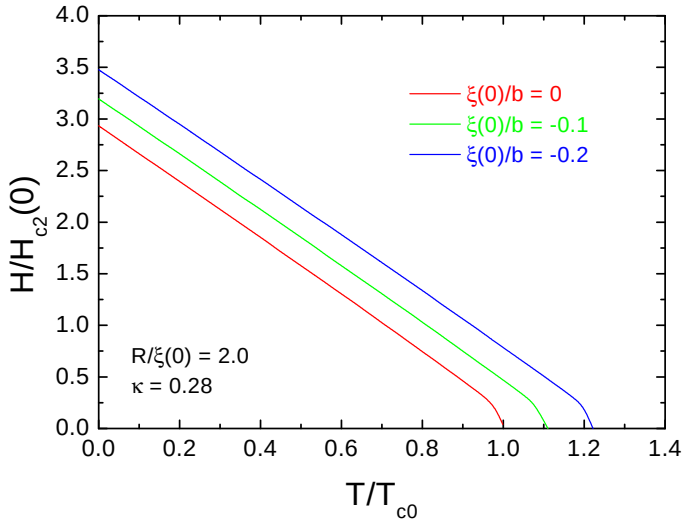

Fig. 4.7 The $H-T$ phase diagram for a superconducting cylinder with radius $R = 2.0\xi$ and $\kappa = 0.28$ for $-\xi/b = 0.0$ (red curve), 0.2 (green curve) and 0.4 (blue curve).

a smaller amount of flux will penetrate into the sample after the first ground state transition. For example, with increasing field at $-\xi/b > 0.8$ the ground state changes from the Meissner state into the $L = 3$ state and at higher fields into states with $L = 4$, 5, 6 and so on. (iii) For high values of $-\xi/b$, the explanation is analogous as above but now the ground state changes from $L = 0$ to $L = 1$, 2, 3 and so forth.

In Fig. 4.7 we plot the $H-T$ phase diagram for a superconducting cylinder with $R = 2.0\xi$ and $\kappa = 0.28$ for $-\xi(0)/b = 0.0$, 0.1 and 0.2. For these values of $-\xi(0)/b$ the superconducting ground state is always given by the Meissner state [see also Fig. 4.5]. The superconducting/normal transition is shown by the red curve for $-\xi(0)/b = 0.0$, by the green curve for $-\xi(0)/b = 0.1$, and by the blue curve for $-\xi(0)/b = 0.2$. For $\kappa = 0$ the superconducting/normal transition is a straight line in the $H-T$ phase diagram. For $\kappa = 0.28$, the superconducting/normal transition is still given by a straight line for $T \ll T_c$, regardless of the value of $-\xi(0)/b$, but it has now a curvature near T_c. With increasing $-\xi(0)/b$ the superconducting/normal transition, which is of first order, moves to higher temperatures for fixed field or to higher fields for fixed temperature.

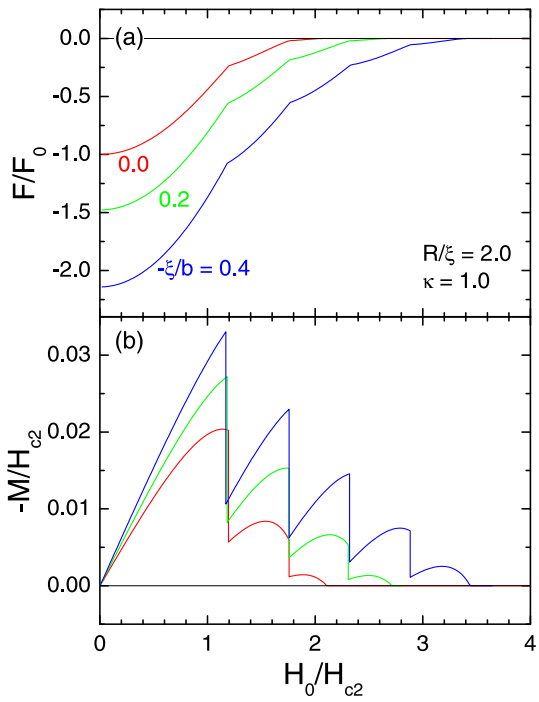

Fig. 4.8 (a) The ground state free energy and (b) the magnetization as a function of the applied magnetic field for a superconducting cylinder with radius $R = 2.0\xi$ for $\kappa = 1.0$ and $-\xi/b = 0$ (red curves), 0.2 (green curves) and 0.4 (blue curves).

4.3.2 Type-II cylinders

We consider infinite cylinders with radius $R = 2.0\xi$ for a Ginzburg-Landau parameter $\kappa = 1.0$.

Figs. 4.8(a,b) show the *ground state* free energy and magnetization as a function of the applied magnetic field for such a superconducting cylinder for $-\xi/b = 0.0$ (red curves), 0.2 (green curves) and 0.4 (blue curves). Now, the superconducting ground state is not always the Meissner state. For example, for the usual boundary condition, i.e. $-\xi/b = 0.0$, the vorticity of the ground state is $L = 0$ for $H_0/H_{c2} \leq 1.195$. At the first transition field $H_0/H_{c2} = 1.195$ the vorticity of the ground state changes from $L = 0$ to $L = 1$ and then it remains $L = 1$ until $H_0/H_{c2} = 1.7575$ where it changes to $L = 2$. At $H_0/H_{c2} = 2.12$ the free energy of the ground state becomes zero and the superconducting/normal transition takes place. The transitions between the different L states are indicated by corners in the free energy and jumps in the magnetization. As for type-I cylinders, the free energy at $H_0 = 0$ becomes more negative with increasing $-\xi/b$, i.e. superconductivity is enhanced, and the transition to the normal state moves to higher fields. Furthermore, the

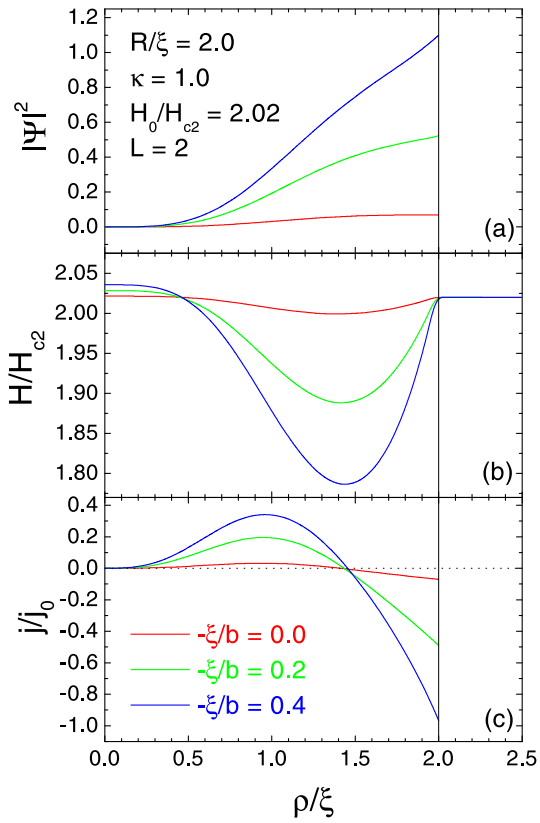

Fig. 4.9 (a) The Cooper-pair density, (b) the magnetic field, and (c) the current density as a function of the radial position for a cylinder with radius $R = 2.0\xi$ and for $\kappa = 1.0$. The external field is $H_0/H_{c2} = 2.02$ and the vorticity is $L = 2$.

vorticity of the ground state can become larger and the peaks in the magnetization are higher, indicating a more efficient expulsion of the magnetic field from the superconductor. Notice that the magnetic fields for the transitions between different L states are almost independent of the value of $-\xi/b$, but the surface critical field H_{c3} is a sensitive function of $-\xi/b$.

Next, we investigate the radial dependence of the Cooper-pair density, the magnetic field and the current density for such a superconducting cylinder. For vorticity $L = 0$ the results are analogous to the results for type-I cylinders which were described in Fig. 4.4. In Figs. 4.9(a-c) we show the radial dependence of, respectively, the Cooper-pair density, the magnetic field and the current density for the ground state at $H_0/H_{c2} = 2.02$, i.e. the giant vortex state with vorticity $L = 2$. The red curves give the result for $-\xi/b = 0$, the green curves for $-\xi/b = 0.2$ and the blue curves for $-\xi/b = 0.4$. In Fig. 4.9(a) it is shown that the Cooper-pair density is zero for all $-\xi/b$ in the center of

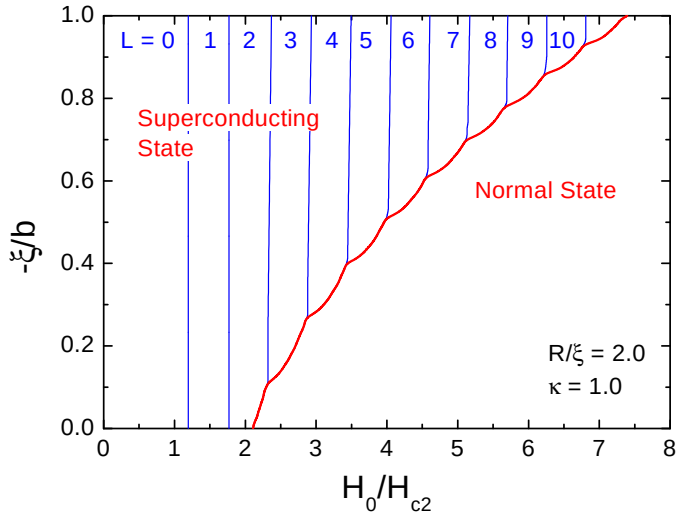

Fig. 4.10 The $(-\xi/b) - H$ phase diagram for a superconducting cylinder with radius $R = 2.0\xi$ and $\kappa = 1.0$. The blue curves indicate the transitions between the different L states and the thick red curve gives the superconducting/normal transition.

the cylinder, i.e. at the position of the giant vortex with vorticity $L = 2$. Near the surface the Cooper-pair density is enhanced, which is understandable because the slope of $|\Psi|$ at $\rho = R$ is given by $-\xi/b$. For the giant vortex state, the magnetic field is not zero in the center, as was the case for $L = 0$, but it can be even higher than the external field $H_0 = 2.02H_{c2}$. With increasing $-\xi/b$, the superconductivity near the boundary is enhanced and, thus, more magnetic field can be expelled from the cylinder and the giant vortex will be more compressed in the center [see Fig. 4.9(b)]. As a consequence, the minimum of magnetic field inside the cylinder decreases and the magnetic field at the position of the vortex increases. To expel the magnetic field more and to compress the giant vortex better in the center, the superconductor has to induce a larger superconducting current. Therefore the superconducting current is more positive close to the giant vortex and more negative near the boundary [see Fig. 4.9(c)].

The fact that the transition fields between different L states are almost independent of the value of $-\xi/b$, can also be seen from the $(-\xi/b) - H$ phase diagram for a superconducting cylinder with radius $R = 2.0\xi$ and $\kappa = 1.0$, which is shown in Fig. 4.10. The blue curves give the ground state transitions between the different L states and the red curve indicates the superconducting/normal transition. For $\kappa = 1.0$ we do not find ground state transitions between a state with vorticity $L = 0$ and vorticity $L > 1$, as was

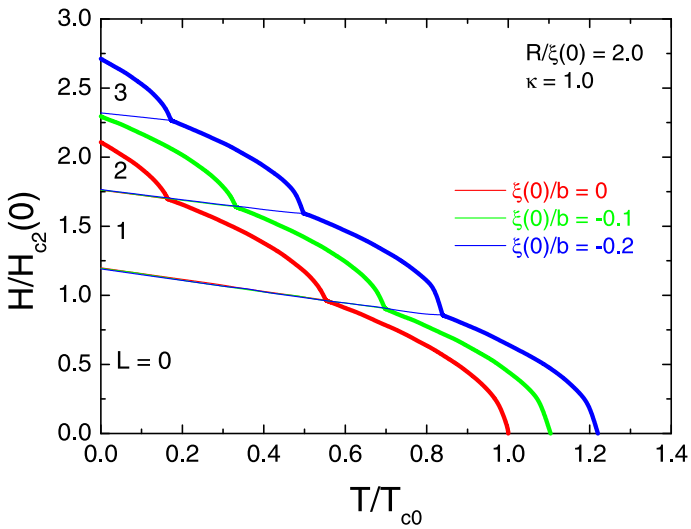

Fig. 4.11 The $H-T$ phase diagram for a superconducting cylinder with radius $R = 2.0\xi$ and $\kappa = 1.0$ for $-\xi/b = 0.0$ (blue curves), 0.2 (green curves) and 0.4 (red curves). The thick curves indicate the superconducting/normal transition and the thinner curves the ground state transitions between the giant vortex states with different vorticity L.

the case for $\kappa = 0.28$. Moreover, the magnetic field range over which the ground state has a particular vorticity L is almost the same for all $L > 0$, namely $\Delta H_L = H_{L\to L+1} - H_{L-1\to L} \approx 0.57 H_{c2}$. Fig. 4.9 indicates that the width of the superconducting sheath in ρ/ξ is independent of b. The value of b influences only the amplitude of the order parameter near the surface [Fig. 4.9(a)], the diamagnetization [Fig. 4.9(b)] and the strength of the currents [Fig. 4.9(c)]. Therefore, the space available for the confined flux in the core region of the cylinder does (almost) not depend on the enhancement. As a consequence, the number of fluxoids, or vorticity L, depends only on the strength of the external field H_0 and almost not on b for fixed temperature.

In Fig. 4.11 we plot the $H-T$ phase diagram for a superconducting cylinder with $R = 2.0\xi$ and $\kappa = 1.0$ for $-\xi(0)/b = 0.0$, 0.1 and 0.2. The ground state transitions are shown by red curves for $-\xi(0)/b = 0.0$, by green curves for $-\xi(0)/b = 0.1$, and by blue curves for $-\xi(0)/b = 0.2$. The thick curves indicate the superconducting/normal transition and the thinner curves (they are almost straight lines) show the ground state transitions between the giant vortex states $L \leftrightarrow L+1$. From Fig. 4.11 it is clear that the transitions between the different L states are (almost) independent of the value of $-\xi/b$, but the superconducting/normal transition is a sensitive function of $-\xi/b$ [see also Fig. 4.10]. With increasing $-\xi(0)/b$ the superconducting/normal transition moves to higher temperatures for fixed field or to higher fields for fixed tem-

perature as was also the case for $\kappa = 0.28$. The zero field critical temperature is the same for $\kappa = 1.0$ as for $\kappa = 0.28$ and depends only on $-\xi(0)/b$. The critical fields at zero temperature are different in both cases. For $-\xi(0)/b = 0.2$, for example, $H_{c3}(0) = 3.5H_{c2}(0)$ for $\kappa = 0.28$ and $H_{c3}(0) = 2.7H_{c2}(0)$ for $\kappa = 1.0$. Another significant difference is that for $\kappa = 1.0$ the superconducting/normal transition is no longer a straight line for temperatures $T \ll T_c$, but consists of corners which indicate the transition between the different L states. These corners are *bicritical points* where three phases become identical for a given value of $-\xi(0)/b$. For example, the normal state coincides with the $L = 0$ state and the $L = 1$ state at $H_0/H_{c2}(0) = 0.86$ and $T/T_{c0} = 0.84$ for $-\xi(0)/b = 0.2$. Note that all transitions between different L states are of first order and correspond to free energy crossings, while the superconducting/normal transition is a second order transition. These bicritical points occur at magnetic fields which are only weakly sensitive to the surface enhancement, while the transition temperatures are quite sensitive to b. Notice further that the superconducting/normal phase transition boundary is exactly the same for a cylinder with $\kappa = 1.0$ as for a very thin disk (thickness $d \ll \xi$) with the same radius, if the same boundary condition (4.1) is taken on the sides, but the standard boundary condition ($-\xi/b = 0$) on the top and the bottom of the disk. This leads to a z-independent order parameter and, as a consequence, to similar physics as for an infinitely long cylinder. This can be seen by comparing Fig. 4.11 with Fig. 14 of Ref. [50]. In the case of the disk, the field is perpendicular to the disk.

4.4 LARGE CYLINDERS: MULTIVORTEX STATES

Up to now, we considered only cylinders with small radii where the confinement effects were dominant and only giant vortex states were stable. Now, we consider superconducting cylinders with a large radius in which multivortex states can nucleate for certain magnetic fields. There exists a crossover radius R_c such that for $R < R_c$ only giant vortex states can nucleate, while for $R \geq R_c$ multivortex states can nucleate for a certain vorticity and magnetic field. The crossover radius R_c depends strongly on the Ginzburg-Landau parameter κ and on $-\xi/b$, and can only be determined numerically. For example, $R_c \approx 2.8\xi$ for $\kappa = 1.0$ and $-\xi/b = 0$, which becomes $R_c \approx 3.0\xi$ for $-\xi/b = 0.4$ and $\kappa = 1.0$. This means that we can no longer limit our calculations to axially symmetric solutions. Nevertheless, from the study of disks [see chapter 2] we know that the transition fields between states with different vorticity do (almost) not depend on the fact whether one considers axial symmetry or not. Therefore, we can still calculate the $(-\xi/b) - H$ phase diagrams using the cylindrical symmetry approach, but if we want to know the real vortex configurations, we have to use the general theory in order to account for multivortices.

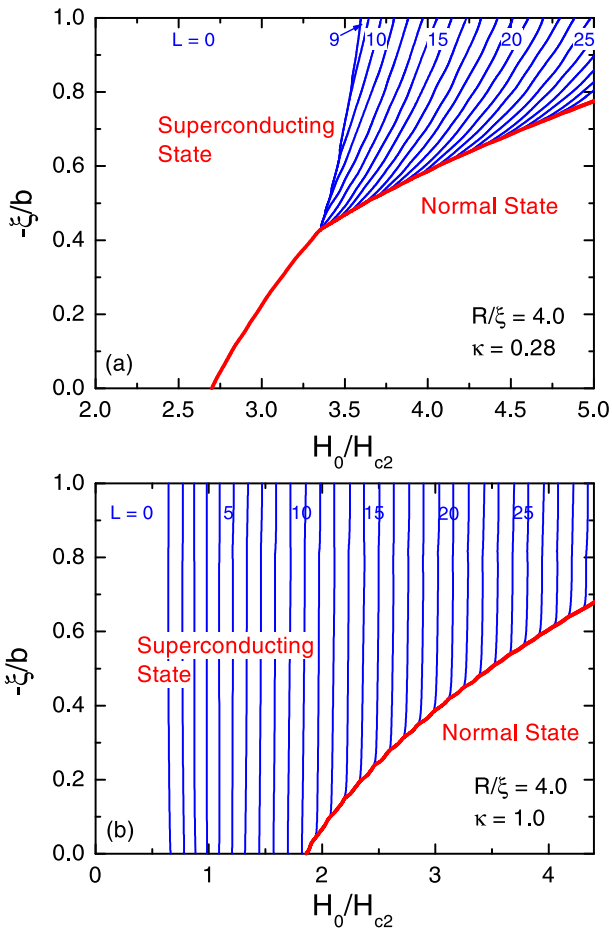

Fig. 4.12 The $(-\xi/b) - H$ phase diagram for a superconducting cylinder with radius $R = 4.0\xi$ for $\kappa = 0.28$ (a) and $\kappa = 1.0$ (b). The blue curves indicate the transitions between the different L states and the thick red curve gives the superconducting/normal transition.

We calculate the $(-\xi/b) - H$ phase diagrams for a superconducting cylinder with radius $R = 4.0\xi$ for $\kappa = 0.28$ and $\kappa = 1.0$, which are shown in Figs. 4.12(a,b), respectively. The blue curves give the ground state transitions between the different L states and the red curve indicates the superconducting/normal transition. The conclusions are similar to those for small cylinders, but with many more transitions between different L states. However, for $\kappa = 0.28$ we find now transitions from the Meissner state immediately to a state with vorticity $L = 13$ as a function of the magnetic field in the range $0.43 \leq -\xi/b \leq 0.47$. With further increasing $-\xi/b$ we find first transitions from $L = 0$ to $L = 12$, 11, 10 and 9, respectively. Notice that *triple points*

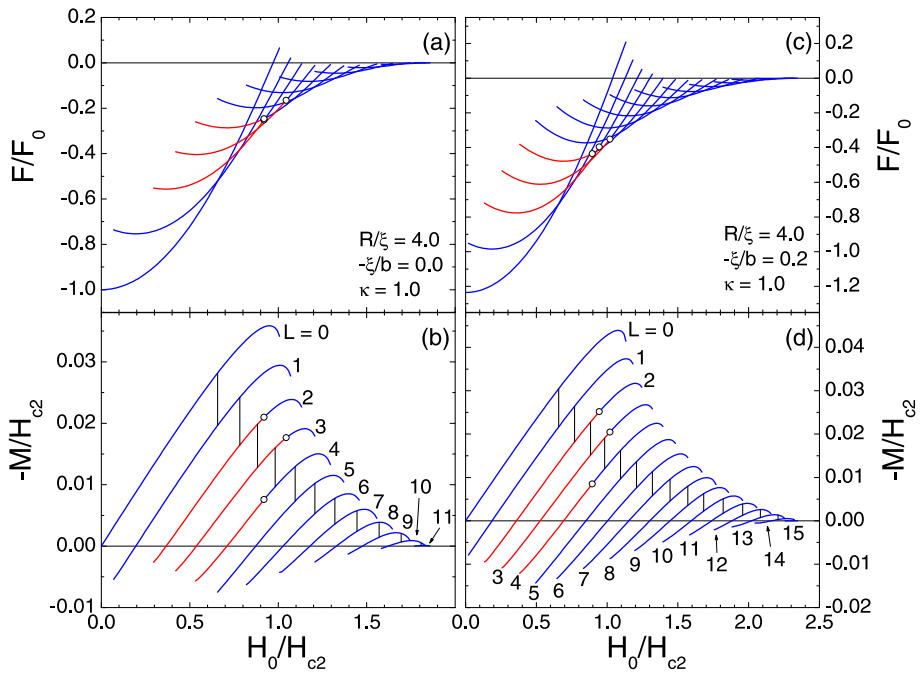

Fig. 4.13 Free energy (a,c) and magnetization (b,d) for vortex states in a superconducting cylinder with radius $R = 4.0\xi$ and $\kappa = 1.0$ for the boundary condition $-\xi/b = 0.0$ (a,b) and 0.2 (c,d). Giant vortex states are given by blue curves, multivortex states by red curves and the open circles indicate the multivortex to giant vortex transition fields. The vertical lines in (b,d) give the ground state transitions.

occur where the Meissner state coexists with two different giant vortex states. For example, at $H_0/H_{c2} \approx 3.4$ and $-\xi/b \approx 0.47$ the Meissner state coexists with the $L = 12$ state and the $L = 13$ state. This means that these three states have the same free energy in that case.

For $\kappa = 1.0$ the magnetic field range over which the ground state has a particular vorticity L is almost the same for all $L > 0$, namely $\Delta H_L \approx 0.125 H_{c2}$, which means that the ground state changes more quickly from vorticity L than for cylinders with radius $R = 2.0\xi$, where $\Delta H_L \approx 0.57 H_{c2}$, which is due to the larger cross section of the cylinder.

Next we will compare the free energy and the magnetization for the usual boundary condition $-\xi/b = 0$ with the case of surface enhancement, $-\xi/b = 0.2$. Figs. 4.13(a,b) show the free energy and the magnetization for a cylinder with radius $R = 4.0\xi$ and $\kappa = 1.0$ for the usual boundary condition. The different giant vortex states are indicated by the blue curves, the multivortex states by the red curves and the multivortex to giant vortex transition fields H_{MG} by the open circles. Notice that we find superconducting states up to vorticity $L = 11$ and that the superconducting/normal transition field

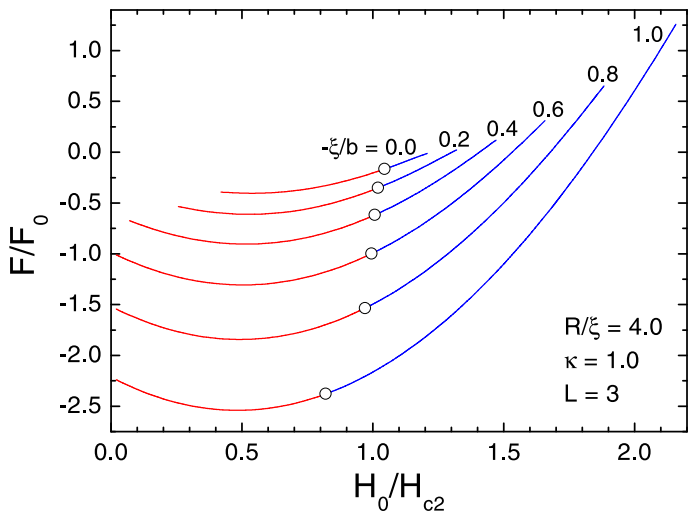

Fig. 4.14 Free energy for the $L = 3$ state in a superconducting cylinder with radius $R = 4.0\xi$ and $\kappa = 1.0$ for $-\xi/b = 0.0$, 0.2, 0.4, 0.6, 0.8 and 1.0. Giant vortex states are given by blue curves, multivortex states by red curves and the open circles indicate the multivortex to giant vortex transition fields.

is $H_{c3}/H_{c2} \approx 1.85$ [see also Fig. 4.12(b)]. Multivortices can nucleate for vorticities $L = 2$, 3, and 4. The multivortex state with $L = 2$ can nucleate for $0.295 \leq H_0/H_{c2} \leq 0.92$, with $L = 3$ for $0.42 \leq H_0/H_{c2} \leq 1.045$, and with $L = 4$ for $0.5325 \leq H_0/H_{c2} \leq 0.92$. In Fig. 4.13(b) the equilibrium ground state transitions are indicated by the vertical curves.

Figs. 4.13(c,d) show the free energy and the magnetization for a cylinder with radius $R = 4.0\xi$ and $\kappa = 1.0$ for $-\xi/b = 0.2$. For this boundary condition the superconducting/normal transition field is $H_{c3}/H_{c2} \approx 2.35$ which is appreciably higher than for $-\xi/b = 0$. Also vortex states with higher vorticity are stable, up to 15 instead of up to 11 for $-\xi/b = 0$. Multivortex states can nucleate with $L = 2$ for $0.1325 \leq H_0/H_{c2} \leq 0.945$, with $L = 3$ for $0.2575 \leq H_0/H_{c2} \leq 1.02$, and with $L = 4$ for $0.3825 \leq H_0/H_{c2} \leq 0.895$.

How does the value of $-\xi/b$ influence the nucleation of the multivortex states? Fig. 4.14 shows the free energy of the $L = 3$ state for a superconducting cylinder with radius $R = 4.0\xi$ and $\kappa = 1.0$ for $-\xi/b = 0.0$, 0.2, 0.4, 0.6, 0.8 and 1.0 as a function of the applied magnetic field. Giant vortex states are given by blue curves and multivortex states by red curves. The transitions from a multivortex state to a giant vortex state are indicated by the open circles. With increasing $-\xi/b$ the $L = 3$ state can nucleate up to larger fields, i.e. $H_{nuc}/H_{c2} = 1.21$, 1.32, 1.47, 1.66, 1.88 and 2.16 for $-\xi/b = 0.0$, 0.2, 0.4, 0.6, 0.8 and 1.0, respectively. On the other hand the multivortex to giant vortex transition field decreases, i.e. $H_{MG}/H_{c2} = 1.045$, 1.02, 1.0075, 0.995, 0.97 and 0.82 for $-\xi/b = 0.0$, 0.2, 0.4, 0.6, 0.8 and 1.0, respectively.

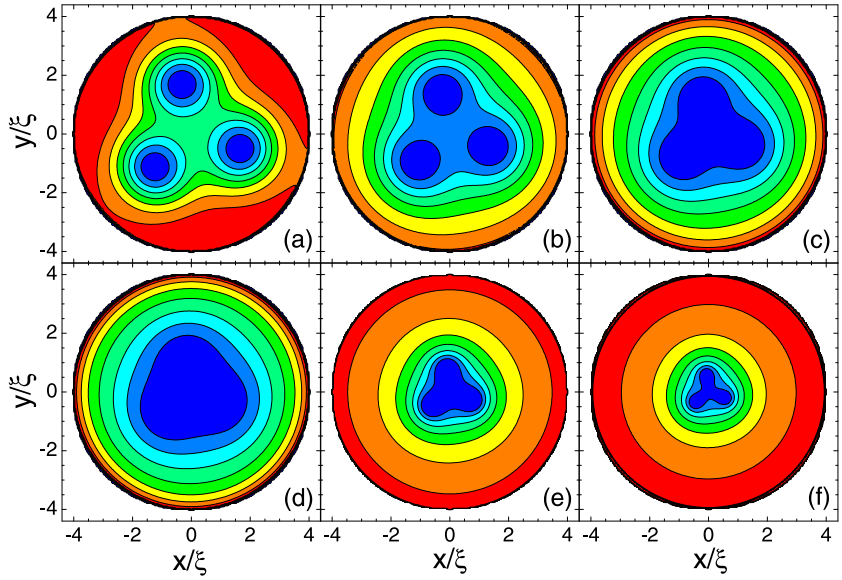

Fig. 4.15 The Cooper-pair density for the multivortex state with $L = 3$ in a cylinder with $R/\xi = 4.0$ and $\kappa = 1.0$ at $H_0/H_{c2} = 0.445$ for $-\xi/b = 0.0$ (a), 0.2 (b), 0.4 (c), 0.6 (d), and the logarithm of the Cooper-pair density for $-\xi/b = 0.8$ (e) and 1.0 (f). High (low) Cooper-pair density is given by red (blue) regions.

This means that with increasing $-\xi/b$ the magnetic field region over which the giant vortex state exists increases and the one of the multivortex state decreases. The reason is that increasing $-\xi/b$ corresponds to an enhancement of superconductivity near the boundary. Therefore, it is more difficult for the magnetic field to penetrate near the cylinder edge than in the center. Since multivortices are situated more closely to the cylinder edge, it is obvious that multivortices become unstable at lower fields for increasing $-\xi/b$. Or alternatively, the confinement effects become more important for increasing surface superconductivity.

To illustrate this better, we show the Cooper-pair density of the $L = 3$ state for such a cylinder in Figs. 4.15(a-f) at $H_0/H_{c2} = 0.445$ for $-\xi/b = 0.0$, 0.2, 0.4, 0.6, 0.8 and 1.0, respectively. High Cooper-pair density is given by red regions, low Cooper-pair density by blue regions. The three vortices correspond to the three blue spots. For the usual boundary condition $-\xi/b = 0.0$ the vortices are clearly separated. With increasing $-\xi/b$ the vortices are *pushed* to the center and at $-\xi/b = 0.4$ they already start to overlap. For $-\xi/b = 0.8$ and 1.0 the vortices are very close to each other. Therefore, we plotted the logarithm of the Cooper-pair density to show the positions of the vortices and to prove that it it still a multivortex state. Thus, by the enhancement of the Cooper-pair density near the boundary the vortices

move to the center and for increasing $-\xi/b$ they will recombine in the center creating a giant vortex state.

4.5 CONCLUSIONS

We investigated the effect of the enhancement of surface superconductivity on the critical field and the critical temperature for superconducting cylinders with radii comparable to the coherence length ξ. We also studied the influence of the Ginzburg-Landau parameter κ. A distinction was made between cylinders with small radii where the confinement effects dominate and only giant vortex states exist, and cylinders with a larger radius where multivortices can nucleate for certain magnetic fields and vorticities.

Generally, increasing $-\xi/b$ leads to a more negative free energy at $H = 0$ and to a higher superconducting/normal transition field. We also studied the magnetic field distribution, the Cooper-pair density and the current density for different values of the surface enhancement. For higher values of $-\xi/b$ more magnetic field can be expelled from the cylinder and the giant vortex in the center is compressed more. Therefore, higher currents are induced near the boundary and near the giant vortex. The Cooper-pair density close to the boundary increases, and for small cylinders this also influences the Cooper-pair density in the center.

From the $H - T$ phase diagrams we found that the critical temperature depends on $-\xi/b$, while it is independent of κ (cf. Ref. [71]). With increasing $-\xi/b$ the critical temperature increases for fixed magnetic field and the critical magnetic field increases for fixed temperature.

We also obtained $(-\xi/b) - H$ phase diagrams. In type-I cylinders the surface enhancement has drastic consequences. Even at low κ the surface enhancement leads to transitions between different L states and thus to type-II behavior. Moreover, as a function of the magnetic field the superconducting ground state transits from the Meissner state to a vortex state with $L > 1$ over a range of $-\xi/b$ values. Therefore, we can conclude that increasing $-\xi/b$ for type-I superconductors seems to have a similar effect as increasing κ for fixed $-\xi/b$ for certain properties of the superconducting cylinder. In type-II cylinders we found that the magnetic field range over which the ground state has a particular vorticity L is almost the same for all $L > 1$. This magnetic field range decreases with increasing cylinder radius.

If the cylinder radius is sufficiently large multivortex states can nucleate and we studied the influence of the surface enhancement on the nucleation of these states. We found that at fixed field and with increasing $-\xi/b$ the multivortices move to the center creating a giant vortex state. Thus, surface enhancement destabilizes the multivortex state.

Publications. The results presented in this chapter were published as:

- B. J. Baelus, S. V. Yampolskii, F. M. Peeters, E. Montevecchi, and J. O. Indekeu, *Superconducting properties of mesoscopic cylinders with enhanced surface superconductivity*, Phys. Rev. B. **65**, 024510 (2002) *(10 pages)*.

5

Superconducting rings

5.1 INTRODUCTION

Until now, we investigated singly connected superconductors, which are superconductors with only one superconducting/normal interface. In the present chapter we will study superconducting rings which are doubly connected systems: One inner and one outer boundary separate the superconducting material from the vacuum region. We study the properties and the vortex states of superconducting thin disks with a hole. In the past, two limiting cases were studied: (i) a disk without a hole (see chapter 2) and (ii) the thin-wire loop.

In 1962 Little and Parks studied a thin-wire loop in an axial magnetic field [77]. The $T_c - H$ phase diagram showed a periodic component. Each time a flux quantum $\phi_0 = hc/2e$ penetrates the system, $T_c(H)$ exhibits an oscillation. Berger and Rubinstein [78, 79] studied mesoscopic superconducting loops using the nonlinear Ginzburg-Landau (GL) theory. They assumed that the induced magnetic field can be neglected for samples with sufficiently small thickness. In the limit of thin loops, the transition between states with different angular momentum L (also called vorticity) occurs when the enclosed flux ϕ equals $(L + 1/2)\,\phi_0$ [34].

The intermediate case of finite width loops was studied previously by Bardeen [80] within the London theory. He showed that in tubes of very small diameter and with wall thickness of the order of the penetration depth the flux through the tube is quantized in units of $\nu\phi_0$ where $\nu < 1$ depends on the dimensions of the system. Arutunyan and Zharkov [81, 82] found that the flux through the effective area $\pi\,(\rho^*)^2$ is equal to $m\phi_0$, where the effec-

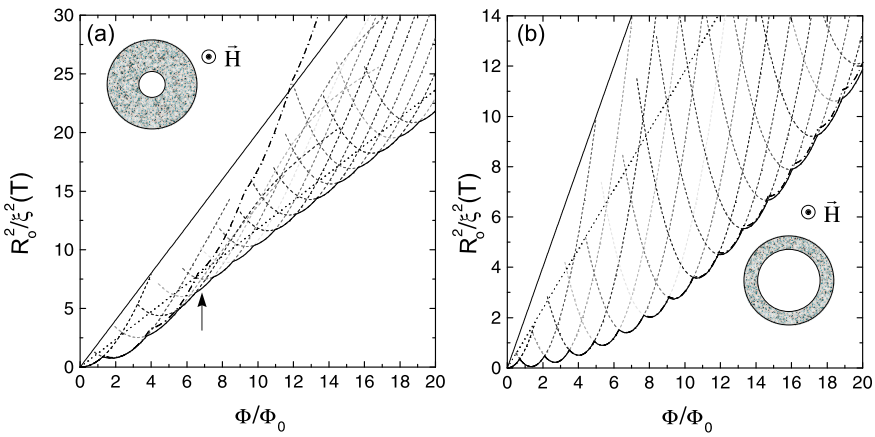

Fig. 5.1 Phase diagram for a superconducting loop (dashed lines) with different ratio of inner to outer radius $R_i/R_o = 0.3$ (a) and 0.7 (b). The ground state is given by the thicker curves. The solid and dotted straight lines correspond to the bulk values of $H_{c2}(T)$ and $H_{c3}(T)$, respectively. R_o is the outer radius of the ring and Φ is the applied flux. [From Ref. [83]]

tive radius ρ^* is approximately equal to the geometric mean square of the inner radius R_i and the outer radius R_o of the cylinder; i.e. $\rho^* = (R_i R_o)^{1/2}$. Fomin *et al.* [61] studied square loops with leads attached to it and found inhomogeneous Cooper-pair distributions in the loop with enhancements near the corners of the square loop.

Bruyndoncx *et al.* [83] investigated infinitely thin loops of finite width. In this case, the magnetic field induced by the supercurrents can be neglected and the total magnetic field equals the external applied magnetic field. Furthermore, they used the linearized GL equation which is only valid near the superconductor/normal boundary where the density of the superconducting condensate $|\psi|^2$ is small. Only the giant vortex state with a definite angular momentum L was studied and they concentrated on the two- (2D) to three-dimensional (3D) crossover (see also Fig. 5.1). Berger and Rubinstein [84] also studied infinitely thin loops of finite width using the nonlinear GL theory and they also neglected the induced field.

Contrary to all previous theoretical studies, we consider circular flat disks of nonzero thickness with a circular hole in it, which is not necessary in the center of the disk. The superconducting properties are also studied deep inside the superconducting state where: i) nonlinear effects are important, i.e. $|\psi|$ is not necessarily small, and the nonlinear GL equations have to be solved, ii) the total magnetic field is not homogeneous, i.e. it is spatial varying due to the Meissner effect and the flux quantization condition which may enhance or diminish the magnetic field through the hole as compared to the applied magnetic field, and iii) due to nonlinear effects the circular

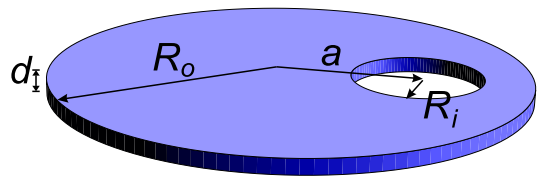

Fig. 5.2 The configuration: a superconducting disk with radius R_o and thickness d with a hole inside with radius R_i which is placed a distance a away from the center.

symmetric giant vortex states are not necessarily the lowest energy states and the magnetic field can penetrate the superconductor through single vortices creating a multivortex state.

In section 5.2 we present the theoretical model. In section 5.3 we consider a small superconducting disk with a hole in the center. In this case we find that only the giant vortex state appears. We study the influence of the radius of the hole on the superconducting state. For such a small system the relation between the local magnetic field, the current density and the Cooper-pair density is investigated. Next, in section 5.4, we consider the case of a larger superconducting disk with a hole in the center. For increasing magnetic field, we find re-entrant behaviour; i.e. transition from the giant vortex state to the multivortex state and back to the giant vortex state before superconductivity is destroyed. In section 5.5, we investigate the influence of the position of the hole on the vortex configuration. What happens if we break the axial symmetry? In section 5.6 we investigate the quantization of the flux through the hole. Recently, Pederson *et al.* [32] performed Hall magnetometry experiments on circular superconducting rings. In section 5.7 their experimental results on superconducting rings are discussed. Finally, our results are summarized in section 5.8.

5.2 THEORETICAL FORMALISM

We consider superconducting disks with radius R_o and thickness d with a hole inside with radius R_i which is placed a distance a away from the center of the disk [see Fig. 5.2]. These superconducting 'rings' are immersed in an insulating medium with a perpendicular uniform magnetic field H_0.

To solve this problem we extend the theoretical formalism for disks (see chapter 2). For small rings only giant vortex states can nucleate and we can use the 2D formalism (see paragraph 2.2.1), while for larger rings multivortices become stable and we have to use the 3D formalism (see paragraph 2.2.2).

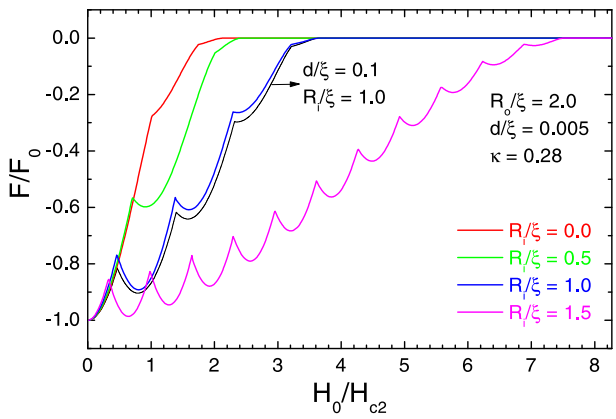

Fig. 5.3 The ground state free energy as a function of the applied magnetic field H_0 of a superconducting disk with radius $R_o = 2.0\xi$, thickness $d = 0.005\xi$ and $\kappa = 0.28$ for a hole in the center with radius $R_i/\xi = 0.0$, 0.5, 1.0 and 1.5 respectively. The thin black curve gives the free energy of a thicker ring with thickness $d = 0.1\xi$ and $R_i = 1.0\xi$. The free energy is in units of $F_0 = H_c^2 V/8\pi$.

Boundary condition (2.3) can be written as follows for a superconducting ring:

$$\vec{n} \cdot \left(-i\vec{\nabla}_{2D} - \vec{A}\right) \Psi \Big|_{\vec{r}=\vec{R}_i} = 0, \tag{5.1}$$

$$\vec{n} \cdot \left(-i\vec{\nabla}_{2D} - \vec{A}\right) \Psi \Big|_{\vec{r}=\vec{R}_o} = 0, \tag{5.2}$$

while the boundary condition for the vector potential is still given by Eq. (2.4).

5.3 SMALL RINGS: GIANT VORTEX STATES

First we discuss a small superconducting ring. For sufficiently small rings the confinement effects are dominant and this imposes a circular symmetry on the superconducting condensate.

5.3.1 Free energy and magnetization

The ground state free energy F of a superconducting disk with radius $R_o = 2.0\xi$ and thickness $d = 0.005\xi$ and GL parameter $\kappa = 0.28$ is shown in Fig. 5.3 for a hole in the center with radius $R_i/\xi = 0.0$, 0.5, 1.0 and 1.5, respectively. The situation with $R_i = 0$ corresponds to the situation of a superconducting disk without a hole which was already studied in chapter 2 and Ref. [28]. With increasing hole radius R_i, we find that the superconducting/normal transition shifts appreciably to higher magnetic fields and more transitions between different L states are possible before superconductivity disappears.

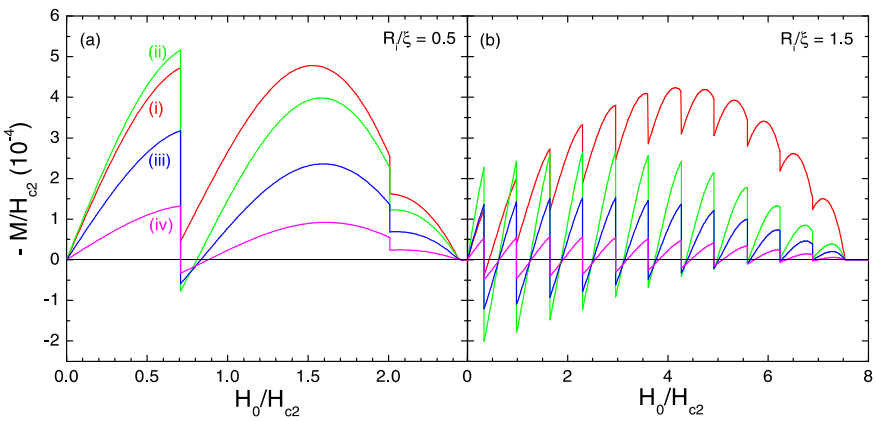

Fig. 5.4 The magnetization as a function of the applied magnetic field H_0 for a superconducting disk with radius $R_o = 2.0\xi$ and thickness $d = 0.005\xi$ and $\kappa = 0.28$ for a hole in the center with radius $R_i/\xi = 0.5$ (a) and $R_i/\xi = 1.5$ (b). Curve (i) is the calculated magnetization if we average the magnetic field over the superconducting volume; curve (ii) after averaging the field over the area with radius R_o, i.e. superconductor and hole; curves (iii) and (iv) after averaging the magnetic field over a square region with widths equal to $2R_o$ and $(2 + 1/2)R_o$, respectively.

Furthermore, the thin black curve gives the free energy for a thicker ring with thickness $d = 0.1\xi$ and $R_i = 1.0\xi$. In comparison with the previous results for $d = 0.005\xi$, the free energy becomes more negative, but the transitions between the different L states occur almost at the same magnetic fields. Thus increasing the thickness of the ring increases superconductivity which is a consequence of the smaller penetration of the magnetic field into the superconductor.

Experimentally, using magnetization measurements one can investigate the effect of the geometry and the size of the sample on the superconducting state. By measuring the Hall resistance, one obtains the average magnetic field, and consequently, the magnetic field expelled from the Hall cross, which is a measure for the magnetization of the superconductor [54]. As in the case of a superconducting disk [54], the field distribution in the case of thin superconducting rings is extremely non-uniform inside as well as outside the sample and therefore the detector size will have an effect on the measured magnetization. To understand this effect of the detector, we calculate the magnetization for a superconducting ring with outer radius $R_o = 2.0\xi$, thickness $d = 0.005\xi$ and two values of the inner radius $R_i = 0.5\xi$ and $R_i = 1.5\xi$ by averaging the magnetic field over several detector sizes S. The results are shown in Figs. 5.4(a,b) as a function of the applied magnetic field for $R_i = 0.5\xi$ and $R_i = 1.5\xi$, respectively. The red curve [curve (i)] shows the calculated magnetization if we average the magnetic field over the superconducting volume, and curve (ii) is the magnetization after averaging the field over a circular area

with radius R_o, i.e. superconductor and hole. Notice that in the Meissner regime, i.e. $H_0/H_{c2} < 0.7$ where $L = 0$, the magnetization of superconductor + hole is larger than the one of the superconductor alone which is due to flux expulsion from the hole. For $L \geq 1$ the reverse is true because now flux is trapped in the hole. Experimentally, one usually averages the magnetic field over a square Hall cross region. Therefore, we calculated the magnetization by averaging the magnetic field over a square region [curve(iii)] with width equal to $2R_o$, i.e. the diameter of the ring. Curve (iv) shows the magnetization if the sides of the square detector are equal to $(2 + 1/2)R_o$. Increasing the size of the detector, decreases the observed magnetization because the magnetic field is averaged over a larger region which brings $\langle H \rangle$ closer to the applied field H_0.

5.3.2 Phase diagrams

Having the free energies of the different giant vortex configurations for several values of the hole radius varying from $R_i = 0.0\xi$ to $R_i = 1.8\xi$, we construct an equilibrium vortex phase diagram. Fig. 5.5(a) shows this phase diagram for a superconducting disk with radius $R_o = 2.0\xi$, thickness $d = 0.005\xi$ and for $\kappa = 0.28$. The blue curves indicate where the ground state of the free energy changes from one L state to another and the red curve gives the superconducting/normal transition. The latter exhibits a small oscillatory behavior which is a consequence of the Little-Parks effect. Notice that the superconducting/normal transition is moving to larger fields with increasing hole radius R_i and more and more flux can be trapped. In the limit $R_i \to R_o$, the critical magnetic field is infinite and there are an infinite number of L states possible which is a consequence of the enhancement of surface conductivity for very small samples [49, 55]. Because of the finite grid, we were not able to obtain accurate results for $R_i \approx R_o$. The dashed lines connect our results for hole radius $R_i = 1.8\xi$ with the results for $R_i \to R_o$ [34], where the transitions between the different L states occur when the enclosed flux is $\phi = (L + 1/2)\phi_0$, where $\phi_0 = ch/2e$ is the elementary flux quantum. Notice that for rings of nonzero width, i.e. $R_i \neq R_o$, the $L \to L + 1$ transition occurs at higher magnetic field than predicted from the condition $\phi = (L + 1/2)\phi_0$. The discrepancy increases with increasing width of the ring and with increasing L. Starting from $R_i = 0$ we find that with increasing R_i the Meissner state disappears at smaller H_0. The hole in the center of the disk allows for a larger penetration of the magnetic field which favors the $L = 1$ state. This is the reason why the $L = 0 \to L = 1$ transition moves to a lower external field while the $L = 1 \to L = 2$ transition initially occurs for larger H_0 with increasing R_i. When the hole size becomes of the order of the width of one vortex the $L = 1 \to L = 2$ transition starts to move to lower fields and the $L = 2$ state becomes more favorable.

The effect of the thickness of the ring on the phase diagram is investigated in Fig. 5.5(b). The blue curves indicate again where the ground state of the

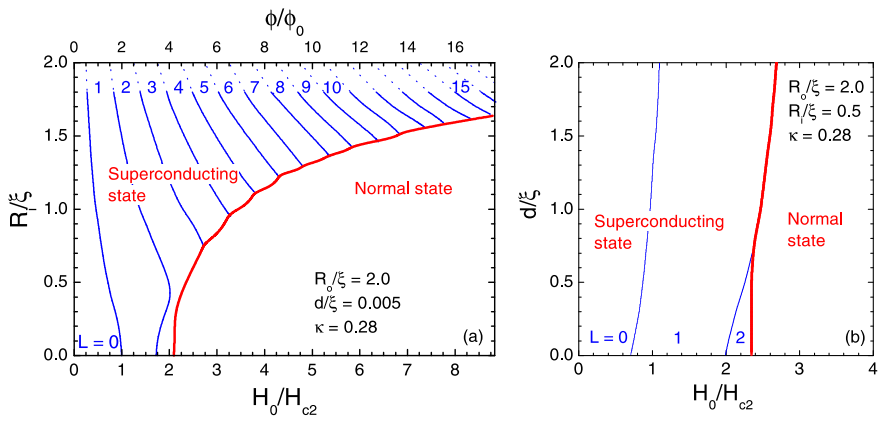

Fig. 5.5 Phase diagrams: the relation between (a) the hole radius R_i, (b) the thickness d and the magnetic fields H_0 at which giant vortex transitions $L \to L+1$ takes place for the parameters indicated in the figures. The blue curves indicate where the ground state of the free energy changes from one L state to another one and the red curve gives the superconducting/normal transition.

free energy changes from one L state to another one, while the red curve gives the superconducting/normal transition. Notice that the transition from the $L = 0$ to the $L = 1$ state and the superconducting/normal transition depends weakly on the thickness of the ring. For increasing thickness d, the $L = 2$ state becomes less favorable and disappears for $d \gtrsim 0.7\xi$. In this case, there is a transition from the $L = 1$ state directly to the normal state. Increasing d stabilizes the different L states up to larger magnetic fields. This is due to the increased expulsion of the applied field from the superconducting ring.

5.3.3 Cooper-pair density, magnetic field distribution and current density

In the next step, we investigate three very important and mutually dependent quantities: the local magnetic field H, the Cooper-pair density $|\Psi|^2$ and the current density j. We will discuss these quantities as a function of the radial position ρ. For this study we distinguish two situations, i.e. $R_i \ll R_o$ and $R_i \lesssim R_o$. In the first case the sample behaves more like a superconducting disk, and in the second case like a superconducting loop.

A. $\mathbf{R}_i \ll \mathbf{R}_o$

First, we consider a superconducting disk with radius $R_o = 2.0\xi$ and thickness $d = 0.1\xi$ with a hole with radius $R_i = 0.5\xi$ in the center. The free energy and the magnetization (after averaging over the superconductor+hole) for such a ring are shown in Fig. 5.6. The blue curves give the free energy and the magnetization for the different L states, and the red curve is the result for

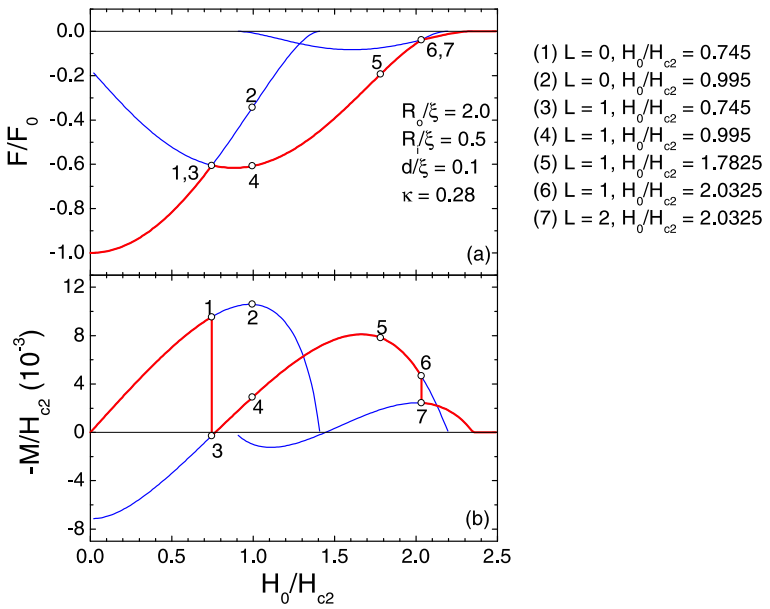

Fig. 5.6 (a) The free energy and (b) the magnetization after averaging over the superconductor+hole as a function of the applied magnetic field for a superconducting disk with outer radius $R_o = 2.0\xi$ and thickness $d = 0.1\xi$ with a hole with radius $R_i = 0.5\xi$ in the center ($\kappa = 0.28$) for the different L states (blue curves) and for the ground state (red curves).

the ground state. Figs. 5.7(a,b) show the local magnetic field H, Figs. 5.7(c,d) the Cooper-pair density $|\Psi|^2$, and Figs. 5.7(e,f) the current density j as function of the radial position ρ for such a ring at the L states and magnetic fields as indicated by the open circles in Figs. 5.6(a,b).

For low magnetic fields, the system is in the $L = 0$ state, i.e. the Meissner state, and the flux trapped in the hole is considerably suppressed. Hence, the local magnetic field inside the hole is lower than the external applied magnetic field as is shown in Fig. 5.7(a) by curves 1 and 2. Please notice that the plotted magnetic field is scaled by the applied field H_0. In the $L = 0$ state the superconductor expels the magnetic field by inducing a supercurrent which tries to compensate the applied magnetic field in the superconductor and inside the hole. This is called the *diamagnetic Meissner effect.* As long as L equals zero, the induced current has only to compensate the magnetic field at the outside of the ring and, therefore, the current flows in the whole superconducting material in the same direction and the size increases with increasing field. This is clearly shown in Fig. 5.7(e) by curves 1 and 2 where the current density j becomes more negative for increasing H_0/H_{c2}. Notice also that the current density is more negative at the outside than at the inside of the superconducting ring which leads to a stronger depression of the

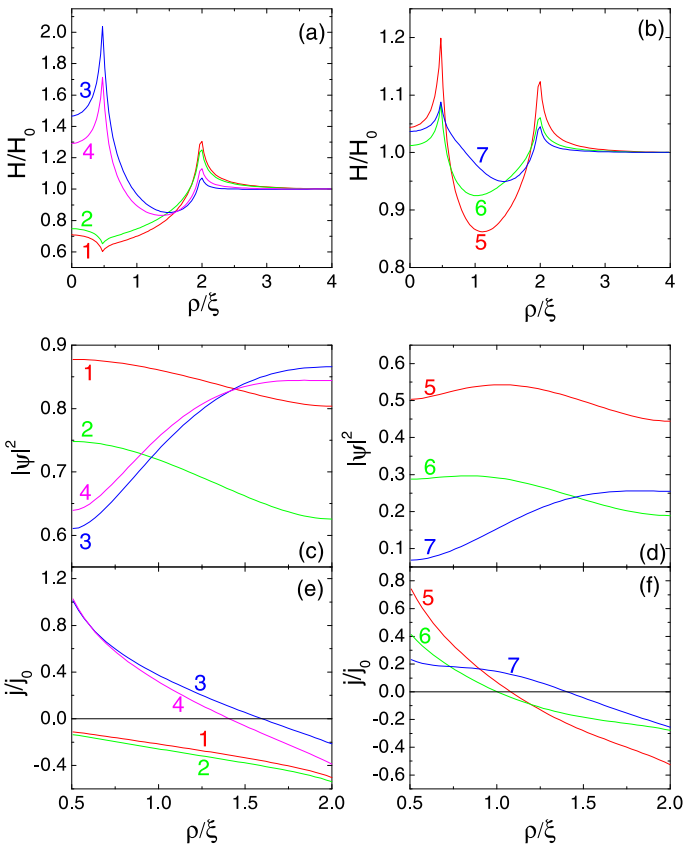

Fig. 5.7 (a,b) The local magnetic field H, (c,d) the Cooper-pair density $|\Psi|^2$ and (e,f) the current density j for the situations indicated by the open circles in Fig. 5.6 as a function of the radial position ρ for the same configuration as in Fig. 5.6.

Cooper-pair density at the outer edge as compared to the inner edge of the ring [see curves 1 and 2 in Fig. 5.7(c)].

At $H_0/H_{c2} = 0.745$, the ground state changes from the $L = 0$ to the $L = 1$ state [see Fig. 5.6(a)]. Suddenly more flux becomes trapped in the hole [compare curve 1 with curve 3 in Fig. 5.7(a)], the local magnetic field inside the hole increases and becomes larger than the external magnetic field H_0. In the $L = 1$ state, there is a sharp peak in the magnetic field at the inner boundary because of demagnetization effects. Consequently, more current is needed to compensate the magnetic field near the inner boundary than near the outer boundary [see curve 3 in Fig. 5.7(e)]. The sign of the current near the inner boundary becomes positive (the current direction reverses), but the sign of the current near the outer boundary does not change. This can be explained as follows: Near the inner boundary ($\rho \gtrsim 1.0\xi$) the magnetic field is compressed

into the hole (*paramagnetic effect*), while near the outer boundary ($\rho \lesssim 2.0\xi$) the magnetic field is expelled to the insulating environment (diamagnetic effect). The sign reversal of j occurs at $\rho = \rho^*$ and later we will show that the flux through the circular area with radius ρ^* is exactly quantized (see section 5.6). At the $L = 0$ to the $L = 1$ transition the maximum in the Cooper-pair density [compare curves 1 and 3 in Fig. 5.7(c)] shifts from $\rho = R_i$ to $\rho = R_o$. Further increasing the external field increases the Cooper-pair density near the inner boundary initially [compare curve 3 and 4 in Fig. 5.7(c)], because the flux in the hole has to be compressed less. The point ρ^*, where $j = 0$, shifts towards the inner boundary of the ring. Further increasing the external magnetic field, the Cooper-pair density starts to decrease [see curves 5 and 6 in Fig. 5.7(d)] and attains its maximum near the inner boundary. The current near the inner boundary becomes less positive [see curves 5 and 6 in Fig. 5.7(f)], i.e. less shielding of the external magnetic field inside the hole [see curves 5 and 6 in Fig. 5.7(b)], and near the outer boundary j becomes less negative which shields the magnetic field from the superconductor+hole. Thus at the outer edge the local magnetic field has a local maximum which decreases with applied magnetic field H_0.

At $H_0/H_{c2} \approx 2.0325$, the ground state changes from the $L = 1$ state to the $L = 2$ state and extra flux is trapped in the hole. The changes in the magnetic field distribution, the Cooper-pair density and the current density are analogous to the changes at the first transition. For example, the magnetic field inside the hole increases compared to the external magnetic field [curve 7 in Fig. 5.7(b)], the radius ρ^* increases substantially [curve 7 in Fig. 5.7(f)] and the maximum in the Cooper-pair density shifts to the outer boundary [curve 7 in Fig. 5.7(d)].

B. $\mathbf{R}_i \lesssim \mathbf{R}_o$

For $R_i \ll R_o$ and $L > 0$, the superconducting state consists of a combination of the paramagnetic and the diamagnetic Meissner state, like for a disk. For $R_i \lesssim R_o$ we expect that the sample behaves like a loop and, hence, the superconducting state is a pure paramagnetic Meissner state or a pure diamagnetic Meissner state.

We consider a superconducting disk with radius $R_o = 2.0\xi$ and thickness $d = 0.1\xi$ with a hole with radius $R_i = 1.8\xi$ in the center. The free energy and the magnetization (after averaging over the superconductor+hole) for such a ring are shown in Fig. 5.8. The blue curves give the free energy and the magnetization for the different L states, and the red curve is the result for the ground state. Figs. 5.9(a,b) show the local magnetic field H, and Figs. 5.9(c,d) the current density j as function of the radial position ρ for such a ring at the L states and magnetic fields as indicated by the open circles in Figs. 5.8(a,b). The Cooper-pair density has almost no structure and is practically constant over the ring and will, therefore, not be shown.

For $L = 0$, the situation is the same as for $R_i \ll R_o$. The magnetic field is expelled from the superconductor and the hole to the outside of the system,

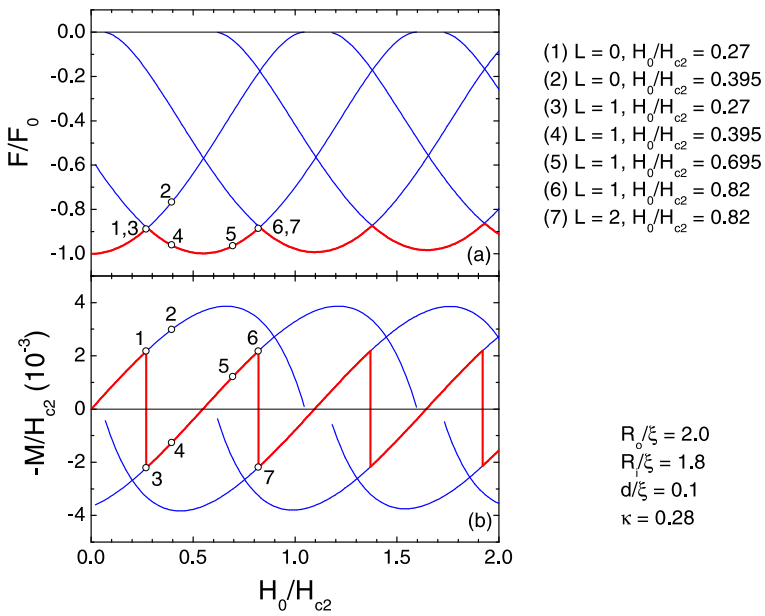

Fig. 5.8 (a) The free energy and (b) the magnetization after averaging over the superconductor+hole as a function of the applied magnetic field for a superconducting disk with outer radius $R_o = 2.0\xi$ and thickness $d = 0.1\xi$ with a hole with radius $R_i = 1.8\xi$ in the center ($\kappa = 0.28$) for the different L states (blue curves) and for the ground state (red curves).

i.e. diamagnetic Meissner effect. The current flows in the whole superconducting material in the same direction [curves 1 and 2 in Fig. 5.9(a)] and the size increases with increasing external field H_0 [curves 1 and 2 in Fig. 5.9(c)]. At $H_0/H_{c2} = 0.27$, the ground state changes from the $L = 0$ state to the $L = 1$ state and suddenly more flux is trapped in the hole. The local magnetic field inside the hole becomes larger than the external field H_0 and there is a sharp peak near the inner boundary [curves 3 and 4 in Fig. 5.9(a)]. In contrast to the situation for $R_i \ll R_o$, there is no peak near the outer boundary, which means that the magnetic field is only expelled to the hole, i.e. paramagnetic Meissner effect. The induced current flows in the reverse direction in the whole superconductor [curves 3 and 4 in Fig. 5.9(c)]. For increasing external magnetic field, the magnetic field inside the hole, the height of the demagnetization peak and hence the size of the current decrease [see curves 3 and 4 in Fig. 5.9(a,c)]. Further increasing the field, the superconducting state transforms into a diamagnetic Meissner state. The magnetic field is now expelled to the outside of the sample [curves 5 and 6 in Fig. 5.9(b)] and the direction of the current is the same everywhere in the ring [curves 5 and 6 in Fig. 5.9(d)]. At $H_0/H_{c2} = 0.82$, the ground state changes from the $L = 1$

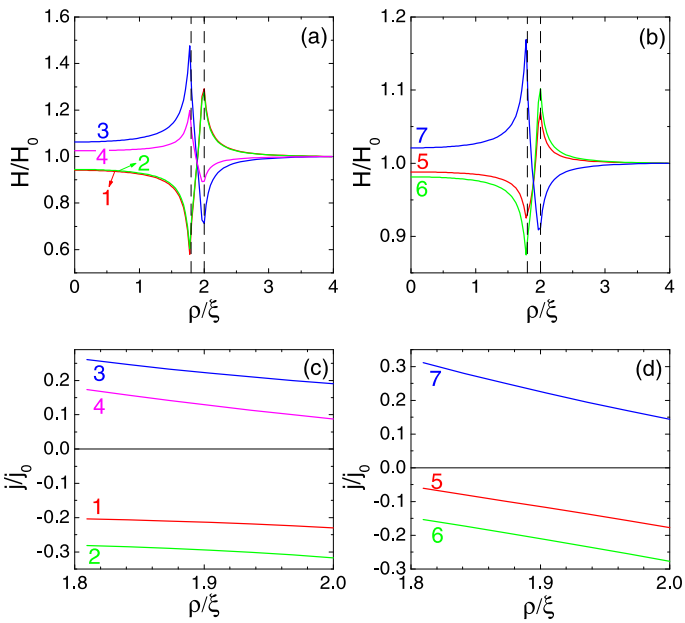

Fig. 5.9 (a,b) The local magnetic field H and (c,d) the current density j for the situations indicated by the open circles in Fig. 5.8 as a function of the radial position ρ for the same configuration as in Fig. 5.8.

state to the $L = 2$ state. The changes in the magnetic field distribution [see curve 7 in Fig. 5.9(b)] and the current density [see curve 7 in Fig. 5.9(c)] are analogous to the changes at the first transition. The diamagnetic state transforms into a paramagnetic state.

For a narrow ring with finite width, the superconductor is in the paramagnetic or the diamagnetic Meissner state, like for a superconducting loop. Contrary to this infinitely narrow ring case, for narrow finite width rings the superconducting state can also consist of a combination of these two states, i.e. the direction of the supercurrent in the inner part of the ring is opposite to the outer part.

5.4 LARGER RINGS: MULTIVORTEX STATES

Until now, we considered only small rings. In such rings, the confinement effect dominates and only the giant vortex states are stable. Now we will consider larger superconducting disks in which multivortex states can nucleate for certain magnetic fields. As an example we take a fat ring with outer radius $R_o = 4.0\xi$, thickness $d = 0.005\xi$, $\kappa = 0.28$ and for different values of the inner radius.

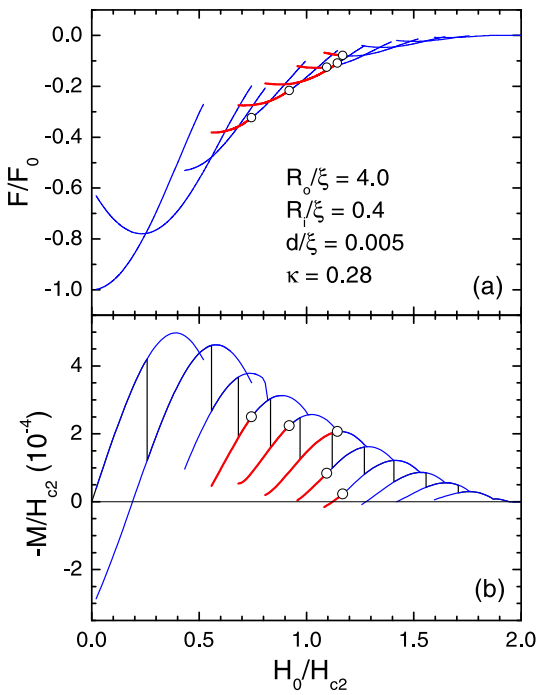

Fig. 5.10 (a) The free energy as function of the applied magnetic field for a superconducting ring with $R_o = 2.0\xi$, $R_i = 0.4\xi$, $d = 0.005\xi$, and $\kappa = 0.28$. (b) The magnetization for the same sample after averaging over the superconducting ring only. The different L states are given by the blue curves and the multivortex states by the red curve. The black vertical lines are the ground state transitions and the transitions from multivortex state to giant vortex state are indicated by the open circles.

5.4.1 Free energy and magnetization

Fig. 5.10(a) shows the free energy for such a ring with inner radius $R_i = 0.4\xi$ as a function of the applied magnetic field H_0. The different giant vortex states are given by the blue curves and the multivortex states by the red curves. The open circles indicate the transitions from the multivortex state to the giant vortex state. In this ring, multivortex states exist with vorticity $L = 3$ up to 7. For $L = 3, 4, 5$ multivortices occur both as metastable states as well as in the ground state, while for $L = 6, 7$ they are only found in the metastable state. Notice there is no discontinuity in the free energy at the transitions from the multivortex state to the giant vortex state for fixed vorticity L. Fig. 5.10(b) shows the magnetization M for this ring as a function of H_0 after averaging the field H over the superconducting ring (without the hole). The blue curves give the results for the different L states and the red curves for the different multivortex states. The black vertical lines indicate the ground state

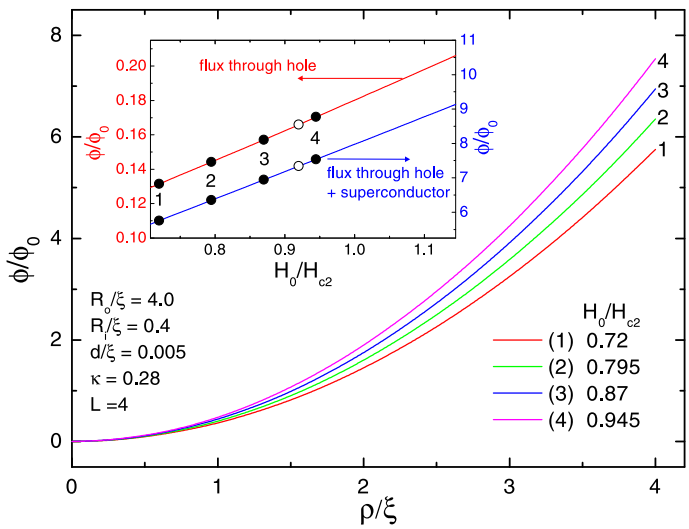

Fig. 5.11 The flux ϕ through a circular area of radius ρ for different values of the applied magnetic field H_0. Curves 1, 2, 3 give the results for multivortex states and curve 4 for a giant vortex state. The inset shows the flux through the hole with radius $R_i = 0.4\xi$ (red curves) and through the superconductor + hole (blue curves) as a function of the applied magnetic field for a $L = 4$. The solid circles indicate the magnetic fields considered in the main figure and the open circles indicate the transition from multivortex to giant vortex state.

transitions and the open circles the transition from the multivortex state to the giant vortex states. Notice that the latter transitions are smooth, there are no discontinuities in the magnetization.

5.4.2 Flux through the hole

Now, we investigate the flux ϕ through the hole for the $L = 4$ multivortex and giant vortex state for the case of the above ring. Fig. 5.11 shows the flux ϕ through a circular area of radius ρ for different values of the applied magnetic field H_0. Curves 1, 2, 3 and 4 are the results for $H_0/H_{c2} = 0.72$, 0.795, 0.87 (i.e. multivortex states) and 0.945 (i.e. giant vortex state), respectively. There is no qualitative difference between the 4 curves, i.e. no qualitative difference between the multivortex states and the giant vortex state. In the inset, we show the flux through the hole with radius $R_i = 0.4\xi$ and through the superconductor+hole as a function of the applied magnetic field for a fixed value of the vorticity, i.e. $L = 4$. The solid circles indicate the magnetic fields considered in the main figure and the open circle indicates the position of the transition from multivortex state to giant vortex state. The slope of the curves increases slightly at the applied magnetic field, where there is a transition form

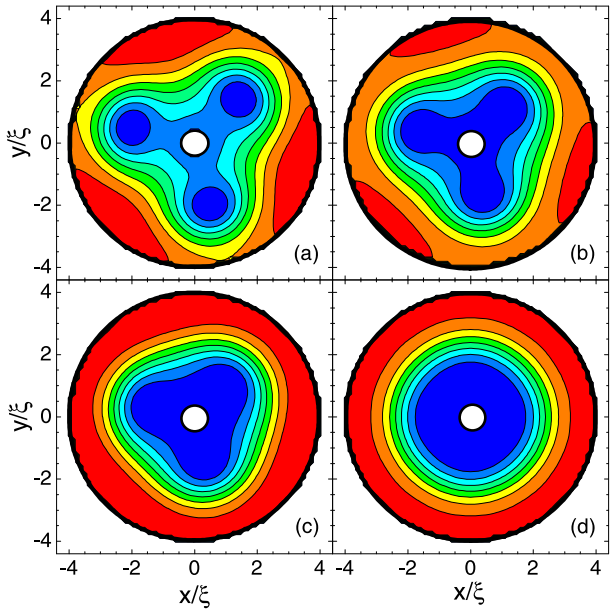

Fig. 5.12 The Cooper-pair density corresponding to the four situations of Fig. 5.11: $H_0/H_{c2} = 0.72$ (a); $H_0/H_{c2} = 0.795$ (b); $H_0/H_{c2} = 0.87$ (c); and $H_0/H_{c2} = 0.945$ (d). Red regions indicate high density, blue regions low density. The thick circles indicate the inner and the outer edge of the ring.

the multivortex state to the giant vortex state. This agrees with the result for a disk (see section 2.4) that the giant↔multivortex transition is a second-order phase transition.

The Cooper-pair density $|\psi|^2$ for the previous four configurations is shown in Fig. 5.12. Blue regions are regions with low Cooper-pair density and thus vortices are given by blue regions. Red regions indicate high Cooper-pair density. At the magnetic field $H_0/H_{c2} = 0.72$ [Fig. 5.12(a)] we see clearly three multivortices. With increasing magnetic field, these multivortices start to overlap and move to the center [Figs. 5.12(b,c)] and finally they combine to one giant vortex in the center [Fig. 5.12(d)].

5.4.3 Phase diagrams

The free energies of the different vortex configurations were calculated for different values of the hole radius which we varied from $R_i = 0$ to $R_i = 3.6\xi$. From these results we constructed an equilibrium vortex phase diagram. First, we assumed axial symmetry, where only giant vortex states occur and the order parameter is given by $\Psi(\vec{\rho}) = F(\rho)\, e^{iL\varphi}$. In the phase diagram (Fig. 5.13) the blue curves separate the regions with different number of vor-

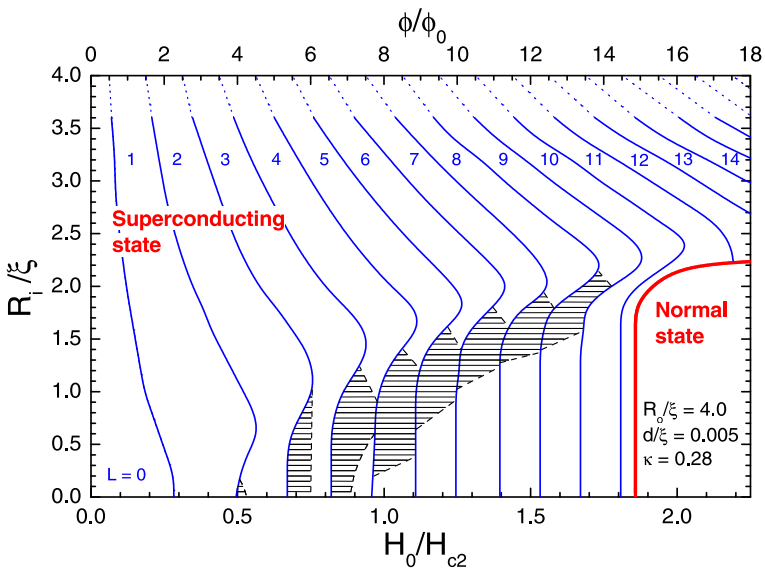

Fig. 5.13 Equilibrium vortex phase diagram for a superconducting disk with radius $R_o = 4.0\xi$, thickness $d = 0.005\xi$ with a hole with radius R_i in the center. The blue curves show the transitions between the different L states, the red curve shows the superconducting/normal transition and the dotted blue lines connect the results for $R_i = 3.6\xi$ with the results in the limit $R_i \to R_o$. The shaded regions indicate the multivortex states and the dashed curves separate the multivortex states from the giant vortex states.

tices (different L states). In the limit $R_i \to 0$ we find the previous results of Ref. [39] for a superconducting disk. The radius of the giant vortex R_L in the center of the disk increases with increasing L, because it has to accommodate more flux, i.e. $R_L/\xi \sim \sqrt{L/(H_0/H_{c2})}$. Hence, if we make a little hole in the center of the disk, this will not influence the $L \to L+1$ transitions as long as $R_i \ll R_L$ as is apparent from Fig. 5.13. For sufficient large hole radius R_i, the hole starts to influence the giant vortex configuration and the magnetic field needed to induce the $L \to L+1$ transition increases. For example, the transition field from the $L = 7$ state to the $L = 8$ state reaches its maximum for a hole radius $R_i \approx 2.0\xi$ which occurs for $H_0/H_{c2} \approx 1.5$. The above rough estimate gives $R_L/\xi \sim 2.16$ which is very close to $R_i/\xi \sim 2.0$. Further increasing R_i, the hole becomes so large that more and more flux is trapped inside the hole, and consequently a smaller field is needed to induce the $L \to L+1$ transition. Because of finite grid size, we were limited to $R_i \leq 3.6\xi$. The results we find for $R_i = 3.6\xi$ are extrapolated to $\phi = (L + 1/2)\phi_0$ for $R_i = R_o$. The red curve in Fig. 5.13 gives the superconducting/normal transition. For low values of R_i, this critical magnetic field is independent of R_i, because the hole is smaller than the giant vortex state in the center and hence the hole does not

influence the superconducting properties near the superconducting/normal transition. For $R_i \gtrsim 2.0\xi$, this field starts to increase drastically. Therefore, more and more L states appear. In the limit $R_i \to R_o$, the critical magnetic field is infinite and there are an infinite number of L states possible which is a consequence of the enhancement of surface conductivity for very small superconducting samples [49].

Next, we consider the general situation where the order parameter is allowed to be a mixture of different giant vortex states and thus we no longer assume axial symmetry of the superconducting wavefunction. We found that the transitions between the different L states are not influenced by this generalization, but that for certain magnetic fields the ground state is given by the multivortex state instead of the giant vortex state. In Fig. 5.13 the shaded regions correspond to the multivortex states and the dashed curves are the boundaries between the multivortex and the giant vortex states. For $L = 1$, the single vortex state and the giant vortex state are identical. In the limit $R_i \to 0$, the results for a superconducting disk are recovered. For increasing hole radius R_i, the $L = 2$ multivortex state disappears as a ground state for $R_i > 0.15\xi$. If R_i is further increased, the ground state for $L = 5$ up to $L = 9$ changes from giant vortex state to multivortex state and again to giant vortex state. For example, for $R_i = 2.0\xi$ the multivortex state exists only in the $L = 9$ state. Notice that for small R_i the region of multivortex states increases and consequently the hole in the center of the disk stabilizes the multivortex states, at least for $L > 2$. For large R_i, i.e. narrow rings, the giant vortex state is the energetically favorable one because confinement effects start to dominate which impose the circular symmetry on Ψ. For fixed hole radius $R_i \leq 2.0\xi$ and increasing magnetic field we find always at least one transition from giant vortex state to multivortex state and back to giant vortex state (*re-entrant behaviour*). Remark that the ground state for $L \geq 10$ is in the giant vortex state irrespective of the value of the magnetic field. Near the superconducting/normal transition the superconducting ring is in the giant vortex state because now superconductivity exists only near the edge of the sample and consequently the superconducting state will have the same symmetry as the outer edge of the ring and thus it will be circular symmetric.

Finally, for $L \geq 3$ the multivortex state not necessarily consists of L vortices in the superconducting material. Often they consist of a combination of a big vortex trapped in the hole and some multivortices in the superconducting material. This is clearly shown in Fig. 5.14 where a contour plot of the local magnetic field is given for a superconducting disk with radius $R_o = 4.0\xi$ and thickness $d = 0.005\xi$ with a hole in the center with radius $R_i = 0.6\xi$ [Fig. 5.14(a)] and $R_i = 1.0\xi$ [Fig. 5.14(b)]. As usual we took $\kappa = 0.28$. The black circles are the inner and outer radius of the ring. Low magnetic fields are given by blue regions, higher magnetic fields by red regions and green indicate the external magnetic field. In this way, multivortices in the superconducting area are red spots. In Fig. 5.14(a) the local magnetic field is shown for an applied magnetic field $H_0/H_{c2} = 0.895$. Although the winding number is

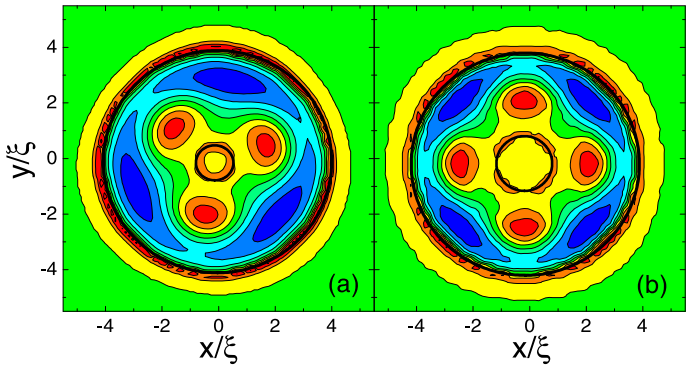

Fig. 5.14 Contour plot of the local magnetic field for a superconducting disk with radius $R_o = 4.0\xi$ and thickness $d = 0.005\xi$ ($\kappa = 0.28$) with a hole in the center with (a) radius $R_i = 0.6\xi$ at $H_0/H_{c2} = 0.895$ for $L = 4$; and (b) radius $R_i = 1.0\xi$ at $H_0/H_{c2} = 1.145$ for $L = 6$. The black circles indicate the inner and outer edge of the ring. Low (high) magnetic fields are given by blue (red) regions and green regions indicate the external field.

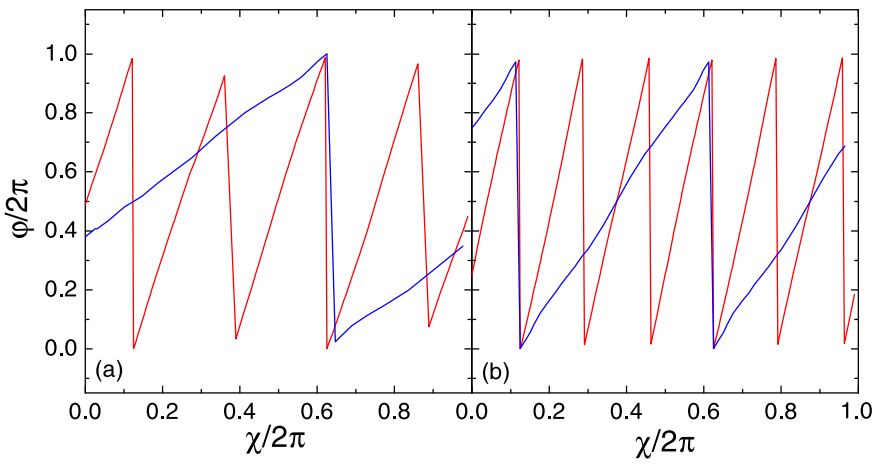

Fig. 5.15 The phase φ of the order parameter calculated on a circle $\mathbf{r} \to Ce^{i\chi}$ as a function of the angle χ for a superconducting ring with $R_o = 4.0\xi$, $d = 0.005\xi$ and $\kappa = 0.28$; (a) $R_i = 0.6\xi$, $H_0/H_{c2} = 0.895$, $L = 4$ and $C = 3.95\xi$ (red curve) and $C = 0.7\xi$ (blue curve); (b) $R_i = 1.0\xi$, $H_0/H_{c2} = 1.145$, $L = 6$ and $C = 3.95\xi$ (red curve) and $C = 1.2\xi$ (blue curve).

$L = 4$, there are only 3 vortices in the superconducting material and one vortex appears in the hole in the center of the disk. This is clearly shown in Fig. 5.15(a) where the phase φ of the order parameter is shown along different circular loops $\vec{r} \to Ce^{i\chi}$ inside the superconductor. The red curve gives the phase near the outer edge of the ring ($C = 3.95\xi$) and the blue curve near

the inner edge of the ring ($C = 0.7\xi$). When encircling the ring, the phase difference $\Delta\varphi$ in the first case is 4 times 2π, while in the second case it is $\Delta\varphi = 1 \times 2\pi$. The phase difference is always given by $\Delta\varphi = L \times 2\pi$, with L the vorticity. In Fig. 5.14(b) a contour plot of the local magnetic field is shown for a ring with $R_i = 1.0\xi$ which leads to $L = 6$ at $H_0/H_{c2} = 1.145$. Only 4 vortices are in the superconducting material and one giant vortex in the center (partially in the hole) with $L = 2$. Fig. 5.15(b) shows the phase φ of the order parameter for $C = 3.95\xi$ (red curve) and 1.2ξ (blue curve), where the phase differences are $\Delta\varphi = 6 \times 2\pi$ and $2 \times 2\pi$, respectively. Notice that the flux ϕ through the hole equals $\phi \approx 0.19\phi_0$ for the case of Fig. 5.14(a) and $\phi \approx 0.36\phi_0$ for the case of Fig. 5.14(b) and is thus not equal to a multiple of the flux quantum ϕ_0 (see also section 5.6).

5.5 NON-SYMMETRIC GEOMETRY

So far, we investigated the influence of the size of the hole on the vortex configuration for superconducting rings of different sizes. We found that for small rings, only the axially symmetrical situation occurs, i.e. the giant vortex states. For large rings the multivortex state can be stabilized for certain values of the magnetic field. In the next step, we purposely break the axial symmetry by moving the hole away from the center of the superconducting disk over a distance a (see Fig. 5.2).

5.5.1 Small systems

As an example, we consider a superconducting disk with radius $R_o = 2.0\xi$ and thickness $d = 0.005\xi$ with a hole with radius $R_i = 0.5\xi$ moved over a distance $a = 0.6\xi$ in de x-direction. Fig. 5.16 shows the free energy and magnetization (defined through the field expelled from the superconducting ring without the hole) as a function of the magnetic field. The red curve indicates the ground state, while the blue curves indicate the metastable states for increasing and decreasing field. The vertically dotted lines separate the regions with different vorticity L. Notice that hysteresis is only found for the first transition from the $L = 0$ to the $L = 1$ state and not for the higher transitions which are continuous. At the transition from the $L = 1$ state to the $L = 2$ state and further to the $L = 3$ state, the free energy and the magnetization vary smoothly [see Figs. 5.16(a,b)]. In the insets of Fig. 5.16(a), we show the Cooper-pair density for such a sample at magnetic field $H_0/H_{c2} = 0.145$, 1.02, 2.145 and 2.52, respectively, where the ground state is given by a state with $L = 0, 1, 2, 3$ respectively. High Cooper-pair density is given by red regions, while blue regions indicate low Cooper-pair density. For $H_0/H_{c2} = 0.145$, we find a high Cooper-pair density in the entire superconducting ring. There is almost no flux trapped in the circular area with radius smaller than R_o. After

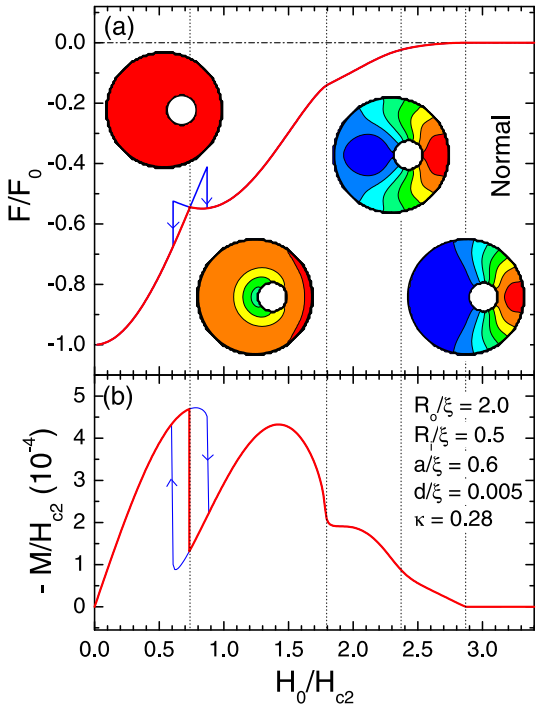

Fig. 5.16 (a) The free energy and (b) magnetization after averaging over the superconducting ring only as function of the applied magnetic field for a superconducting disk with radius $R_o = 2.0\xi$ and thickness $d = 0.005\xi$ with a hole with radius $R_i = 0.5\xi$ moved over a distance $a = 0.6\xi$ in the x-direction. The red curve indicates the ground state, the blue curve the results for increasing and decreasing field. The vertically dotted lines separate the regions with different vorticity L. The insets show the Cooper-pair density at magnetic field $H_0/H_{c2} = 0.145$, 1.02, 2.145 and 2.52, where the ground state is given by a state with $L = 0, 1, 2, 3$ respectively. High (low) Cooper-pair density is given by red (blue) regions.

the first transition at $H_0/H_{c2} \approx 0.75$, suddenly more flux is trapped in the hole which substantially lowers the Cooper-pair density in the superconductor. Notice that the trapped flux tries to restore the circular symmetry in the Cooper-pair density and that the density of the superconducting condensate is largest in the narrowest region of the superconductor. The next inset shows the Cooper-pair density of the $L = 2$ state where an additional vortex appears. Some flux is passing through the hole (i.e. the winding number L is one around the hole), while one flux line is passing through the superconducting ring and a local vortex is created. In the $L = 3$ state superconductivity is destroyed in part of the sample which contains flux with vorticity $L = 2$ and the rest of the flux passes through the hole. Hence, by breaking the circular symmetry of the system, multivortex states are stabilized. Remember that

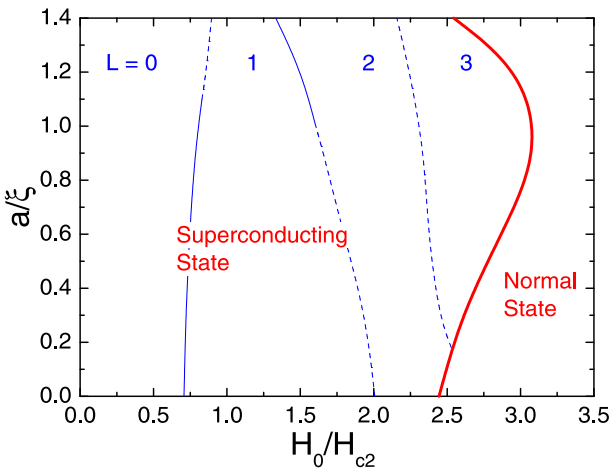

Fig. 5.17 The relation between the displacement a and the transition magnetic fields for a superconducting ring with $R_0/\xi = 2.0$, $d/\xi = 0.005$, $R_i/\xi = 0.5$ and $\kappa = 0.28$. The blue solid curves give the $L \to L+1$ transitions when it corresponds to a first-order phase transition while a dashed curve is used when it is continuous. The red curve is the superconducting/normal transition.

for the corresponding symmetric system, i.e. $a = 0$, only giant vortex states were found.

Having the magnetic fields for the different $L \to L+1$ transitions for superconducting rings with different positions of the hole, i.e. different values of a, we constructed the phase diagram shown in Fig. 5.17. The blue curves (solid curves when the magnetization is discontinuous and dashed curves when the magnetization is continuous) indicate the magnetic field at which the transition from the L state to the $L+1$ state occurs, while the red curve gives the superconducting/normal transition.

5.5.2 Large systems

In order to show that the stabilization of the multivortex state due to an off-center hole is not peculiar for $R_o = 2.0\xi$, we repeated the previous calculation for a larger superconducting disk with radius $R_o = 5.0\xi$ and thickness $d = 0.005\xi$ containing a hole with radius $R_i = 2.0\xi$. In Fig. 5.18(a) the Cooper-pair density is shown for such a system with the hole in the center, while in Fig. 5.18(b) the hole is moved away form the center over a distance $a = 1.0\xi$ in the negative y-direction. The externally applied magnetic field is the same in both cases, $H_0/H_{c2} = 0.77$, which gives vorticity $L = 4$ and $L = 5$ for the ground state of the symmetric and the non-symmetric geometry, respectively. The assignment of the vorticity can be easily checked from Figs. 5.18(c,d) which show contour plots of the corresponding phase of the superconducting

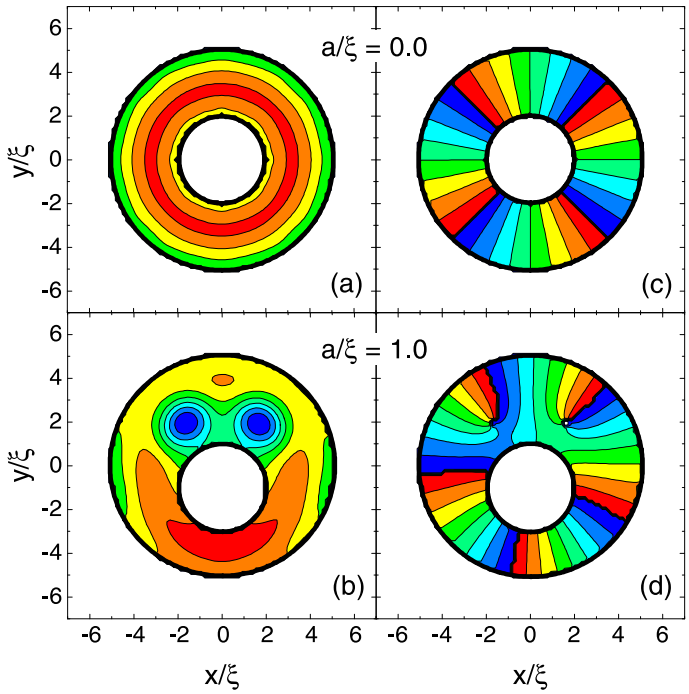

Fig. 5.18 The Cooper-pair density for a superconducting disk with radius $R_o = 5.0\xi$ and thickness $d = 0.005\xi$ with a hole with radius $R_i = 2.0\xi$ (a) in the center, and (b) moved away form the center over a distance $a = 1.0\xi$ in the negative y-direction. The applied magnetic field is the same in both cases: $H_0/H_{c2} = 0.77$. High (low) Cooper-pair density is given by red (blue) regions. The corresponding contour plot of the phase of the order parameter is given in (c) and (d).

wavefunction. If the hole is at the center of the disk, the ground state is a giant vortex state. Moving the center of the hole to the position $(x/\xi, y/\xi) = (0, -1)$, two vortices appear in the superconducting material while the hole contains three vortices. Notice that in this case, although the magnetic field is kept the same and the amount of superconducting material is not altered, changing the symmetry of the system alters the vorticity.

5.6 FLUX QUANTIZATION

Now we will investigate the flux quantization in a small fat ring. Fig. 5.19 shows the flux through the hole (a) and through the superconductor+hole (b) as function of the applied magnetic field H_0 for a superconducting disk with radius $R_o = 2.0\xi$ and thickness $d = 0.1\xi$ with a hole in the center with radius $R_i = 1.0\xi$. The blue curves show the flux for the different L states and the red

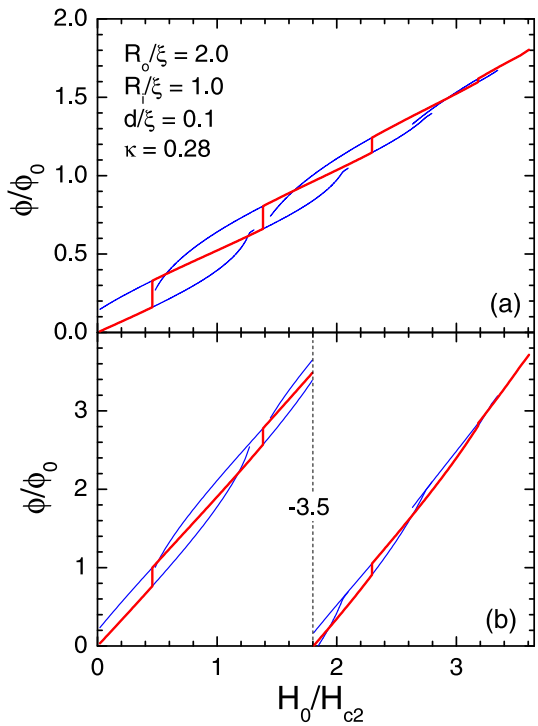

Fig. 5.19 The flux through (a) the hole and (b) the superconductor + the hole as a function of the applied magnetic field H_0 for a superconducting disk with radius $R_o = 2.0\xi$ and thickness $d = 0.1\xi$ with a hole in the center with radius $R_i = 1.0\xi$. The blue curves show the flux for the different L states, the red curve for the ground state.

curve for the ground state. It is apparent that the flux through the hole (or through the superconducting ring + hole) is *not quantized* [see Fig. 5.19(a)]. At $H_0/H_{c2} = 0.4575$ suddenly more flux enters the hole and the ground state changes from the $L = 0$ state to the $L = 1$ state. At this transition also the flux increase through the hole is not equal to one flux quantum ϕ_0. It is generally believed that the flux through a superconducting ring is quantized. But as was shown in Ref. [85] this is even no longer true for hollow cylinders when the penetration length is larger than the thickness of the cylinder wall. The present result is a generalization of this observation to mesoscopic ring structures. Note that for the case of Fig. 5.19 the penetration length is $\lambda/\xi = 0.28$ and the effective penetration length $\Lambda/\xi = 0.78$ is comparable to the width of the ring $(R_o - R_i)/\xi = 1.0$.

For $L > 0$, the superconducting current equals zero at a certain 'effective' radial position $\rho = \rho^*$. It is the flux through the circular area with radius ρ^* which is quantized and not necessarily the flux through the hole of our disk.

Inserting the order parameter $\Psi = |\Psi| \exp(i\varphi)$ into the current operator we obtain

$$\vec{j} = \frac{e\hbar}{m} |\Psi|^2 \left(\vec{\nabla}\varphi - \frac{2e}{\hbar c}\vec{A} \right) , \tag{5.3}$$

which after integration over a closed contour C inside the superconductor leads to

$$\oint_C \left(\frac{mc}{2e^2 |\Psi|^2} \vec{j} + \vec{A} \right) \cdot d\vec{l} = L\phi_0 . \tag{5.4}$$

When the contour C is chosen along a path such that the superconducting current is zero we obtain, using Stokes' theorem, that

$$L\phi_0 = \oint_C \vec{A} \cdot d\vec{l} = \int rot\vec{A} \cdot d\vec{S} = \int \vec{H} \cdot d\vec{S} = \phi , \tag{5.5}$$

which tells us that the flux through the area encircled by C is quantized. In our wide superconducting ring the current is non-zero at the inner boundary of the ring and, consequently, the flux through the hole does not have to be quantized.

To demonstrate that this is indeed true we show in Fig. 5.20(a) the current density as a function of the radial position ρ and in Fig. 5.20(b) the flux through a circular area with radius ρ for a superconducting disk with radius $R_o = 2.0\xi$ and thickness $d = 0.1\xi$ with a hole in the center with radius $R_i = 1.0\xi$ in the presence of an external magnetic field $H_0/H_{c2} = 1.6075$ for the case of three different giant vortex states; i.e. $L = 1, 2, 3$. In the $L = 1$ state, the current density equals zero at a distance $\rho^*/\xi \approx 1.16$ from the center and the flux through an area with this radius is exactly equal to one flux quantum ϕ_0. For $L = 2$ and $L = 3$, the current density j equals zero at $\rho^*/\xi \approx 1.56$ and 1.91, respectively, and the flux through the area with this radius ρ^* is exactly equal to $2\phi_0$ and $3\phi_0$, respectively. We find that ρ^* depends on the external applied magnetic field and on the value of L, contrary to the results of Arutunyan and Zharkov [81, 82] who found that the effective radius ρ^* is approximately equal to the geometric mean square of the inner radius R_i and the outer radius R_o of the cylinder; i.e. $\rho^* = (R_i R_o)^{1/2}$, which for the case of Fig. 5.21(a) would give $\rho^* = 1.41\xi$. The results of Refs. [81, 82] were obtained within the London limit. The dependence of ρ^* as function of the applied magnetic field is shown in Fig. 5.21(a). The blue curves give the ρ^* of the different L states. For increasing magnetic field and fixed L, the value of ρ^* decreases, i.e. the "critical" radius moves towards the inner boundary. The red curve gives ρ^* for the ground state. At the $L \to L+1$ transitions, ρ^* jumps over a considerable distance towards the outside of the superconducting ring, the size of the jumps decreases with increasing L. The dotted lines in the figure give the two boundaries of the superconducting ring: the outer boundary $R_o = 2.0\xi$ and the inner boundary $R_i = 1.0\xi$. Remark that in

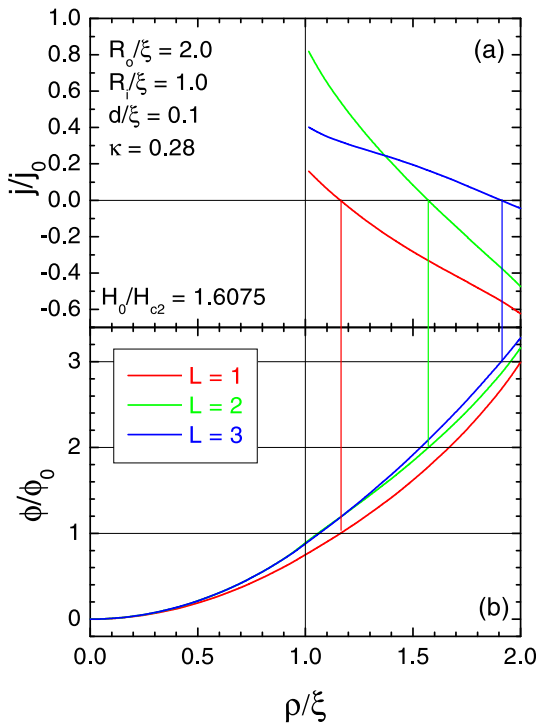

Fig. 5.20 The current density (a) and the flux (b) as a function of the radial position ρ for a superconducting ring with $R_o = 2.0\xi$, $R_i = 1.0\xi$, $d = 0.1\xi$ and $\kappa = 0.28$ for $L = 1$, $L = 2$ and $L = 3$ at an applied magnetic field $H_0/H_{c2} = 1.6075$.

Fig. 5.21 there is no ρ^* given for the $L = 0$ state, because only the external magnetic field has to be compensated so that the current has the same sign everywhere inside the ring and there exists no ρ^*. In Fig. 5.21(b) we repeated this calculation for a hole with radius $R_i = 1.5\xi$ where superconductivity remains to higher magnetic fields and many more $L \to L + 1$ transitions are possible. The result of Refs. [81, 82] gives in this case $\rho^* = 1.73\xi$. Remark that the results for the $L = 1$ and the $L = 2$ states are not connected. The reason is that just before the $L = 1 \to L = 2$ transition the critical current for the $L = 1$ state is strictly positive in the whole ring and hence ρ^* is not defined. Notice that the results in Fig. 5.21(a,b) oscillate around the average value $\rho^* = \sqrt{R_i R_o}$ as given by Refs. [81, 82].

The magnetic field increment ΔH or the flux increase $\Delta\phi = \pi R_o^2 \Delta H$ to induce the $L \to L + 1$ transition is only quantized for narrow rings. This is illustrated in Fig. 5.22 in case of $R_o = 4.0\xi$ for different values of the inner radius. Notice that for $R_i \ll R_o$ we find that $\Delta\phi$ is an oscillating function of L. It is substantially larger than ϕ_0 for small L, it is smaller than ϕ_0 for intermediate L and it approaches ϕ_0 from above for large L. We

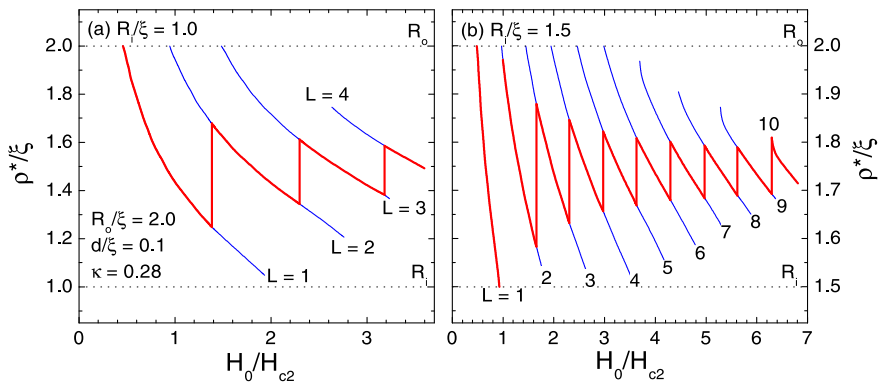

Fig. 5.21 The dependence of the effective radius ρ^* as function of the applied magnetic field for a superconducting disk with radius $R_o = 2.0\xi$ and thickness $d = 0.1\xi$ with a hole in the center with radius $R_i = 1.0\xi$ (a), and $R_i = 1.5\xi$ (b). The blue curves show ρ^* for the different L states and the red curve is for the ground state.

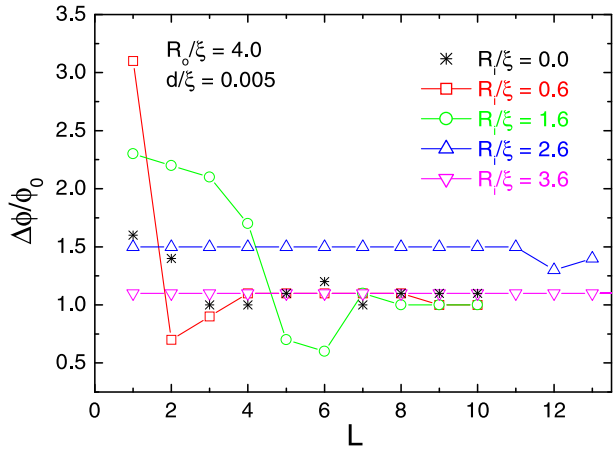

Fig. 5.22 The flux increase $\Delta\phi = \pi R_o^2 \Delta H$ needed to induce the $L \to L+1$ transition for a superconducting ring with $R_o = 4.0\xi$ for different values of the inner radius R_i. The interconnecting lines are a guide to the eye.

found earlier that for $R_i \approx R_o$ the flux through $\rho^* = \sqrt{R_i R_o}$ is quantized in ϕ_0 and therefore we expect $\Delta\phi^* = \pi\left(\rho^*\right)^2 \Delta H = \phi_0$. Our definition of $\Delta\phi$ considers the flux through the superconducting ring + hole which for the condition $\Delta\phi^* = \phi_0$ gives $\Delta\phi/\phi_0 = \Delta\phi/\Delta\phi^* \approx 6.67, 2.5, 1.54$ and 1.11 for $R_i/\xi = 0.6, 1.6, 2.6$ and 3.6, respectively. These results for $R_i/\xi = 2.6$ and 3.6 agree rather well with our numerical results presented in Fig. 5.22; i.e. $\Delta\phi/\phi_0 \approx 1.5$ and 1.1, respectively. The results presented in Fig. 5.22 agree

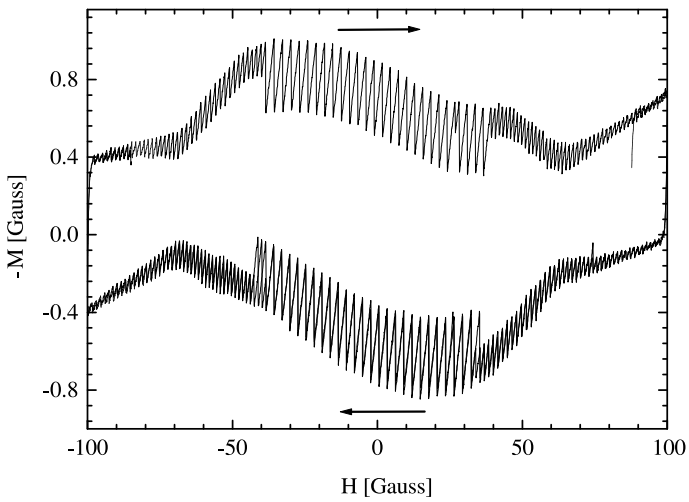

Fig. 5.23 The measured magnetization as a function of the applied magnetic field for a superconducting loop with mean radius $R = 2.16\mu m$ and averaged wire width $w = 314nm$. [From Ref. [32].]

qualitatively with the theoretical results of Bruyndoncx *et al.* [83] who studied rings in a homogeneous magnetic field.

5.7 EXPERIMENTAL RESULTS

Inspired by our work, Pedersen *et al.* [32] investigated experimentally the magnetization of mesoscopic aluminium loops at temperatures well below the superconducting transition temperature T_c. They studied the flux quantization of the superconducting loop with a μ-Hall magnetometer in magnetic field intensities between ± 100Gauss. The experimental configuration is shown in Fig. 1.7. They measured the local magnetization as a function of the applied magnetic field. Fig. 5.23 shows the result for a loop with mean radius $R = 2.16\mu m$ and averaged wire width $w = 314nm$. The measurement was performed at $T = 0.36K$. The curve displays a series of distinct jumps corresponding to the abrupt changes in the magnetization of the superconducting loop.

Compared to Fig. 5.4 they find much more jumps, indicating transitions between different L states. The reason is that in their experiment much larger and narrow rings are considered. The estimated inner and outer radius are $R_i \approx 10.5\xi$ and $R_o \approx 12\xi$. From Fig. 5.4 we can see that increasing the hole radius for fixed outer radius increases drastically the number of jumps and the critical magnetic field. Notice that in Fig 5.4 we plot the ground state magnetization and, therefore, the hysteresis of Fig. 1.7 does not appear. By

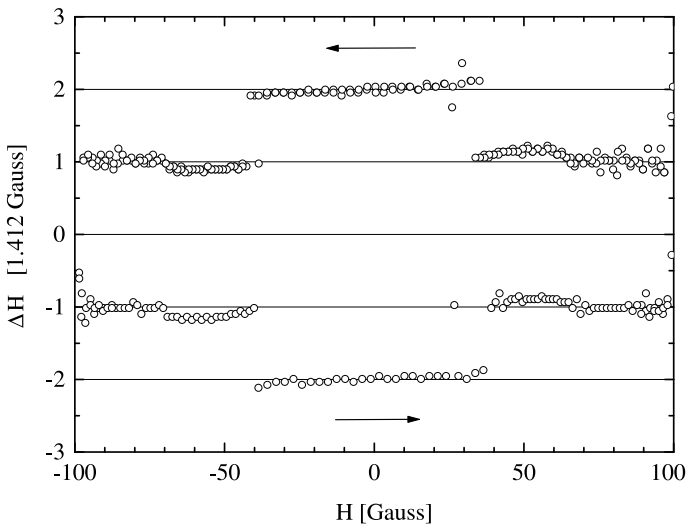

Fig. 5.24 The magnetic field difference between two successive jumps in the magnetization as a function of the applied magentic field for the system of Fig. 5.23. The positive (negative) flux values correspond to the case where H_0 was decreased (increased) during the measurements. [From Ref. [32].]

comparing Fig. 5.5(a) with Fig. 5.13 we found that increasing the ring radius from $R_o = 2.0\xi$ to $R_o = 4.0\xi$ leads to much more transition fields. Since in the experimental setup the radius is $R_o \approx 12\xi$ much more jumps are expected in the magnetization. Unfortunately, we are not able to verify more quantitatively the experimental results because the ring size in our calculations is limited by the number of grid points.

Pedersen *et al.* also studied the magnetic field difference between two successive jumps ΔH, in units of 1.412Gauss, which corresponds to one flux quantum ϕ_0. In Fig. 5.24 this magnetic field increase is plotted as a function of the applied magnetic field for the configuration of Fig. 5.23. It is seen that the magnetic field difference between the observed jumps is, to a high accuracy, given by integer values of 1.412Gauss. At applied magnetic fields lower than 40Gauss double flux jumps dominate, whereas at higher magnetic fields only single flux jumps are observed. The figure shows both an up-sweep and a down-sweep as indicated by the arrows.

From Fig. 5.22 we also concluded that for sufficiently narrow rings the flux increase $\Delta\phi$ to induce the $L \to L+1$ transition is quantized. The experimental results are in good agreement with our theoretical results.

5.8 CONCLUSIONS

In conclusion, we studied the superconducting state of thin superconducting disks with a hole. The effect of the size and the position of the hole on the vortex configuration was investigated. For small superconducting disks with a hole in the center, only giant vortex states exist and for increasing hole radius R_i more and more L states occur before the superconductor becomes normal. For larger superconducting disks with a hole in the center, we found multivortex states in a certain magnetic field range. For certain fixed hole radius, and for increasing magnetic field, the giant vortex state changes into a multivortex state and back into the giant-vortex state (re-entrant behaviour) before superconductivity is destroyed. Near the superconducting/normal transition and for a narrow superconducting ring (i.e. $R_i \approx R_o$) we always found the giant vortex state as the ground state irrespective of the size, thickness and width of the ring. The effect of the position of the hole, i.e. decreasing the symmetry of the system, was also investigated. Moving the hole off-center: 1) can transform the $L \to L+1$ transition into a continuous one, 2) the stability of metastable states is strongly reduced, 3) it favours the multivortex state even for small disks, and 4) the winding number L can increase even at a fixed magnetic field.

The flux through the hole is *not* quantized. We were able to define an effective ring size ρ^* such that inside this ring the flux is exactly quantized. The value of $R_i \leq \rho^* \leq R_o$ depends on L and is an oscillating function of the magnetic field. For narrow rings it is only possible to define such a ρ^* in narrow ranges of the magnetic field and the flux through the hole is very close to the applied flux. The magnetic fields from the screening currents are too small to substantially modify the flux inside the ring. On the other hand, the flux increase $\Delta\phi = \pi R_o^2 \Delta H$ to induce the $L \to L+1$ transition is only quantized for narrow rings.

Experimentally, large and narrow superconducting mesoscopic rings are studied by Pedersen *et al.* [32] using Hall magnetometry. The experimental results were qualitatively in good agreement with our numerical results. They found, for example, that the flux increase to induce the transition from one L state to another is quantized in their large and narrow rings.

Publications. The results presented in this chapter were published as:

- B. J. Baelus, F. M. Peeters, and V. A. Schweigert, *Vortex states in superconducting rings*, Phys. Rev. B **61**, 9734-9747 (2000).

- F. M. Peeters, V. A. Schweigert, B. J. Baelus, and P. S. Deo, *Vortex matter in mesoscopic superconducting disks and rings*, Physica C **332**, 255-262 (2000).

- S. V. Yampolskii, F. M. Peetes, B. J. Baelus, and H. J. Fink, *Effective radius of superconducting rings and hollow cylinders*, Phys. Rev. B **64**, 052504 (2001) *(4 pages)*.

6

Two coupled superconductors

6.1 INTRODUCTION

In the present chapter we want to understand what will happen if two or more mesoscopic superconductors are put close to each other but are electrically isolated. When an uniform magnetic field is applied, it will be locally altered by the single superconductors. In some regions of space the field will be expelled from the single superconducting disk or ring, while in other regions it will be compressed into vortices penetrating the sample or compressed into the inside of a superconducting ring. This results in a strongly nonuniform total field, which is the superposition of the applied field and the field created by the supercurrents. Another superconductor will interact with this nonuniform field. In this way the superconductors are coupled by the magnetic field and they are interacting with each other. This coupling will influence the properties of the two superconductors. It is this coupling that will be studied in the present chapter. Therefore, it is very important that we take into account the finite thickness of the sample and the demagnetization effects, because they will strongly influence the magnetic coupling between the different superconductors.

Recently, Morelle *et al.* [26] studied experimentally the magnetic interaction between two superconducting mesoscopic aluminium rings, close to the superconducting/normal phase transition. In their sample, a smaller ring was placed in the center of a larger ring. Using resistivity measurements the phase boundary was obtained for the two-ring structure as well as for the reference single ring. In both systems, Little-Parks oscillations were observed in the

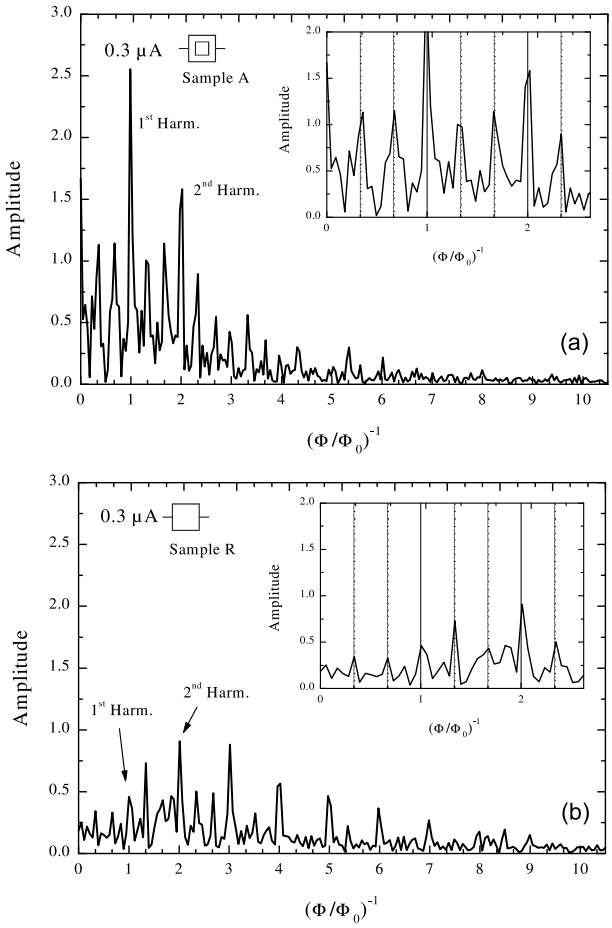

Fig. 6.1 Fourier transform of the phase boundary after substraction of the fitted parabolas within each oscillation period, for a transport current $I_t = 0.3\mu A$ for (a) a double ring configuration and (b) the single outer ring. The inset shows the zoom of the plot for the low frequency region. [from Ref. [26].]

$H - T$ phase diagram. The modification of the $T_c(H)$ oscillations of the outer ring is seen in the Fourier spectrum of the $T_c(H)$ line due to the coupling between the outer and the inner ring [see Fig. 6.1]. They suggested that an inner ring made from a different superconductor with a higher critical temperature would increase the magnetic coupling between the two rings.

We present a theoretical investigation of the properties of two coupled mesoscopic superconductors. Our main attention will go to the interaction between the two superconductors. How are they influencing each other? How do the superconducting properties of a single ring change when another su-

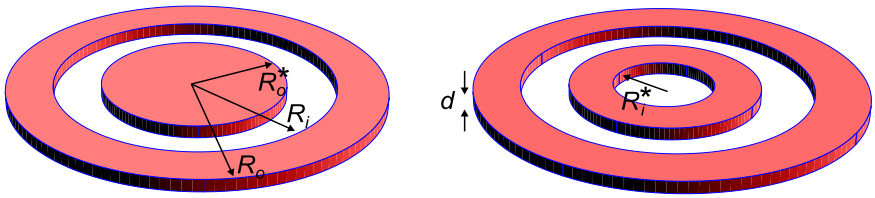

Fig. 6.2 Schematical outline of the considered configurations; the ring-disk configuration (left) and the ring-ring configuration (right).

perconductor is placed in its center? Therefore, we consider two different configurations: (i) a ring-disk configuration, where a small disk is placed in the center of a larger ring (see section 6.3), and (ii) a ring-ring configuration, where a small ring is placed in the center of the larger ring as in the experiment of Ref. [26] (see section 6.4). We will also give an example of a ring-ring system where the inner ring is made from a different superconductor with a higher critical temperature (see section 6.5). Our theoretical analysis is based on a full self-consistent numerical solution of the coupled nonlinear Ginzburg-Landau equations (see section 6.2). Since we consider sufficiently narrow rings and small disks, only axial symmetric giant vortex states will nucleate. Therefore, the equations can be solved for a fixed value of the vorticity. The magnetic field profile outside and inside the superconductor is obtained self-consistently and the full demagnetization effect is included in our approach. In section 6.6 an analytical expression for the magnetic coupling is given for thin rings and extreme type-II superconductors. Finally, in section 6.7 our results are summarized.

6.2 THEORETICAL FORMALISM

We consider a superconducting ring with inner radius R_i, outer radius R_o and thickness d immersed in a insulating medium (for example vacuum). In the center of this ring a superconducting disk with radius R_o^* or another superconducting ring with inner radius R_i^* and outer radius R_o^* is placed with the same thickness (see Fig. 6.2). The whole sample is placed in a perpendicular uniform magnetic field $\overrightarrow{H} = (0, 0, H_0)$. To solve this problem, we expand our previous approach for thin superconducting disks (see section 2.2) to a system of two axial symmetric superconductors each made of a different material.

We consider sufficiently narrow rings and small disks where only axial symmetric giant vortex states will nucleate (see previous chapters). Consequently, the equations can be solved for a fixed value of the angular momentum L_{out} in the outer ring and L_{in} in the inner superconductor that leads to the order

parameter

$$\Psi(\rho,\phi) = f(\rho)e^{iL_{in,out}\phi} \ , \tag{6.1}$$

where $L_{in,out} = L_{out}$ in the outer ring and $L_{in,out} = L_{in}$ in the inner superconductor. Both the vector potential and the superconducting current density are directed along the azimuthal direction $\vec{e}_\phi$. For the system of two coupled axially symmetric superconductors, Eqs. (2.13)-(2.14) can be changed into

$$-\frac{1}{\rho}\frac{\partial}{\partial\rho}\rho\frac{\partial f}{\partial\rho} + \left\langle\left(\frac{L_{in,out}}{\rho} - A\right)^2\right\rangle f = f\left(\frac{\xi_o^2}{\xi_{i,o}^2} - \frac{\kappa_{i,o}^2}{\kappa_o^2}f^2\right) \ , \tag{6.2}$$

and

$$-\kappa_o^2\left(\frac{\partial}{\partial\rho}\frac{1}{\rho}\frac{\partial\rho A}{\partial\rho} + \frac{\partial^2 A}{\partial z^2}\right) = \left(\frac{L_{in,out}}{\rho} - A\right)f^2\theta\left(\frac{2\,|z|}{d}\right) \ , \tag{6.3}$$

where $\xi_{i,o} = \xi_i$, $\kappa_{i,o} = \kappa_i$ in the inner superconductor and $\xi_{i,o} = \xi_o$, $\kappa_{i,o} = \kappa_o$ in the outer ring. $\theta(x) = 1$ for $x < 1$ and $\theta(x) = 0$ for $x > 1$, $\vec{A} = A\vec{e}_\phi$ and $\langle\rangle$ indicates averaging over the sample thickness $\langle f(\vec{r})\rangle = \frac{1}{d}\int_{-d/2}^{+d/2} f(z,\rho)dz$.

Because the superconducting condensates of the inner and outer superconductors are disconnected from each other they can not influence each other directly. The coupling is entirely due to the magnetic field, or equivalently the vector potential. The total magnetic field is a sum of the applied field and the field created by the superconducting currents of the inner and the outer superconductor which is described by Eq. (6.3) where $f(\rho) = f_{in}(\rho) + f_{out}(\rho)$ and $f_{in}(\rho)$ $[f_{out}(\rho)]$ is only different from zero in the interval $R_i^* < \rho < R_o^*$ $[R_i < \rho < R_o]$.

The boundary conditions (2.18) for the order parameter can be written as

$$\left.\frac{\partial f}{\partial\rho}\right|_{\rho=R_1^*,R_2^*,R_1,R_2} = 0 \ , \tag{6.4}$$

for the ring-ring configuration, and

$$\left.\frac{\partial f}{\partial\rho}\right|_{\rho=R_2^*,R_1,R_2} = 0 \ , \quad \rho\left.\frac{\partial f}{\partial\rho}\right|_{\rho=0} = 0 \ , \tag{6.5}$$

for the ring-disk configuration. The condition for the vector potential is still given by Eqs. (2.15)-(2.16):

$$A(z,\rho = R_s) = \frac{1}{2}H_0R_s \ , \quad A(|z| = d_s,\rho) = \frac{1}{2}H_0\rho \ . \tag{6.6}$$

For the system of two coupled axially symmetric superconductors the finite difference representation of the Ginzburg-Landau equations, Eqs. (2.20)-

(2.21), can be written as:

$$\eta_f f_n^k - \frac{2}{\rho_{n+1/2}^2 - \rho_{n-1/2}^2}\left(\rho_{n+1/2}\frac{f_{n+1}^k - f_n^k}{\rho_{n+1} - \rho_n} - \rho_{n-1/2}\frac{f_n^k - f_{n-1}^k}{\rho_n - \rho_{n-1}}\right)$$
$$+\left\langle\left(\frac{L_{in,out}}{\rho} - A\right)^2\right\rangle_n f_n^k - \frac{\xi_o^2}{\xi_{i,o}^2} f_n^k + 3\frac{\kappa_{i,o}^2}{\kappa_o^2}\left(f_n^{k-1}\right)^2 f_n^k$$
$$= \eta_f f_n^{k-1} + 2\frac{\kappa_{i,o}^2}{\kappa_o^2}\left(f_n^{k-1}\right)^3 , \tag{6.7}$$

and

$$-\frac{2\kappa_o^2}{\rho_{n+1/2} - \rho_{n-1/2}}\left(\frac{\rho_{n+1}A_{m,n+1}^k - \rho_n A_{m,n}^k}{\rho_{n+1}^2 - \rho_n^2} - \frac{\rho_n A_{m,n}^k - \rho_{n-1}A_{m,n-1}^k}{\rho_n^2 - \rho_{n-1}^2}\right)$$
$$-\frac{2\kappa_o^2}{z_{m+1/2} - z_{m-1/2}}\left(\frac{A_{m+1,n}^k - A_{m,n}^k}{z_{m+1} - z_m} - \frac{A_{m,n}^k - A_{m-1,n}^k}{z_m - z_{m-1}}\right)$$
$$-\left(\frac{L_{in,out}}{\rho_n} - A_{m,n}^k\right)\left(f_n^k\right)^2 + \eta_a A_{m,n}^k = \eta_a A_{m,n}^{k-1} , \tag{6.8}$$

where $A_{m,n} = A(z_m, \rho_n)$, $f_n = f(\rho_n)$, $\rho_{n+1/2} = (\rho_{n+1} + \rho_n)/2$ and $z_{m+1/2} = (z_{m+1} + z_m)/2$. The upper index k denotes the iteration step.

6.3 RING-DISK CONFIGURATION

First, we consider a superconducting ring with a superconducting disk in the center. We investigate the influence of the disk on the properties of the ring. As an example, we take a ring with inner radius $R_i = 1.5\xi$ and outer radius $R_o = 2.0\xi$ and a disk in the center with radius $R_o^* = 1.0\xi$. Both superconductors have the same thickness, $d = 0.15\xi$, and the Ginzburg-Landau parameter was taken to be $\kappa = 0.28$, which is a typical value for mesoscopic Al superconductors [2, 28].

6.3.1 Free energy

Fig. 6.3(a) shows the free energy for the considered system as a function of the applied magnetic field. First we considered the uncoupled system and calculated the free energy for the disk in the center and the free energy for the different giant vortex states in the outer ring. The results for single rings and disks were exhaustively described in previous chapters. Notice that, in this chapter, the free energy is expressed in units of $F_0 = H_c^2 V/8\pi$, where V is the sum of the disk and the ring volume. This is the reason why the free energy of the disk and the ring are not equal to $-F_0$ at zero magnetic field as it was in chapters 2 and 5. The size of the disk is such that only

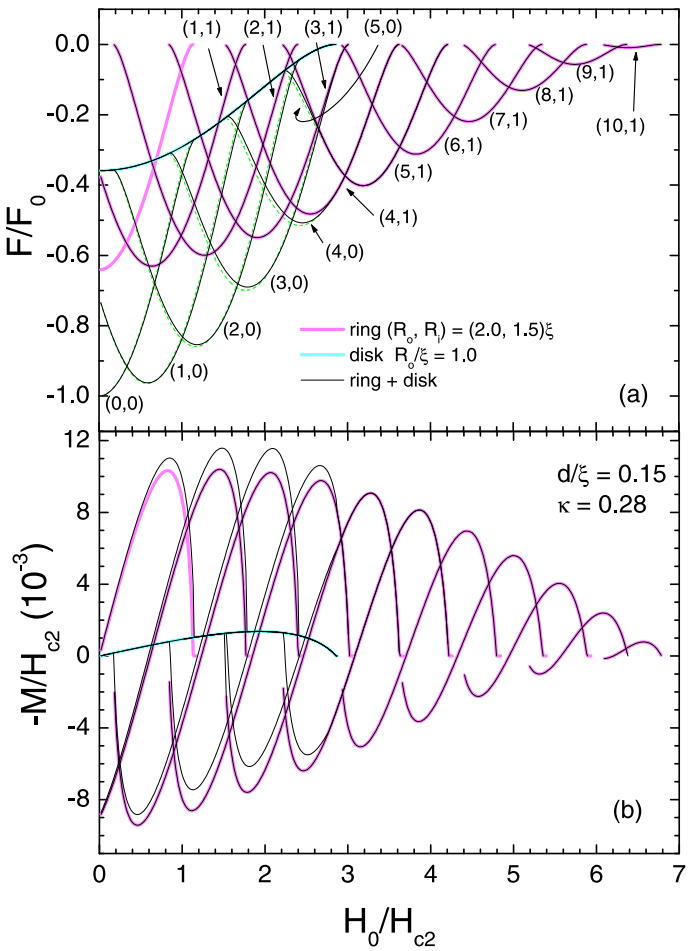

Fig. 6.3 (a) The free energy and (b) the expelled field as a function of the applied field for a ring with inner radius $R_i = 1.5\xi$ and outer radius $R_o = 2.0\xi$ (light magenta curves), for a disk in its center with radius $R_o^* = 1.0\xi$ (light cyan curves) and for the coupled ring-dot configuration (black curves). All superconductors have the same thickness $d = 0.15\xi$, and $\kappa = 0.28$. The green dashed curves give the sum of the free energies of the single disk and the single ring.

the Meissner state, i.e. the $L_{in} = 0$ state, can nucleate. At applied magnetic fields $H_0/H_{c2} \gtrsim 2.9$ the disk is in the normal state, which results in $F = 0$. In the single ring, on the other hand, different giant vortex states with vorticity $L_{out} = 0$ up to $L_{out} = 10$ can nucleate before the ring becomes normal at $H_0/H_{c2} \approx 6.8$. Next, we introduced the magnetic coupling between the disk and the ring and the results are given by the black curves in Fig. 6.3(a). The different axial symmetric states are determined by the vorticity of the

disk L_{in} and the total vorticity L_{out}, which is equal to the vorticity of the ring. Therefore, we characterize the states by (L_{out}, L_{in}). For the considered configuration, we find states with $L_{in} = 0$ and $L_{out} = 0$ up to $L_{out} = 5$. We also find states with $L_{in} = 1$ and $L_{out} = 0$ up to $L_{out} = 10$, which equal the giant vortex states of the single ring, because the disk is now in the normal state. Notice further that we could also write $(6, 0)$ instead of $(6, 1)$ because for the applied magnetic fields where the $L_{out} = 6$ state in the ring exists the disk is normal even for $L_{in} = 0$. We have chosen to write $L_{in} = 1$ because this expresses more clearly that there is flux going through the disk. If both the disk and the ring are superconducting, the free energy of the total sample is different from the sum of the free energies of the single disk and the single ring.

6.3.2 Cooper-pair density, magnetic field distribution and current density

To investigate these new states in more detail we consider as an example the $(2, 0)$ state. Figs. 6.4(a-c) show the magnetic field distribution, the current density and the Cooper-pair density, respectively, as a function of the radial position for five different applied magnetic fields, i.e., $H_0/H_{c2} = 0.1$, 0.5, 1.5, 2.0, and 2.5. Near $H_0/H_{c2} = 0$ the $(2, 0)$ state equals the $L_{in} = 0$ state of the disk and the ring is in the normal state. The reason is that the applied field is so low that a lot of magnetic flux has to be attracted to create a state with $L_{out} = 2$ in the outer ring. Therefore, a very high superconducting current has to flow through the outer ring which leads to the destruction of superconductivity in this ring. The red curves in Figs. 6.4(a-c) show that the Cooper-pair density and the current density are indeed zero in the ring. The magnetic field distribution shows the flux expulsion from the disk. Inside the disk the field decreases and at the edge there is a peak which illustrates a higher concentration of field because of the demagnetization effects. With increasing external field less flux has to be attracted and the current in the outer ring decreases. At $H_0/H_{c2} \approx 0.17$ superconductivity is restored in the external ring [see the green curves in Fig. 6.4(c)]. The green curves in Fig. 6.4(b) show that the current in the outer ring flows in the opposite direction than the current in the disk. The superconducting currents in the disk expel the flux, while the currents in the ring are attracting flux, which is compressed in the region between the disk and the ring [see the green curve in Fig. 6.4(a)]. The free energy becomes now more negative as compared to the free energy of the single disk [see Fig. 6.3(a)]. Increasing the magnetic field further leads to less attraction of flux and, hence, to a higher Cooper-pair density in the ring and a more negative free energy. When the external flux becomes comparable with the flux needed for the $L_{out} = 2$ state, the outer part of the ring expels the flux to the outside, while the inner part of the ring still expels flux to the hole region. Therefore, the superconducting current changes sign in the

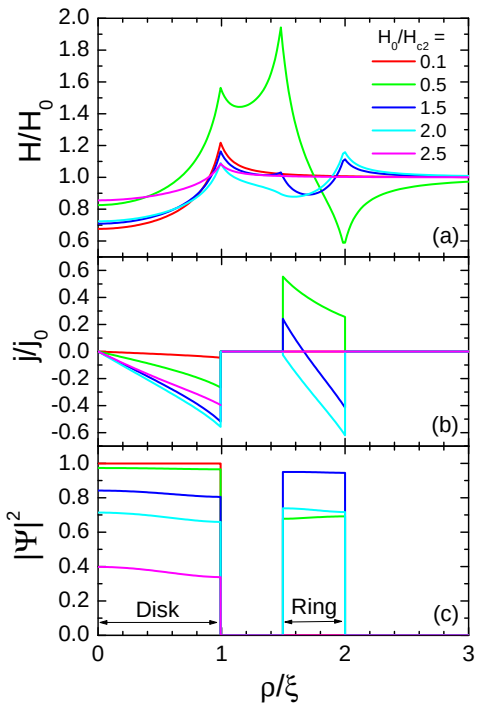

Fig. 6.4 (a) The magnetic field distribution, (b) the current density and (c) the Cooper-pair density in the plane of the superconductors as a function of the radial position for the $(L_{out}, L_{in}) = (2, 0)$ state of the ring-dot configuration of Fig. 6.3 at $H_0/H_{c2} = 0.1$, 0.5, 1.5, 2.0, and 2.5.

ring region [see the blue curve in Fig. 6.4(b)]. Since the flux is expelled in both directions, the blue curve in Fig. 6.4(a) shows a positive peak at both ring boundaries. Further increasing the external field leads to external fluxes larger than the flux needed for the $L_{out} = 2$ state and, hence, the ring has to expel flux in order to keep vorticity $L_{out} = 2$. As a consequence, the current in the ring has to flow in the same direction as the current in the disk, which is shown by the cyan curve in Fig. 6.4(b). Because of the expulsion, the field between the two superconductors is lower than the external field [see the cyan curve in Fig. 6.4(a)]. If we further increase the magnetic field, the superconducting currents in the outer ring have to increase in order to expel more flux and consequently the Cooper-pair density decreases in the outer ring. At $H_0/H_{c2} \approx 2.4$ the supercurrent becomes too high and the ring becomes normal again [see the magenta curves in Figs. 6.4(a-c)]. At this field, the free energy equals the free energy of the single disk.

6.3.3 Interaction between the disk and the ring

The above discussion shows clearly the interplay between the superconducting state of the disk and the ring. Next, we investigate the interaction between the disk and the ring. Therefore, we added the sum of the free energies of the single disk and the single ring [green dashed curves in Fig. 6.3(a)] and compare this result with the result of the ring-disk configuration [black curves in Fig. 6.3(a)]. Notice that there is a small difference between the two set of curves, which is due to the coupling between the two superconductors. Below we will show that this difference becomes more pronounced for thicker samples.

Now, we will determine the attraction or expulsion of the magnetic field by the coupled superconducting system. Fig. 6.3(b) shows the magnetic field expelled from the sample, $-M$, as a function of the applied magnetic field:

$$M = \frac{\langle H \rangle - H_0}{4\pi} ,$$

where $\langle H \rangle$ is the magnetic field averaged over the area $\rho < R_o$, i.e. the outer radius of the ring and H_0 is the applied field. The cyan and magenta curves are the results for the single disk and the single ring and the black curves for the total ring-disk system. By putting a disk in the center of the ring, more field is expelled and less field is attracted. Of course, for $H_0/H_{c2} \gtrsim 2.9$ the disk is in the normal state and we recover the result for the single ring case.

6.4 RING-RING CONFIGURATION

In this section we replace the disk in the center by a second ring and the influence of this inner ring on the outer ring will be investigated. As an example for this ring-ring configuration, we consider a superconducting ring with inner radius $R_i = 1.5\xi$ and outer radius $R_o = 2.0\xi$ and a second ring in the center with inner radius $R_i^* = 0.6\xi$ and outer radius $R_o^* = 1.1\xi$. Both rings have the same thickness, $d = 0.15\xi$ and the same Ginzburg-Landau parameter $\kappa = 0.28$.

6.4.1 Free energy

Fig. 6.5 shows the free energy as a function of the applied magnetic field for the small single ring by cyan curves, for the larger single ring by magenta curves and for the coupled ring-ring situation by the thin black curves. In the inner ring superconducting states can nucleate with vorticity $L_{in} = 0$, 1 and 2 and the superconducting/normal transition field is at $H_0/H_{c2} \approx 6.4$. In the outer ring states with vorticity $L_{out} = 0$ up to $L_{out} = 10$ exist and superconductivity is destroyed at $H_0/H_{c2} \approx 6.75$. The superconducting states nucleating in the double ring system can be characterized again by the indices

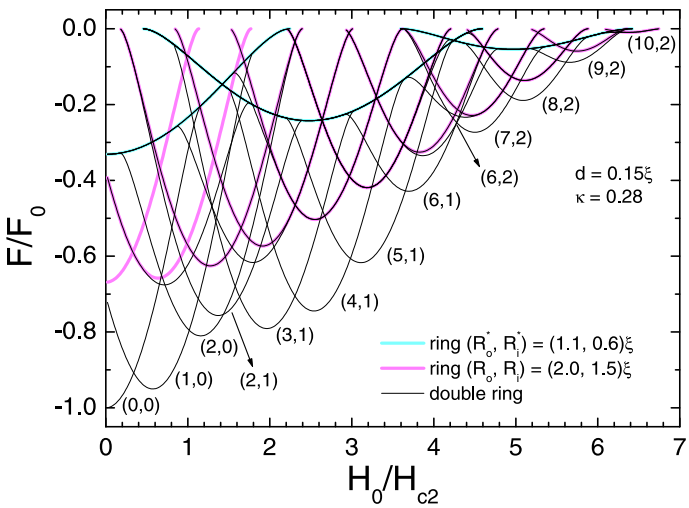

Fig. 6.5 The free energy as a function of the applied magnetic field for a superconducting ring with radii $R_i = 1.5\xi$ and $R_o = 2.0\xi$ (light magenta curves), a ring with $R_i^* = 0.6\xi$ and $R_o^* = 1.1\xi$ (light cyan curves) and the double ring configuration (black curves). Both rings have the same thickness, $d = 0.15\xi$, and $\kappa = 0.28$. The indices indicate the ground state vorticities (L_{out}, L_{in}).

(L_{out}, L_{in}). For $L_{in} = 0$, superconducting states can nucleate with $L_{out} = 0$ up to 4, for $L_{in} = 1$ with $L_{out} = 1$ up to $L_{out} = 8$, and for $L_{in} = 2$ with $L_{out} = 5$ up to 10. For $L_{in} \geqslant 3$ the states equal the states of the single outer ring because the inner ring will be normal.

The indices in the figure correspond to the ground state of the double ring system. For the numerical example studied in the previous section the number and the position of the ground state transitions are the same as for the outer ring. In the present two ring system this is no longer the case and the number of transitions in the coupled system are larger than for the single outer ring case. The inner ring induces extra transitions in the coupled system each time when the vorticity of the inner ring changes with one unit. The first extra transition is the transition from $(2,0)$ to $(2,1)$ and the second one is the transition from $(6,1)$ to $(6,2)$. The $(2,1)$ state is the ground state in the magnetic field region $1.43 \lesssim H_0/H_{c2} \lesssim 1.63$ and the $(6,2)$ state in the region $4.27 \lesssim H_0/H_{c2} \lesssim 4.28$. Hence, by putting a ring in the center of the larger ring, the ground state shows extra transitions. This result corresponds to the experimental result of Morelle *et al.* [26], who saw modifications of the $T_c(H)$ oscillations of the outer ring in the Fourier spectrum of the $T_c(H)$ line due to the coupling between the outer and the inner ring (see also Fig. 6.1).

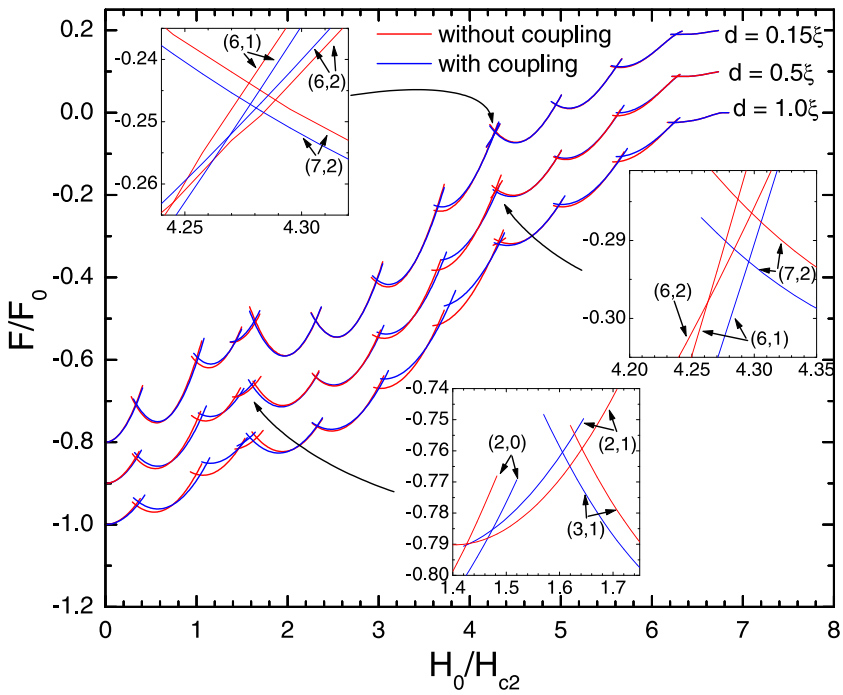

Fig. 6.6 The ground state free energy of the double ring configuration of Fig. 6.5 (blue curves) and the sum of the free energies of the two rings (red curves) for $d = 0.15\xi$ (upper curves, shifted by $+0.2$), for $d = 0.5\xi$ (middle curves, shifted by $+0.1$) and for $d = 1.0\xi$ (lower curves). The insets show some of the crossings in more detail.

6.4.2 Interaction between the two rings

To investigate the interaction between the inner ring and the outer ring, we plot in Fig. 6.6 the ground state free energy of the coupled rings (blue curves) and the sum of the free energies of the two single rings (red curves) for the previous configuration (upper curves which are shifted by $+0.2$), i.e. $d = 0.15\xi$, and for a thicker samples with $d = 0.5\xi$ (middle curves, shifted by $+0.1$) and with $d = 1.0\xi$ (lower curves). For $d = 0.15\xi$ the difference is most pronounced for the $(2,0)$, the $(5,1)$ and the $(6,1)$ state. Both the value of the free energy and the transition magnetic fields are influenced by the interaction between the two rings. The upper inset shows the $(6,1) \to (6,2) \to (7,2)$ transition in more detail. Notice that the interaction significantly decreases the magnetic field region where the $(6,2)$ state is the ground state. For $d = 0.5\xi$ and 1.0ξ the demagnetization effects become more important and therefore the interaction between the two rings gains importance too. This results in a larger difference between the red and blue curves. The value of the free energy and the transition fields are changing considerably by the fact that both rings are

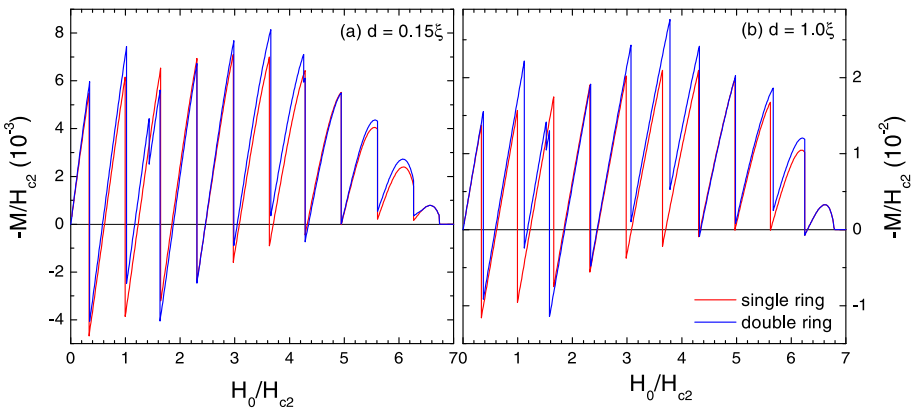

Fig. 6.7 The magnetic field expelled from the sample, $-M$, as a function of the applied magnetic field for the single outer ring (red curve) and for the double ring configuration (blue curve). The sample is the same as in Fig. 6.5 with thickness $d = 0.15\xi$ (a) and $d = 1.0\xi$ (b).

influencing each other. The two lower insets show the $(2,0) \to (2,1) \to (3,1)$ and the $(6,1) \to (7,2)$ transitions in more detail for $d = 0.5\xi$. The magnetic field region where the ground state is given by the $(2,1)$ state decreases due to the interaction. For the $(6,1) \to (7,2)$ transition coupling between the two rings leads to the interesting result that the $(6,2)$ state is no longer a ground state.

6.4.3 Magnetization and transition fields

Figs. 6.7(a,b) shows the magnetic field expelled from the sample, $-M$, as a function of the applied magnetic field for the single outer ring (red curve) and for the double ring configuration (blue curve) for thickness $d = 0.15\xi$ and $d = 1.0\xi$ respectively. For $d = 0.15\xi$, the two extra transitions, resulting from the influence of the inner ring, are clearly visible by the jumps at $H_0/H_{c2} = 1.43$ and 4.28. Notice further that for some L states the expulsion of the field and for other L states the attraction becomes more pronounced by putting the inner ring in the center of the outer ring. For $d = 1.0\xi$ one extra transition results from the influence of the inner ring, i.e. at $H_0/H_{c2} = 1.58$. The difference between the transition fields of the single ring and the coupled ring system becomes larger [see also the lower curve in Fig. 6.6] and the expulsion or attraction becomes more pronounced with increasing the sample thickness, which indicates again that the interaction between the two rings increases with increasing d.

In Figs. 6.8(a,b) the magnetic field range, ΔH_0, over which the (L_{out}, L_{in}) state is the ground state, is plotted as a function of L_{out} for thickness $d = 0.15\xi$ and $d = 1.0\xi$ respectively. This magnetic field range corresponds to the

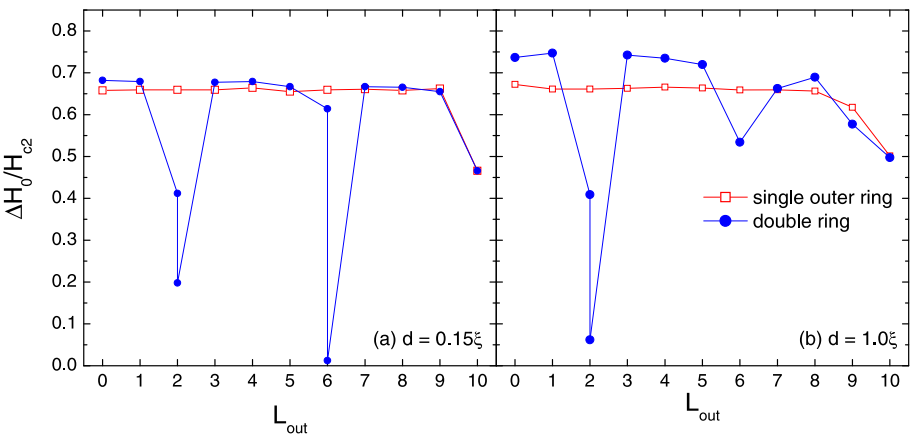

Fig. 6.8 The magnetic field range, ΔH_0, over which the (L_{out}, L_{in}) state is the ground state, as a function of L_{out} for the single outer ring (red squares) and for the double ring system (blue circles). The sample is the same as in Fig. 6.7 with thickness $d = 0.15\xi$ (a) and $d = 1.0\xi$ (b).

distance between two consecutive jumps in the expelled field [see Fig. 6.7]. The results for the single outer ring are given by the red squares and for the double ring system by the blue circles. The curves are guides to the eye. For $d = 0.15\xi$ the extra transitions are clearly visible at $L_{out} = 2$ and 6 and for $d = 1.0\xi$ at $L_{out} = 2$ where for the same L_{out} two jumps occur due to a transition of the inner ring. Also for the other vorticities L_{out}, there is a difference between ΔH_0 for the single ring and the double ring. The reason is that the ground state transition fields are influenced by the interaction between the two rings. This was also visible in Fig. 6.7. If the free energy of the double ring was just the sum of the free energies of the two single rings, ΔH_0 would be the same for the single outer ring and the double ring, except for $L_{out} = 2$ and 6, where extra transitions occur because L_{in} changes with one unit. Notice further that the difference between the results for the single outer ring and the double ring enhances with increasing sample thickness.

6.4.4 Current density

We investigate the effect of the interaction between the two rings on the superconducting current density in the rings for $d = 0.15\xi$. Figs. 6.9(a,b) show the averaged current density for the ground state in the inner ring and the outer ring, respectively, as a function of the applied magnetic field. The results for the single ring are given by red curves, these for the double ring configuration by blue curves. First, we describe what happens if there is no interaction between the two rings. In this case we can consider them as two single rings. At low fields, the ground state of a single ring is given by the

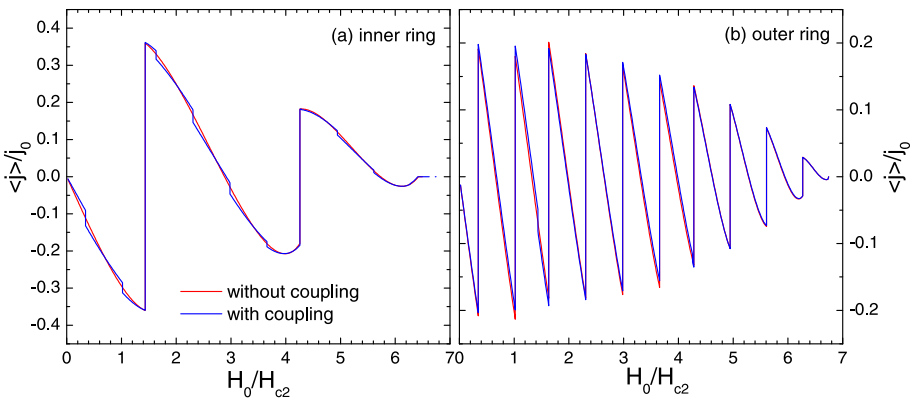

Fig. 6.9 The averaged current density for the ground state in the inner ring (a) and the outer ring (b) as a function of the applied magnetic field for the same double ring configuration as in Fig. 6.5. The results for the single rings are given by red curves, these for the double ring configuration by blue curves.

$L = 0$ state or Meissner state and the ring expels the field to the outside of the sample. With increasing external field, more flux has to be expelled from the ring which leads to a higher current density. After the first transition the ground state is given by the $L = 1$ state and initially flux will be trapped in the ring and the flux going through the ring is larger than the flux of the external field. To compress this extra magnetic field, the superconducting current in the ring has to flow in the opposite direction. At the transition, the current shows a jump from a negative to a positive value, i.e. from expulsion to compression. With increasing external field, less flux has to be compressed to achieve vorticity one and the current density in the outer ring decreases. Further increasing the field, the external flux becomes larger than the flux needed for $L = 1$ and flux has to be expelled. Therefore, the current in the ring changes sign. Without interaction between the two rings, the current density in one ring exhibits only jumps when the vorticity of the ground state of this ring changes [see red curves in Figs. 6.9(a,b)].

In the coupled two rings situation $\langle j \rangle$ shows small jumps on top of the previously described expulsion $\rightarrow$ compression jumps. At low fields, the ground state is given by the $(0,0)$ state or Meissner state. Both rings expel the field to the outside of the sample, which means that the current flows in the same direction in each ring. Since some flux is already expelled by the outer ring, the inner ring has to expel less and therefore the current is less negative. After the first transition the groundstate changes into the $(1,0)$ state. Now, the outer ring compresses the field to achieve vorticity one, and, as a consequence, the field in the hole of the outer ring is larger than the external field. This means that the inner ring has to expel more field and the current density jumps to a value more negative than its value without interaction. The other

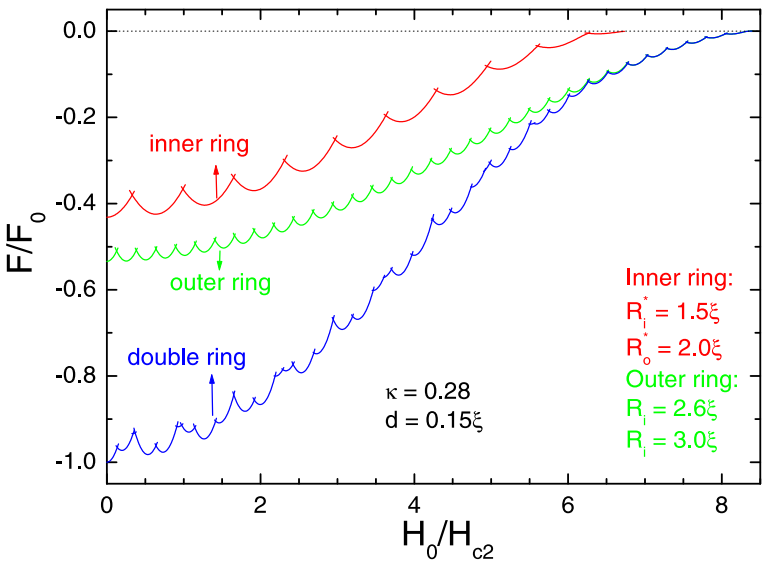

Fig. 6.10 The ground state free energy for a single inner ring with radii $R_o^* = 2.0\xi$ and $R_i^* = 1.5\xi$, for a single outer ring with radii $R_o = 3.0\xi$ and $R_i = 2.6\xi$ and for the double ring configuration, i.e. the combination of these two rings. The sample thickness is $d = 0.15\xi$ and the Ginzburg-Landau parameter $\kappa = 0.28$.

transitions can be explained analogously. From Figs. 6.9(a,b) it is clear that the two rings are influencing each other and that the interaction between the two rings results in extra jumps in the current density in one ring when the vorticity of the other ring changes. These jumps are smaller than the jumps when the vorticity of the considered ring increases, but they are not negligible.

6.4.5 Larger systems

Up to now, we considered rather small samples. For the single ring it is known that by increasing the sample size (i) more L states are possible and (ii) the magnetic field range over which the state with vorticity L is the ground state decreases (see chapter 5). Therefore, for a larger radius of the double ring configuration, we expect many more ground state transitions. Fig. 6.10 shows the ground state free energy for a single inner ring with radii $R_o^* = 2.0\xi$ and $R_i^* = 1.5\xi$, for a single outer ring with radii $R_o = 3.0\xi$ and $R_i = 2.6\xi$ and for the coupled ring-ring configuration. The sample thickness is $d = 0.15\xi$ and the Ginzburg-Landau parameter $\kappa = 0.28$. For the single inner ring, the ground state changes from vorticity $L_{in} = 0$ up to $L_{in} = 10$ and the superconducting/normal transition field is at $H_0/H_{c2} = 6.73$. For the single outer ring the ground state changes from vorticity $L_{out} = 0$ up to $L_{out} = 32$ and superconductivity is destroyed at $H_0/H_{c2} = 8.40$. By comparing the free

energy of the double ring with the one of the outer ring, we notice that there are many more ground state transitions as a consequence of the transitions in the inner ring. For the single ring the minimum in the free energy of the $L+1$ state is always less negative than the one of the L state. Due to the interaction between the two rings, this is no longer always the case for the double ring configuration. At $H_0/H_{c2} > 6.73$ the free energy of the double ring configuration equals the one of the outer ring since the inner ring is in the normal state.

6.5 TWO COUPLED RINGS OF DIFFERENT MATERIALS

Until now, we considered always two superconductors made of the same material. This means that both superconductors have the same coherence length, penetration depth and critical temperature, i.e. $\xi_i = \xi_o$, $\lambda_i = \lambda_o$, and $T_{c,i} = T_{c,o}$. Since both rings have the same width and the radius of the inner ring is smaller than the one of the outer ring, the inner ring becomes normal at a smaller field than the outer ring. As a consequence, no effect of the magnetic coupling can be observed in the $H-T$ phase diagram. To circumvent this problem the T_c of the outer ring was artificially lowered in the experiment of Ref. [26] by applying a sufficiently large external current through the outer ring. An alternative approach will be followed in the present section where we take the inner ring of a different material such that it has a higher critical temperature than the outer ring, and also a different coherence length and penetration depth, which leads to a different Ginzburg-Landau parameter.

As an example, we take for the outer ring the values used by Geim *et al.* [2] for Al, i.e. $\xi_o\,(T=0) = 250nm$, $\lambda_o\,(T=0) = 70nm$ and thus $\kappa_o = 0.28$, resulting in a critical temperature $T_{c,o}(H=0) = 1.3K$. For the inner ring, we assume a higher critical temperature $T_{c,i} = 1.2T_{c,o} = 1.56K$, and $\xi_i\,(T=0) = 160nm$, $\lambda_i\,(T=0) = 80nm$ and thus $\kappa_i = 0.5$. For the radii of the outer ring we take as an example $R_i = 375nm$, $R_o = 500nm$, and for the inner ring $R_i^* = 125nm$ and $R_o^* = 250nm$. The $H-T$ phase diagram is shown in Fig. 6.11 for the uncoupled situation for the inner ring (cyan curves) and for the outer ring (magenta curves) and the coupled double ring situation (black curve). At $T=0$ the outer ring has a much higher critical field ($H_{nuc}/H_{c2,o} = 6.74$) than the inner ring ($H_{nuc}/H_{c2,o} = 4.34$). Therefore, the superconducting/normal transition of the double ring configuration equals the one of the outer ring for low temperatures. With increasing temperature, the nucleation field of the outer ring, i.e. the one of the double ring system, changes more quickly than the one of the inner ring. The oscillations are the well known Little-Parks oscillations. At $T/T_{c,o} = 0.912$ both single rings have the same transition field $H_{nuc}/H_{c2,o} = 1.91$. At higher temperatures, the superconducting/normal transition is determined by the inner ring.

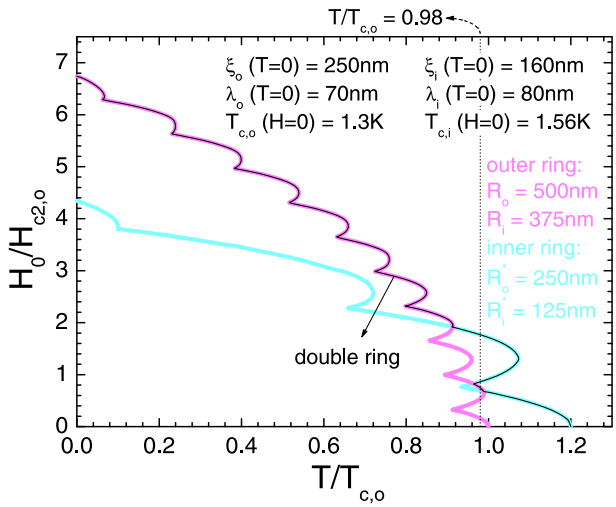

Fig. 6.11 The $H-T$ phase diagram for the inner ring (light cyan curves), the outer ring (light magenta curves) and the double ring configuration (black curves). The material parameters and the sizes of both rings are different and are given in the figure.

The situation where the critical field of the outer ring is larger than the one of the inner ring is exhaustively described in the previous sections. In Fig. 6.12 we show the free energy for the configuration of Fig. 6.11 at $T = 0.98T_{c,o}$ where the superconductivity of the inner ring exists at larger fields than the one of the outer ring. The free energy of the superconducting states of the inner ring are given by the cyan curves, the states of the outer ring by the magenta curves and the double ring configuration by the black curves. Both in the inner and the outer ring, superconducting states with vorticity $L = 0$ and $L = 1$ exist. At $T = 0.98T_{c,o}$, the critical fields of the inner and the outer ring are $H_0/H_{c2,o} = 1.77$ and 0.69, respectively. Notice that in both rings the free energies of the $L = 0$ state and the $L = 1$ state do not cross, which means that with increasing field the ground state changes from the Meissner state into the normal state and, with further increasing the field, into the $L = 1$ state and back into the normal state. The reason is that near T_c the superconductivity of the ring has decreased. This means that only rather small currents can be induced and thus only a small flux can be attracted or expelled by the ring. In the region between the existence of the $L = 0$ state and the $L = 1$ state the currents, which have to be induced to expel or attract the necessary flux to achieve vorticity $L = 0$ and $L = 1$, are too high. With increasing temperature, the $L = 1$ state can not nucleate anymore and the superconducting/normal transition jumps to the field where the $L = 0$ state is destroyed. The corresponding oscillations in the $H-T$ phase diagram [see Fig. 6.11] are the Little-Parks oscillations. For

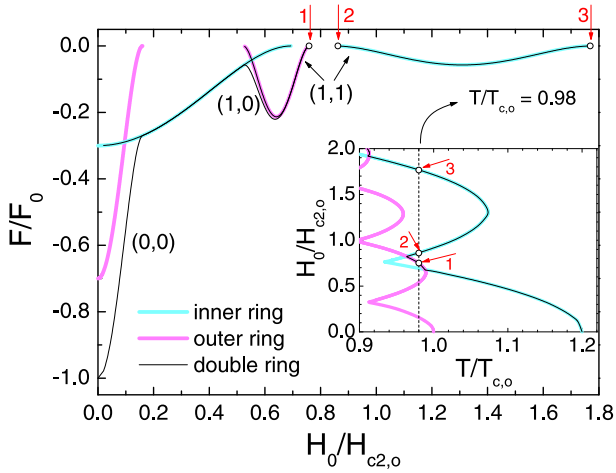

Fig. 6.12 The free energy as a function of the applied magnetic field for the inner ring (light cyan curves), the outer ring (light magenta curves) and the double ring configuration (black curves) for the system of Fig. 6.11 at $T = 0.98T_{c,o}$.

the double ring configuration the $(0,0)$, the $(1,0)$ and the $(1,1)$ state can nucleate. The $(1,1)$ state is split into two parts corresponding to the $L = 1$ states in the two single rings with an intermediate magnetic field region in which both superconductors are normal. The ground state changes from the Meissner state $(0,0)$ into the $(1,0)$ state at $H_0/H_{c2,o} \approx 0.53$, which equals the $(1,1)$ state at $H_0/H_{c2,o} > 0.69$. Further increasing the field the ground state changes into the normal state at $H_0/H_{c2,o} \approx 0.76$, then back into the $(1,1)$ state at $H_0/H_{c2,o} \approx 0.86$ and further back into the normal state at $H_0/H_{c2,o} \approx 1.77$. Compared to the uncoupled inner ring and the outer ring situation, extra ground state transitions occur for the double ring case with interesting re-entrant superconducting behavior and a switching on and off of the superconducting state in the inner and outer ring.

6.6 TWO COUPLED THIN RINGS IN THE LIMIT $\kappa \gg 1$

Dr. Yampolskii showed that in the limit of thin rings it is possible to obtain analytical results for the coupling energy between the two rings [86]. This also corresponds to the case of $\kappa \gg 1$ and allows to solve the problem analytically with the small parameter $d/\kappa^2 \ll 1$. From the numerical calculations of the previous sections it follows that the radial dependences of the order parameter in the inner and the outer ring are slow and smooth. For the analytical calulation, one assumes that the order parameter in the ring and the outer ring, f_{in} and f_{out}, are constant.

When both rings are superconducting, the total free energy F is given by [86]

$$F = F_{in} + F_{out} + F_{int} \ , \tag{6.9}$$

where the self energy of the inner and the outer ring are given by

$$F_{in} = -\frac{S_{in}}{S}\frac{\kappa_o^4}{\kappa_i^4}\left(\frac{\xi_o^2}{\xi_i^2} - \frac{I_{in}^{(0)}}{S_{in}}\right)^2 \left[\frac{\kappa_i^2}{\kappa_o^2} + \frac{2d}{\kappa_i^2}\frac{I_{in}^{(1)}}{S_{in}} + O\left(\frac{d^2}{\kappa_i^4}\right)\right] \ , \tag{6.10}$$

and

$$F_{out} = -\frac{S_{out}}{S}\left(1 - \frac{I_{out}^{(0)}}{S_{out}}\right)^2 \left[1 + \frac{2d}{\kappa_o^2}\frac{I_{out}^{(1)}}{S_{out}} + O\left(\frac{d^2}{\kappa_o^4}\right)\right] \ . \tag{6.11}$$

The interaction energy between the two rings is given by

$$F_{int} = -\frac{2d}{\kappa_i^2}\left(1 + \frac{\kappa_o^2}{\kappa_i^2}\right)\left(\frac{\xi_o^2}{\xi_i^2} - \frac{I_{in}^{(0)}}{S_{in}}\right)\left(1 - \frac{I_{out}^{(0)}}{S_{out}}\right)\frac{I^{(2)}}{S} + O\left(\frac{d^2}{\kappa^4}\right) \ , \tag{6.12}$$

where $S_{in} = \pi\left(R_o^{*2} - R_i^{*2}\right)$, $S_{out} = \pi\left(R_o^2 - R_i^2\right)$, $S = S_{in} + S_{out}$, and

$$\begin{aligned} I_{out(in)}^{(0)} &= 2\pi L_{out(in)}^2 \ln\left(R_o^{(*)}/R_i^{(*)}\right) - H_0 L_{out(in)} S_{out(in)} \\ &\quad + H_0^2 S_{out(in)}\left(R_o^{(*)2} + R_i^{(*)2}\right)/8 \ , \end{aligned} \tag{6.13}$$

$$I^{(2)} = S_{in}\left[L_{in} - H_0\left(R_i^{*2} + R_o^{*2}\right)/4\right]\left[L_{out}\ln\left(R_o/R_i\right) - H_0 S_{out}/4\pi\right] \ , \tag{6.14}$$

$$\begin{aligned} I_{out(in)}^{(1)} &= 2\left(L_{out(in)}\ln R_o^{(*)} - H_0 R_o^{(*)2}/4\right) J_{out(in)}^{(1)} \\ &\quad - R_i^{(*)2}\left(L_{out(in)} - H_0 R_i^{(*)2}/4\right) J_{out(in)}^{(2)} - J_{out(in)}^{(3)} \ , \end{aligned} \tag{6.15}$$

$$J_{out(in)}^{(1)} = \pi\int_{R_i^{(*)}}^{R_o^{(*)}} d\rho\,\rho^2\left(\frac{L_{out(in)}}{\rho} - \frac{H_0\rho}{2}\right) \ , \tag{6.16}$$

$$J_{out(in)}^{(2)} = \pi\int_{R_i^{(*)}}^{R_o^{(*)}} d\rho\left(\frac{L_{out(in)}}{\rho} - \frac{H_0\rho}{2}\right) \ , \tag{6.17}$$

$$J_{out(in)}^{(3)} = \pi\int_{R_i^{(*)}}^{R_o^{(*)}} d\rho\,\rho^2\left(\frac{L_{out(in)}}{\rho} - \frac{H_0\rho}{2}\right)\left[L_{out(in)}\left(2\ln\rho - 1\right) - \frac{H_0\rho^2}{4}\right] \ . \tag{6.18}$$

One can see that the interaction between the rings (i.e., the coupling) exists only when both rings are superconducting. The energy of the ring-ring coupling in the considered limit is proportional to the sample thickness. Due to the interaction between the rings the Cooper-pair density in each ring has a small (proportional to d/κ^2) contribution of the other ring.

6.7 CONCLUSIONS

We investigated the magnetic coupling between two concentric mesoscopic superconductors with nonzero thickness. When a second superconductor is placed in the center of a superconducting ring, it feels a non-uniform field, which is the superposition of the uniform applied field and the field expelled from the outer ring. Also the first ring will be influenced by the magnetic field expelled from the superconductor in the center. So, both superconductors are coupled magnetically. This results in substantial changes of the superconducting properties.

From the study of the free energy we learned that extra ground state transitions occur in comparison with the single ring case. These are transitions where the total vorticity stays the same, but the vorticity of the inner superconductor changes by one unit. We also found that the free energy of the double ring system is not exactly the same as the sum of the free energies of the two uncoupled single rings which is another signature of the magnetic coupling of both rings. This interaction enhances with increasing sample thickness. We calculated the expelled field for the ring-ring configuration which showed that as compared with a single ring more, or less, field can be expelled or attracted depending on the vorticities of both superconductors.

The behaviour of the Cooper-pair density, the magnetic field profile and the current density was calculated. Since an extra superconductor is placed in the center, the magnetic field will be expelled from this superconductor or will be compressed in the center of it, which results in a higher or a lower magnetic field density between the two superconductors. The current in both rings exhibits extra jumps at the transition fields where the vorticity of the other ring increases or decreases by one.

Finally, we calculated a $H - T$ phase diagram. Up to now, both rings had the same width and the same critical temperature. Therefore, only the outer ring would be superconducting at the superconducting/normal transition and the $H - T$ phase diagram shows no effect of the magnetic coupling. To circumvent this problem the T_c of the outer ring was artificially lowered in the experiment of Ref. [26] by applying a sufficiently large external current through the outer ring. Theoretically, we investigated what happens if the inner ring is made of a different material with a higher critical temperature. The $H - T$ phase diagram showed that the nucleation field of the double ring equals the one of the outer ring at low temperatures and the one of the inner ring at higher temperatures.

Publications. The results presented in this chapter were published as:

- B. J. Baelus, S. V. Yampolskii, and F. M. Peeters, *Coupled mesoscopic superconductors*, cond-mat/0112122 and submitted to Phys. Rev. B.
- B. J. Baelus, S. V. Yampolskii, and F. M. Peeters, *Magnetic coupling between mesoscopic superconducting rings*, Physica C **369**, 366-369 (2002).

7

Saddle point and energy barrier for flux penetration and expulsion

7.1 INTRODUCTION

From our study of mesoscopic superconducting disks (chapter 2) and rings (chapter 5) we know that, as a function of the applied field, there are transitions between vortex states with different vorticity L. Experimentally, it was found that the magnetic field at which the transition $L \to L+1$ occurs does not necessarily coincides with the magnetic field H_{tr} where the vorticity of the ground state changes from L to $L+1$, i.e. it is possible to drive the system in a metastable state (see for example Ref. [2]). This is typical for first order phase transitions. For increasing applied field, the state with vorticity L remains stable up to the penetration field $H_p > H_{tr}$ and transits then to the superconducting state with vorticity $L+1$. For decreasing applied field, the state with vorticity $L+1$ remains stable down to the expulsion field $H_e < H_{tr}$ before going to the state with vorticity L. This hysteresis effect is a consequence of the presence of an energy barrier between the states with vorticity L and $L+1$. The latter corresponds to different minima of the free energy in configurational space and the lowest barrier between those two minima is a saddle point [see Fig. 7.1]. The barrier arises from the fact that the superconducting current around a vortex is in the opposite direction to the screening currents at the surface of the sample [87]. This Bean-Livingston model has been refined to different sample geometries [88–98]. The time of flux penetration and expulsion is determined by the height of the energy barrier.

The experimental consequences of the existence of these metastable states are: (i) hysteretic behavior [2], (ii) paramagnetic Meissner effect [23, 29, 48,

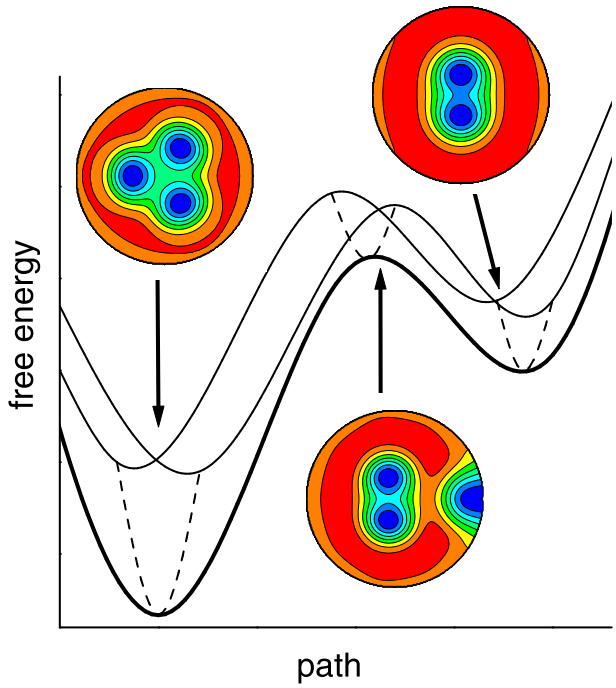

Fig. 7.1 Schematical view of the free energy in functional space depicting two minima with $L = 2$ and $L = 3$ and the saddle point connecting them. The Cooper-pair densities of these three states are shown in the insets. High (low) Cooper-pair density is given by red (blue). [From Ref. [49].]

56, 76, 99], (iii) fractional flux penetration [30], and (iv) negative flux entrance [30], i.e. a decrease of the flux penetration through the superconducting disk with increasing vorticity and increasing magnetic field.

Schweigert and Peeters [49] studied flux penetration and expulsion in thin superconducting disks and presented an approach to find the saddle point states. They calculated the height of the free energy barriers which separate the stable states with different vorticity L. We extend their approach and present a systematic study of flux penetration and expulsion in thin superconducting disks and rings.

Horane *et al.* [100] studied the saddle points between two vortex states of a one dimensional wire of zero width. They allowed for more possible non-uniform perturbations which may make the vortex state unstable. They found that the transition between two angular momentum states occurs through a saddle point which has a zero in the order parameter at some point along the ring. Such a zero creates a phase slip center, allowing the phase winding required for the transition. Our systems have a nonzero radial width and

consequently such a scenario is not possible because the order parameter is not allowed to be zero along a radial line. In fact it was found in Ref. [49] that for a disk geometry, the saddle point for flux penetration corresponds to a state with suppressed superconductivity at the disk edge which acts as a nucleus for the following vortex creation. In the present chapter we will find that for rings with a finite width this picture has to be modified because of the presence of two boundaries, i.e. two edges.

Palacios [48] calculated saddle point states and the energy barriers responsible for the metastabilities of superconducting mesoscopic disks using the lowest Landau level approximation. The central idea of his method was to find generic stationary solutions of the Ginzburg-Landau functional and to project the order parameter onto smaller subspaces spanned by a finite number l of eigenfunctions, $\{L_1, L_2, ..., L_l\}$, where $0 \leq L_1 \leq L_2 \leq ... \leq L_l$. Palacios restricted himself to $l \leq 3$ and therefore his approach is a special case of the one of Ref. [49] where no such restriction on l was imposed and where also different radial states were included. In our group, Yampolskii and Peeters [50] investigated the influence of the boundary condition (surface enhancement) on the superconducting states and the energy barriers between those vortex states. They also restricted their calculations to $l \leq 3$.

In section 7.2 we present the theoretical model and the calculation method to obtain the saddle points. In section 7.3 we study thin superconducting disks and extend and supplement our previous results (see chapter 2). We make again a distinction between small and large superconducting disks. In small disks only the giant vortex state appears, while in larger disks multivortices can nucleate and transitions between different multivortices are possible [31, 101]. In section 7.4 we consider superconducting rings, where we also make a distinction between small and large rings. Our results are summarized in section 7.5.

7.2 THEORETICAL FORMALISM

We consider very thin superconducting disks with radius R and thickness d, and superconducting rings with inner radius R_i and outer radius R_o. These mesoscopic superconducting systems are immersed in an insulating medium in the presence of a perpendicular uniform magnetic field H_0. To solve this problem, we follow the numerical approach of Schweigert and Peeters [49]. For very thin disks and rings, i.e. $Wd \ll \lambda^2$, with $W = R$ the radius of the disk or $W = R_o - R_i$ the width of the ring, the demagnetization effects can be neglected and the Ginzburg-Landau functional can be written as

$$G = G_n + \int d\vec{r} \left(\alpha \left|\Psi\right|^2 + \frac{\beta}{2} \left|\Psi\right|^4 + \Psi^* \widehat{L} \Psi \right), \tag{7.1}$$

where G, G_n are the free energies of the superconducting and the normal states, Ψ is the complex order parameter, α and β are the GL coefficients

which depend on the sample temperature. $\widehat{L}$ is the kinetic energy operator for Cooper-pairs of charge $e^* = 2e$ and mass $m^* = 2m$, i.e.

$$\widehat{L} = (-i\hbar\vec{\nabla} - e^*\vec{A}/c)/2m^*, \tag{7.2}$$

where $\vec{A} = \vec{e}_\phi H_0\rho/2$ is the vector potential of the uniform magnetic field H_0 written in cylindrical coordinates ρ and ϕ.

By expanding the order parameter $\Psi = \sum_i^N C_i\varphi_i$ in the orthonormal eigenfunctions of the kinetic energy operator $\widehat{L}\varphi_i = \epsilon_i\varphi_i$ [39, 46, 47, 55], the difference between the superconducting and the normal state Gibbs free energy can be written in terms of complex variables as

$$F = G - G_n = (\alpha + \epsilon_i)\, C_i C_i^* + \frac{\beta}{2} A_{kl}^{ij} C_i^* C_j^* C_k C_l, \tag{7.3}$$

where the matrix elements $A_{kl}^{ij} = \int d\vec{r}\,\varphi_i^*\varphi_j^*\varphi_k\varphi_l$ are calculated numerically. The boundary condition for these φ_i, corresponding to zero current density in the insulator media, is

$$\vec{n}\cdot\left(-i\hbar\vec{\nabla} - \frac{e^*\vec{A}}{c}\right)\varphi_i\Bigg|_{boundary} = 0\ . \tag{7.4}$$

These eigenenergies ϵ_i and the eigenfunctions φ_i depend on the sample geometry. For thin axial symmetric samples the eigenfunctions have the form $\varphi_{j=(n,l)}(\rho,\phi) = exp(il\phi)f_n(\rho)$, where l is the angular momentum and the index n counts different states with the same l and equals the number of nodes in the radial direction. Thus, the order parameter Ψ can be written as

$$\psi = \sum_n \sum_l C_{n,l}\varphi_{n,l}\ . \tag{7.5}$$

We do not restrict ourselves to the lowest landau level approximation (i.e. $n = 1$) and expand the order parameter over all eigenfunctions with energy $\epsilon_i < \epsilon_*$, where the cutting parameter ϵ_* is chosen such that increasing it does not influence the results. The typical number of complex components used are in the range $N = 30 - 50$. Thus the superconducting state is mapped into a 2D cluster of N particles with coordinates $(x_i, y_i) \leftrightarrow (\mathrm{Re}(C_i), \mathrm{Im}(C_i))$, whose energy is determined by the Hamiltonian (7.3). The energy landscape in this $2N + 1$ dimensional space is studied where the local minima and the saddle points between them will be determined together with the corresponding vortex states.

To find the superconducting states and the saddle point states we use the technique described in Ref. [49]. A particular state is given by its set of coefficients $\{C_i\}$. We calculate the free energy in the vicinity of this point $\delta G = G(C^n) - G(C)$ where $\{C^n\}$ is the set of coefficients of a state very

close to the initial one. This free energy is expanded to second order in the deviations $\delta = C^n - C$,

$$\delta G = F_m \delta_m^* + B_{mn} \delta_n \delta_m^* + D_{mn} \delta_n^* \delta_m^* + c.c. \ , \tag{7.6}$$

where

$$F_m = (\alpha + \epsilon_i) C_m + \beta A_{kl}^{mj} C_j C_k^* C_l \ , \tag{7.7}$$

$$B_{mn} = (\alpha + \epsilon_m) I_{mn} + 2\beta A_{kl}^{mn} C_k C_l^* \ , \tag{7.8}$$

$$D_{mn} = \beta A_{kl}^{mn} C_k C_l \ , \tag{7.9}$$

and I_{mn} is the unit matrix. Using normal coordinates $\delta_m = x_k Q_m^k$ we can rewrite the quadratic form as $\delta G = 2\left(\gamma_k x_k + \eta_k x_k^2\right)$. To find the eigenvalues η_k and the eigenvectors γ_k we solve numerically the following equation:

$$\begin{vmatrix} B + \mathrm{Re}(D) & \mathrm{Im}(D) \\ \mathrm{Im}(D) & B - \mathrm{Re}(D) \end{vmatrix} \cdot \begin{vmatrix} \mathrm{Re}(Q^k) \\ \mathrm{Im}(Q^k) \end{vmatrix} = \eta_k \begin{vmatrix} \mathrm{Re}(Q^k) \\ \mathrm{Im}(Q^k) \end{vmatrix} \ . \tag{7.10}$$

Starting from a randomly choosen initial set of coefficients, we calculate a nearby minimum of the free energy by moving in the direction of the negative free energy gradient $-\gamma_k$. The set of coefficients of this minimum determines then the ground state or a metastable state. Starting from the initial set of coefficients we can also calculate a nearby saddle point state by moving to a minimum of the free energy in all directions, except the one which has the lowest eigenvalue. In this direction we move to a local maximum. Repeating this procedure for many randomly choosen initial sets of coefficients $\{C_i\}$ for fixed magnetic field, we find the different possible superconducting states and saddle point states. To calculate the magnetic field dependence we start from a superconducting state at a certain field and we change the applied field by small increments. By moving into the direction of the nearest minimum or saddle point, the corresponding state will be found for the new magnetic field, provided that the field step is small enough.

7.3 SUPERCONDUCTING DISKS

In the present section we discuss superconducting disks. For the same reason as in chapter 2 we make a distinction between small and large disks.

7.3.1 Small disks: giant vortex states

We consider superconducting disks with radius $R = 2.0\xi$. First we investigate the influence of the number of terms in the expansion of Eq. (7.5) on the energy of the minima and the saddle points. For the approach that $n = 1$ (i.e. lowest Landau level) and if only one l is taken into account for each state, i.e. $\Psi = C_l \varphi_l$, we find three different states for three different values

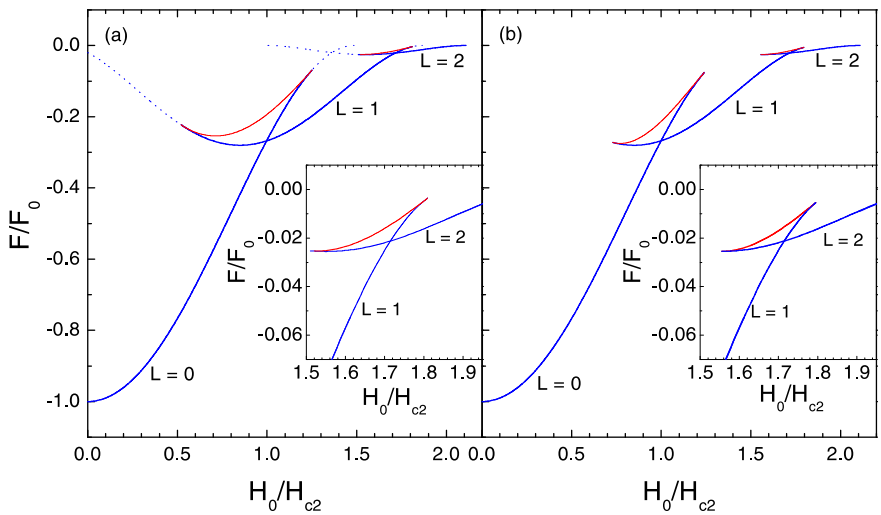

Fig. 7.2 The energy of the minima in the free energy F and the energy of the saddle points as a function of the applied magnetic field H_0 for a superconducting disk with radius $R = 2.0\xi$. (a) When only one term is included, i.e. $(n, l) = (1, l)$ (dotted blue curves), when two l-values are included, i.e. (n, l_1) and (n, l_2) (solid blue curves), with the corresponding energy of the saddle point (red curves); (b) The giant vortex energy (blue curves) and the saddle point energy (red curves) when an arbitrary large number of terms are included. The free energy is scaled with the condensation energy $F_0 = \alpha^2 \pi R^2 d/2\beta$.

of l, $l = 0$, 1 and 2, in different magnetic field regions. In Fig. 7.2(a) the free energy F of these L states, measured in units of the condensation energy $F_0 = \alpha^2 \pi R^2 d/2\beta$, is shown by the dotted blue curves as a function of the applied magnetic field H_0. Next, we take into account two values of l and $n = 1$, i.e. $\Psi = C_{l_1}\varphi_{l_1} + C_{l_2}\varphi_{l_2}$ as was done in e.g. Ref. [48]. With this approach we find L states with $L = 0, 1, 2$ and because of the concomittant existence of two minima also saddle point states with $(l_1, l_2) = (0, 1)$ and $(1, 2)$ appear. These are the saddle point states for the transition between L states with $L = l_1$ and $L = l_2$. In Fig. 7.2(a) the L states for this approach are given by the solid blue curves and the saddle point states by the red curves. The inset shows the transition between the $L = 1$ state and the $L = 2$ state in more detail. Notice that including one extra term in Eq. (7.5) reduces appreciably the stability region of the different giant vortex states, i.e. its metastable region is strongly reduced. The L states are only stable up to the point where its energy equals the saddle point states.

Fig. 7.2(b) shows the free energy as a function of the applied magnetic field if we do not restrict ourselves to the lowest landau level and if we expand the order parameter over all eigenfunctions with energy $\epsilon_i < \epsilon_*$, where the cutting parameter ϵ_* is chosen such that increasing it does not influence the results.

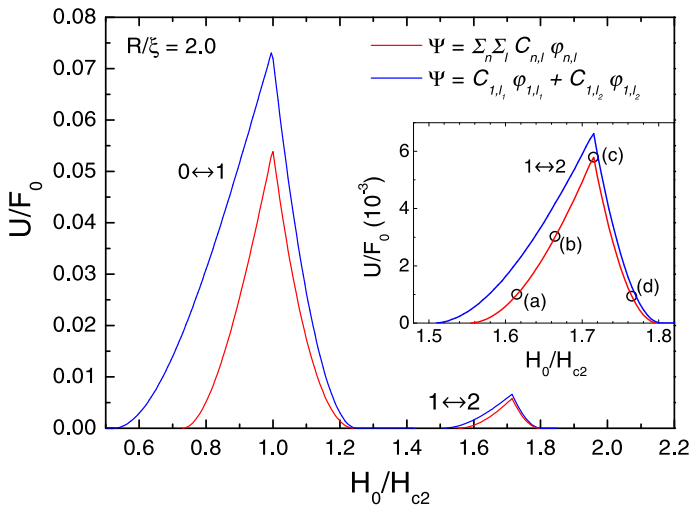

Fig. 7.3 The transition barrier U for transitions between different L states for a superconducting disk with radius $R = 2.0\xi$ when taking into account only two values of l (blue curves) and for the numerical 'exact' result (red curves). The inset shows the second barrier in more detail.

The blue and the red curves indicate respectively the stable L states and the saddle point states. The transition between the $L = 1$ state and the $L = 2$ state is enlarged in the inset. Notice that the stability region of the L states is further reduced. Allowing more basis functions in Eq. (7.5) does not have a strong influence on the energy of the L states, e.g. compare the dotted and the solid curves in Fig. 7.2(a), but it considerably decreases the energy of the saddle point between the L states. In doing so, it reduces strongly the stability range of the metastable states, and consequently it reduces the size, i.e. the width in the magnetic field range, of the hysteresis effect [98]. For example, we found $(H_{tr}/H_{c2}, H_e/H_{c2}, H_p/H_{c2}) \approx (1.0, 0.52, 1.25)$, $(1.0, 0.715, 1.245)$ and $(1.0, 0.73, 1.24)$ for the $L = 0 \leftrightarrow L = 1$ transition when we include two, three and an arbitrary number of basis function in Eq. (7.5), respectively. Similarly, we found for the $L = 1 \leftrightarrow L = 2$ transition $(H_{tr}/H_{c2}, H_e/H_{c2}, H_p/H_{c2}) \approx (1.715, 1.52, 1.81)$, $(1.715, 1.535, 1.80)$, and $(1.715, 1.555, 1.795)$ including two, three and an arbitrary number of basis functions, respectively. These results clearly show that one has to exert some caution to cutoff the expansion in Eq. (7.5) when calculating the saddle point and thus the energy barriers. Notice that the expulsion field H_e/H_{c2} is most strongly influenced by the number of terms in Eq. (7.5).

In Fig. 7.3 the transition barriers U, i.e. the energy difference between the saddle point state and the nearby metastable states are plotted. We show the 'exact' numerical results (red curves) and the results when including only two values of l with $n = 1$, i.e. $\Psi = C_{l_1}\varphi_{l_1} + C_{l_2}\varphi_{l_2}$ (blue curves). Notice

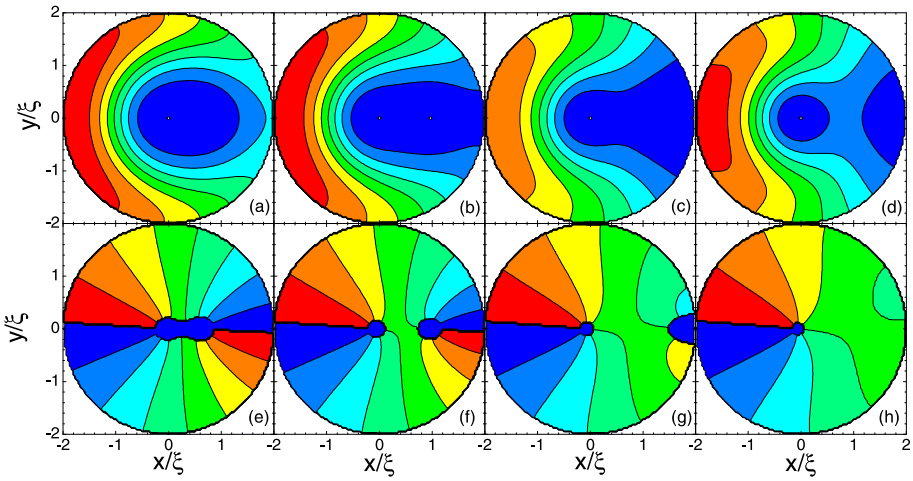

Fig. 7.4 Contour plot of the Cooper-pair density $|\Psi|^2$ (a-d) and the phase of the order parameter (e-h) in the saddle point state corresponding to the transition from the $L = 1$ state to the $L = 2$ state in a superconducting disk with radius $R = 2.0\xi$ for the magnetic fields indicated by the open circles in the inset of Fig. 7.3; $H_0/H_{c2} = 1.615$ (a,e), 1.665 (b,f), 1.715 (i.e. the maximum of the barrier) (c,g) and 1.765 (d,h). High (low) Cooper-pair density is given by red (blue) regions. Phases near 2π (0) are given by red (blue) regions.

that by approximating the order parameter better: (i) it substantially lowers the energy barriers, (ii) it increases the expulsion fields H_e, and (iii) it lowers the penetration fields H_p slightly. The energy barrier is smaller for higher $L \to L+1$ transitions which occur at larger magnetic fields. The inset shows the barrier between the $L = 1$ and the $L = 2$ state in more detail.

The spatial distribution of the superconducting electron density $|\Psi|^2$ in the saddle point state corresponding to the transition from the $L = 1$ state to the $L = 2$ states is depicted in Figs. 7.4(a-d) for the magnetic fields indicated by the open circles in the inset of Fig. 7.3, i.e. $H_0/H_{c2} = 1.615$, 1.665, 1.715 (i.e. the maximum of the barrier) and 1.765, respectively. In Ref. [49] similar results were shown for the $L = 0 \leftrightarrow L = 1$ saddle point. High (low) Cooper-pair density is given by red (blue) regions. With increasing field, one vortex moves from the center to the outer region of the disk, and the state changes from $L = 2$ to $L = 1$. This is better illustrated by the contour plots of the phase of the order parameter which is shown in Figs. 7.4(e-h) for the same configurations. Along a closed path, which lies near the edge of the superconductor, the phase difference $\Delta\varphi$ is always given by L times 2π, with L the vorticity or winding number. Blue regions indicate phases $\varphi \gtrsim 0$ and red regions $\varphi \lesssim 2\pi$. When encircling the superconductor near the boundary, we find that the phase difference $\Delta\varphi$ is equal to $2 \times 2\pi$ in Figs. 7.4(e-g) and $\Delta\varphi = 1 \times 2\pi$ in Fig. 7.4(h), which means vorticy $L = 2$ and 1, respectively.

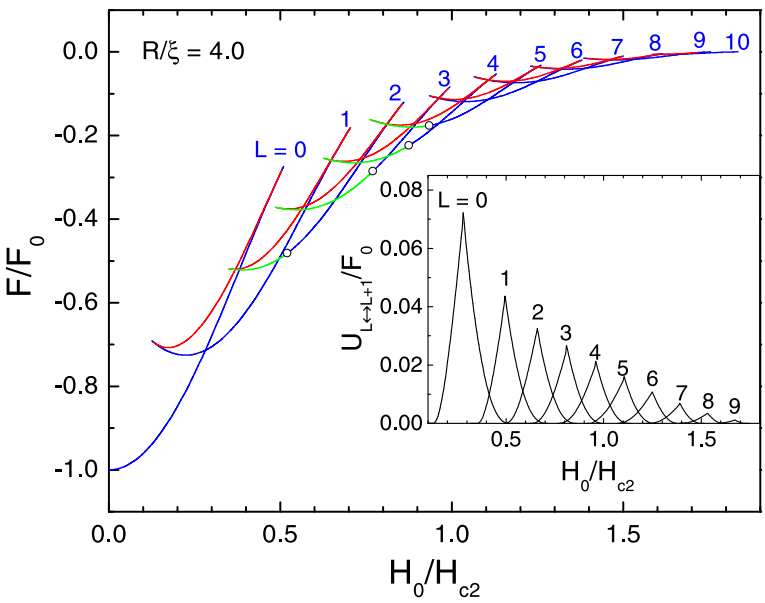

Fig. 7.5 The free energy as a function of the applied magnetic field H_0 for a disk with radius $R = 4.0\xi$. The different L states are given by blue curves when in the giant vortex states and by green curves when in the multivortex states, while the saddle point states are given by the red curves. The open circles correspond to the transitions between the multivortex state and the giant vortex state for fixed L. The inset shows the transition barrier U as a function of the applied field for the different $L \leftrightarrow L+1$ transitions.

At the maximum of the barrier, i.e. when the energy of state $L = 1$ and $L = 2$ are identical, the saddle point transits from vorticity $L = 2$ to $L = 1$. At this point the Cooper-pair density is zero at the boundary of the disk which acts as a nucleation center for flux penetration and expulsion [49].

7.3.2 Large disks: multivortex states

We consider now a larger superconducting disk with radius $R = 4.0\xi$ in which multivortex states can nucleate in certain magnetic field ranges (see chapter 2 and Refs. [39, 101]). Fig. 7.5 shows the free energy as a function of the applied magnetic field H_0. The energy of the different L states is given by blue curves when they are in the giant vortex state and by green curves when they are in the multivortex state, while the saddle point states are given by the red curves. The open circles give the transition points between the multivortex state and the giant vortex state for fixed L. The inset shows the transition barrier U as a function of the applied field for the different $L \leftrightarrow L+1$ transitions. To distinguish qualitatively the giant vortex state from the multivortex state for

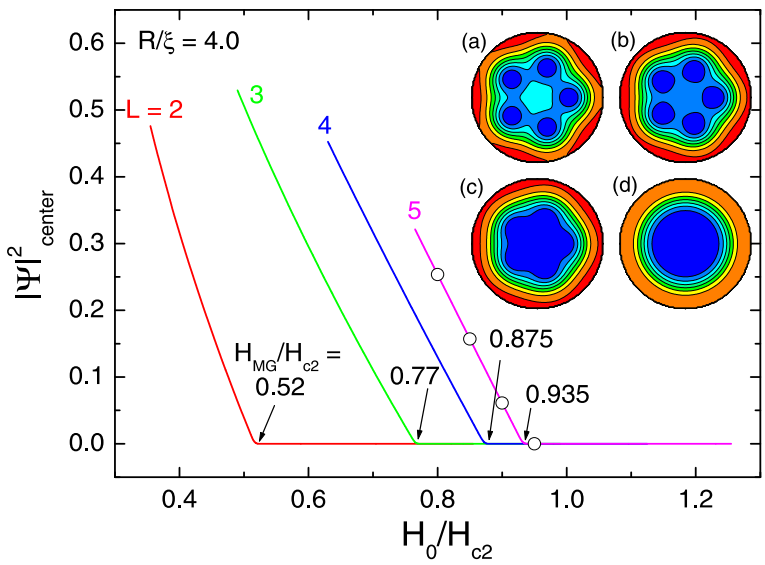

Fig. 7.6 The Cooper-pair density $|\Psi|^2$ in the center of the disk with radius $R = 4.0\xi$ for $L = 2$, 3, 4 and 5. The insets (a-d) show contour plots of the Cooper-pair density for $L = 5$ at the magnetic fields corresponding to the open circles; i.e. $H_0/H_{c2} = 0.8$, 0.85, 0.9 and 0.95, repectively. The transition from multivortex state to giant vortex state occurs at the transition field H_{MG}.

fixed L we considered the value of the Cooper-pair density $|\Psi|^2$ in the center of the disk. Fig. 7.6 shows $|\Psi|^2_{center}$ which is zero for a giant vortex state and non zero for the multivortex states when there is no vortex in the center of the disk. For $R = 4.0\xi$ we find only multivortex states for $L = 2$, 3, 4 and 5 and the transition from the multivortex state to the giant vortex state occurs at $H_{MG}/H_{c2} = 0.52$, 0.77, 0.875 and 0.935, respectively. Of course, for $L = 1$ there is no distinction between the giant and the multivortex state. For $L = 5$ the spatial distribution of the superconducting electron density is given in the insets (a-d) of Fig. 7.6 at the magnetic fields corresponding to the open circles in Fig. 7.6, i.e. $H_0/H_{c2} = 0.8$, 0.85, 0.9 and 0.95, repectively. In the multivortex state the vortices move towards the center with increasing magnetic field and at the same time the vortices become wider, and therefore, the Cooper-pair density in the center decreases until the axial symmetry is recovered at the transition field $H_{MG} = 0.935H_{c2}$.

Next, we will study the energy barriers U in more detail. For a superconducting disk with radius $R = 4.0\xi$ the energy barriers for the different $L \leftrightarrow L+1$ transitions are shown in the inset of Fig. 7.5. The height of the energy barrier for the $L \leftrightarrow L+1$ transition decreases with increasing L. The difference between penetration and expulsion field decreases also with increasing L. Fig. 7.7(a) shows the free energy of the $L = 4$ and the $L = 5$ states

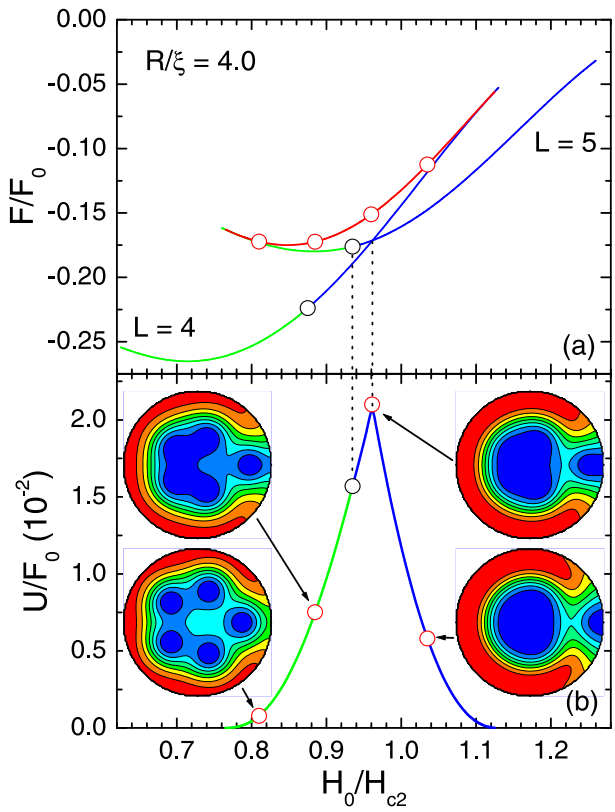

Fig. 7.7 (a) The free energy of the $L = 4$ and the $L = 5$ states (blue curves for giant vortex states and green curves for multivortex states) and the saddle point states between these states (red curve) for a superconducting disk with radius $R = 4.0\xi$; and (b) the energy barrier corresponding with this transition. The black circles correspond with the transition from multivortex to giant vortex state for fixed L. The insets show contour plots of the Cooper-pair density $|\Psi|^2$ for the saddle point states indicated by the red circles, i.e. at the magnetic fields $H_0/H_{c2} = 0.81$, 0.885, 0.96 (the barrier maximum) and 1.035. It is the transition between a multivortex state with $L = 5$ and a giant vortex state with $L = 4$.

in more detail (blue curves for the giant vortex state and green curves for the multivortex state) together with the energy of the saddle point state between these states (red curve). Fig. 7.7(b) gives the corresponding energy barrier. The black circles correspond to the transition from multivortex to giant vortex state. The barrier height is clearly not influenced by the transition from multivortex to giant vortex state, i.e. there are no jumps or discontinuities at the transition. The spatial distribution of the superconducting electron density $|\Psi|^2$ for this saddle point state is depicted in the insets of Figs. 7.7(b) for the configurations indicated by the red circles, i.e. $H_0/H_{c2} = 0.81$, 0.885,

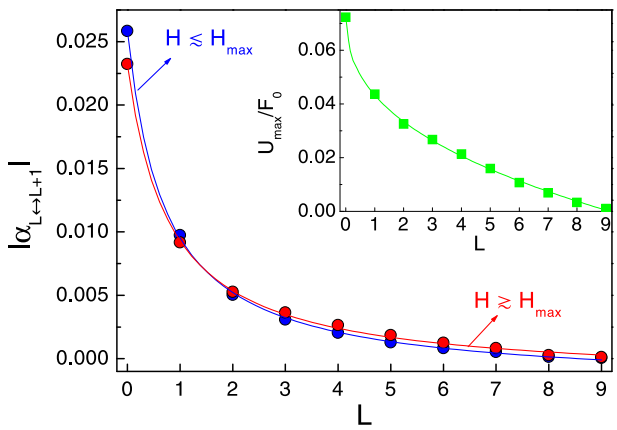

Fig. 7.8 The absolute value of the slope $|\alpha|$ of the energy barrier for a superconducting disk with $R = 4.0\xi$ as a function of L for $H \lesssim H_{max}$ (blue circles) and for $H \gtrsim H_{max}$ (red circles). The red and blue curves are the results of a fit. The inset shows the maximum barrier height as a function of the vorticity L.

0.96 (the barrier maximum) and 1.035, respectively. Notice that also in the saddle point the transition between a multivortex state with $L = 5$ and a giant vortex state with $L = 4$ is clearly visible.

Near the maximum of the barrier, the barrier height changes linearly with magnetic field. Therefore, we can approximate the energy barrier U near its maximum U_{max} by

$$\frac{U}{F_0} = \frac{U_{max}}{F_0} + \alpha \frac{H - H_{max}}{H_{c2}} \ ,$$

where the slope α is positive for $H \lesssim H_{max}$ and negative for $H \gtrsim H_{max}$. In Fig. 7.8 the absolute value of the slope $|\alpha|$ is given as a function of L for $H \lesssim H_{max}$ by the blue circles and for $H \gtrsim H_{max}$ by the red circles. The absolute value of the slope is different for the left and the right side of the maximum of the barrier. Notice that for $L = 0$ and $L = 1$, $|\alpha|$ is larger for $H \lesssim H_{max}$ as compared to $H \gtrsim H_{max}$, while for $L > 1$ the reverse is true. For increasing L the slope decreases and the behavior could be fitted to

$$|\alpha_{L \leftrightarrow L+1}(L)| = \frac{a + bL}{1 + cL} \ ,$$

with $a = 0.02586$, $b = -0.00300$ and $c = 1.40357$ for $H \lesssim H_{max}$, and $a = 0.02322$, $b = -0.00217$ and $c = 1.26502$ for $H \gtrsim H_{max}$. These fitting curves are shown in Fig. 7.8 by the blue line for $H \lesssim H_{max}$ and by the red line for $H \gtrsim H_{max}$. In the inset of Fig. 7.8 the maximum of the barrier height U_{max} is given by the green symbols as a function of the vorticity L. The barrier

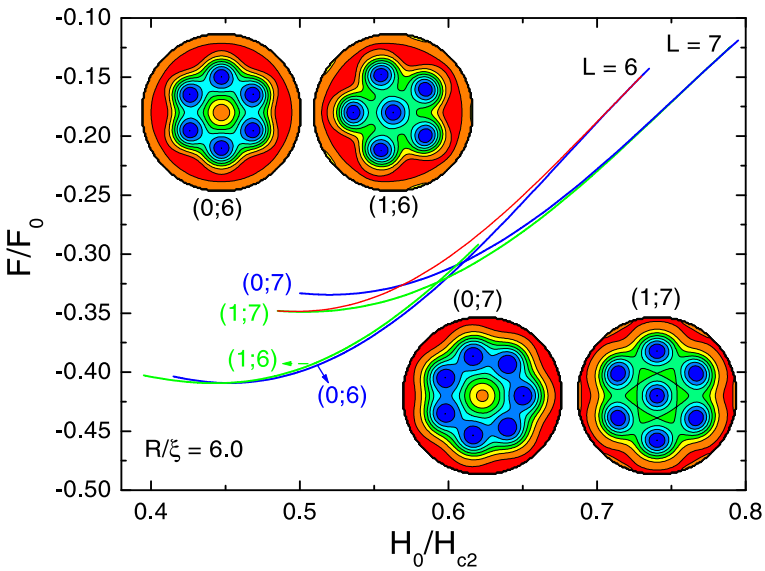

Fig. 7.9 The free energy F as a function of the applied magnetic field H_0 of the $(0;6)$ and the $(0;7)$ state (blue curves), the $(1;6)$ and the $(1;7)$ state (green curves), and the saddle point state (red curve) between the $(1;7)$ and $(0;6)$ state for a superconducting disk with radius $R = 6.0\xi$. The insets show the Cooper-pair density of the $(0;6)$ state, the $(1;6)$ state, the $(0;7)$ state, and the $(1;7)$ state at the thermodynamic transition field $H_0/H_{c2} = 0.6$ between the $(0;6)$ and the $(1;7)$ state.

height decreases for increasing vorticity and the behavior could be fitted to

$$\frac{U_{max}}{F_0}(L) = \frac{a + bL}{1 + c\sqrt{L}} \ ,$$

with $a = 0.07229$, $b = -0.00791$ and $c = 0.48657$, which is shown by the green curve.

For larger superconducting disks and higher values of L, different configurations of multivortices can occur with the same vorticity [31, 56, 99]. Fig. 7.9 shows the free energy as a function of the applied field for the superconducting states with vorticity $L = 6$ and $L = 7$. For both vorticities two configurations are possible; (i) L vortices on a ring and no vortex in the center (blue curve) and (ii) $L - 1$ vortices on a ring and 1 in the center (red curve). The vortex state is completely determined by the number of vortices in the center L_{center} and the total number of vortices L. For this reason we characterized the states by the indices $(L_{center}; L)$ in Fig. 7.9. The insets show the Cooper-pair density at $H_0/H_{c2} = 0.6$ for the $(0;6)$ state, the $(1;6)$ state, the $(0;7)$ state, and the $(1;7)$ state, respectively. Notice further that for such large radius, there is no transition from a multivortex to a giant vortex state for these values of L. For the sake of clarity, only the free energy of the saddle point state between

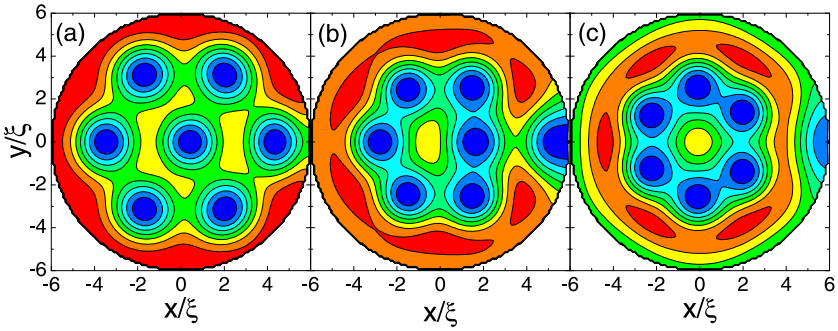

Fig. 7.10 The Cooper-pair density $|\Psi|^2$ for the transition between the $L = 6$ state and the $L = 7$ state for a superconducting disk with radius $R/\xi = 6.0$ at the applied magnetic fields $H_0/H_{c2} = 0.5$ (a), 0.6 (b) and 0.7 (c).

the $(1;7)$ state and the $(0;6)$ state is given by the red curve in Fig. 7.9. This state describes the expulsion of one vortex when the system transits from the $L = 7$ to the $L = 6$ configuration and is illustrated in Figs. 7.10(a-c) where we show the spatial distribution of the superconducting electron density $|\Psi|^2$ in the saddle point state at $H_0/H_{c2} = 0.5$, 0.6 and 0.7, respectively. To transit from $L = 7$ to $L = 6$, one vortex on the ring moves towards the outside of the disk and the vortex in the center takes the free place on the ring. High (low) Cooper-pair density is given by red (blue) regions.

7.4 SUPERCONDUCTING RINGS

Now, we will consider superconducting disks with radius R_o with a hole in the center with radius R_i. For the same reason as in section 7.3 we make a distinction between small and large systems.

7.4.1 Small rings: giant vortex states

As an example, we consider a superconducting ring with radius $R_o = 2.0\xi$ and hole radius $R_i = 1.0\xi$. In Fig. 7.11 the free energy is shown as a function of the applied magnetic field for the different L states (blue curves) together with the saddle point states (red curves). We find giant vortex states with $L = 0, 1, 2, 3, 4$. Comparing this result with the result for a disk with radius $R = 2.0\xi$, more L states are possible and the superconducting/normal-transition moves to larger magnetic fields (see also chapter 5). The inset shows the energy barrier U for the transitions between the different L states as a function of the difference between the applied magnetic field H_0 and the $L \to L + 1$ transition field $H_{L\to L+1}$. For increasing L, the height of the energy barrier and the difference between the penetration and the expulsion field decreases. The

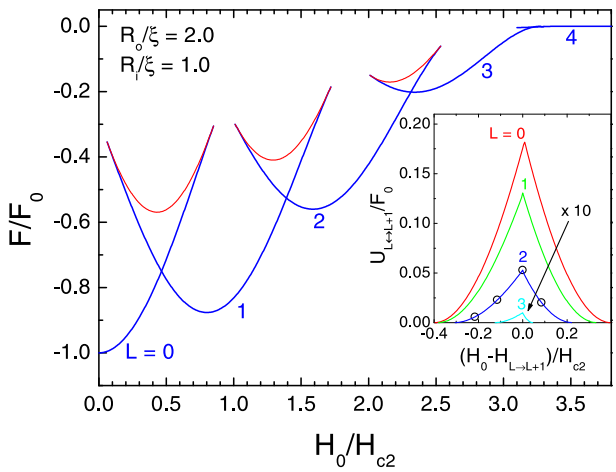

Fig. 7.11 The free energy for a superconducting ring with radius $R_o = 2.0\xi$ and hole radius $R_i = 1.0\xi$ as a function of the applied magnetic field for the different giant vortex states (blue curves) and for the saddle point states (red curves). The inset shows the energy barrier U for the transitions between different L states as a function of the difference between the applied magnetic field H_0 and the $L \to L+1$ transition field $H_{L\to L+1}$.

energy barrier near its maximum can be approximated by $U/F_0 = U_{max}/F_0 + \alpha(H - H_{max})/H_{c2}$, and we determined the slope $\alpha_{L\to L+1}$; $\alpha_{0\to 1} = -0.8$ for $H \lesssim H_{max}$ and 0.9 for $H \gtrsim H_{max}$, $\alpha_{1\to 2} = -0.6$ for $H \lesssim H_{max}$ and 0.75 for $H \gtrsim H_{max}$, $\alpha_{2\to 3} = -0.3$ for $H \lesssim H_{max}$ and 0.42 for $H \gtrsim H_{max}$, and $\alpha_{3\to 4} = -0.013$ for $H \lesssim H_{max}$ and 0.038 for $H \gtrsim H_{max}$. The slope decreases again for increasing L and the absolute value of the slope for $H \lesssim H_{max}$ is smaller than for $H \gtrsim H_{max}$ for every L, although the difference is relatively smaller than in the previous disk case where we found $\alpha_{0\to 1} = -0.31$ for $H \lesssim H_{max}$ and 0.44 for $H \gtrsim H_{max}$, and $\alpha_{1\to 2} = -0.06$ for $H \lesssim H_{max}$ and 0.1 for $H \gtrsim H_{max}$.

Next, we investigate the $2 \leftrightarrow 3$ saddle point. At $H_0/H_{c2} = 2.01$ (expulsion field) and 2.535 (penetration field) the saddle point state equals the giant vortex states with $L = 3$ and $L = 2$, respectively. The transition between these two giant vortex states is illustrated in Figs. 7.12(a-d) which show the spatial distribution of the superconducting electron density $|\Psi|^2$ corresponding with the open circles in the inset of Fig. 7.11 at $H_0/H_{c2} = 2.1$, 2.2, 2.315 (i.e. the barrier maximum) and 2.4, respectively. High (low) density is given by red (blue) regions. With increasing field one vortex moves from inside the ring, through the superconducting material, to outside the ring. From Fig. 7.12(c) one may infer that the Cooper-pair density is zero along a radial line and that the vortex is, in fact, a sort of line. That this is not the case can be seen from the left inset of Fig. 7.13 which shows the Cooper-pair density $|\psi|^2$

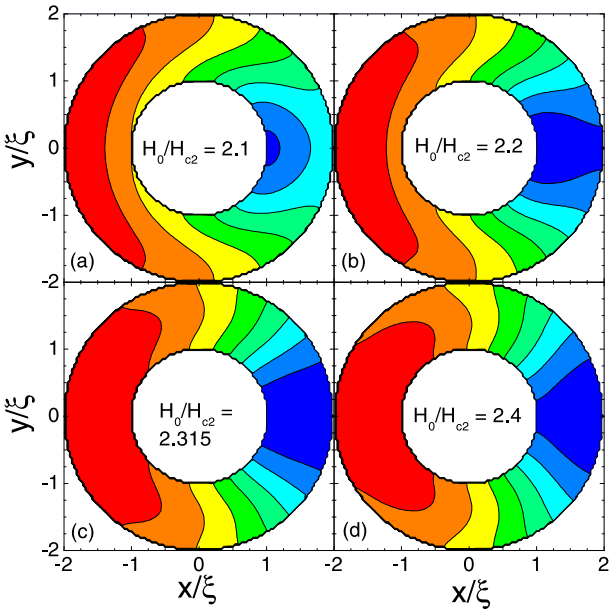

Fig. 7.12 The Cooper-pair density $|\Psi|^2$ of the transition between the giant vortex states with $L = 2$ and $L = 3$ for a superconducting ring with $R_o = 2.0\xi$ and $R_i = 1.0\xi$ at $H_0/H_{c2} = 2.1$ (a), 2.2 (b), 2.315 (c) and 2.4 (d). High density is given by red regions and low density by blue regions.

along this radial line for $H_0/H_{c2} = 2.315$. The Cooper-pair density in the superconducting material is zero only at the center of the vortex which is situated at $x_{min}/\xi \approx 1.5$ and $|\Psi|^2$ is very small otherwise, i.e. $|\Psi|^2 < 0.01$. In Fig. 7.13 the position of the vortex, i.e. of x_{min}, is shown as a function of the applied field. Over a narrow field region the vortex moves from the inner boundary towards the outer boundary. From $H_0/H_{c2} = 2.01$ to 2.25 the center of the vortex is still situated in the hole but the vortex already influences the superconducting state [see for example Figs. 7.12(a,b)]. From $H_0/H_{c2} = 2.36$ to 2.535 the center of the vortex lies outside the ring, but it has still an influence on the saddle point [see for example Fig. 7.12(d)]. In the region $H_0/H_{c2} = 2.25 - 2.36$ the center of the vortex is situated inside the superconductor. This is also illustrated by the contourplot [right inset of Fig. 7.13] for the phase of the order parameter at $H_0/H_{c2} = 2.315$, corresponding with the open circle in Fig. 7.13. When encircling the superconductor near the inner boundary of the ring, we find that the phase difference $\Delta\varphi$ is equal to $2 \times 2\pi$ which implies vorticity $L = 2$. When encircling the superconductor near the outer boundary, we find vorticity $L = 3$. If we choose a path around the vortex (located at x_{min}), the phase changes with 2π and thus $L = 1$. At the transition field ($H_0/H_{c2} = 2.315$) the center of the vortex

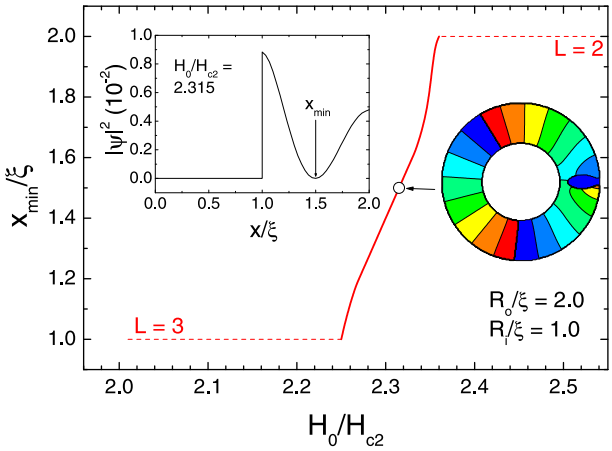

Fig. 7.13 The radial position of the vortex in the saddle point for the $2 \leftrightarrow 3$ transition through the superconductor with radius $R_o = 2.0\xi$ and $R_i = 1.0\xi$. The left inset shows the Cooper-pair density along de x-direction at $H_0/H_{c2} = 2.315$, and the right inset is a contour plot of the phase of the order parameter at $H_0/H_{c2} = 2.315$.

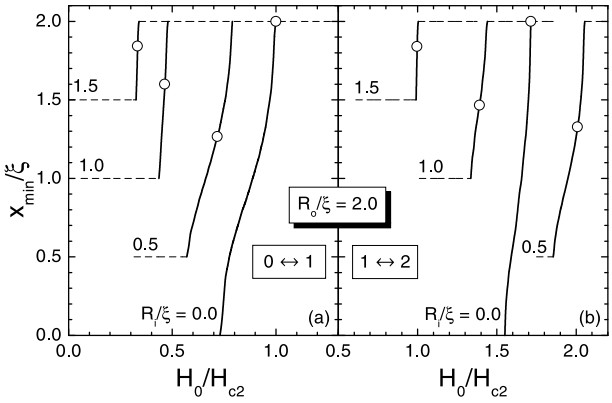

Fig. 7.14 The radial position of the vortex for (a) the $0 \leftrightarrow 1$ and (b) the $1 \leftrightarrow 2$ saddle point transition as a function of the applied magnetic field for a superconducting ring with radius $R_o = 2.0\xi$ and $R_i = 0.0$, 0.5, 1.0 and 1.5ξ. The open circles indicate the transition fields.

of the saddle point is clearly not situated at the outer boundary as was the case for superconducting disks [see for example Figs. 7.4(c,g), 7.7(b), 7.10(b) and Ref. [49]].

To illustrate this more clearly, Figs. 7.14(a,b) show the radial position of the vortex during the transition between the Meissner state and the $L = 1$ state, and between the $L = 1$ state and the $L = 2$ state for a superconducting ring with radius $R_o = 2.0\xi$ and for several values of the hole radius, i.e.

$R_i/\xi = 0.0$, 0.5, 1.0 and 1.5. The open circles indicate the ground state transition fields. Only for the case of the disk without a hole the center of the vortex at the saddle point occurs at the outer boundary of the disk for the magnetic field at which the ground state changes from L to $L+1$. When the disk contains a hole in the center there are two boundaries and the center of the above vortex is now located between those two boundaries. For a small hole with radius $R_i = 0.5\xi$ the position of the vortex can be approximated by the arithmetic mean of the inner and the outer radius, i.e. $x_{min}/\xi \approx (R_o + R_i)/2$, and for a larger hole with radius $R_i = 1.5\xi$ by the geometric mean $\sqrt{R_o R_i}$. The transition field increases and the magnetic field range, over which the transition occurs, decreases with increasing L. Notice that the transition field for the $L = 1 \leftrightarrow 2$ transition for $R_i/\xi = 0.5$ is larger than the one for $R_i/\xi = 0.0$ [see Fig. 7.14(b)], which agrees with Fig. 5.5(a).

7.4.2 Large rings: multivortex states

First, we consider superconducting rings with radius $R_o = 4.0\xi$ and hole radius $R_i = 1.0\xi$. In Fig. 7.15 the free energy is shown as a function of the applied magnetic field. The different L states are given by blue curves for giant vortex states and green curves for multivortex states, while the saddle point states are given by the red curves. The open circles correspond to the transition between the multivortex state and the giant vortex state for fixed L. These transitions occur at $H_{MG}/H_{c2} = 0.93$, 1.035 and 1.14 for $L = 4$, 5 and 6, respectively. Notice that for such a small hole in the disk the maximum number of L, i.e. $L = 10$, is the same as for the disk case without a hole [see Fig. 7.5]. The spatial distribution of the superconducting electron density $|\Psi|^2$ is depicted in the insets (a-c) of Fig. 7.15 for the multivortex state with $L = 4$ at $H_0/H_{c2} = 0.8$, $L = 5$ at $H_0/H_{c2} = 0.9$ and $L = 6$ at $H_0/H_{c2} = 1.0$, respectively. High (low) Cooper-pair density is given by red (blue) regions. Notice that there are always $L-1$ vortices in the superconducting material and one vortex appears in the hole, i.e. in the center of the ring.

The energy barriers for the transitions between the different L states are shown in Fig. 7.16 as a function of the applied magnetic field. By comparing this with the energy barriers for a disk with no hole, we see that the barrier heights and the transition fields are strongly different [see the inset of Fig. 7.5]. Therefore we show in the insets of Fig. 7.16 the maximum height of the energy barrier U_{max} and the $L \leftrightarrow L+1$ transition field H_{tr} as a function of L for superconducting disks with no hole (red symbols) and with a hole of radius $R_i = 1.0\xi$ (green symbols), 2.0ξ (blue symbols) and 3.0ξ (magenta symbols). In all cases the height of the energy barrier decreases and the transition fields increases with increasing L. By comparing the situation with no hole and with a small hole with $R_i = 1.0\xi$, we see that the barriers for $L \leq 1$ are higher for the disk with a hole with $R_i = 1.0\xi$ than for $R_i = 0.0\xi$, while they are smaller when $L > 1$. Notice also that the value of the $L \rightarrow L+1$

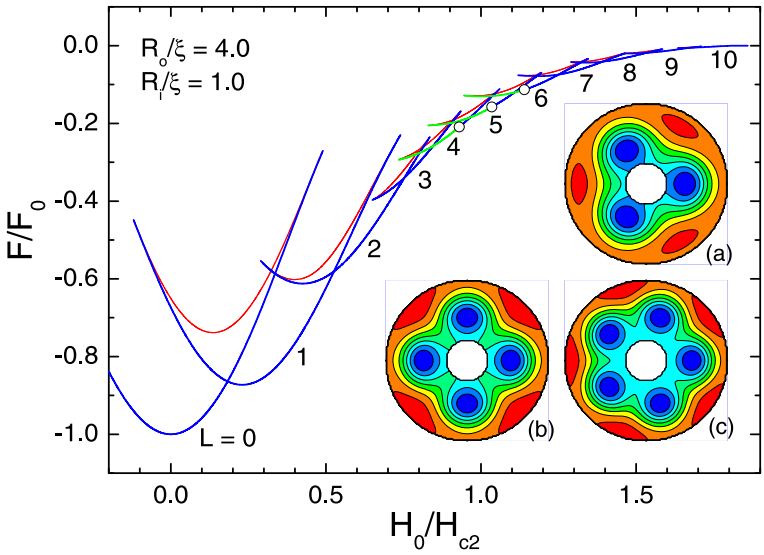

Fig. 7.15 The free energy for a superconducting ring with $R_o = 4.0\xi$ and $R_i = 1.0\xi$ as a function of the applied magnetic field for the different L states (blue curves for giant vortex states and green curves for multivortex states), and the saddle point states (red curves). The open circles correspond to the transition between the multivortex state and the giant vortex state for fixed L. The insets show contour plots of the Cooper-pair density $|\Psi|^2$ for the multivortex state with $L = 4$ at $H_0/H_{c2} = 0.8$ (a), $L = 5$ at $H_0/H_{c2} = 0.9$ (b) and $L = 6$ at $H_0/H_{c2} = 1.0$ (c). High Cooper-pair density is given by red regions, low Cooper-pair density by blue regions.

transition field is sensitive to the presence of the hole with radius $R_i = 1.0\xi$ for small L and insensitive for larger L. The reason is that for small $L > 0$ such a central hole has always one vortex localised inside which favors certain vortex configurations above others, while for larger L in both cases only giant vortices appear with sizes larger than the hole size and the presence of the hole no longer matters. For larger holes the energy barrier decreases more slowly, because the free energy of the different L states shows a more parabolical type of behavior as a function of the magnetic field.

Next, we investigate the saddle point states in these superconducting rings. We make a distinction between different kinds of saddle point states; i) between two giant vortex states, ii) between a multivortex and a giant vortex state, iii) between two multivortex states with the same vorticity in the hole and different vorticity in the superconducting material, and iv) between two multivortex states with the same vorticity in the superconducting material but different vorticity in the hole. The first saddle point transition was already described for the case of small superconducting rings [see Figs. 7.12 and 7.13]. Next, we study the saddle point state between a multivortex state with $L = 5$ and a giant vortex state with $L = 4$ for the previous considered

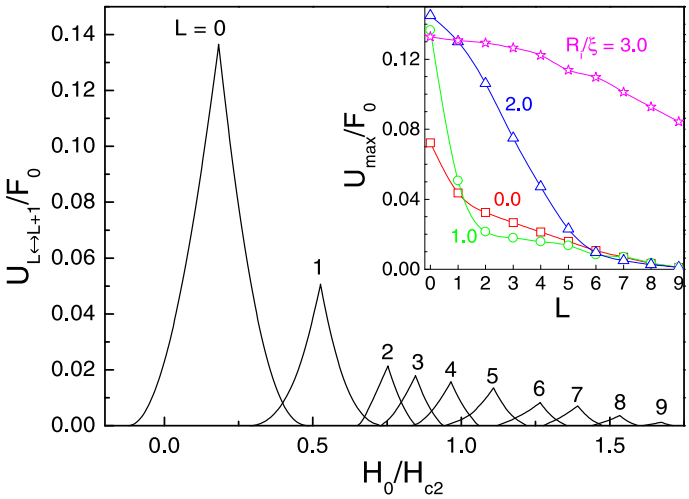

Fig. 7.16 The energy barrier U for the transitions between the different L states in a superconducting ring with $R_o = 4.0\xi$ and $R_i = 1.0\xi$ as a function of the applied magnetic field. The inset shows the maximum height of the energy barrier U_{max} as a function of L for rings with $R_o = 4.0\xi$ and $R_i = 0.0$, 1.0, 2.0, and 3.0ξ.

ring with radius $R_o = 4.0\xi$ and hole radius $R_i = 1.0\xi$. Figs. 7.17(a-f) show the Cooper-pair density for these saddle point states at $H_0/H_{c2} = 0.83$, 0.88, 0.93, 0.965 (i.e. the barrier maximum), 1.03 and 1.06, respectively. High (low) Cooper-pair density is given by red (blue) regions. For increasing field one vortex moves to the outer boundary, while the others move to the center of the ring where they create a giant vortex state. Remark that the giant vortex state is larger than the hole and therefore it is partially situated in the superconductor itself.

To study saddle point transitions between different multivortex states we have to increase the radius of the ring to favour the multivortex states. Therefore, we consider a ring with radius $R_o = 6.0\xi$ and hole radius $R_i = 2.0\xi$. Fig. 7.18 shows the free energy of multivortex states with $L = 8$ and $L = 9$. In both cases 3 vortices are trapped in the hole. The lower insets show the spatial distribution of the superconducting electron density $|\Psi|^2$ at the transition field $H_0/H_{c2} = 0.695$ for $L = 8$ and $L = 9$. It is clear that there are only 5 and 6 vortices in the superconducting material, respectively. The free energy of these multivortex states is shown by the blue curves, while the saddle point energy between these states is given by the red curve. Notice further, that there is no transition from the multivortex states to the giant vortex states with $L = 8$ and 9 as long as these states are stable. The spatial distribution of the superconducting electron density $|\Psi|^2$ for this saddle point state is depicted in the upper insets at the magnetic fields $H_0/H_{c2} = 0.63$, 0.695 (the barrier maximum) and 0.76, respectively. For increasing field one

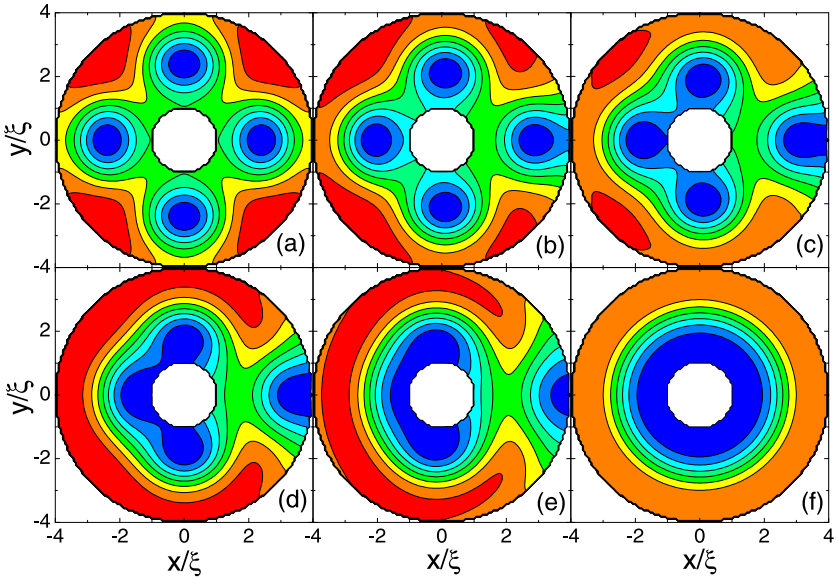

Fig. 7.17 The Cooper-pair density for the saddle point state transition between a multivortex state with $L = 5$ and a giant vortex state with $L = 4$ at $H_0/H_{c2} = 0.83$ (a), 0.88 (b), 0.93 (c), 0.965 (d), 1.03 (e) and 1.06 (f). High Cooper-pair density is given by red regions, low Cooper-pair density by blue regions.

vortex moves from the superconducting material to the outer boundary and hence the vorticity changes from $L = 9$ to $L = 8$. Notice that the vorticity of the interior boundary of the ring does not change.

The fourth type of saddle point state to discuss is the $L \to L+1$ transition between two multivortex states with the same vorticity in the superconducting material but with a different vorticity in the hole. For $R_o/\xi = 4$ and $R_o/\xi = 6$ we did not find such transitions regardless of the hole radius. This means that at least for these radii there is no transition between such states which describes the motion of one vortex from the hole through the superconducting material towards the outer insulator.

Finally, we investigated the influence of the hole radius on the barrier for a fixed outer ring radius. Fig. 7.19(a) shows the maximum barrier height, i.e. the barrier height at the thermodynamic equilibrium $L \to L + 1$ transition, as a function of the hole radius R_i for a ring with radius $R_o = 4.0\xi$ for the transition between the Meissner state and the $L = 1$ state (red curve) and for the transition between the $L = 1$ and the $L = 2$ state (blue curve). For increasing hole radius, the barrier height of the first transition rapidly increases in the range $R_i = 0.1\xi$ to $R_i = 1.5\xi$ and decreases slowly afterwards. For a superconducting disk with radius $R_o = 4.0\xi$ with a hole in the center with radius $R_i = 1.5\xi$ the maximum barrier height for the $0 \to 1$ transition

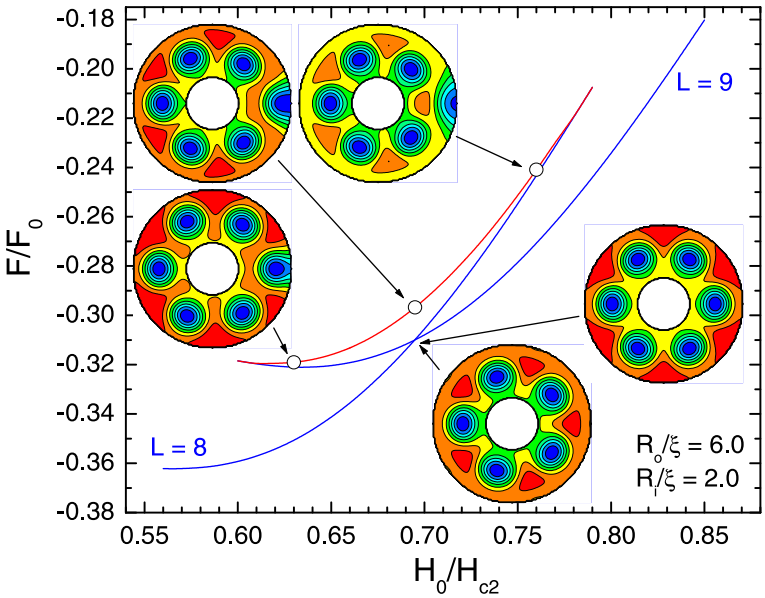

Fig. 7.18 The free energy of the multivortex states with $L = 8$ and $L = 9$ (blue curves) and the saddle point state (red curves) between these multivortex states for a superconducting ring with $R_o = 6.0\xi$ and $R_i = 2.0\xi$ as a function of the applied magnetic field. The lower insets show the Cooper-pair density $|\Psi|^2$ at the transition field $H_0/H_{c2} = 0.695$ for $L = 8$ and $L = 9$. The upper insets show the Cooper-pair density $|\Psi|^2$ for the saddle point states indicated by the open circles, i.e. at $H_0/H_{c2} = 0.63$ (a), 0.695 (b) and 0.76 (c). High Cooper-pair density is given by red regions, low Cooper-pair density by blue regions.

is twice as large as for a superconducting disk without a hole. The barrier height of the second transition first decreases, then rapidly increases in the range $R_i = 0.6\xi$ to $R_i = 2.5\xi$ and then slowly decreases again. In this case the maximum barrier height for a superconducting disk with a hole with radius $R_i = 2.5\xi$ is three times as large as for a superconducting disk without a hole. Hence, changing the hole radius strongly influences the maximum height of the barrier. In Fig. 7.19(b) we plot the characteristic magnetic fields of the barrier as a function of the hole radius, i.e. the transition magnetic field H_{tr}, the expulsion magnetic field H_e and the penetration magnetic field H_p, for the $0 \to 1$ transition by red curves and for the $1 \to 2$ transition by the blue curve. For the $0 \to 1$ transition the characteristic magnetic fields decrease with increasing hole radius. For the $1 \to 2$ transition the characteristic magnetic fields first increase to a maximum and then decrease. This behaviour was described and explained in previous chapters [see e.g. Fig. 5.13]. Notice that the position of the minimum in U_{max} coincides with the position of the maximum in H_{tr}.

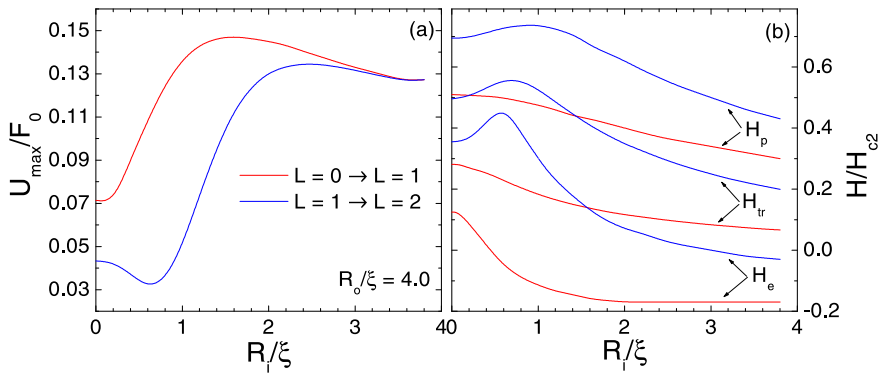

Fig. 7.19 (a) The maximum barrier height as a function of the hole radius R_i for a ring with radius $R_o = 4.0\xi$ for the transition between the Meissner state and the $L = 1$ state (red curve) and the transition between the $L = 1$ state and the $L = 2$ state (blue curve); and (b) the transition magnetic field H_{tr}, the expulsion magnetic field H_e and the penetration magnetic field H_p as a function of the hole radius R_i for the transition between the Meissner state and the $L = 1$ state (red curve) and the transition between the $L = 1$ state and the $L = 2$ state (blue curve).

7.5 CONCLUSIONS

We studied the saddle points for transitions between different vortex states for thin superconducting disks and rings. A distinction was made between small systems where the confinement effects dominate and larger systems where multivortices can nucleate for certain magnetic fields. At the entrance of the vortex into the superconducting material the superconducting density becomes zero at a certain point at the edge of the disk or ring. Such a zero in the order parameter acts as a phase slip center which allows the vorticity to increase with one unit. For the case of the ring the vortex may enter (or exit) the superconducting material from the inner boundary or from the outer boundary of the ring.

We studied the transition between two giant vortex states with different vorticity L. One vortex moves through the superconducting material to the center of the disk or to the hole. During the transition the position of this vortex in the superconductor can be determined very precisely, because the Cooper-pair density is exactly zero in the center of this vortex. The transition between a multivortex state and a giant vortex state with different vorticity L is also described. One vortex leaves (enters) the superconductor while the other vortices move towards (away from) the center of the disk. For large enough disk/ring radii, we calculated the transition between two multivortex states. We found such transitions between two multivortex states with different vorticity L in the superconductor but with the same vorticity in the center/hole. One vortex enters/leaves the superconductor while the other vor-

tices rearrange themselves. Transitions between different multivortex states with the same vorticity in the superconducting material but different vorticity in the hole were not found for the considered ring configurations, which means that transitions between such states do not occur in these particular cases.

The maximum height of the energy barrier always decreases for increasing L. Near the maximum, the barrier height decreases linearly and its slope at the left side ($H \lesssim H_{max}$) of the maximum is not equal to the slope at the right side ($H \gtrsim H_{max}$). The barrier shape and height strongly depend on the radius of the hole in the center of the disk.

Publications. The results presented in this chapter were published as:

- B. J. Baelus, F. M. Peeters, and V. A. Schweigert, *Saddle point states and energy barriers for vortex entrance and exit in superconducting disks and rings*, Phys. Rev. B **63**, 144517 (2001) *(12 pages)*.

8

Summary

In this thesis we investigated theoretically how the critical parameters of mesoscopic superconductors can be improved and how the superconducting state looks alike. Mesocopic superconducting samples have sizes comparable to one of the two characteristic length scales: the coherence length ξ or the magnetic penetration length λ. While in bulk superconductors penetrating vortices form a triangular lattice due to the vortex-vortex repulsion and the critical parameters and the properties are determined by the material, in mesoscopic superconductors the situation is more complicated. In mesoscopic superconductors there is a competition between the triangular configuration of the vortex lattice and the boundary which tries to impose its geometry on the vortex lattice.

On the one hand we investigated the influence of the sample geometry on the critical parameters and on the vortex configuration. Changing the sample size and geometry effects the critical field and the critical current, but not the critical temperature. On the other hand we investigated the influence of the sample surface on the critical parameters. Changing the properties of the surface does effect the critical temperature.

In the first part of this thesis, we considered singly connected mesoscopic superconductors, which have only one closed superconductor/vacuum boundary in the plane of the superconductor, like superconducting disks, squares, triangles and cylinders. In the second part, multiply connected superconductors were studied, like rings.

In **chapter 1** a general introduction was given. We also derived the Ginzburg-Landau equations, which are the central equations in the theoretical framework of this thesis. Furthermore, the characteristic length scales and the

difference between type-I and type-II superconductors were discussed. Next, we defined giant vortex and multivortex states for mesoscopic superconductors, and the vorticity L which characterizes the different vortex configurations.

In **chapter 2** the results of Schweigert, Peeters and Deo were discussed. They considered mesoscopic superconducting disks, which are the most simple singly connected superconductors. Therefore, they developed two theoretical formalisms, which will be adapted and used in this thesis. The 2D formalism assumes axial symmetry, which means that only the giant vortex state can be described. The advantage of this assumption is that the dimensions of the Ginzburg-Landau equations and, thus, the computer time, is reduced. The 3D formalism does not assume axial symmetry and solves the general Ginzburg-Landau equations. Within this theory it is also possible to study multivortices.

Schweigert, Peeters and Deo found that in small disks only the giant vortex state nucleates because the circular symmetric sample boundary imposes its symmetry on the vortex configuration. In larger disks, on the other hand, multivortex states can nucleate in some magnetic field regions and the multivortices are situated on a ring. By changing the radius and the thickness of the disk, one alters the critical magnetic field, the number of possible L states and the vortex configuration. The theoretical results obtained within the Ginzburg-Landau theory correspond with the experimental results of Geim *et al.* using Hall magnetometry [2, 59].

The effect of the geometry of thin superconductors on the vortex state is the subject of **chapter 3**. Therefore, we considered superconducting disks, squares and triangles with the same surface area $S = \pi 16\xi^2$ and the same thickness $d = 0.1\xi$ for $\kappa = 0.28$. For these three geometries the free energy and the magnetization of the different giant and multivortex states is calculated as a function of the applied magnetic field.

Multivortex states were found for disks as well as for squares and triangles for several values of the vorticity. For given L, the vortex state was different in the three geometries due to the fact that the vortex lattice tries to adapt to the geometry of the sample. This influences considerably the stability range of the different vortex states. For squares and triangles we found magnetic field regions where there is a coexistence between a giant vortex state in the center and several separated vortices in the direction of the sample corners. Near the superconducting/normal transition we do not find multivortices, anti-vortices or a combination of them, but we find surface superconductivity. Only extremely close to the superconducting/normal transition vortex configurations containing anti-vortices are possible [63, 64].

The study of the magnetic field distribution across and around the superconductor showed clearly the demagnetization effects, which are very important for samples of finite thickness. The vector plots of the superconducting current showed spots where the current flows in clockwise direction, which

could indicate anti-vortices. From the phase of the order parameter and the Cooper-pair density we conclude that these spots are not anti-vortices, but correspond to back flow currents which are typically present near sharp obstacles, i.e. corners in our case.

We also investigated the stability of the vortex states with vorticity L by calculating the magnetic field range over which the vortex states with vorticity L are stable. We found that this stability range sensitively depends on the sample geometry. As a function of L we found enhanced stability for the triangle for $L = 3$ and for the square for $L = 4$.

Finally, we also included temperature by calculating a $H - T$ phase diagram for the disk, the square and the triangle. With sharper sample corners, we found that for fixed temperature, the superconducting/normal transition field H_{c3} moves to higher fields, and for fixed field, the critical temperature increases. The theoretical phase boundaries were in good agreement with the experimentally measured results of Refs. [24, 63, 64].

In **chapter 4** we investigated the effect of the enhancement of surface superconductivity on the critical field and the critical temperature for superconducting cylinders with radii comparable to the coherence length ξ. We also studied the influence of the Ginzburg-Landau parameter κ. A distinction was made between cylinders with small radii where the confinement effects dominate and only giant vortex states exist, and cylinders with a larger radius where multivortices can nucleate for certain magnetic fields and vorticities.

Generally, increasing surface superconductivity leads to a more negative free energy at zero magnetic field and to a higher superconducting/normal transition field. We also studied the magnetic field distribution, the Cooper-pair density and the current density for different values of the surface enhancement. For increasing surface superconductivity more magnetic field can be expelled from the cylinder and the giant vortex in the center is compressed more. Therefore, higher currents are induced near the boundary and near the giant vortex. The Cooper-pair density close to the boundary increases, and for small cylinders this also influences the Cooper-pair density in the center.

The $H - T$ phase diagrams showed that the critical temperature depends on the surface superconductivity, while it is independent of κ. With increasing surface superconductivity the critical temperature increases for fixed magnetic field and the critical magnetic field increases for fixed temperature.

We also obtained $(-\xi/b) - H$ phase diagrams, where a higher value of $-\xi/b$ corresponds to an enhancement of the surface superconductivity. In type-I cylinders the surface enhancement has drastic consequences. Even at low κ the surface enhancement leads to transitions between different L states and thus to type-II behavior. Moreover, as a function of the magnetic field the superconducting ground state transits from the Meissner state to a vortex state with $L > 1$ over a range of $-\xi/b$ values. Therefore, we can conclude that increasing $-\xi/b$ for type-I superconductors seems to have a similar effect as increasing κ for fixed $-\xi/b$ for certain properties of the superconducting

cylinder. In type-II cylinders we found that the magnetic field range over which the ground state has a particular vorticity L is almost the same for all $L > 1$. This magnetic field range decreases with increasing cylinder radius.

If the cylinder radius is sufficiently large multivortex states can nucleate and we studied the influence of the surface enhancement on the nucleation of these states. We found that at fixed field and with increasing surface superconductivity the multivortices move to the center creating a giant vortex state. Thus, surface enhancement destabilizes the multivortex state.

Up to now, we considered singly connected superconductors. In the second part of this thesis we considered multiply connected superconductors. The superconducting state and the critical parameters of superconducting disks with a hole inside, or, briefly, superconducting rings, are investigated in **chapter 5**. These rings are the most simple example of doubly connected superconductors.

The effect of the size and the position of the hole on the vortex configuration was investigated. For small superconducting disks with a hole in the center, only giant vortex states exist and for increasing hole radius R_i more and more L states occur before the superconductor becomes normal. For larger superconducting disks with a hole in the center, we found multivortex states in a certain magnetic field range. For certain fixed hole radius, and for increasing magnetic field, the giant vortex state changes into a multivortex state and back into the giant-vortex state (re-entrant behaviour) before superconductivity is destroyed. Near the superconducting/normal transition and for a narrow superconducting ring (i.e. $R_i \approx R_o$) we always found the giant vortex state as the ground state irrespective of the size, thickness and width of the ring. The effect of the position of the hole, i.e. decreasing the symmetry of the system, was also investigated. Moving the hole off-center: 1) can transform the $L \to L+1$ transition into a continuous one, 2) the stability of metastable states is strongly reduced, 3) it favours the multivortex state even for small disks, and 4) the winding number L can increase even at a fixed magnetic field.

The flux through the hole is *not* quantized. We were able to define an effective ring size ρ^* such that inside this ring the flux is exactly quantized. The value of ρ^* depends on L and is an oscillating function of the magnetic field. For narrow rings it is only possible to define such a ρ^* in narrow ranges of the magnetic field and the flux through the hole is very close to the applied flux. The magnetic fields from the screening currents are too small to substantially modify the flux inside the ring.

Experimentally, large and narrow superconducting mesoscopic rings were studied by Pedersen *et al.* [32] using Hall magnetometry. The experimental results were qualitatively in good agreement with our numerical results. They found, for example, that the flux increase to induce the transition from one L state to another is quantized in their large and narrow rings.

In **chapter 6** we investigated the magnetic coupling between two concentric mesoscopic superconductors with nonzero thickness. When a second superconductor is placed in the center of a superconducting ring, it feels a non-uniform field, which is the superposition of the uniform applied field and the field expelled from the outer ring. Also the first ring will be influenced by the magnetic field expelled from the superconductor in the center. So, both superconductors are coupled magnetically. This results in substantial changes of the superconducting properties.

From the study of the free energy we learned that extra ground state transitions occur in comparison with the single ring case. These are transitions where the total vorticity stays the same, but the vorticity of the inner superconductor changes by one unit. We also found that the free energy of the double ring system is not exactly the same as the sum of the free energies of the two uncoupled single rings which is another signature of the magnetic coupling of both rings. This interaction enhances with increasing sample thickness. We calculated the expelled field for the ring-ring configuration which showed that as compared with a single ring more, or less, field can be expelled or attracted depending on the vorticities of both superconductors.

The behaviour of the Cooper-pair density, the magnetic field profile and the current density was calculated. Since an extra superconductor is placed in the center, the magnetic field will be expelled from this superconductor or will be compressed in the center of it, which results in a higher or a lower magnetic field density between the two superconductors. The current in both rings exhibits extra jumps at the transition fields where the vorticity of the other ring increases or decreases by one. The reason is that at these applied fields the total magnetic field in the region between the two superconductors changes.

Finally, we calculated a $H - T$ phase diagram. Up to now, both rings had the same width and the same critical temperature. Therefore, only the outer ring would be superconducting at the superconducting/normal transition and the $H - T$ phase diagram shows no effect of the magnetic coupling. To circumvent this problem the T_c of the outer ring was artificially lowered in the experiment of Ref. [26] by applying a sufficiently large external current through the outer ring. Theoretically, we investigated what happens if the inner ring is made of a different material with a higher critical temperature. The $H - T$ phase diagram showed that the nucleation field of the double ring equals the one of the outer ring at low temperatures and the one of the inner ring at higher temperatures.

Finally, the energy barriers and the saddle points for transitions between different vortex states for thin superconducting disks and rings are studied in **chapter 7**. Again, a distinction was made between small systems where the confinement effects dominate and larger systems where multivortices can nucleate for certain magnetic fields. At the entrance of the vortex into the superconducting material the superconducting density becomes zero at a cer-

tain point at the edge of the disk or ring. Such a zero in the order parameter acts as a phase slip center which allows the vorticity to increase with one unit. For the case of the ring the vortex may enter (or exit) the superconducting material from the inner boundary or from the outer boundary of the ring.

We studied the transition between two giant vortex states with different vorticity L. One vortex moves through the superconducting material to the center of the disk or to the hole. During the transition the position of this vortex in the superconductor can be determined very precisely, because the Cooper-pair density is exactly zero in the center of this vortex. The transition between a multivortex state and a giant vortex state with different vorticity L is also described. One vortex leaves (enters) the superconductor while the other vortices move towards (away from) the center of the disk. For large enough disk/ring radii, we calculated the transition between two multivortex states. We found such transitions between two multivortex states with different vorticity L in the superconductor but with the same vorticity in the center/hole. One vortex enters or leaves the superconductor while the other vortices rearrange themselves. Transitions between different multivortex states with the same vorticity in the superconducting material but different vorticity in the hole were not found for the considered ring configurations, which means that transitions between such states do not occur in these particular cases.

The maximum height of the energy barrier always decreases for increasing L. Near the maximum, the barrier height decreases linearly and its slope at the left side of the maximum is not equal to the slope at the right side. The barrier shape and height strongly depend on the radius of the hole in the center of the disk.

9

Samenvatting

In deze thesis onderzoeken we theoretisch hoe de kritische parameters van mesoscopische supergeleiders verbeterd kunnen worden en hoe de supergeleidende toestand eruitziet. Mesoscopische supergeleiders hebben afmetingen vergelijkbaar met de coherentielengte ξ of de penetratiediepte λ. Terwijl in bulksupergeleiders de binnendringende vortices een driehoekig rooster vormen tengevolge van de vortex-vortexafstoting en de kritische parameters en de eigenschappen bepaald worden door het materiaal, is de situatie in mesoscopische supergeleiders veel complexer. In mesoscopische supergeleiders is er een competitie tussen de driehoekige configuratie en de rand die zijn symmetrie probeert op te leggen aan de vortexconfiguratie.

Aan de ene kant bestuderen we de invloed van de vorm van de supergeleider op de kritische parameters en de vortexconfiguratie. Een verandering van de vorm en de grootte zal leiden tot een wijziging van het kritische magneetveld en de kritische stroom, maar niet van de kritische temperatuur. Aan de andere kant onderzoeken we de invloed van de rand van de supergeleider op de kritische parameters. Het veranderen van de randeigenschappen beïnvloedt wel degelijk de kritische temperatuur.

In het eerste deel van de thesis worden enkelvoudig samenhangende supergeleiders bestudeerd. Dit zijn supergeleiders die maar door één rand gescheiden worden van het omringende vacuüm, zoals bijvoorbeeld supergeleidende schijfjes, vierkanten, driehoeken en cilinders. In het tweede deel worden dan de meervoudig samenhangende supergeleiders bestudeerd, zoals ringen.

In **hoofdstuk 1** wordt een algemene inleiding over supergeleiding gegeven. We leiden ook de Ginzburg-Landauvergelijkingen af, de centrale vergelijkingen in het theoretische kader van deze thesis. Verder worden de karakteristieke

lengteschalen en het verschil tussen type-I en type-II supergeleiders besproken. Voor mesoscopische supergeleiders worden vervolgens de "giant"-vortextoestand en de multi-vortextoestand gedefinieerd, evenals de vorticiteit L die de verschillende vortexconfiguraties karakteriseert.

In **hoofdstuk 2** worden de resultaten van de studie van Schweigert, Peeters en Deo over supergeleidende schijfjes, de meest eenvoudige enkelvoudig samenhangede supergeleiders, besproken. Hiervoor ontwikkelden zij twee theoretische formalismes. Het zijn deze numerieke formalismes die in deze thesis gebruikt zullen worden. Het 2D formalisme gaat uit van axiale symmetrie waardoor enkel de axiaal symmetrische giant-vortextoestanden beschreven kunnen worden. Deze veronderstelling heeft als voordeel dat de dimensies van de Ginzburg-Landauvergelijkingen gereduceerd worden, waardoor ook de rekentijd drastisch afneemt. Het 3D formalisme maakt deze veronderstelling niet en lost de Ginzburg-Landauvergelijking op in hun algemene vorm. Met deze theorie is het dan ook mogelijk om multi-vortices te bestuderen.

Schweigert, Peeters en Deo vonden dat in kleine schijfjes enkel de giant-vortextoestand voorkomt omdat de rand van de supergeleider zijn axiale symmetrie oplegt aan de vortextoestand. In grotere schijfjes, daarentegen, kan de multi-vortextoestand bij bepaalde magneetvelden voorkomen. In het geval van een schijfje bevinden de multi-vortices zich op een ring. Door de straal en de dikte van de schijf te veranderen, wijzigt men het kritische magneetveld, het aantal mogelijke L-toestanden en de vortexconfiguratie. De theoretische resultaten verkregen met de Ginzburg-Landautheorie corresponderen bovendien goed met de experimentele resultaten van Geim *et al.* waarbij gebruik gemaakt wordt van een Hallmagnetometer [A. K. Geim *et al.*, Nature (London) **390**, 256 (1997); F. M. Peeters *et al.*, Phys. C **332**, 255 (2000)].

Het effect van de geometrie van dunne supergeleiders op de vortextoestand is het onderwerp van **hoofdstuk 3**. Hiervoor beschouwen we supergeleidende schijven, vierkanten en driehoeken met dezelfde oppervlakte $S = \pi 16\xi^2$ en dezelfde dikte $d = 0.1\xi$ bij $\kappa = 0.28$. Voor deze drie geometrieën wordt de vrije energie en de magnetisatie van de verschillende giant-vortextoestanden en multi-vortextoestanden berekend als een functie van het aangelegde magneetveld.

Multi-vortextoestanden worden zowel voor de schijf als voor het vierkant en de driehoek gevonden voor verschillende waarden van de vorticiteit L. Voor gegeven L is de vortextoestand verschillend voor de drie geometrieën, omdat het vortexrooster zich probeert aan te passen aan de vorm van de supergeleider. Hierdoor wordt het stabiliteitsgebied van de verschillende vortextoestanden sterk beïnvloed. Verder vinden we voor vierkanten en driehoeken magneetveldgebieden waar voor een bepaalde vorticiteit de vortextoestand gegeven wordt door een combinatie van een giant-vortex in het centrum en verschillende multi-vortices naar de hoeken toe. In de buurt van de supergeleidende/normaal-overgang vinden we geen multi-vortices, anti-vortices of een combinatie van deze, maar wel oppervlaktesupergeleiding. Enkel extreem

dicht bij de supergeleidende/normaal overgang kunnen anti-vortices stabiel worden [L. F. Chibotaru *et al.*, Nature (London) **408**, 833 (2000); Phys. Rev. Lett. **86**, 1323 (2001)].

De studie van het magneetveldprofiel in en rond de supergeleider toont duidelijk de demagnetisatie-effecten die heel belangrijk zijn voor supergeleiders met eindige dikte. De vectorplots van de supergeleidende stroomdichtheid tonen plaatsen waar de stroom in tegengestelde richting beweegt, wat zou kunnen duiden op anti-vortices. Maar, door een onderzoek van de fase van de ordeparameter en de Cooper-paardichtheid weten we dat het niets te maken heeft met deze anti-vortices.

We bestuderen ook de stabiliteit van de verschillende vortextoestanden met vorticiteit L door het magneetveldgebiedje te berekenen waar deze L-toestanden stabiel zijn. Het stabiliteitsgebied hangt zeer sterk af van de vorm van de supergeleider. Als een functie van de vorticiteit vinden we een verhoogde stabiliteit voor de driehoek bij $L = 3$ en voor het vierkant bij $L = 4$.

Tenslotte wordt ook de temperatuur in rekening gebracht en stellen we een $H - T$ fasediagram op voor de schijf, het vierkant en de driehoek. Naargelang de hoeken van de supergeleider scherper worden, stijgt het kritische magneetveld bij een gegeven temperatuur en de kritische temperatuur bij een gegeven magneetveld. Het theoretische fasediagram komt bovendien goed overeen met de experimenteel gemeten fasediagrammen [V. Bruyndoncx *et al.*, Phys. Rev. B 60, 4285 (1999); L. F. Chibotaru *et al.*, Nature (London) **408**, 833 (2000); Phys. Rev. Lett. **86**, 1323 (2001)].

In **hoofdstuk 4** bestuderen we het effect van de verhoging van de oppervlaktesupergeleiding op het kritische magneetveld en de kritische temperatuur. Voor deze studie worden supergeleidende cilinders beschouwd met stralen vergelijkbaar met de coherentielengte ξ. Ook de invloed van de Ginzburg-Landauparameter κ wordt bekeken. Opnieuw wordt er een onderscheid gemaakt tussen cilinders met kleine stralen, waar enkel de giant-vortextoestand voorkomt, en cilinders met grotere stralen, waar ook multi-vortices kunnen verschijnen.

In het algemeen leidt een vermeerdering van de oppervlaktesupergeleiding tot een meer negatieve vrije energie bij magneetveld nul en tot een hoger kritisch magneetveld. Ook wordt het magneetveldprofiel, de Cooper-paardichtheid en de stroomdichtheid bekeken voor verschillende waarden van de oppervlaktesupergeleiding. Door een toename van de oppervlaktesupergeleiding kan het magneetveld sterker afgestoten worden door de supergeleider en wordt de giant-vortex in het centrum meer comprimeerd. Daardoor worden hogere stromen in de buurt van het oppervlak en van de giant-vortex geïnduceerd. Door de toename van de oppervlaktesupergeleiding vermeerdert vanzelfsprekend ook de Cooper-paardichtheid in de buurt van het oppervlak, en voor cilinders met kleinere stralen beïnvloedt dit ook de Cooper-paardichtheid in het centrum.

De $H-T$ fasediagrammen tonen aan dat de kritische temperatuur afhangt van de oppervlaktesupergeleiding, terwijl ze onafhankelijk is van κ. Met de toename van de oppervlaktesupergeleiding verhoogt het kritische magneetveld bij een gegeven temperatuur en ook de kritische temperatuur voor een gegeven magneetveld.

Ook $(-\xi/b) - H$ fasediagrammen worden berekend, waarbij een hogere waarde van $-\xi/b$ overeenkomt met een toename van de oppervlaktesupergeleiding. In type-I cilinders heeft een verhoging van de oppervlaktesupergeleiding drastische gevolgen. Zelfs bij lage κ leidt een toename van de oppervlaktesupergeleiding tot overgangen tussen verschillende L-toestanden en dus tot type-II gedrag. Bovendien gaat de grondtoestand voor bepaalde waarden van $-\xi/b$ over van de Meissnertoestand naar een vortextoestand met $L > 1$ als een functie van het magneetveld. Daarom kunnen we concluderen dat bij type-I materialen een vermeerdering van $-\xi/b$ hetzelfde effect lijkt te hebben als een verhoging van κ bij vaste $-\xi/b$. In type-II cilinders vonden we dat het magneetveldinterval waar de grondtoestand vorticiteit L heeft bijna hetzelfde is voor alle waarden van $L > 1$. Dit interval verkleint met toenemende cilinderstraal.

Als de straal van de cilinder voldoende groot is, kunnen multi-vortices stabiel worden en kunnen we de invloed van de toename van de oppervlaktesupergeleiding op de multi-vortextoestanden bestuderen. We vinden dat bij een gegeven magneetveld en met toenemende $-\xi/b$ de multi-vortices naar het centrum bewegen om daar samen te smelten tot een giant-vortex. Dit betekent dus dat een vermeerdering van de oppervlaktesupergeleiding de multi-vortextoestand destabiliseert.

Tot nu toe bestudeerden we enkelvoudig samenhangende supergeleiders. In het tweede deel van deze thesis bekijken we meervoudig samenhangende supergeleiders. De supergeleidende toestand en de kritische parameters van supergeleidende schijven met een holte erin of, korter gezegd, supergeleidende ringen worden onderzocht in **hoofdstuk 5**. Deze ringen zijn het meest eenvoudige voorbeeld van een meervoudig samenhangende supergeleider. Het effect van de grootte en de positie van de holte op de vortexconfiguratie en de kritische parameters wordt bestudeerd. In kleine schijven met een holte in het centrum komt alleen de giant-vortextoestand voor en met toenemende holtestraal R_i verschijnen meer en meer L-toestanden voordat de supergeleider normaal wordt. In grotere schijven met een holte in het centrum vinden we multi-vortextoestanden bij bepaalde magneetvelden. Voor een bepaalde vaste holtestraal en bij toenemend magneetveld verandert de giant-vortextoestand in een multi-vortextoestand en terug in een giant-vortextoestand ('re-entrant' gedrag) voordat de supergeleiding vernietigd wordt. In de buurt van de supergeleidende/normaal overgang is de grondtoestand altijd een giant-vortextoestand ongeacht de grootte, de dikte of de breedte van de ring. De invloed van de positie op de holte wordt ook onderzocht. Door de holte weg van het centrum te plaatsen: 1) kan de $L \to L+1$ overgang continu worden,

2) wordt de stabiliteit van de metastabiele toestanden sterk gereduceerd, 3) wordt de multi-vortextoestand zelfs energetisch voordeliger bij kleine schijven, en 4) kan de vorticiteit L toenemen, zelfs bij een vast magneetveld.

De flux door de holte is niet gekwantiseerd. Men kan een effectieve ringstraal ρ^* definiëren zodat binnen deze straal de flux exact gekwantiseerd is. De waarde van ρ^* hangt af van L en is een oscillerende functie van het magneetveld. In het geval van smalle ringen is het alleen mogelijk zo'n ρ^* te definiëren in kleine magneetveldintervallen en kan de flux door de holte benaderd worden door de externe flux. De magneetvelden afkomstig van de geïnduceerde stromen zijn dan immers te klein om de flux in de ring substantieel te wijzigen.

Experimenteel werden grote maar smalle ringen bestudeerd door Pedersen *et al.* met behulp van een Hallmagnetometer. De experimentele resultaten komen kwalitatief goed overeen met de numerieke. Zo vonden ze bijvoorbeeld dat de flux die nodig is om van één L-toestand naar een andere te gaan gekwantiseerd is in grote maar smalle ringen [S. Pedersen *et al.*, Phys. Rev. B **64**, 104522 (2001)].

In **hoofdstuk 6** wordt de magnetische koppeling tussen twee supergeleiders met eindige dikte onderzocht. Een tweede supergeleider, geplaatst in het centrum van een supergeleidende ring, voelt een niet-uniform magneetveld, namelijk de superpositie van het uniforme externe magneetveld en het veld dat afgestoten wordt door de buitenste ring. Ook deze ring zal beïnvloed worden door het magneetveld afgestoten door de supergeleider in het centrum. Dit maakt dat beide supergeleiders magnetisch gekoppeld zijn wat resulteert in een verandering van de supergeleidende eigenschappen.

Door de vrije energie te bestuderen ontdekken we extra grondtoestandsovergangen vergeleken met de enkele ring. Bij deze extra overgangen blijft de vorticiteit van de buitenste ring gelijk, maar verandert de vorticiteit van de supergeleider in het centrum met één eenheid. We vonden ook dat de vrije energie van de dubbele ring niet exact gelijk is aan de som van de vrije energieën van de ontkoppelde enkele ringen. Dit is opnieuw een indicatie van de magnetische koppeling tussen de twee ringen. Deze interactie vermeerdert met een grotere dikte van de schijven. Uit de berekening van de magnetisatie blijkt dat de dubbele ring meer of minder veld afstoot in vergelijking met een enkele ring, afhankelijk van de vorticiteiten van beide supergeleiders.

Het gedrag van de Cooper-paardichtheid, het magneetveldprofiel en de stroomdichtheid wordt berekend. Door de extra supergeleider in het centrum werd het magneetveld ofwel afgestoten door deze supergeleider ofwel gecomprimeerd in het centrum, wat resulteert in een vermeerdering of vermindering van het magneetveld tussen de twee supergeleiders. De stroom in beide ringen vertoont extra sprongen bij de overgangsmagneetvelden waar de vorticiteit van de andere ring verandert. De reden is dat bij deze velden het totale magneetveld in het gebied tussen de twee supergeleiders verandert.

Tenslotte wordt ook het $H - T$ fasediagram berekend. Tot nu toe werd enkel de situatie beschouwd waarbij beide ringen dezelfde breedte en dezelfde kritische temperatuur hadden. In dit geval zou in de buurt van de supergeleidende/normaal overgang enkel de buitenste ring supergeleidend zijn en heeft de magnetische koppeling geen invloed op het $H - T$ fasediagram. Experimenteel omzeilt men dit probleem door een een voldoende hoge stroom door de buitenste ring te sturen waardoor de kritische temperatuur van deze ring verlaagt [Morelle *et al.*, Phys. Rev. B. **64**, 064516 (2001)]. Theoretisch onderzoeken we wat er gebeurt als de binnenste ring gemaakt is van een ander materiaal met een hogere kritisch temperatuur. Het $H - T$ fasediagram toont dat het kritische magneetveld van de dubbele ring gelijk is aan dit van de buitenste ring bij lage temperaturen en aan dit van de binnenste ring bij hogere temperaturen.

De energiebarrières en de zadelpunten die de overgangen beschrijven tussen verschillende supergeleidende toestanden in schijven en ringen worden bestudeerd in **hoofdstuk 7**. Opnieuw wordt er een onderscheid gemaakt tussen kleine systemen waarin enkel de giant-vortextoestand voorkomt en grotere systemen waar ook multi-vortices stabiel kunnen zijn. Bij het binnenkomen van een vortex in het supergeleidende materiaal wordt de Cooper-paardichtheid nul op een bepaalde plaats op de rand van de schijf of de ring. Dit punt fungeert dan als een centrum waar de fase kan veranderen, wat toelaat dat de vorticiteit met één eenheid verandert. In het geval van de ring kan de vortex het materiaal binnendringen langs de binnenrand of de buitenrand.

We bestuderen de overgang tussen twee giant-vortextoestanden met verschillende vorticiteit L. Eén vortex beweegt door het supergeleidende materiaal naar het centrum van de schijf of naar de holte van de ring. Gedurende deze overgang kan de positie van de vortex exact bepaald worden omdat de Cooper-paardichtheid nul is in het centrum van de vortex. De overgang tussen een multi-vortextoestand en een giant-vortextoestand met verschillende vorticiteit L wordt ook beschreven. Eén vortex verlaat (komt binnen in) de supergeleider terwijl de andere vortices naar het centrum toe (van het centrum weg) bewegen. Als de schijf of de ring groot genoeg is, kan ook de overgang tussen twee multi-vortextoestanden berekend worden. We vonden zulke overgangen in een ring tussen twee multi-vortextoestanden met een verschillende vorticiteit L in de supergeleider, maar dezelfde vorticiteit in de holte. Eén vortex verlaat of komt binnen in de supergeleider en de andere vortices herschikken zich. Overgangen tussen verschillende multi-vortextoestanden met dezelfde vorticiteit in het supergeleidende materiaal maar een verschillende L in de holte worden niet gevonden voor de beschouwde ringconfiguraties.

De maximale hoogte van de energiebarrières vermindert altijd naarmate L groter wordt. In de buurt van het maximum verandert de barrièrehoogte lineair en de helling aan de linkerzijde en de rechterzijde van het maximum is verschillend. De vorm en de hoogte van de barrière hangen ook sterk af van de straal van de holte in het centrum van de schijf.

References

1. V. V. Moshchalkov, L. Gielen, C. Strunk, R. Jonckheere, X. Qiu, C. Van Haesendonck and Y. Bruynseraede, Nature (London) **373**, 319 (1995).

2. A. K. Geim, I. V. Grigorieva, S. V. Dubonos, J. G. S. Lok, J. C. Maan, A. E. Filippov, and F. M. Peeters, Nature (London) **390**, 256 (1997).

3. H. Kamerlingh Onnes, Leiden Comm. **122b**, 124 (1911).

4. W. Meissner and R. Ochsenfeld, Naturwiss. **21**, 787 (1933).

5. C. Kittel, Introduction to Solid State Physics (John Wiley & Sons, New York, 1996).

6. F. London and H. London, Proc. Roy. Soc. **A149**, 71 (1935).

7. V. L. Ginzburg and L. D. Landau, Zh. Eksperim. i. Teor. Fiz. **20**, 1064 (1950).

8. A. A. Abrikosov, Sov. Phys. JETP **5**, 1175 (1957).

9. J. Bardeen, L. N. Cooper, and J. R. Schrieffer, Phys. Rev. **108**, 1175 (1957).

10. L. P. Gor'kov, Sov. Phys. JETP **9**, 1364 (1959).

11. J. G. Bednorz and K. A. Müller, Z. Phys. B **64**, 189 (1986).

12. A. Schilling, M. Cantoni, J. D. Guo, and H. R. Ott, Nature **363**, 56 (1993).

13. S. N. Putilin, E. V. Antipov, A. M. Abakumov, M. G. Rozova, K. A. Lokshin, D. A. Pavlov, A. M. balagurov, D. V. Sheptyakov, M. Marezio, Physica C **338**, 52 (2000).

14. A. F. Hebard, M. J. Rosseinsky, R. C. Haddon, D. W. Murphy, S. H. Glarum, T. T. M. Palstra, A. P. Ramirex, and A. R. Kortan, Nature **350**, 600 (1991).

15. J. H. Schön, C. Kloc, and B. Batlogg, Nature **408**, 549 (2000).

16. J. H. Schön, M. Dorget, F. C. Beuran, X. Z. Xu, E. Arushanov, M. Lagues, and C. D. Cavellin, Science **293**, 2430 (2001).

17. J. H. Schön, C. Kloc, and B. Batlogg, Science **293**, 2432 (2001).

18. E. Dagotto, Science **293**, 2410 (2001).

19. M. Côté, J. C. Grossman, M. L. Cohen, and S. G. Louie, Phys. Rev. Lett. 81, 697 (1998).

20. V. V. Schmidt, P. Müller, A. V. Ustinov, *The Physics of Superconductors: Introduction to Fundamentals and Applications* (Springer-Verlag, Berlin Heidelberg, 1997).

21. L. D. Landau and E. M. Lifshitz, *Statistical Physics*, 3rd edn., part 1 (Pergamon Press, Oxford, 1980).

22. L. N. Cooper, Phys. Rev. **104**, 1189 (1956).

23. V. V. Moshchalkov, X. G. Qiu, and V. Bruyndoncx, Phys. Rev. B **55**, 11793 (1997).

24. V. Bruyndoncx, J. G. Rodrigo, T. Puig, L. Van Look, and V. V. Moshchalkov, Phys. Rev. B 60, 4285 (1999).

25. V. Bruyndoncx, *Nucleation of Superconductivity and Flux Confinement in Mesoscopic Structures*, PhD thesis, Katholieke Universiteit Leuven, Leuven, 2000.

26. M. Morelle, V. Bruyndoncx, R. Jonckheere, and V. V. Moshchalkov, Phys. Rev. B. **64**, 064516 (2001).

27. F. M. Peeters and X. Q. Li, Appl. Phys. Lett. **72**, 572 (1998).

28. P. Singha Deo, V. A. Schweigert, F. M. Peeters, and A. K. Geim, Phys. Rev. Lett. **79**, 4653 (1997).

29. A.K. Geim, S.V. Dubonos, J.G.S. Lok, M. Henini, and J.C. Maan, Nature (London) **396**, 144 (1998).

30. A. K. Geim, S. V. Dubonos, I. V. Grigorieva, K. S. Novoselov, F. M. Peeters, and V. A. Schweigert, Nature (London) **407**, 55 (2000).

31. A. K. Geim, S. V. Dubonos, J. J. Palacios, I. V. Grigorieva, M. Henini, and J. J. Schermer, Phys. Rev. Lett. **85**, 1528 (2000).

32. S. Pedersen, G. R. Kofod, J. C. Hollingbery, C. B. Sørensen, and P. E. Lindelof, Phys. Rev. B **64**, 104522 (2001).

33. P. G. de Gennes, *Superconducting of Metals and Alloys* (Benjamin, New York, 1966).

34. M. Tinkham, *Introduction to Superconductivity* (McGraw Hill, New York, 1975).

35. D. Saint-James, G. Sarma, and E. J. Thomas, *Type II Superconductivity* (Pergamon Press, Oxford, 1969).

36. L. Neumann and L. Tewordt, Z. Phys. **189**, 55 (1966).

37. A. C. Rose-Innes and E. H. Rhoderick, *Introduction to Superconductivity* (Pergamon Press, Oxford, 1969).

38. C. P. Poole Jr., H. A. Farach, and R. J. Creswick, *Superconductivity* (Academic Press, San Diego, 1995).

39. V. A. Schweigert, F. M. Peeters, and P. Singha Deo, Phys. Rev. Lett. **81**, 2783 (1998).

40. G. F. Zharkov, V. G. Zharkov, and A. Yu. Zvetkov, Phys. Rev. B **61**, 12293 (2000).

41. O. Buisson, P. Gandit, R. Rammel, Y. Y. Wang, and B. Pannetier, Phys. Lett. A **150**, 36 (1990).

42. A. K. Geim, S. V. Dubonos, J. G. S. Lok, I. V. Grigorieva, J. C. Maan, L. Theil Hansen, and P. E. Lindelof, Appl. Phys. Lett. **71**, 2379 (1997).

43. P. Singha Deo, V. A. Schweigert, F. M. Peeters, and A. K. Geim, Physica E **1**, 297 (1997).

44. F. M. Peeters, V. A. Schweigert, and B. J. Baelus, Physica C **369**, 158 (2002).

45. R. Benoist and W. Zwerger, Z. Phys. B **103**, 377 (1997).

46. J. J. Palacios, Physica B **256-258**, 610 (1998).

47. J. J. Palacios, Phys. Rev. B **58**, R5948 (1998).

48. J. J. Palacios, Phys. Rev. Lett. **84**, 1796 (2000).

49. V. A. Schweigert and F. M. Peeters, Phys. Rev. Lett. **83**, 2409 (1999).

50. S. V. Yampolskii and F. M. Peeters, Phys. Rev. B **62**, 9663 (2000).

51. E. Akkermans and K. Mallick, Physica C **332**, 250 (2000).

52. E. Akkermans, D. M. Gangardt, and K. Mallick, Phys. Rev. B **62**, 12427 (2000).

53. E. Akkermans and K. Mallick, J. Phys. A **32**, 7133 (1999).

54. P. Singha Deo, F. M. Peeters, and V. A. Schweigert, Supperlatt. and Microstruct. **25**, 1195 (1999).

55. V. A. Schweigert and F. M. Peeters, Phys. Rev. B **57**, 13817 (1998).

56. V. A. Schweigert and F. M. Peeters, Physica C **332**, 426 (2000).

57. V. A. Schweigert and F. M. Peeters, Phys. Rev. B **60**, 3084 (1999).

58. R. Kato, Y. Enomoto, and S. Maekawa, Phys. Rev. B **47**, 8016 (1993).

59. F. M. Peeters, V. A. Schweigert, B. J. Baelus, and P. S. Deo, Physica C **332**, 255 (2000).

60. V. M. Fomin, V. R. Misko, J. T. Devreese, and V. V. Moshchalkov, Solid State Comm. **101**, 303 (1997).

61. V. M. Fomin, V. R. Misko, J. T. Devreese, and V. V. Moshchalkov, Phys. Rev. B **58**, 11703 (1998).

62. H. T. Jadallah, J. Rubinstein, and P. Sternberg, Phys. Rev. Lett. **82**, 2935 (1999).

63. L. F. Chibotaru, A. Ceulemans, V. Bruyndoncx and V. V. Moshchalkov, Nature (London) **408**, 833 (2000).

64. L. F. Chibotaru, A. Ceulemans, V. Bruyndoncx and V. V. Moshchalkov, Phys. Rev. Lett. **86**, 1323 (2001).

65. J. Bonča and V. V. Kabanov, Phys. Rev. B **65**, 012509 (2002).

66. A. Aftalion and Q. Du, cond-mat/0101370 (2001).

67. S. N. Klimin, V. M. Fomin, J. T. Devreese, and V. V. Moshchalkov, Solid State Commun. **111**, 589 (1999).

68. J. T. Devreese, Physica C **332**, 242 (2000).

69. H. J. Fink and W. C. H. Joiner, Phys. Rev. Lett. **23**, 120 (1969).

70. J. O. Indekeu, F. Clarysse, and E. Montevecchi, in "High-T_c superconductors and Related Materials", Eds. S.-L. Drechsler and T. Mishonov, 487-504 (Kluwer Academic Publishers, Dordrecht, 2001).

71. E. Montevecchi and J. O. Indekeu, Phys. Rev. B **62**, 14359 (2000).

72. E. Montevecchi and J. O. Indekeu, Europhys. Lett. **51**, 661 (2000).

73. E. Montevecchi, *Theory of confinement effects on superconductivity*, Ph. D. Thesis, Katholieke Universiteit Leuven, Leuven (2000).

74. H. J. Fink and A. G. Presson, Phys. Rev. **151**, 219 (1966).

75. H. J. Fink and A. G. Presson, Phys. Rev. **168**, 399 (1968).

76. G. F. Zharkov, cond-mat/0009043.

77. W. A. Little and R. D. Parks, Phys. Rev. Lett. **9**, 9 (1962).

78. J. Berger and J. Rubinstein, Phys. Rev. Lett. **75**, 320 (1995)

79. J. Berger and J. Rubinstein, Phys. Rev. B **56**, 5124 (1997).

80. J. Bardeen, Phys. Rev. Lett. **7**, 162 (1961).

81. G. F. Zharkov, in *Superconductivity, superdiamagnetism, superfluidity*, Ed. V.L. Ginzburg (MIR publishers, Moscow, 1987), p. 126.

82. R. M. Arutynyan and G. F. Zharkov, J. Low Temp. Phys. **52**, 409 (1983).

83. V. Bruyndoncx, L. Van Look, M. Verschuere, and V. V. Moshchalkov, Phys. Rev. B **60**, 10468 (1999).

84. J. Berger and J. Rubinstein, Phys. Rev. B **59**, 8896 (1999).

85. R. P. Groff and R. D. Parks, Phys. Rev. **176**, 567 (1968).

86. B. J. Baelus, S. V. Yampolskii, and F. M. Peeters, cond-mat/0112122 and submitted to Phys. Rev. B.

87. C. P. Bean and J. B. Livingston, Phys. Rev. Lett. **12**, 14 (1964).

88. V. P. Galaiko, Zh. Eksp. Teor. Fiz. **50**, 1322 (1966) [Sov. Phys. JETP **23**, 878 (1966)].

89. B. V. Petukhov and V. R. Chechetkin, Zh. Eksp. Teor. Fiz. **65**, 1653 (1973) [Sov. Phys. JETP **38**, 827 (1974)].

90. A. L. Fetter, Phys. Rev. B **22**, 1200 (1980).

91. V. G. Kogan, Phys. Rev. B **49**, 15874 (1994).

92. A. V. Kuznetsov, D. V. Eremenko, and V. N. Trofimov, Phys. Rev. B **59**, 1507 (1999).

93. M. V. Indenbom, H. Kronmüller, T. W. Li, P. H. Kes, and A. A. Menovsky, Physica C **222**, 203 (1994).

94. Th. Schuster, M. V. Indenbom, H. Kuhn, E. H. Brandt, and M. Konczykowski, Phys. Rev. Lett. **73**, 1424 (1994).

95. E. Zeldov, A. I. Larkin, V. B. Geshkenbein, M. Konczykowski, D. Majer, B. Khaykovich, V. M. Vinokur, and H. Schtrikman, Phys. Rev. Lett. **73**, 1428 (1994).

96. J. S Langer and V. Ambegaokar, Phys. Rev. **164**, 498 (1967).

97. X. Zhang and J. C. Price, Phys. Rev. B **55**, 3128 (1997).

98. P. Singha Deo, V. A. Schweigert, and F. M. Peeters, Phys. Rev. B **59**, 6039 (1999).

99. E. Akkermans, D. M. Gangardt, and K. Mallick, Phys. Rev. B **63**, 064523 (2001).

100. E. M. Horane, J. J. Castro, G. C. Buscaglia, and A. Lopez, Phys. Rev. B **53**, 9296 (1995).

101. M. Zalalutdinov, H. Fujioka, Y. Hashimoto, S. Katsumoto, and Y. Iye, J. Phys. Soc. Jpn. **68**, 2872 (1999).

List of publications

1. B. J. Baelus and F. M. Peeters, *Hall potentiometer in the ballistic regime*, Appl. Phys. Lett. **74**, 1600-1602 (1999).

2. B. J. Baelus, F. M. Peeters, and V. A. Schweigert, *Vortex states in superconducting rings*, Phys. Rev. B **61**, 9734-9747 (2000).

3. F. M. Peeters, V. A. Schweigert, B. J. Baelus, and P. S. Deo, *Vortex matter in mesoscopic superconducting disks and rings*, Physica C **332**, 255-262 (2000).

4. B. J. Baelus, F. M. Peeters, and V. A. Schweigert, *Saddle-point states and energy barriers for vortex entrance and exit in superconducting disks and rings*, Phys. Rev. B **63**, 144517 (2001) *(12 pages)*.

5. S. V. Yampolskii, F. M. Peetes, B. J. Baelus, and H. J. Fink, *Effective radius of superconducting rings and hollow cylinders*, Phys. Rev. B **64**, 052504 (2001) *(4 pages)*.

6. J. J. Palacios, F. M. Peeters, and B. J. Baelus, *Effective lowest Landau level treatment of demagnetization in superconducting mesoscopic disks*, Phys. Rev. B **64**, 134514 (2001) *(6 pages)*.

7. S. V. Yampolskii, B. J. Baelus, F. M. Peeters, and J. Koláček, *Vortex charge in mesoscopic superconductors*, Phys. Rev. B **64**, 144511 (2001) *(10 pages)*.

8. B. J. Baelus, S. V. Yampolskii, F. M. Peeters, E. Montevecchi, and J. O. Indekeu, *Superconducting properties of mesoscopic cylinders with enhanced surface superconductivity*, Phys. Rev. B. **65**, 024510 (2002) *(10 pages)*.

9. S. V. Yampolskii, B. J. Baelus, F. M. Peeters, and J. Koláček, *Electric charges in superconducting mesoscopic samples*, Czech. J. Phys. **52**, 303-306 (2002).

10. B. J. Baelus and F. M. Peeters, *Dependence of the vortex configuration on the geometry of mesoscopic flat samples*, Phys. Rev. B **65,** 104515 (2002) *(12 pages)*.

11. B. J. Baelus, S. V. Yampolskii, and F. M. Peeters, *Magnetic coupling between mesoscopic superconducting rings*, Physica C **369**, 366-369 (2002).

12. F. M. Peeters, V. A. Schweigert, and B. J. Baelus, *Fractional and negative flux penetration in mesoscopic superconducting disks*, Physica C **369**, 158-164 (2002).

13. F. M. Peeters and B. J. Baelus: *Vortex structure in mesoscopic superconductors*, will be published in the proceedings of the NATO Advanced Research Workshop on: "New trends in superconductivity" (Yalta (Ukraine), September 16-20, 2001).

14. B. J. Baelus, S. V. Yampolskii, and F. M. Peeters, *Coupled mesoscopic superconductors*, cond-mat/0112122 and submitted to Phys. Rev. B *(± 10 pages)*.

15. D. Y. Vodolazov, B. J. Baelus, and F. M. Peeters, *Stationary phase slip in quasi one-dimensional rings*, submitted to Phys. Rev. B *(± 6 pages)*.